Fachbereich Chemie, Pharmazie, Geographie
und Geowissenschaften der
Johannes Gutenberg-Universität Mainz

Computation of Molecular Magnetic Properties using Cholesky Decomposition

Dissertation zur Erlangung des Grades
Doktor der Naturwissenschaften
im Promotionsfach Chemie

von

Sophia Burger

geboren in Idar-Oberstein

Mainz, 2025

1. Gutachter: [redacted]
2. Gutachter: [redacted]
Tag der Prüfung: 03.12.2025

Danksagung

Da mein Weg ohne die Unterstützung vieler Menschen nicht möglich gewesen wäre, möchte ich dieses Kapitel nutzen, ihnen meinen Dank auszusprechen.
Selbstverständlich gebührt meinen Eltern [redacted] und [redacted] Dank, die mir das Studium überhaupt ermöglicht und mich bei jeder Entscheidung unterstützt haben. Danken möchte ich in diesem Zuge auch meinem Bruder [redacted], der sich die Zeit genommen hat, meine Arbeit zu lesen, obwohl er sich sonst eher für Finanzen und Kapitalmärkte interessiert. Danke auch an [redacted], der einige Teile meiner Arbeit gelesen hat. Insbesondere meinem langjährigen Partner und besten Freund [redacted] möchte ich danken für die unermüdliche Unterstützung, den unerschütterlichen Glauben an mich und dafür, dass er mir jeden Tag mindestens ein Lächeln beschert - einen besseren Partner kann ich mir nicht vorstellen. Meiner besten Freundin [redacted] möchte ich dafür danken, dass sie mich in jeder Lebenslage versteht, mir viel über Geschichte und Kultur beibringt und schon die ein oder andere töricht anmutende fachliche Frage meinerseits beantwortet hat. Ich bin froh, dass wir trotz großer räumlicher Distanz den täglichen Kontakt pflegen, der mir so viel bedeutet. In diesem Sinne muss auch meinen lieben Kollegen gedankt werden, denn ich genieße die familiäre Atmosphäre in unserer Arbeitsgruppe wirklich sehr (insbesondere in Büro BOB). Ein wesentlicher Beitrag zur guten Stimmung in der Gruppe leistet [redacted], dem ich dafür danken will, dass er immer ein offenes Ohr hat und sich oft und gerne die Zeit genommen hat, einige meiner fachlichen Fragen zu beantworten. Dies gilt selbstverständlich auch für meine zweite Betreuerin [redacted], mit der ich die Zusammenarbeit in den letzten Jahren mehr als genossen habe. Ich möchte ihr für die langjährige fachliche und persönliche Unterstützung, sowie für die fruchtvollen Diskussionen während meiner Promotion danken.
Der größte Dank gebührt jedoch meinem ersten Betreuer [redacted] und zwar nicht nur dafür, dass er mich herzlich in seiner Gruppe aufgenommen und mir die Forschung an spannenden Themen ermöglicht hat, sondern noch für vieles Weitere. Ich bin dankbar für die vielen Stunden, in denen er mir mit Geduld und Ausdauer zahlreiche Themen der Theoretischen Chemie nähergebracht hat. Dank ihm habe ich mich nicht nur fachlich, sondern auch persönlich weiterentwickeln können (hierzu trug auch der ein oder andere Opernbesuch bei). Ich weiß zu schätzen, dass er immer hinter mir steht und an mich und meine fachlichen Kompetenzen glaubt - insbesondere in den Momenten, in denen es mir selbst schwerfällt. Weiterhin möchte ich ihm herzlich dafür danken, dass er mir die Teilnahme an einigen Sommerschulen und Konferenzen sowie einen längeren Aufenthalt in Oslo ermöglicht hat - und einfach generell für die herausragende Betreuung und die interessanten sieben Jahre, die ich nun schon in seiner Forschungsgruppe verbringen durfte.

Contents

1 Introduction

When most people think of the scientific field of chemistry, they often envision people in laboratory coats pouring colorful liquids from one test tube into another. While experimental work is undoubtedly crucial, chemistry also encompasses theoretical approaches that are equally important to scientific progress. The subfield of theoretical chemistry combines mathematical methods and physical principles in order to gain a deeper understanding of the properties of chemical systems and to investigate chemically relevant processes. For example, the mechanism of the prominent Grignard reaction, which is used to synthesize carbon-carbon bonds, could only be fully elucidated through computer simulations in combination with high-level quantum-chemical data.[1] In addition to mechanistic insights, theoretical chemistry has found application in a wide range of other contexts. In cases where experimentalists synthesize a substance but encounter difficulties determining its structure or properties, for example, insights from computational chemistry can often provide the missing piece of the puzzle. Obtaining such insights requires the application of various so-called quantum-chemical methods. They allow the computation of molecular properties that can not only help unravel experimental data but also point the way toward future experiments.[2,3] One example in this context is the existence of the stable cation of cycloheptatriene and the stable anion of cyclopentadiene which were initially predicted theoretically before they were confirmed experimentally.[4,5]

The foundation for quantum-chemical methods is the electronic Schrödinger equation (or the Dirac equation when also considering relativistic effects), whose solution provides not only the energy, but by extension also a plethora of molecular properties like the equilibrium structure, magnetizability, dipole moment, polarizability and more.[2,4] However, an analytic solution to this equation is only possible for up to two particles, but in general not for molecules. Head-Gordon aptly wrote: „The general problem of electronic structure theory is how to apply the principles of quantum mechanics to molecular problems, when we cannot solve the underlying equations exactly“.[6] Approximate solutions to the electronic Schrödinger equation are commonly divided into semi-empirical approaches[7] and ab initio (latin: „from the beginning“) methods, where the former rely on empirical parameters within the theoretical model, whereas the latter are based solely on first-principles calculations.[8] In this work, ab initio methods were employed. The simplest theoretical model in the context of ab initio methods to solve the electronic Schrödinger equation is the Hartree-Fock (HF) approach, a mean field theory that neglects the effect of the so-called electron correlation. The electron correlation energy is given as the difference between the exact energy of the system, i.e. the energy obtained from a solution of the Schrödinger equation, and the HF energy.[9] To obtain more reliable results, approaches to the correlation problem like second-order Møller-Plesset (MP2) perturbation theory[10] or highly accurate coupled-cluster

(CC)[11,12] methods are necessary. In cases where molecules exhibit a multi-configurational character, these so-called single-reference methods break down, making multi-reference approaches[13–18] indispensable. However, none of the mentioned quantum-chemical methods are universally applicable and depending on the problem and the system size, an individual decision must be made as to which method is most suitable. Unfortunately, the more accurate approaches are associated with a significantly higher computational cost and are therefore limited to small or medium-sized systems.

A powerful technique in chemistry for determining molecular structure, stereochemistry, and the electronic environment in synthesized compounds is nuclear magnetic resonance (NMR) spectroscopy.[19] NMR spectra can often be interpreted directly, but there are cases where this is not possible without the support of quantum-chemical calculations. Specifically for exploring exotic molecules, theoretical predictions are of great importance[20–24] since the relationship between the experimentally measured parameters, the NMR shifts, and the structural parameters is not trivial.[3,25,26] The foundations for the prediction of NMR parameters (NMR shielding constants) calculations were established 1950 by Ramsey.[27,28] 20 years later, Ditchfield wrote that „accurate calculations of magnetic shielding constants are still not routinely achieved even for small molecules“.[29] A major issue in the context of computing magnetic properties was the unphysical finding that the results depend on the position of the molecule in the Cartesian coordinate system, the so-called „gauge problem“.[25,26] As early as 1937, Fritz London studied molecular diamagnetism and introduced gauge-including atomic orbitals (GIAOs) in conjunction with magnetic properties.[30] This approach was adapted for NMR shielding calculations several years later, in 1958 by Hameka[31] and later by Ditchfield.[32] Even then, the use of GIAOs was not widespread due to the difficulties associated with GIAO-based expressions, especially the evaluation of the integrals required for the quantum-chemical predictions. Consequently, in the 1980s the individual gauges for localized molecular orbitals (IGLO) method proposed by Schindler and Kutzelnigg[33–35] was favored by the computational chemistry community. The breakthrough of the GIAO ansatz in quantum chemistry was made possible by the pioneering work of Pulay *et al.*[26] who showed how the integrals over GIAOs can be computed efficiently in magnetic property computations. In addition to solving the gauge problem, GIAOs also lead to increased accuracy (due to more rapid convergence to the so-called basis set limit).[2,36] Referring back to Ditchfield's quotation, it can be concluded that since then, the GIAO approach is nowadays routinely used to compute magnetic properties[37–48] because it can be considered the best choice for calculating NMR parameters,[37] but there is the question of whether GIAO-based calculations can provide accurate results, even for larger systems.

Unlike IGLO*, the GIAO approach can be combined with any quantum-chemical ab initio method and, as indicated previously, a compromise must be found between accuracy and computational cost. In Ref. [49], Gauss and Stanton state that „it would be desirable if the currently available methods were extended to treat larger molecules. On the other hand, there is a demand for more accurate treatment of correlation in the calculations of magnetic properties“. Here, the MP2 method appears promising, as it offers a good compromise between accuracy and computational efficiency.[3] The GIAO-MP2 method was first formulated and implemented by Gauss in 1992[37] and the successful applicability of this method has been amply demonstrated.[20,22,50–60]

* A generalization of IGLO to all quantum-chemical schemes is hampered by the necessity of using localized occupied orbitals.

At the time the GIAO-MP2 scheme was developed, calculations on systems comprising more than 150 to 200 basis functions were not feasible.[61] For a long time, various attempts have been made to improve the efficiency of GIAO-MP2 calculations, for instance through integral-direct schemes,[61] which are based on so-called direct methods[62–67] that avoid disk space bottlenecks by calculating the required two-electron integrals on-the-fly. This scheme has been refined later through the exploitation of molecular point group symmetry and coarse-grain parallelization,[68] enabling calculations with more than 600 basis functions. As emphasized in Ref. [68], localized orbitals or an approximate treatment of the electron repulsion integrals might be required to achieve further reductions in the computational cost. This was, for example, realized by Loibl and Schütz who expanded localized occupied orbitals in a basis of GIAOs and used density fitting[69–73] to factorize the two-electron integrals.[47] Maurer and Ochsenfeld[74] proposed an atomic-orbital (AO) based formulation, which reduces the scaling behavior of NMR chemical shift calculations to linear. Density fitting and a local treatment are also used in the recently presented domain-based local pair natural orbital (DLPNO) MP2 scheme for computing polarizabilities and NMR parameters,[75] allowing calculations on system with up to 4700 basis functions. However, the density fitting approach has two major drawbacks: on the one hand, auxiliary basis sets are needed and on the other hand, the error cannot be rigorously controlled.[76] These limitations can be overcome by applying Cholesky decomposition (CD) to the electron repulsion integrals; a computationally efficient approach with reduced memory requirements[77] that tackles the bottleneck associated with storing and handling the two-electron integrals. While CD has been exploited in energy calculations,[76,78–88] fewer developments have been reported regarding molecular property computations. In this context, analytic MP2 gradients[89–92] (required for the determination of equilibrium and transition state structures) are to be mentioned, where nuclear-coordinate derivatives of the two-electron integrals are decomposed. In particular, CD was never used in connection with magnetic properties which would require the CD of perturbed two-electron integrals, i.e. the differentiated two-electron integrals with respect to the magnetic field component,[93] when GIAOs are used to ensure gauge-origin invariance. One of the main challenges in developing a CD-based scheme for calculating magnetic properties lies in the fact that the differentiated two-electron integrals are not positive semidefinite, which is a prerequisite for applying the CD.[93,94] As suggested in Ref. [90], the CD of derivative integrals can be carried out by differentiation of the corresponding CD equations for the unperturbed integrals.

The goal of this thesis is the application of CD in MP2 calculations of magnetic properties, including NMR shifts, magnetizabilities, and ring-current densities in order to facilitate computations on medium-sized systems comprising around 100 atoms and more than 1000 basis functions, which were previously infeasible due to computational time and memory limitations. One notable advantage of the CD is the control of the accuracy and the rank of the decomposition via a single parameter, the Cholesky threshold.[78,84] This enables the investigation of comparatively large systems with respect to their magnetic properties without a significant loss of accuracy, offering the possibility to support or even guide experiments. There are also remarkable opportunities in the context of a quantum mechanics/molecular mechanics (QM/MM) approach,[95] as the application of the CD allows for an extension of the QM region, providing increased accuracy and a better representation of environmental effects. The CD-based MP2 scheme for computing NMR parameter, which applies the CD to first-derivative integrals, can not only be used to predict NMR spectra but also to examine molecules with regard to other molecular properties

like aromaticity that can, for example, be quantified by computing the ring-current strength based on NMR shielding calculations.[96] The developments introduced in this work contribute to improve the accuracy of magnetic molecular property calculations for large systems. Additionally, the implementation of such a CD-GIAO-MP2 scheme is the foundation for further applications and can be extended toward different quantum-chemical methods, like the complete active space self-consistent field (CASSCF) method.[97] Prior to this work, CD has never been applied to second-derivative integrals[94] as required for computing magnetizabilities. In this context, the question is whether a CD scheme for magnetizabilities can be realized by differentiating the equations for the unperturbed electron repulsion integrals as well. Furthermore, the CD algorithm for the magnetic first- and second-derivative integrals provides a guideline for the application of the CD in the computation of other second-order properties, like polarizabilities[75,98–105] or harmonic force constants[106–113] to obtain harmonic vibrational frequencies. For this reason, this work extends the theoretical study of molecular properties to enable the computation of larger and chemically interesting molecules using an electron-correlated approach, thereby contributing to a fruitful interplay between experiment and theory.

The structure of this thesis is as follows: In Chapter 2, the theoretical foundations are discussed, including the quantum-chemical methods relevant to this work, the calculation of magnetic molecular properties via energy derivatives as well as the evaluation of electron repulsion integrals using the McMurchie-Davidson[114] scheme. Furthermore, the concept of the CD is presented and how CD can be applied to the magnetic first-derivative integrals. After introducing the QM/MM approach, the new theoretical developments within the framework of this thesis are presented in Chapter 3. This chapter addresses improvements in the CD of perturbed two-electron integrals required for NMR computations, achieved through the exploitation of permutational symmetry and the use of a more efficient CD algorithm. With these developments, the computational demands can be reduced even further. Additionally, the CD of the magnetic second-order derivative integrals is discussed, where three different schemes are proposed. Chapter 4 deals with the implementation of the presented schemes and includes computational details about the calculations carried out in the course of this work. The results obtained with these implementations are presented in Chapter 5, where the accuracy and efficiency of the CD-based GIAO-MP2 scheme is analyzed. Calculations involving more than 1000 basis functions demonstrate the applicability of this scheme. The CD algorithm was also incorporated into QM/MM calculations to determine the NMR shifts of liquid water. The application of CD allows for an extension of the QM region, which is necessary to provide reliable results. Next, the three proposed schemes for the CD of the magnetizability integrals are examined with respect to efficiency and accuracy. All developed schemes are applied in the investigation of the aromaticity of coronene and bridged annulene derivatives, for which ring-current densities and ring-current strengths are computed. Finally, the work is summarized in Chapter 6 and ends with an outlook on future developments.

2 Fundamental Theory

The theoretical background of this work is presented in two separate chapters in order to distinguish the theory developed in the context of this work from already existing theories. The first chapter briefly reviews the basic and established theories in quantum chemistry, starting with an overview of the electronic Schrödinger equation and its approximate solutions in the form of quantum-chemical methods like Hartree-Fock (HF) and second-order Møller-Plesset (MP2) perturbation theory. This is followed by a section about magnetic molecular properties, with a focus on qualitative explanations of nuclear magnetic resonance (NMR) spectroscopy, magnetically induced ring currents and magnetizabilities. After introducing the molecular Hamiltonian in the presence of a magnetic field, the section ends with a discussion of the explicit quantum-chemical computation of these properties by means of energy derivatives. In order to compute these energy derivatives, the evaluation of two-electron integrals is required, which is why the McMurchie-Davidson scheme for computing unperturbed and magnetic first-derivative integrals is presented. Since the evaluation of the two-electron integrals is often a bottleneck in quantum-chemical calculations, Cholesky decomposition (CD) is introduced, which makes it possible to reduce the computational effort for handling the two-electron integrals. In this context, it is explained how to use CD for calculating NMR shieldings both at the HF and MP2 level of theory. The first part ends with a concise introduction into multiscale approaches, that is the Quantum mechanics/Molecular mechanics (QM/MM) method, and how a CD-based scheme can be embedded in a QM/MM framework.
In the second part, the theory developed within the scope of this thesis is presented, starting with ideas of how to improve the CD of the magnetic first-derivative integrals, the so-called NMR integrals, by exploiting permutational symmetry on the one hand and by utilizing a different algorithm on the other hand. In this context, the CD procedure for the second-derivative integrals, i.e. the magnetizability integrals, is elucidated, with a particular focus on the differences compared to the NMR integrals, the associated difficulties of this approach and how to overcome them. A brief discussion about the computation of the magnetizability tensor using CD at the HF level of theory marks the end of the theory chapter.

2.1 Electronic Schrödinger Equation

The time-independent Schrödinger equation

$$\hat{H}\Psi = E\Psi \tag{2.1}$$

is the fundamental equation in quantum chemistry. This eigenvalue problem involves the wave function Ψ, which fully describes the state of the system, the total energy E and the molecular Hamiltonian $\hat{H}$. Since this equation cannot be solved analytically for systems composed of more than two particles, approximate solutions are inevitable. The Born-Oppenheimer approximation is based on the fact that the mass of the nuclei is about a factor of 2000 larger than the mass of the electrons, which enables the separation of the electron motion from the nuclear motion. Hence, a nuclear and an electronic Schrödinger equation can be formulated. This work aims at solving the electronic Schrödinger equation

$$\hat{H}_{\mathrm{el}}\Psi_{\mathrm{el}} = E_{\mathrm{el}}\Psi_{\mathrm{el}}, \tag{2.2}$$

where the electronic Hamiltonian $\hat{H}_{\mathrm{el}}$ acts on the electronic wavefunction Ψ_{el}, resulting in the electronic energy E_{el}. Solving this equation provides information about the electronic structure and molecular properties of a given molecule. As a result, the potential for the motion of the nuclei, the Born-Oppenheimer potential V^{BO},

$$V^{\mathrm{BO}} = E_{\mathrm{el}} + \hat{V}_{KK}, \tag{2.3}$$

is obtained, where $\hat{V}_{KK}$ denotes the potential of the nuclear repulsion potential. The electronic Hamiltonian for a system with N electrons and M nuclei involves three operators: the kinetic energy $\hat{T}_e$, the Coulomb interaction of the electrons $\hat{V}_{ee}$ and the nuclei and electrons $\hat{V}_{Ke}$, respectively,

$$\begin{aligned}\hat{H}_{\mathrm{el}} &= \hat{T}_{\mathrm{e}} + \hat{V}_{\mathrm{Ke}} + \hat{V}_{\mathrm{ee}} \\ &= \underbrace{-\frac{1}{2}\sum_{i}^{N}\nabla_i^2 - \sum_{i}^{N}\sum_{A}^{M}\frac{Z_A}{|\mathbf{R}_A - \mathbf{r}_i|}}_{\sum_{i}^{N}\hat{h}_i} + \sum_{i>j}^{N}\frac{1}{|\mathbf{r}_i - \mathbf{r}_j|}.\end{aligned} \tag{2.4}$$

Here, atomic units are used and the indices i and A denote electrons and nuclei, respectively. Z_A is the nuclear charge, while the electronic and nuclear coordinates are described by $\mathbf{r}$ and $\mathbf{R}$. $\hat{h}$ is the one-electron Hamiltonian. In the following, $\hat{H}$ and E always refer to $\hat{H}_{\mathrm{el}}$ and E_{el}, respectively.

As it is not possible to solve the electronic Schrödinger equation for most systems analytically, approximate solutions are necessary, resulting in a multitude of different quantum-chemical methods. The methods used in this thesis have in common that they use one or more Slater determinants as ansatz for the electronic wavefunction. A Slater determinant $\Psi(\boldsymbol{\tau}_1, .., \boldsymbol{\tau}_N)$ for a system with N electrons

$$\Psi(\boldsymbol{\tau}_1, .., \boldsymbol{\tau}_N) = \frac{1}{\sqrt{N!}}\begin{vmatrix} \varphi_1(\boldsymbol{\tau}_1) & \varphi_2(\boldsymbol{\tau}_1) & \dots & \varphi_N(\boldsymbol{\tau}_1) \\ \varphi_1(\boldsymbol{\tau}_2) & \varphi_2(\boldsymbol{\tau}_2) & \dots & \varphi_N(\boldsymbol{\tau}_2) \\ \vdots & \vdots & \ddots & \vdots \\ \varphi_1(\boldsymbol{\tau}_N) & \varphi_2(\boldsymbol{\tau}_N) & \dots & \varphi_N(\boldsymbol{\tau}_N) \end{vmatrix} \tag{2.5}$$

considers the anti-symmetry of electrons (Pauli principle) and is constructed from N orthonormal spin orbitals φ_i,

$$\varphi_i(\boldsymbol{\tau}_j) = \phi_i(\mathbf{r}_j)\chi_i(\sigma_j), \tag{2.6}$$

where $\boldsymbol{\tau}_j$ represents the spatial and (fictitious) spin coordinates $\mathbf{r}$ and σ of the electron j while $\phi_i(\mathbf{r}_j)$ and $\chi_i(\sigma_j)$ describe the ith spatial orbital and spin function, respectively.[115] The latter can be either $\alpha(\sigma)$ or $\beta(\sigma)$.
The methods relevant for this work are all based on one of the following standard procedures to solve the electronic Schrödinger equation approximately:

1. Variational Method (Hartree-Fock Theory[116,117] → subsection 2.2.1)
2. Perturbation theory (Møller-Plesset Perturbation theory[10] → subsection 2.2.2)
3. Projective Techniques (Coupled-Cluster[11,12,118,119] methods → subsection 2.2.3)

In the next sections, the different methods will be explained in more detail.

2.2 Quantum-Chemical Methods

2.2.1 Hartree-Fock Theory

HF theory[116,117] is the simplest approximation for solving the electronic Schrödinger equation and can be considered a basic approach for further, more accurate methods.
The idea is to use a single Slater determinant Ψ as wavefunction to obtain the best spin orbitals, that is the orbitals which minimize the energy, using the variational method. This method is based on the variational principle[120]

$$\frac{\langle\tilde{\Psi}|\hat{H}|\tilde{\Psi}\rangle}{\langle\tilde{\Psi}|\tilde{\Psi}\rangle} \geq E_{\text{exact}}, \tag{2.7}$$

which states that the energy expectation value for a test wavefunction $\tilde{\Psi}$ is always higher than or equal to the exact (non-relativistic) energy.
The energy expectation value for a Slater determinant reads

$$\langle\Psi|\hat{H}|\Psi\rangle = E_{\text{HF}} = \sum_i^N h_{ii} + \frac{1}{2}\sum_{ij}^N \left(\langle ij|ij\rangle - \langle ij|ji\rangle\right), \tag{2.8}$$

where the first term consists of the one-electron integrals $h_{ii} = \langle i|\hat{h}|i\rangle = \langle\varphi_i|\hat{h}|\varphi_i\rangle$ with the one-electron Hamiltonian $\hat{h}$, while the second term contains the two-electron integrals, i.e. the Coulomb integral

$$\langle ij|ij\rangle = \left\langle \varphi_i(\mathbf{r}_1)\varphi_j(\mathbf{r}_2)\middle|\frac{1}{r_{12}}\middle|\varphi_i(\mathbf{r}_1)\varphi_j(\mathbf{r}_2)\right\rangle \tag{2.9}$$

and the exchange integral

$$\langle ij|ji\rangle = \left\langle \varphi_i(\mathbf{r}_1)\varphi_j(\mathbf{r}_2)\middle|\frac{1}{r_{12}}\middle|\varphi_j(\mathbf{r}_1)\varphi_i(\mathbf{r}_2)\right\rangle. \tag{2.10}$$

Next, the energy is minimized with respect to the choice of the spin orbitals φ_i in order to obtain the „best“ orbitals, i.e. those that provide the lowest energy, following the variational principle.

The orthonormality of the orbitals

$$\langle\varphi_i|\varphi_j\rangle = \delta_{ij} \tag{2.11}$$

needs to be taken into account, which can be done using the method of Lagrange multipliers. This means that instead of the energy, the Lagrange functional containing the side conditions is minimized, and as a result the general HF equations are obtained. Application of a unitary transformation to the spin orbitals and introducing canonical orbitals that diagonalize the matrix of Lagrange multipliers leads to the canonical HF equations, which in turn can be converted into the so-called restricted HF (RHF) equations for closed-shell systems

$$\hat{F}\phi_i = \varepsilon_i\phi_i \tag{2.12}$$

after spin integration, with ε_i as the orbital energy of the molecular orbital ϕ_i and $\hat{F}$ as the Fock operator. The Fock operator

$$\hat{F} = \hat{h} + \sum_{j}^{N/2}(2\hat{J}_j - \hat{K}_j) \tag{2.13}$$

involves the Coulomb and the exchange operator $\hat{J}_j$ and $\hat{K}_j$, respectively. They are defined by their effect on electron 1 in the spatial orbital ϕ_i,

$$\begin{aligned}\hat{J}_j\phi_i(\mathbf{r}_1) &= \int \phi_j^*(\mathbf{r}_2)\frac{1}{r_{12}}\phi_i(\mathbf{r}_1)\phi_j(\mathbf{r}_2)d\mathbf{r}_2 \\ \hat{K}_j\phi_i(\mathbf{r}_1) &= \int \phi_j^*(\mathbf{r}_2)\frac{1}{r_{12}}\phi_j(\mathbf{r}_1)\phi_i(\mathbf{r}_2)d\mathbf{r}_2.\end{aligned} \tag{2.14}$$

The exchange term has no classical interpretation and arises from the indistinguishability of electrons and the Pauli principle.[115] As seen in eq. (2.14), the Coulomb operator describes the interaction through charge distributions and does not involve the explicit dependence of the motion of the electrons with respect to each other, which is called electron correlation. This is why the HF method is also referred to as *mean field* theory. The corresponding RHF energy is given via

$$E_{\mathrm{RHF}} = \sum_{i}^{N/2} 2h_{ii} + \frac{1}{2}\sum_{ij}^{N/2}(4\langle ij|ij\rangle - 2\langle ij|ji\rangle). \tag{2.15}$$

In contrast to the energy expression in eq. (2.8), the sum runs over the $N/2$ spatial orbitals. The RHF equations are only valid for closed-shell systems, i.e. systems with only doubly occupied orbitals.

Solving the RHF equations leads to two challenges: first, a direct solution is not possible since the Fock operator itself depends via $\hat{J}_j$ and $\hat{K}_j$ on the orbitals ϕ_i. The RHF equations are hence pseudo eigenvalue equations. Secondly, the question arises as to how the orbitals can be represented since numerical solutions are possible but inefficient.

Concerning the representation of the orbitals, the ansatz introduced by Roothaan[121] and Hall[122] is widespread, where the molecular orbitals (MOs) ϕ_i are expanded in a basis of known atomic orbitals (AOs) or basis functions χ_μ,

$$\phi_i = \sum_{\mu}^{M} c_{\mu i}\chi_\mu. \tag{2.16}$$

In eq. (2.16), M denotes the number of basis functions and $c_{\mu i}$ are the expansion coefficients in this so-called linear combination of atomic orbitals (LCAO) ansatz. As basis functions χ_μ, hydrogen-like contracted Gaussian functions are used. Insertion of the LCAO ansatz in the RHF equations (eq. (2.12)) and subsequent projection with $\langle\chi_\nu|$ (in the following denoted as $\langle\nu|$) leads to the Roothaan-Hall equations[121,122]

$$\mathbf{FC} = \mathbf{SC}\boldsymbol{\varepsilon}, \tag{2.17}$$

where $\mathbf{C}$ is the MO coefficient matrix, $\boldsymbol{\varepsilon}$ the diagonal matrix of the orbital energies and $\mathbf{F}$ and $\mathbf{S}$ are the Fock and the overlap matrices with the matrix elements $F_{\nu\mu} = \langle\nu|\hat{F}|\mu\rangle$ and $S_{\nu\mu} = \langle\nu|\mu\rangle$, respectively. Now the Fock operator no longer depends on the orbitals but on the coefficients. However, the Roothaan-Hall equations are still pseudo eigenvalue equations. Usually, an iterative method called self-consistent field (SCF) method, is used to solve the equations, in which a guessed coefficient matrix is used to construct the Fock matrix in the first step. With this Fock matrix, the generalized eigenvalue problem can be solved, resulting in a new coefficient matrix, which is then used in the next iteration step to construct a new Fock matrix. The procedure is repeated until self-consistency is achieved, i.e. the coefficient matrices from two iterations agree to a given numerical accuracy.
Insertion of the LCAO ansatz (eq. (2.16)) in the energy expression in eq. (2.15), leads to the RHF energy in the AO basis (hereinafter denoted as E),

$$E = \sum_{\mu\nu}^{M} D_{\mu\nu} h_{\mu\nu} + \frac{1}{2} \sum_{\mu\nu\sigma\rho}^{M} D_{\mu\nu} D_{\sigma\rho} \left(\langle\mu\sigma|\nu\rho\rangle - \frac{1}{2} \langle\mu\sigma|\rho\nu\rangle \right), \tag{2.18}$$

with the following definition of the one-electron density matrix $D_{\mu\nu}$,

$$D_{\mu\nu} = 2 \sum_{i}^{N/2} c_{\mu i}^{*} c_{\nu i}. \tag{2.19}$$

Compared to more sophisticated methods, the HF ansatz is associated with a low computational effort since it scales only with $\mathcal{O}(M^4)$, where M is the number of basis functions. However, electron correlation is not taken into account. For numerous systems, a single Slater determinant is an appropriate approximation for the wavefunction and the results obtained by the HF method are considered as qualitatively good. In this case, the electron correlation is referred to as *dynamic* correlation and incorporating electron correlation can be seen as a small correction to the ground state wavefunction. Methods like Møller-Plesset perturbation theory[10] and Coupled-Cluster Theory[11,12,118] belong to the methods that take dynamic electron correlation into account, and they are called single-reference or *post*-HF methods. The term *static* correlation is used, if one Slater determinant leads to a qualitatively wrong result. In this case, multi-reference methods like the Complete Active Space SCF (CASSCF) approach are required, where the wavefunction ansatz consists of several Slater determinants right from the beginning. Both single- and multi-reference methods are explained in more detail in the following sections.

2.2.2 Second-Order Møller-Plesset Perturbation Theory

Focusing on dynamic electron correlation, the correlation energy E_{corr}

$$E_{\text{corr}} = E_{\text{exact,non-relativistic}} - E_{\text{HF}} \tag{2.20}$$

has only a relatively small impact, which is why a perturbative treatment is plausible. In Rayleigh-Schrödinger perturbation theory, $\hat{H}$ is divided in an unperturbed Hamiltonian $\hat{H}^{(0)}$, for which the solutions are known, and a perturbed part $\hat{H}'$,

$$\hat{H} = \hat{H}^{(0)} + \lambda \hat{H}', \tag{2.21}$$

where the perturbation parameter λ controls the perturbation, which means that $\lambda = 1$ corresponds to the real problem while $\lambda = 0$ corresponds to the unperturbed problem. Energy and wavefunction are expanded in a Taylor series in powers of the perturbation parameter λ and the expansion is inserted in the Schrödinger equation (eq. (2.1)),

$$\begin{aligned}(\hat{H}^{(0)}+\lambda\hat{H}')(\Psi^{(0)} + \lambda\Psi^{(1)} + \lambda^2\Psi^{(2)} + \ldots) \\ = (E^{(0)} + \lambda E^{(1)} + \lambda^2 E^{(2)} + \ldots)(\Psi^{(0)} + \lambda\Psi^{(1)} + \lambda^2\Psi^{(2)} + \ldots).\end{aligned} \tag{2.22}$$

Next, the terms with the same power of λ are separated and projection with $\langle\Psi^{(0)}|$ leads to the corresponding energy corrections,

$$\begin{aligned} E^{(0)} &= \langle\Psi^{(0)}|\hat{H}^{(0)}|\Psi^{(0)}\rangle \quad \text{0. order} \\ E^{(1)} &= \langle\Psi^{(0)}|\hat{H}'|\Psi^{(0)}\rangle \quad \text{1. order} \\ E^{(2)} &= \langle\Psi^{(0)}|\hat{H}'|\Psi^{(1)}\rangle \quad \text{2. order} \\ &\vdots \end{aligned} \tag{2.23}$$

Here, only terms up to second order are shown because the perturbation is assumed to be small and thus contributions of higher order are considered negligible. According to eq. (2.23), the perturbed first-order wavefunction $\Psi^{(1)}$ is required for computing the second-order energy correction. $\Psi^{(1)}$ can be expanded in the solutions of the unperturbed Schrödinger equation $|\Phi_i^{(0)}\rangle$ because they constitute a complete basis,[8]

$$\Psi^{(1)} = \sum_{i\neq 0} c_i^{(1)} \, |\Phi_i^{(0)}\rangle \, . \tag{2.24}$$

Projection with $\langle\Phi_j^{(0)}|$ on the first-order equation gives an expression for $\Psi^{(1)}$ that can be inserted in the second-order energy correction, which can then be reformulated as

$$E^{(2)} = \sum_{j\neq 0} \frac{|\langle\Phi_j^{(0)}|\hat{H}'|\Phi_0^{(0)}\rangle\,|^2}{E_0^{(0)} - E_j^{(0)}}, \tag{2.25}$$

where $j \neq 0$ means that the sum runs over excited states. However, the perturbed and unperturbed Hamiltonian $\hat{H}'$ and $\hat{H}^{(0)}$ are not defined yet. Within the ansatz of Møller and Plesset[10] (MP) the unperturbed Hamiltonian is given as sum over the known Fock operators,

$$\hat{H}^{(0)} = \sum_i \hat{F}(i), \tag{2.26}$$

and consequently $\Psi^{(0)} = \Psi_{\mathrm{HF}}$ is an eigenfunction of $\hat{H}^{(0)}$. Using this ansatz leads to explicit expressions for the energy corrections in eq. (2.23). For the zeroth-order energy

$$E^{(0)} = \sum_i \varepsilon_i, \tag{2.27}$$

the sum of the MO energies ε_i is obtained, and the sum of zeroth- and first-order energy results in the HF energy

$$E^{(0)} + E^{(1)} = E_{\mathrm{HF}}. \tag{2.28}$$

The first contribution to electron correlation is included in the second-order energy correction

$$E^{(2)} = \frac{1}{4} \sum_{ij} \sum_{ab} \frac{|\langle ab|ij\rangle - \langle ab|ji\rangle|^2}{\varepsilon_i + \varepsilon_j - \varepsilon_a - \varepsilon_b} = \frac{1}{4} \sum_{ij} \sum_{ab} \frac{|\langle ab||ij\rangle|^2}{\varepsilon_i + \varepsilon_j - \varepsilon_a - \varepsilon_b}, \tag{2.29}$$

and is called MP2 or second-order many-body perturbation theory (MBPT2), where $i, j, \ldots$ and $a, b, \ldots$ denote indices for occupied and virtual orbitals, respectively. This expression can be derived by exploiting Brillouin theorem, which states that for HF orbitals the matrix element of the Hamilton operator between a singly excited and the ground state determinant vanishes, i.e. $\langle \Phi_i^a | \hat{H} | \Phi_0 \rangle = 0$. The two-electron integral

$$\langle ab||ij\rangle = \langle \Phi_{ij}^{ab} | \hat{H} | \Phi_0 \rangle \tag{2.30}$$

is related to a double excitation from the HF ground state, as it is exemplified in fig. 2.1.

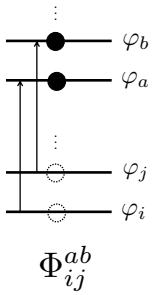

Figure 2.1: Illustration of a double excitation.

The final MP2 energy expression E_{MP2} is given via

$$E_{\mathrm{MP2}} = E_{\mathrm{HF}} + \frac{1}{4} \sum_{ij} \sum_{ab} t_{ij}^{ab} \langle ij||ab\rangle, \tag{2.31}$$

with the MP2 amplitudes t_{ij}^{ab},

$$t_{ij}^{ab} = \frac{\langle ab||ij\rangle}{\varepsilon_i + \varepsilon_j - \varepsilon_a - \varepsilon_b}. \tag{2.32}$$

As it is the case for HF, there is also a way to exploit spin symmetry for closed-shell systems

and

$$E_{\mathrm{MP2}} = E_{\mathrm{RHF}} + \sum_{ij}\sum_{ab} \tilde{t}_{ij}^{ab} \langle ij|ab\rangle \tag{2.33}$$

is obtained after spin adaption, where the sum runs over spatial instead of spin orbitals, as it is the case for eq. (2.31). In eq. (2.33), the spin-adapted MP2 amplitude $\tilde{t}_{ij}^{ab}$ is given by

$$\tilde{t}_{ij}^{ab} = \frac{2\langle ab|ij\rangle - \langle ab|ji\rangle}{\varepsilon_i + \varepsilon_j - \varepsilon_a - \varepsilon_b} = 2t_{ij}^{ab} - t_{ji}^{ab}, \tag{2.34}$$

where the definition of the MP2 amplitude in the spatial orbital basis does not contain the antisymmetrized integral,

$$t_{ij}^{ab} = \frac{\langle ab|ij\rangle}{\varepsilon_i + \varepsilon_j - \varepsilon_a - \varepsilon_b}. \tag{2.35}$$

In this work, only closed-shell systems are considered, and therefore eqs. (2.33) to (2.35) will always be used in later sections.
The MP2 expression is given in the MO basis while the corresponding one- and two-electron integrals are given in the AO basis after the HF calculation. Hence, a transformation of these integrals from the AO to the MO basis is required, which results in the computational cost of MP2 scaling with $\mathcal{O}(M^5)$ instead of $\mathcal{O}(M^4)$, as it is the case for HF.

The MP2 ansatz is both a simple and comparatively favorable electron correlation method with regard to computational effort and typically yields about $80 - 90\%$ of the electron correlation energy.[8] In order to improve the results, a logical step would be to consider higher order energy corrections. However, it was found that the MP series suffers from poor convergence,[123] and the assumption that the zeroth order wavefunction is a good approximation to the real wavefunction limits the applicability of perturbation methods.[8] To obtain more accurate results, superior methods, such as Coupled-Cluster (CC) methods, have to be used.

2.2.3 Coupled-Cluster Theory

In CC theory,[11,12,118,119] an exponential ansatz is chosen as wavefunction

$$\Psi = e^{\hat{T}} |\Phi_0\rangle , \tag{2.36}$$

where $|\Phi_0\rangle$ is the reference wavefunction, which in this work is chosen as the HF wavefunction, $|\Phi_0\rangle = |\Psi_{\mathrm{HF}}\rangle$. The exponential operator is defined via a Taylor series,

$$e^{\hat{T}} = 1 + \hat{T} + \frac{1}{2}\hat{T}^2 + \frac{1}{3!}\hat{T}^3 + ..., \tag{2.37}$$

with $\hat{T}$ as the cluster operator,

$$\hat{T} = \hat{T}_1 + \hat{T}_2 + ... + \hat{T}_N, \tag{2.38}$$

where the operators $\hat{T}_n$ generate n-excited determinants when applied to $|\Phi_0\rangle$,

$$\hat{T}_n |\Phi_0\rangle = \left(\frac{1}{n!}\right)^2 \sum_{ij...}\sum_{ab...} t_{ij...}^{ab...} \Phi_{ij...}^{ab...}. \tag{2.39}$$

The expansion coefficients t are called CC amplitudes and can be regarded as a weighting factor for the corresponding determinant.
Insertion of the Coupled-Cluster ansatz (eq. (2.36)) into the electronic Schrödinger equation (eq. (2.1)) leads to

$$\hat{H}e^{\hat{T}}\left|\Phi_0\right\rangle = Ee^{\hat{T}}\left|\Phi_0\right\rangle. \tag{2.40}$$

Since it would be impractical to solve this equation variationally,[124] a projective technique is used instead. First, eq. (2.40) is multiplied by the inverse of the exponential operator and then projected onto the HF reference and the excited determinants, respectively, leading to an expression for the CC energy

$$E = \langle\Phi_0|e^{-\hat{T}}\hat{H}e^{\hat{T}}|\Phi_0\rangle \tag{2.41}$$

and the amplitude equations

$$0 = \langle\Phi_{ij\ldots}^{ab\cdots}|e^{-\hat{T}}\hat{H}e^{\hat{T}}|\Phi_0\rangle. \tag{2.42}$$

Using the Baker-Campbell-Hausdorff expansion and Wick's Theorem, these expressions can be evaluated, resulting in an expression for the electronic energy and equations for the amplitudes.[124] Consideration of all excitations in the cluster operator $\hat{T}$ would be accompanied by a too high computational effort. Thus, truncated CC methods are usually employed, such as the CC singles and doubles (CCSD) method,[125] where $\hat{T} = \hat{T}_1 + \hat{T}_2$ is chosen and the projection is carried out onto the singly and doubly excited determinants. For CCSD, a scaling behavior of $\mathcal{O}(M^6)$ is obtained. Another example is the CCSD(T) method,[126] where the triple excitations are treated perturbatively after a standard CCSD calculation and a scaling behavior of $\mathcal{O}(M^7)$ is reached. Today, CCSD(T) calculations are considered to be the „gold standard“ in quantum chemistry,[127] but it should be noted that these computations are still associated with a high computational effort compared to many other quantum-chemical methods.

The methods presented so far are well suited for the treatment of dynamic electron correlation. However, single-reference methods fail in certain cases of static correlation. For example, if a system undergoes significant electronic rearrangement, as for bond breaking cases and the formation of new bonds.[128] Systems like this are called strongly correlated or multi-reference systems. As a single-determinant description, i.e. a single determinant or configuration, is inflexible for systems like this,[129] multi-reference methods like the CASSCF ansatz are inevitable.

2.2.4 Complete Active Space SCF

The CASSCF approach[128,130–132] is a special case of multi-configurational SCF (MCSCF) methods,[13–18] where the wavefunction ansatz is chosen as a linear combination of Slater determinants

$$\Psi = \sum_I c_I \Phi_I, \tag{2.43}$$

and is used for the qualitative description of static electron correlation. The sum runs over few but important configurations, and the orbitals in the determinant Φ_I as well as the coefficients c_I are determined via the variational principle. An alternative formulation of the CASSCF wavefunction is[133]

$$\Psi = e^{i\hat{\kappa}}e^{i\hat{S}}\left|0\right\rangle, \tag{2.44}$$

where

$$|0\rangle = \sum_I C_I |I\rangle \tag{2.45}$$

is the MCSCF reference state that is expanded in configuration state functions (CSFs) $|I\rangle$ with the CI coefficients C_I.[134] In eq. (2.44), $\hat{\kappa}$ and $\hat{S}$ are the orbital and configurational rotation operators,

$$\hat{\kappa} = \sum_{p>q} \kappa_{pq} \hat{E}^+_{pq}, \tag{2.46}$$

$$\hat{S} = \sum_{J\neq 0} S_J \left(|J\rangle \langle 0| + |0\rangle \langle J| \right), \tag{2.47}$$

and since $e^{i\hat{\kappa}}$ and $e^{i\hat{S}}$ are unitary, the orthonormality of the orbitals and the norm of the wavefunction are preserved.[135] Here, $p, q, \ldots$ refer to generic MOs, while $\hat{E}^+_{pq}$ denotes a singlet excitation operator and $|J\rangle$ is a generic state orthogonal to the reference state.
A major difficulty of the MCSCF ansatz is the selection of the determinants, which are required to describe the properties of interest.[8] In the CASSCF ansatz, the determination of configurations is realized by partitioning the orbitals manually in three subsets: active, inactive and virtual, which is exemplified in Figure 2.2.

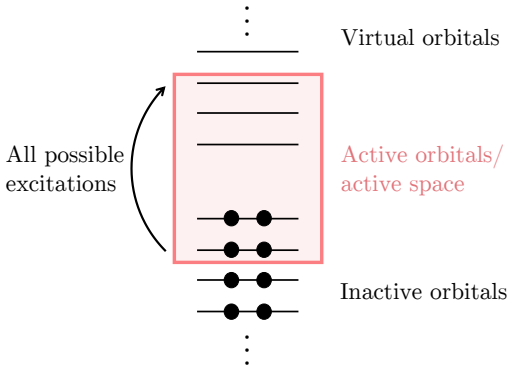

Figure 2.2: Illustration of the orbital partitions.

The orbitals in the inactive space are all always doubly occupied while the virtual ones are always unoccupied. In the active space, there are no restrictions regarding the orbital occupation, and a so-called Full Configuration Interaction (FCI) calculation is performed, generating all possible excitations, which means that the configuration expansion is complete.[128] CASSCF calculations are often denoted as CAS(X,Y) with X as the number of electrons that are distributed in Y active orbitals. Using this approach, systems for which a description by single-reference methods is not possible, like transition metals or radicals, can be described adequately, with the advantage that the selection of dominant configurations is avoided.[128]

So far, only the computation of the energy and the wavefunction for different methods was discussed, but of course the energy is not the only property that characterizes a molecule. In quantum chemistry, a further topic of interest is the calculation of molecular properties that can be measured in experiments.[2,33] As an example, the calculation of vibrational frequencies that can be measured by means of IR- and Raman spectroscopy[136–138] is to be mentioned, as well as the calculation of rotational constants, electric field gradients and dipole moments to

predict and assign rotational spectra.[139–143] Neither theory nor a purely experimental approach can exist alone without an interplay between both, enabling the mutual verification of each other. Regarding the focus of this work, the computation of magnetic molecular properties like nuclear magnetic resonance (NMR) chemical shifts,[3,25,31,35,144–147] magnetizabilities,[35,148–151] magnetically induced ring-current strengths and ring-current densities[96,152–158] also allows to build a bridge between theory and experiments. These quantities provide information about the functional groups and general molecular structure of a molecule or its behavior in an external magnetic field, and the results obtained by quantum-chemical calculations are useful to support experiments, e.g. in order to varify and interpret experimental results and to assign spectra.[2,3] The fundamentals for the computation of magnetic molecular properties are presented in the following, starting with a qualitative introduction to the physical and chemical principles of NMR shieldings, ring currents and magnetizability. After introducing the theory for molecules in an external magnetic field, i.e. the Hamiltonian in the presence of a magnetic field, the explicit calculation of these molecular properties is described.

2.3 Magnetic Molecular Properties

2.3.1 Nuclear Magnetic Resonance

Many nuclei have an inherent nuclear spin $\mathbf{I}$ which is directly connected to a magnetic moment $\mathbf{m}_K$

$$\mathbf{m}_K = \gamma_K \mathbf{I} \tag{2.48}$$

via the gyromagnetic ratio γ_K of the considered nucleus. Because of this magnetic moment, the energy of the nuclei depends on the orientation of the nuclear spin in the magnetic field. Without a magnetic field, the m_I states of a system are degenerate, where m_I is the magnetic spin quantum number. Applying an external magnetic field $\mathbf{B}$ causes the states to split, where the interaction energy with the field is given as

$$\Delta E = -\mathbf{m}_K \mathbf{B}. \tag{2.49}$$

The splitting for a nucleus with spin $\frac{1}{2}$ is illustrated in Figure 2.3

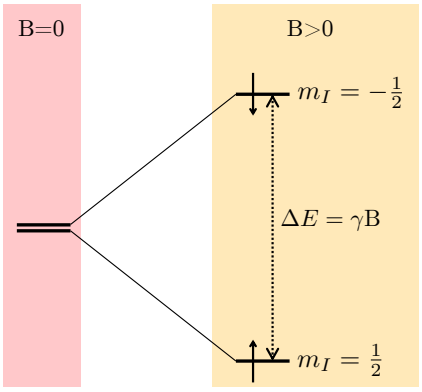

Figure 2.3: Splitting of the energy states for a nucleus with spin $\frac{1}{2}$ in a magnetic field.

In the NMR experiment, electromagnetic radiation in the radiofrequency range is applied in

addition to the magnetic field. If the frequency of the external electromagnetic radiation matches the intrinsic frequency of the nuclei, resonance occurs, i.e. the energy of electromagnetic radiation equals the difference between the energy levels ΔE.[19] So far, only the type of nuclei and not the chemical surrounding affects the energy difference. If there were no further interactions, every type of nuclei would have a characteristic resonance energy and NMR measurements could not provide any information about the structure of molecules. Regarding the electrons, the external magnetic field $\mathbf{B}$ induces an electronic current that in turn induces a magnetic field $\mathbf{B}_{\text{ind}}$

$$\mathbf{B}_{\text{ind}} = -\boldsymbol{\sigma}\mathbf{B}, \tag{2.50}$$

which shields the nuclei, where the shielding is given by the 3×3 shielding tensor $\boldsymbol{\sigma}$. This results in the nuclei experiencing a weakened magnetic field $\mathbf{B}_{\text{local}}$

$$\begin{aligned} \mathbf{B}_{\text{local}} &= \mathbf{B} + \mathbf{B}_{\text{ind}} \\ &= \mathbf{B} - \boldsymbol{\sigma}\mathbf{B} \\ &= (1 - \boldsymbol{\sigma})\mathbf{B}, \end{aligned} \tag{2.51}$$

and the expression in eq. (2.49) changes to[2]

$$\begin{aligned} \Delta E &= -\mathbf{m}_K \mathbf{B}_{\text{local}} \\ &= -\mathbf{m}_K (1 - \boldsymbol{\sigma})\mathbf{B}. \end{aligned} \tag{2.52}$$

In isotropic media, like water or in solid states, the shielding constant σ

$$\sigma = \frac{1}{3}\text{Tr}(\boldsymbol{\sigma}) \tag{2.53}$$

is the quantity of interest, where $\frac{1}{3}$ trace indicates an averaging over all spatial directions.
In fact, it is not the shielding tensor that is measured in NMR experiments, but the chemical shift δ,

$$\delta = \sigma_{\text{ref}} - \sigma, \tag{2.54}$$

which is relative to a given reference σ_{ref} (for ^{1}H and ^{13}C, tetramethylsilane is chosen as reference). Based on NMR chemical shifts, which depend on the chemical surrounding of the nuclei, conclusions can be drawn about the electronic and geometric structure of a molecule, and thus NMR shifts are of particular interest for chemists. It has also been observed that nuclei (typically protons) of molecules, that sustain a ring current, are shielded or deshielded compared to molecules in which no ring currents occur.[159] This means, NMR experiments can be used to appraise the induced ring current in cyclic molecules,[154] which allows estimates regarding aromaticity.[152] At this point, it should be mentioned that the shielding or deshielding of nuclei is not a universally valid argument for aromaticity (some molecules do not have hydrogens and a deshielding of ^{13}C shifts is not observed),[159] and that it is more reliable to compute the ring current quantum-chemically to make statements about aromaticity,[152] as demonstrated in section 2.3.10. Beforehand, the relationship between ring currents and aromaticity is given.

2.3.2 Magnetically Induced Ring Currents

First, it needs to be mentioned that aromaticity is a concept and not an observable, and thus there are no strict criteria to define aromaticity. Before 1825, classifications were based on the „aromatic“ odor,[159] but today there are more precise criteria.[158] There is, for example, the enhanced stability/large resonance energy of aromatic compounds or a certain chemical behavior in the case of benzene that prefers the electrophilic substitution over the addition.[159] Structural criteria like the negligible bond length alternation and planarity are also to be mentioned, as well as a rule of thumb, the so-called Hückel $(4n+2)\pi$ rule.[5,160] Also, the ring current is a characteristic attribute of aromatic or antiaromatic molecules. A diatropic ring current generates a magnetic field $\mathbf{B}_{\text{ind}}$ that opposes the external magnetic field $\mathbf{B}_{\text{ext}}$ and flows clockwise with respect to $\mathbf{B}_{\text{ext}}$, whereas a paratropic ring current amplifies $\mathbf{B}_{\text{ext}}$ and flows anticlockwise, as illustrated for benzene in fig. 2.4.

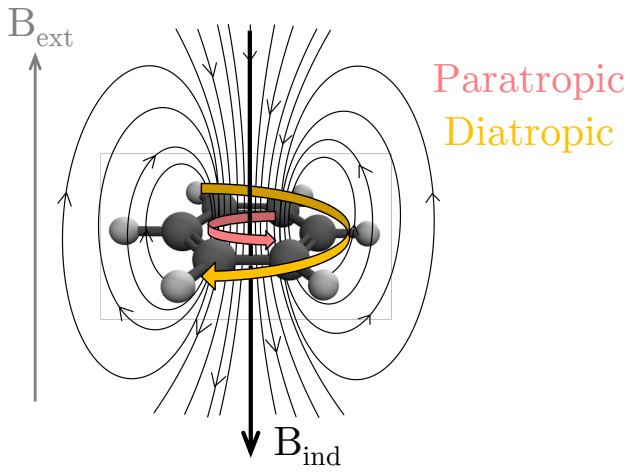

Figure 2.4: Benzene in an external magnetic field $\mathbf{B}_{\text{ext}}$ and the induced dia- and paratropic currents outside and inside the ring, respectively. Since for benzene, a net diatropic ring current is observed, the induced magnetic field $\mathbf{B}_{\text{ind}}$ weakens $\mathbf{B}_{\text{ext}}$.[152]

In general, a diamagnetic molecule with a net diatropic ring current implies aromaticity, as it is the case for benzene, for example. In anti-aromatic molecules, a net paratropic current is observed while a non-aromatic molecule does not exhibit a significant net ring current.[158] Thus, by determining the strengths of the ring current, conclusions about the aromaticity can be drawn, which is described further in section 2.3.10. Regarding the NMR shifts of benzene, the protons are deshielded since the region outside is subject to a stronger magnetic field, while the region inside the ring is shielded. Another property that is associated with aromaticity is the magnetic susceptibility, which is negative/positive for aromatic/anti-aromatic compounds.[159] In the next subsection, the terms „magnetizability“ and „magnetic susceptibility“ are elucidated.

2.3.3 Magnetizability

The magnetization $\mathbf{M}$ describes the alignment of the magnetic dipole moments in the magnetic field $\mathbf{B}$[161] and is given by the induced magnetic moment $\mathbf{m}$ per volume unit $\mathbf{V}$

$$\mathbf{M} = \frac{\mathrm{d}\mathbf{m}}{\mathrm{d}\mathbf{V}}. \tag{2.55}$$

The magnetization is proportional to the magnetic field strength $\mathbf{H}$,

$$\mathbf{M} = \chi\mathbf{H}, \tag{2.56}$$

and relates to the magnetic induction $\mathbf{B}$ via

$$\begin{aligned} \mathbf{B} &= \mu_0(\mathbf{H} + \mathbf{M}) \\ &= \mu_0(1 + \chi)\mathbf{H}, \end{aligned} \tag{2.57}$$

where μ_0 is the vacuum permeability. In both eqs. (2.56) and (2.57), the magnetic susceptibility χ appears. If $\chi > 0$, the system is paramagnetic and is drawn into the magnetic field, i.e. the magnetization amplifies the external field $\mathbf{B}$. By contrast, if $\chi < 0$, the system is diamagnetic.[19] As mentioned above, an applied magnetic field induces a current, which in turn causes a magnetic moment $\mathbf{m}$. The relationship between $\mathbf{m}$ and the external magnetic field $\mathbf{B}$ is given by[19,160]

$$\mathbf{m} = \boldsymbol{\xi}\mathbf{B}, \tag{2.58}$$

and $\boldsymbol{\xi}$ is one of the properties of interest in this thesis, the magnetizability tensor. Inserting eqs. (2.56) and (2.58) into eq. (2.55) leads to

$$\chi\mathbf{H} = \frac{\mathrm{d}}{\mathrm{d}V}(\boldsymbol{\xi}\mathbf{B}). \tag{2.59}$$

Assuming that χ is uniform in the volume, the following relationship between magnetizability and the magnetic susceptibility can be established

$$\chi = \frac{\boldsymbol{\xi}}{V}\frac{\mathbf{B}}{\mathbf{H}} = \frac{\boldsymbol{\xi}}{V}\mu, \tag{2.60}$$

using the definition of the magnetic permeability $\mu = \frac{\mathbf{B}}{\mathbf{H}}$. Equation (2.60) shows the linear relationship between the magnetizability and the magnetic susceptibility. Both terms are often used as synonyms in the literature, i.e. measurements on bulk properties are referred to as magnetic susceptibility while the corresponding results from quantum-chemical calculations are called magnetizability.[162]

Now that the physical and chemical concepts of NMR shieldings, ring currents and magnetizabilities have been established, the question remains how these quantities can be calculated in quantum chemistry. For this purpose, the molecular Hamiltonian in a magnetic field is needed and defined first, followed by the elaboration of how molecular properties of interest can be calculated via derivatives of the energy.

2.3.4 Molecular Magnetic Hamiltonian

If a magnetic field is applied, the electronic Hamiltonian specified in eq. (2.4) changes. To be more specific, only the kinetic energy term $\hat{T}_e$ changes, which is why it is appropriate to rewrite the Hamilton operator as

$$\hat{H} = \hat{T}_e + V(\mathbf{r}). \tag{2.61}$$

$\hat{T}_e$ is defined as

$$\hat{T}_e = \frac{1}{2}\mathbf{p}^2 \tag{2.62}$$

in the field-free case, with the momentum operator $\mathbf{p}$

$$\mathbf{p} = -i\boldsymbol{\nabla}. \tag{2.63}$$

In the presence of an external magnetic field, $\mathbf{p}$ must be replaced by the kinetic momentum operator $\boldsymbol{\pi}$ (see Ref. [2], for example)

$$\boldsymbol{\pi} = \mathbf{p} + \mathbf{A}(\mathbf{r}), \tag{2.64}$$

where $\mathbf{A}(\mathbf{r})$ is the vector potential that generates the magnetic field $\mathbf{B}$ via

$$\mathbf{B} = \boldsymbol{\nabla} \times \mathbf{A}(\mathbf{r}). \tag{2.65}$$

In this work, $\mathbf{A}(\mathbf{r})$ is chosen such that the vector potential becomes divergenceless,

$$\boldsymbol{\nabla} \cdot \mathbf{A}(\mathbf{r}) = 0, \tag{2.66}$$

which is consistent with imposing the Coulomb gauge condition. Hence, a uniform magnetic field can be described adequately by

$$\mathbf{A}^{\mathbf{B}}(\mathbf{r}) = \frac{1}{2}\mathbf{B} \times \mathbf{r}_{\mathrm{O}}, \tag{2.67}$$

using the definition $\mathbf{r}_{\mathrm{O}} = (\mathbf{r} - \mathbf{R}_{\mathrm{O}})$ as the position relative to the gauge origin $\mathbf{R}_{\mathrm{O}}$, an arbitrary point in space. In fact, the total vector potential $\mathbf{A}(\mathbf{r})$ consists of two terms,

$$\mathbf{A}(\mathbf{r}) = \mathbf{A}^{\mathbf{B}}(\mathbf{r}) + \sum_{K}^{M} \mathbf{A}_K(\mathbf{r}), \tag{2.68}$$

where $\mathbf{A}^{\mathbf{B}}(\mathbf{r})$ and $\mathbf{A}_K(\mathbf{r})$,

$$\mathbf{A}_K(\mathbf{r}) = \alpha^2 \frac{\mathbf{m}_K \times (\mathbf{r} - \mathbf{R}_K)}{|\mathbf{r} - \mathbf{R}_K|^3}, \tag{2.69}$$

are the vector potentials associated with the external magnetic field and with the magnetic moments of the M nuclei, respectively. In eq. (2.69), α is the fine structure constant ($\alpha \approx 1/137$). Insertion of the kinetic momentum operator (eq. (2.64))into eq. (2.61) leads to

$$\begin{aligned} \hat{H} &= \frac{(\mathbf{p} + \mathbf{A}(\mathbf{r}))^2}{2} + V(\mathbf{r}) \\ &= \frac{\mathbf{p}^2}{2} + \mathbf{A}(\mathbf{r})\mathbf{p} + \frac{1}{2}\mathbf{A}(\mathbf{r})^2 + V(\mathbf{r}), \end{aligned} \tag{2.70}$$

which can be rewritten using the explicit definition of $\mathbf{p}$ in eq. (2.63) and the vector potential in eqs. (2.67) to (2.69), respectively,

$$\begin{aligned}\hat{H} =& -\frac{1}{2}\boldsymbol{\nabla}^2 - \frac{1}{2}\mathbf{B}(\mathbf{r}_\mathrm{O}\times\boldsymbol{\nabla}) + \frac{1}{8}\left[(\mathbf{B}\cdot\mathbf{B})(\mathbf{r}_\mathrm{O}\cdot\mathbf{r}_\mathrm{O}) - (\mathbf{B}\cdot\mathbf{r}_\mathrm{O})(\mathbf{B}\cdot\mathbf{r}_\mathrm{O})\right] \\ & - i\alpha^2\sum_K \frac{\mathbf{m}_K\cdot(\mathbf{r}-\mathbf{R}_K)\times\boldsymbol{\nabla}}{|\mathbf{r}-\mathbf{R}_K|^3} + V(\mathbf{r}) \\ & + \frac{\alpha^2}{2}\sum_K \frac{(\mathbf{B}\cdot\mathbf{m}_K)(\mathbf{r}_\mathrm{O}\cdot(\mathbf{r}-\mathbf{R}_K)) - (\mathbf{B}\cdot(\mathbf{r}-\mathbf{R}_K))(\mathbf{m}_K\cdot\mathbf{r}_\mathrm{O})}{|\mathbf{r}-\mathbf{R}_K|^3} \\ & + \frac{\alpha^4}{2}\sum_{KL} \frac{(\mathbf{m}_K\cdot\mathbf{m}_L)((\mathbf{r}-\mathbf{R}_K)\cdot(\mathbf{r}-\mathbf{R}_L)) - (\mathbf{m}_K\cdot(\mathbf{r}-\mathbf{R}_L))((\mathbf{r}-\mathbf{R}_K)\cdot\mathbf{m}_L)}{|\mathbf{r}-\mathbf{R}_K|^3|\mathbf{r}-\mathbf{R}_L|^3}\end{aligned} \tag{2.71}$$

However, the introduction of a vector potential for the external magnetic field has consequences for the calculations, leading to the so-called gauge-origin problem, which is explained in the following based on Ref. [2].

Gauge-Origin Invariance

As already mentioned, an arbitrary point in space, the gauge origin $\mathbf{R}_\mathrm{O}$, is introduced in the electronic Hamiltonian. In fact, $\mathbf{B}$ is uniquely defined via the vector potential $\mathbf{A}$, but the opposite does not hold.[33] However, a physically essential demand for quantum-chemical calculations is that the results should be independent of the arbitrary gauge-origin, i.e. the point in space where the vector potential vanishes. This requirement is referred to as gauge-origin invariance.[25] The exact wavefunction and Hamiltonian provide gauge-origin invariant results, which means that the observable properties are not affected by a change of the gauge origin. For approximate solutions, this requirement does not hold.
Schemes like individual gauge for localized orbitals (IGLO)[34,35] and localized orbital/localized origin (LORG)[163] were developed to provide gauge-origin independent results for approximate wavefunctions. In these schemes, the molecular wavefunction is partitioned into local fragments that have their own, individual gauge origin. These methods require localized orbitals and since HF orbitals are usually delocalized, they need to be localized first. A widely used solution to the gauge-origin problem that avoids the need of localized orbitals, is provided by the gauge-including atomic orbitals (GIAO) ansatz,[26,30–32,144] where the gauge-origin is build directly into the atomic orbitals,

$$\chi_\mu(\mathbf{B}) = e^{-\frac{i}{2}\mathbf{B}\times(\mathbf{R}_\mu-\mathbf{R_O})\cdot\mathbf{r}}\chi_\mu(0). \tag{2.72}$$

In eq. (2.72), $\chi_\mu(0)$ is a standard field-independent basis function centered at $\mathbf{R}_\mu$. While the use of GIAOs ensures gauge-origin independence, that is the results are independent of the choice of the gauge origin, true gauge invariance is not achieved.[2]

Regarding eq. (2.52), it can be seen that the nuclear shielding tensor is a second-order property (which also holds for the magnetizability tensor as it is demonstrated in the next section), since both the magnetic moment and the magnetic field appear in the expression. It may therefore initially seem intuitive to use a perturbation theory approach as given in eq. (2.25). In fact, this was done over 70 years ago by Ramsey,[27,28] who used Rayleigh-Schrödinger perturbation theory as a starting point and computed nuclear shieldings via the so-called Lamb expression.[146]

However, it turned out that this approach is not suitable for practical applications, because a sum over all excited states is required and this can only be done for model systems.[25,146] Since an external perturbation, like a magnetic field, can be treated as a weak perturbation, it is also possible to describe the energy of the system via a Taylor series around the field-free case and the response of the system to the perturbation can be described through energy derivatives.

2.3.5 Magnetic Molecular Properties via Energy Derivatives

The Taylor expansion for the energy of a molecular electronic system in the presence of an external magnetic field $\mathbf{B}$ and the nuclear magnetic moments $\mathbf{m}_K$ is given as[3]

$$\begin{aligned} E(\mathbf{m}_K, \mathbf{B}) =& E_0 + \sum_i \frac{\mathrm{d}E}{\mathrm{d}B_i}\Big|_{\mathbf{B}=0} B_i + \sum_K \sum_i \frac{\mathrm{d}E}{\mathrm{d}m_{K_i}}\Big|_{\mathbf{m}_K=0} m_{K_i} + \frac{1}{2}\sum_{ij} \frac{\mathrm{d}^2E}{\mathrm{d}B_i \mathrm{d}B_j}\Big|_{\mathbf{B}=0} B_i B_j \\ &+ \sum_K \sum_{ij} \frac{\mathrm{d}^2E}{\mathrm{d}m_{K_i} \mathrm{d}B_j}\Big|_{\mathbf{B},\mathbf{m}_K=0} m_{K_i} B_j + \ldots, \end{aligned} \tag{2.73}$$

where the indices i and j refer to the x, y or z component of the nuclear magnetic moments and the magnetic field, respectively. Because the considered perturbations of the system are static, the associated properties can be calculated as the derivatives at the point $\mathbf{B} = 0$ and $\mathbf{m}_K = 0$, respectively. The fourth term in eq. (2.73) is identified as magnetizability tensor $\boldsymbol{\xi}$,

$$\xi_{ij} = -\left(\frac{\mathrm{d}^2E}{\mathrm{d}B_i \mathrm{d}B_j}\right)_{\mathbf{B}=0}, \tag{2.74}$$

and describes the direct interaction with the external magnetic field. In accordance with eq. (2.52), the shielding tensor $\boldsymbol{\sigma}$ is obtained via the first term in the second row in eq. (2.73),

$$\sigma_{ij} = \left(\frac{\mathrm{d}^2E}{\mathrm{d}m_{K_i} \mathrm{d}B_j}\right)_{\mathbf{B},\mathbf{m}_K=0}. \tag{2.75}$$

The nuclear shielding tensor gives information about the coupling of the nuclear magnetic moments to the magnetic field and is the starting point for the calculation of ring-current strengths and ring-current densities. Hence, energy derivatives are needed to calculate the molecular properties of interest and an efficient evaluation of these is required. That is why the next part deals with general derivative theory and how this applies to HF and MP2 energy derivatives.

2.3.6 Evaluation of Energy Derivatives

The energy does not only depend explicitly on the perturbation (through the Hamiltonian or in the case of a magnetic field via the $\mathbf{B}$-field dependent basis functions), but also implicitly through the wavefunction parameters (in the following equations denoted as $c(x)$), such as the MO coefficients in eq. (2.19). Using the chain rule and x as generic placeholder for the corresponding perturbation, the first derivative of the energy can be expressed via partial derivatives,

$$\frac{\mathrm{d}E}{\mathrm{d}x} = \left(\frac{\partial E}{\partial x}\right) + \left(\frac{\partial E}{\partial c}\right)\left(\frac{\partial c}{\partial x}\right). \tag{2.76}$$

For fully variational methods

$$\left(\frac{\partial E}{\partial c}\right)_{c=c_{\mathrm{opt}}} = 0 \tag{2.77}$$

holds, since the optimized energy fulfills the variational condition, which means that the energy is minimized with respect to the wavefunction parameters. Hence, knowledge of the differentiated wavefunction parameters is not necessary and

$$\frac{\mathrm{d}E}{\mathrm{d}x} = \left(\frac{\partial E}{\partial x}\right) \tag{2.78}$$

suffices. For HF, this does not apply, because it is necessary to consider the orthonormality of the MOs

$$\delta_{ij} = \sum_{\mu\nu} c^*_{\mu i} S_{\mu\nu} c_{\nu j} \tag{2.79}$$

as a constraint to evaluate HF energy derivatives and therefore, the variation is restricted.[2,164] Regarding MP2 theory, non-variational wavefunction parameters, such as the amplitudes, need to be determined. For such cases, i.e. constrained variations and non-variational parameters, it is convenient to use the method of Lagrange multipliers and start from the energy functional $\tilde{E}$

$$\tilde{E}(x, \lambda(x), c(x)) = E(x, \lambda(x), c(x)) + \sum_i \lambda_i(x) f_i(x, c(x)), \tag{2.80}$$

with one Lagrange multiplier λ_i for each constraint $f_i(x, c(x)) = 0$. Requiring stationarity of this functional with respect to c,

$$\left(\frac{\partial \tilde{E}}{\partial c}\right) \stackrel{!}{=} 0, \tag{2.81}$$

allows to determine the Lagrange multiplier and, at least for the HF case, the MO coefficients. Via

$$\left(\frac{\partial \tilde{E}}{\partial \lambda_i}\right) \stackrel{!}{=} 0, \tag{2.82}$$

the equation for the constraints $f_i(x, c(x)) = 0$ is satisfied, as it is the case for the MP2 amplitudes. Consequently, the first derivative is given by

$$\frac{\mathrm{d}\tilde{E}}{\mathrm{d}x} = \left(\frac{\partial E}{\partial x}\right) + \sum_i \lambda_i \left(\frac{\partial f_i}{\partial x}\right), \tag{2.83}$$

and has in common with eq. (2.78) that the derivative of the wavefunction parameters is not needed. At this point, the $(2n{+}1)$ rule is to be mentioned, which claims that the nth derivative of the wavefunction parameters allows the calculation of the $(2n{+}1)$th energy derivative.[2,165,166] In this context, also the $(2n{+}2)$ rule is relevant, stating that the nth derivative of the Lagrange multiplier suffices to compute the $(2n{+}2)$th derivative of the energy.[2,165]

For some second derivatives, i.e. for nuclear shielding tensors, it can be advantageous to differ-

entiate eq. (2.83) with respect to a second perturbation,[37] yielding

$$\begin{aligned}\frac{\mathrm{d}^2\tilde{E}}{\mathrm{d}x\mathrm{d}y} = &\left(\frac{\partial^2 E}{\partial x \partial y}\right) + \left(\frac{\partial^2 E}{\partial x \partial c}\right)\frac{\partial c}{\partial y} \\ &+ \sum_i \left\{\lambda_i \left(\frac{\partial^2 f_i}{\partial x \partial y}\right) + \lambda_i \left(\frac{\partial^2 f_i}{\partial x \partial c}\right)\left(\frac{\partial c}{\partial y}\right) + \left(\frac{\partial \lambda_i}{\partial y}\right)\left(\frac{\partial f_i}{\partial x}\right)\right\}.\end{aligned} \tag{2.84}$$

In fact, this so-called asymmetric formulation is the preferred choice for the calculation of the nuclear shielding tensor, because only differentiation of the wavefunction parameters with respect to three perturbations (B_x, B_y and B_z) is necessary.[25] A symmetric derivative is obtained by differentiating first with respect to one perturbation and then to the second perturbation, followed by symmetrization of the corresponding expressions. In the case of the nuclear shielding tensor, this would lead to a result in which the derivatives of the wavefunction parameters with respect to all perturbations, i.e. the three magnetic field components and all $3N_{\mathrm{Nuclei}}$ nuclear magnetic moment perturbations, are needed, with N_{Nuclei} as the number of nuclei in the molecule. This would be accompanied by a higher computational effort, especially in view of the fact that the determination of the perturbed wavefunctions is the most time-consuming step.[25] Thus, it can be concluded, that the asymmetric formulation is the preferred choice for computing nuclear shielding tensors. However, as it can be seen from eq. (2.84), the $(2n+2)$ rule does not apply to the asymmetric formulation, and the derivatives of the Lagrange multipliers are necessary. In this work, the asymmetric formulation in eq. (2.84) is also chosen for the calculation of the magnetizability tensor since some required terms are already available from previous implementations for NMR shift calculations.

The following subsection demonstrates how to obtain the second derivatives required to calculate the molecular magnetic properties of interest for the HF and MP2 method based on eq. (2.84).

2.3.7 Calculation of NMR Shifts and Magnetizabilities at the HF Level of Theory

Applying the Lagrangian approach, the RHF energy functional is defined as

$$\begin{aligned}\tilde{E} = &\sum_{\mu\nu} D_{\mu\nu} h_{\mu\nu} + \frac{1}{2}\sum_{\mu\nu\sigma\rho} D_{\mu\nu} D_{\sigma\rho}\left(\langle\mu\sigma|\nu\rho\rangle - \frac{1}{2}\langle\mu\sigma|\rho\nu\rangle\right) \\ &- 2\sum_{ij}\varepsilon_{ji}\left(\sum_{\mu\nu} c^*_{\mu i} S_{\mu\nu} c_{\nu j} - \delta_{ij}\right),\end{aligned} \tag{2.85}$$

where the Lagrange multipliers ε_{ij} constitute a Hermitian matrix and Koopmans' theorem states that the diagonal elements (after diagonalization of the matrix of Lagrange multipliers) ε_{ii} can be interpreted as orbital energies,[2,115,167] Based on the RHF energy functional in eq. (2.85) and eq. (2.84), an expression for the magnetizability tensor ξ_{ij} at the HF level is obtained,

$$\begin{aligned}\xi_{ij} = \left(\frac{\mathrm{d}^2 E}{\mathrm{d}B_i \mathrm{d}B_j}\right)_{\mathbf{B}=0} =& \sum_{\mu\nu} D_{\mu\nu}\left(\frac{\partial^2 h_{\mu\nu}}{\partial B_i \partial B_j}\right) - \sum_{\mu\nu} W_{\mu\nu}\left(\frac{\partial^2 S_{\mu\nu}}{\partial B_i \partial B_j}\right) \\ &+ \frac{1}{2}\sum_{\mu\nu\sigma\rho} D_{\mu\nu} D_{\sigma\rho}\left(\frac{\partial^2 \langle\mu\sigma|\nu\rho\rangle}{\partial B_i \partial B_j} - \frac{1}{2}\frac{\partial^2 \langle\mu\sigma|\rho\nu\rangle}{\partial B_i \partial B_j}\right) \\ &+ \sum_{\mu\nu\sigma\rho}\left(\frac{\partial D_{\mu\nu}}{\partial B_j}\right) D_{\sigma\rho}\left(\frac{\partial \langle\mu\sigma|\nu\rho\rangle}{\partial B_i} - \frac{1}{2}\frac{\partial \langle\mu\sigma|\rho\nu\rangle}{\partial B_i}\right) \\ &+ \sum_{\mu\nu}\left(\frac{\partial D_{\mu\nu}}{\partial B_j}\right)\left(\frac{\partial h_{\mu\nu}}{\partial B_i}\right) - \sum_{\mu\nu}\left(\frac{\partial W_{\mu\nu}}{\partial B_j}\right)\left(\frac{\partial S_{\mu\nu}}{\partial B_i}\right),\end{aligned} \tag{2.86}$$

using the definition of the energy weighted density matrix $W_{\mu\nu}$

$$W_{\mu\nu} = 2\sum_i \varepsilon_i c^*_{\mu i} c_{\nu i}. \tag{2.87}$$

In eq. (2.86), the first three terms account for the diamagnetic contribution, while the last three terms contribute to the paramagnetic term. The required derivatives of the one-electron integrals are evaluated based on the equation for the Hamilton operator in a magnetic field (eq. (2.71)),

$$\frac{\partial h_{\mu\nu}}{\partial B_i} = \frac{1}{2}\langle\chi_\mu|\{\mathbf{r}_\mathrm{O}\times\mathbf{p}\}_i|\chi_\nu\rangle + \left\langle\frac{\partial\chi_\mu}{\partial B_i}\middle|\hat{h}\middle|\chi_\nu\right\rangle + \left\langle\chi_\mu\middle|\hat{h}\middle|\frac{\partial\chi_\nu}{\partial B_i}\right\rangle, \tag{2.88}$$

$$\begin{aligned}\frac{\partial^2 h_{\mu\nu}}{\partial B_i \partial B_j} =& \left\langle\frac{\partial^2\chi_\mu}{\partial B_i\partial B_j}\middle|\hat{h}\middle|\chi_\nu\right\rangle + \left\langle\chi_\mu\middle|\hat{h}\middle|\frac{\partial^2\chi_\nu}{\partial B_i\partial B_j}\right\rangle \\ &+ \left\langle\frac{\partial\chi_\mu}{\partial B_i}\middle|\hat{h}\middle|\frac{\partial\chi_\nu}{\partial B_j}\right\rangle + \left\langle\frac{\partial\chi_\mu}{\partial B_j}\middle|\hat{h}\middle|\frac{\partial\chi_\nu}{\partial B_i}\right\rangle \\ &+ \frac{1}{2}\left\langle\frac{\partial\chi_\mu}{\partial B_j}\middle|\{\mathbf{r}_\mathrm{O}\times\mathbf{p}\}_i\middle|\chi_\nu\right\rangle + \frac{1}{2}\left\langle\frac{\partial\chi_\mu}{\partial B_i}\middle|\{\mathbf{r}_\mathrm{O}\times\mathbf{p}\}_j\middle|\chi_\nu\right\rangle \\ &+ \frac{1}{2}\left\langle\chi_\mu\middle|\{\mathbf{r}_\mathrm{O}\times\mathbf{p}\}_i\middle|\frac{\partial\chi_\nu}{\partial B_j}\right\rangle + \frac{1}{2}\left\langle\chi_\mu\middle|\{\mathbf{r}_\mathrm{O}\times\mathbf{p}\}_j\middle|\frac{\partial\chi_\nu}{\partial B_i}\right\rangle \\ &+ \frac{1}{4}\langle\chi_\mu|(\mathbf{r}_\mathrm{O})^2\delta_{ij} - (\mathbf{r}_\mathrm{O})_j(\mathbf{r}_\mathrm{O})_i|\chi_\nu\rangle\,.\end{aligned} \tag{2.89}$$

The derivative of the basis functions needs to be included because the GIAOs (eq. (2.72)) depend on the magnetic field.[148] For the evaluation of the magnetizability tensor via eq. (2.86), only the first derivatives of the wavefunction parameters, those of the MO coefficients,

$$\begin{aligned}\frac{\partial D_{\mu\nu}}{\partial B_j} &= 2\sum_i\left(\frac{\partial c^*_{\mu i}}{\partial B_i}c_{\nu i} + c^*_{\mu i}\frac{\partial c_{\nu i}}{\partial B_i}\right) \\ \frac{\partial W_{\mu\nu}}{\partial B_j} &= 2\sum_i\left(\frac{\partial c^*_{\mu i}}{\partial B_i}\varepsilon_i c_{\nu i} + c^*_{\mu i}\varepsilon_i\frac{\partial c_{\nu i}}{\partial B_i}\right) + \sum_{ij} c^*_{\mu i}\frac{\partial\varepsilon_{ji}}{\partial B_j}c_{\nu j},\end{aligned} \tag{2.90}$$

are necessary. The derivatives of the MO coefficients are also necessary for the calculation of the nuclear shielding tensor, as seen in

$$\sigma_{ij} = \left(\frac{\mathrm{d}^2 E}{\mathrm{d}m_{K_i}\mathrm{d}B_j}\right)_{\mathbf{B}=0} = \sum_{\mu\nu} D_{\mu\nu}\left(\frac{\partial^2 h_{\mu\nu}}{\partial m_{K_i}\partial B_j}\right) + \sum_{\mu\nu}\left(\frac{\partial D_{\mu\nu}}{\partial B_j}\right)\left(\frac{\partial h_{\mu\nu}}{\partial m_{K_i}}\right). \tag{2.91}$$

Based on the Hamiltonian in eq. (2.71) that also accounts for the additional vector potential due to the magnetic moments, the required derivatives for the one-electron Hamiltonian are given by[2,25,38,148]

$$\frac{\partial h_{\mu\nu}}{\partial m_{K_i}} = -i\alpha^2 \Big\langle \chi_\mu \Big| \frac{\{(\mathbf{r}-\mathbf{R}_K)\times\nabla\}_i}{|\mathbf{r}-\mathbf{R}_K|^3} \Big| \chi_\nu \Big\rangle \tag{2.92}$$

for the first and

$$\begin{aligned} \frac{\partial^2 h_{\mu\nu}}{\partial m_{K_i}\partial B_j} =& \frac{\alpha^2}{2} \Big\langle \chi_\mu \Big| \frac{\mathbf{r}_\mathrm{O}(\mathbf{r}-\mathbf{R}_K)\delta_{ij} - (\mathbf{r}_\mathrm{O})_i(\mathbf{r}-\mathbf{R}_K)_j}{|\mathbf{r}-\mathbf{R}_K|^3} \Big| \chi_\nu \Big\rangle \\ & - i\alpha^2 \Big\langle \frac{\partial\chi_\mu}{\partial B_j} \Big| \frac{\{(\mathbf{r}-\mathbf{R}_K)\times\nabla\}_i}{|\mathbf{r}-\mathbf{R}_K|^3} \Big| \chi_\nu \Big\rangle \\ & - i\alpha^2 \Big\langle \chi_\mu \Big| \frac{\{(\mathbf{r}-\mathbf{R}_K)\times\nabla\}_i}{|\mathbf{r}-\mathbf{R}_K|^3} \Big| \frac{\partial\chi_\nu}{\partial B_j} \Big\rangle \end{aligned} \tag{2.93}$$

for the mixed second derivative. In order to derive eq. (2.91), it is important to first evaluate the derivative with respect to $\mathbf{m}_K$ and then the derivative with respect to $\mathbf{B}^*$ because in this way only three perturbations (B_x, B_y, B_z) instead of $3 \cdot N_\mathrm{Nuclei}$ perturbations are obtained for the coupled-perturbed HF (CPHF)[168] equations (see next section). The solution of the CPHF equations is necessary to determine the derivatives of the wavefunction parameters $\frac{\partial D_{\mu\nu}}{\partial B_j}$ required for both the magnetizability and the nuclear shielding tensor.

The Coupled-Perturbed Hartree-Fock Equations

The CPHF equations[168] are the equations that determine the first derivatives of the MO coefficients with respect to the magnetic field, as required in eq. (2.90). To simplify the theory, the differentiated coefficients are parametrized as linear combination of unperturbed MO coefficients that are already known from the solution of the Roothaan-Hall equations,[164]

$$\frac{\partial c_{\mu p}}{\partial B_i} = \sum_q \frac{\partial U_{qp}}{\partial B_i} c_{\mu q} = \sum_q U_{qp}^{B_i} c_{\mu q}. \tag{2.94}$$

Using this parametrization, the CPHF coefficients $U_{pq}^{B_i}$ are to be determined instead of the differentiated MO coefficients. The indices $p, q, \ldots$ denote generic orbitals that can be occupied (occ) or virtual (virt), leading to the following structure of the matrix $\mathbf{U}$

$$\mathbf{U} = \left(\begin{array}{c|c} \mathrm{occ}-\mathrm{occ} & \mathrm{occ}-\mathrm{virt} \\ \hline \mathrm{virt}-\mathrm{occ} & \mathrm{virt}-\mathrm{virt} \end{array} \right). \tag{2.95}$$

Either via the differentiation of the Roothaan-Hall equations or better the differentiation of the Brillouin theorem (f_{ai}=0),

$$\frac{\mathrm{d}f_{ai}}{\mathrm{d}B_i} = \frac{\mathrm{d}}{\mathrm{d}B_i} \sum_{\mu\nu} c_{\mu a}^* \langle \chi_\mu | \hat{F} | \chi_\nu \rangle c_{\nu i} = 0, \tag{2.96}$$

* It should be noted that the basis functions and therefore the overlap and two-electron integrals do not depend on $\mathbf{m}_K$.

the CPHF equations can be derived; in this work the second option is chosen. Performing the differentiation in eq. (2.96) leads to

$$\sum_{\mu\nu}\left\{\left(\frac{\partial c^*_{\mu a}}{\partial B_i}\right) f_{\mu\nu}c_{\nu i} + c^*_{\mu a}\left(\frac{\partial f_{\mu\nu}}{\partial B_i}\right)c_{\nu i} + c^*_{\mu a}f_{\mu\nu}\left(\frac{\partial c_{\nu i}}{\partial B_i}\right)\right\} = 0. \tag{2.97}$$

In eq. (2.97), the derivatives of the MO coefficients are substituted by the corresponding parametrization of the orbitals in eq. (2.94),

$$\sum_{\mu\nu}\left\{\sum_p c^*_{\mu p}{U^{B_i}_{pa}}^* f_{\mu\nu}c_{\nu i} + c^*_{\mu a}f^{B_i}_{\mu\nu}c_{\nu i} + c^*_{\mu a}f_{\mu\nu}\sum_p c_{\nu p}U^{B_i}_{pi}\right\} = 0, \tag{2.98}$$

where the derivatives are denoted with B_i as superscript. The derivative of the Fock matrix element $f^{B_i}_{\mu\nu}$

$$\begin{aligned} f^{B_i}_{\mu\nu} = \frac{\partial h_{\mu\nu}}{\partial B_i} &+ \sum_{\sigma\rho} D_{\sigma\rho}\left(\frac{\partial\langle\mu\sigma|\nu\rho\rangle}{\partial B_i} - \frac{1}{2}\frac{\partial\langle\mu\sigma|\rho\nu\rangle}{\partial B_i}\right) \\ &+ \sum_{\sigma\rho}\left(\frac{\partial D_{\sigma\rho}}{\partial B_i}\right)\left(\langle\mu\sigma|\nu\rho\rangle - \frac{1}{2}\langle\mu\sigma|\rho\nu\rangle\right), \end{aligned} \tag{2.99}$$

involves the derivative of the MO coefficients (the last term), for which the definition of the density matrix (eq. (2.19)) and the parametrization in eq. (2.94) is used again, as seen in eq. (7.1) in the appendix. Using the LCAO ansatz and the fact that the Fock operator acts on orbitals to yield their orbital energies (eqs. (7.1) to (7.3) in the appendix), eq. (2.98) can be written as

$$\begin{aligned} 0 = \varepsilon_i {U^{B_i}_{ia}}^* + \varepsilon_a U^{B_i}_{ai} + f^{(B_i)}_{ai} + \sum_j\sum_p \Big({U^{B_i}_{pj}}^*(2\langle ap|ij\rangle - \langle ap|ji\rangle) \\ + U^{B_i}_{pj}(2\langle aj|ip\rangle - \langle aj|pi\rangle)\Big). \end{aligned} \tag{2.100}$$

In the last equation, $f^{(B_i)}_{ai}$ denotes the derivative of the Fock matrix element where the derivative of the density matrix and the MO coefficients is excluded,

$$f^{(B_i)}_{ai} = \sum_{\mu\nu} c^*_{\mu a}\left\{\frac{\partial h_{\mu\nu}}{\partial B_i} + \sum_{\sigma\rho} D_{\sigma\rho}\left(\frac{\partial\langle\mu\sigma|\nu\rho\rangle}{\partial B_i} - \frac{1}{2}\frac{\partial\langle\mu\sigma|\rho\nu\rangle}{\partial B_i}\right)\right\} c_{\nu i}. \tag{2.101}$$

Equation (2.100) can be simplified even further by using the differentiated orthogonality constraint*,

$$\frac{\mathrm{d}}{\mathrm{d}B_i}\langle\phi_p|\phi_q\rangle = 0 = {U^{B_i}_{qp}}^* + S^{B_i}_{pq} + U^{B_i}_{pq}, \tag{2.102}$$

which is also used to set the occupied-occupied and virtual-virtual blocks to[2,164]

$$\begin{aligned} U^{B_i}_{ij} &= -\frac{1}{2}S^{B_i}_{ij} \\ U^{B_i}_{ab} &= -\frac{1}{2}S^{B_i}_{ab}. \end{aligned} \tag{2.103}$$

* A detailed derivation of this equation is given in eq. (7.4) in the appendix.

Equation (2.102) can be converted to the following two equations,

$$U_{qp}^{B_i*} + U_{pq}^{B_i} = -S_{pq}^{B_i}, \tag{2.104}$$

$$U_{qp}^{B_i*} = -S_{pq}^{B_i} - U_{pq}^{B_i}, \tag{2.105}$$

which in turn are used to eliminate one of the two matrix elements of the matrix **U**. This means that

$$U_{ia}^{B_i*} = -U_{ai}^{B_i} - S_{ai}^{B_i} \tag{2.106}$$

can be inserted in eq. (2.100), such that

$$\begin{aligned} 0 = (\varepsilon_a - \varepsilon_i)U_{ai}^{B_i} - \varepsilon_i S_{ai}^{B_i} + f_{ai}^{(B_i)} + \sum_j \sum_p \Big(& U_{pj}^{B_i*}(2\langle ap|ij\rangle - \langle ap|ji\rangle) \\ & + U_{pj}^{B_i}(2\langle aj|ip\rangle - \langle aj|pi\rangle)\Big). \end{aligned} \tag{2.107}$$

Equation (2.107) still contains a sum over generic orbitals in the last term, which can be split into two sums, where the first runs over virtual orbitals and the second runs over occupied orbitals (eqs. (7.5) to (7.7) in the appendix). Collecting and rearranging all terms finally yields the CPHF equations[169]

$$\begin{aligned} (\varepsilon_a - \varepsilon_i)U_{ai}^{B_i} + \sum_b \sum_j \Big\{ U_{bj}^{B_i}(4\langle aj|ib\rangle - \langle aj|bi\rangle - \langle ab|ji\rangle)\Big\} \\ = -f_{ai}^{(B_i)} + \varepsilon_i S_{ai}^{B_i} + \sum_{mj} S_{jm}^{B_i}\langle am|ji\rangle, \end{aligned} \tag{2.108}$$

linear equations whose solution allows the determination of the virtual-occupied block $U_{ai}^{B_j}$.

In summary, the CPHF equations enable the derivatives of the MO coefficients to be determined. With this, the magnetizability and the shielding tensor (eqs. (2.86) and (2.91)) can be calculated for HF.
For electron correlation methods such as MP2, further equations for the MP2 density matrix are required. In the next subsection, the determination of the magnetic properties using MP2 is discussed. In this case, also non-variational wavefunction parameters, i.e. the amplitudes, appear.

2.3.8 Calculation of NMR Shifts and Magnetizabilities at the MP2 Level of Theory

As for HF, the starting point for calculating MP2 energy derivatives is not the MP2 energy defined in eq. (2.31), but again an energy functional, for whose construction the method of Lagrange multipliers is used. However, the orthonormality of the spin orbitals ($S_{pq} - \delta_{pq}$) is not the only constraint, but also the variational condition for the HF orbitals, which is taken into account through the Brillouin theorem $f_{ai} = 0$, as well as the MP2 amplitude equation

$$\langle ab|ij\rangle + (\varepsilon_a + \varepsilon_b - \varepsilon_i - \varepsilon_j)t_{ij}^{ab} = 0, \tag{2.109}$$

in accordance with eq. (2.81). In eq. (2.109), canonical orbitals are assumed, which is not the case in the following. Therefore, the orbital energy-based expressions are replaced by the expressions containing Fock matrix elements,

$$\varepsilon_a t_{ij}^{ab} = \sum_e f_{ae} t_{ij}^{eb}. \tag{2.110}$$

The MP2 energy functional reads

$$\begin{aligned}\tilde{E}_{\mathrm{MP2}} =& 2\sum_i h_{ii} + \frac{1}{2}\sum_{ij}\left(4\langle ij|ij\rangle - 2\langle ij|ji\rangle\right) + \sum_{ij}\sum_{ab}\tilde{t}_{ij}^{ab}\langle ij|ab\rangle \\ &+ \sum_{ij}\sum_{ab}\lambda_{ab}^{ij}\Big(\langle ab|ij\rangle + \sum_e f_{ae}t_{ij}^{eb} + \sum_e f_{be}t_{ij}^{ae} - \sum_m f_{mi}t_{mj}^{ab} - \sum_m f_{mj}t_{im}^{ab}\Big) \\ &+ 2\sum_a\sum_i Z_{ai}f_{ai} + \sum_{pq} I_{pq}(S_{pq} - \delta_{pq}),\end{aligned} \tag{2.111}$$

using the expression of the RHF energy in eq. (2.15), and λ_{ab}^{ij}, Z_{ai} and I_{pq} as Lagrange multipliers. The definitions of the MP2 amplitudes and the spin-adapted MP2 amplitudes are given in eq. (2.35) and eq. (2.34), respectively. The prefactors in front of the Lagrange multipliers in eq. (2.111) can be chosen arbitrarily. In this case, they are chosen so that they are advantageous in the following derivations. In accordance with eq. (2.81), the functional needs to be made stationary with respect to the amplitudes and the MO coefficients to obtain equations for the three Lagrange multipliers.

Stationarity Condition with respect to the Amplitudes

The stationarity condition with respect to the MP2 amplitudes is given by

$$\frac{\partial\tilde{E}}{\partial t_{ij}^{ab}} = 2\langle ij|ab\rangle - \langle ji|ab\rangle + \sum_e \lambda_{eb}^{ij}f_{ea} + \sum_e \lambda_{ae}^{ij}f_{eb} - \sum_m \lambda_{ab}^{mj}f_{im} - \sum_m \lambda_{ab}^{im}f_{jm} = 0, \tag{2.112}$$

and a comparison with the amplitude equation allows to identify the Lagrange multiplier λ_{ab}^{ij} with the spin-adapted MP2 amplitude

$$\lambda_{ab}^{ij} = \tilde{t}_{ij}^{ab*}. \tag{2.113}$$

To avoid long equations, it is advantageous to define the MP2 density matrix D_{pq}, where the occupied-occupied, virtual-virtual and occupied-virtual blocks (without HF contribution) are defined as

$$D_{ij} = -2\sum_m\sum_{ef} t_{jm}^{ef\,*}\tilde{t}_{im}^{ef}, \tag{2.114}$$

$$D_{ab} = 2\sum_{mn}\sum_e \tilde{t}_{mn}^{ae\,*}t_{mn}^{be}, \tag{2.115}$$

and

$$D_{ai} = D_{ia}^* = Z_{ai}. \tag{2.116}$$

These expressions are used to simplify the energy functional in eq. (2.111), which is shown in eqs. (7.8) and (7.9) in the appendix.

According to this, the energy functional is given by

$$\begin{aligned}\tilde{E}_{\mathrm{MP2}} = 2\sum_i h_{ii} + \frac{1}{2}\sum_{ij}\left(4\langle ij|ij\rangle - 2\langle ij|ji\rangle\right) + \sum_{pq} D_{pq} f_{pq} + \sum_{pq} I_{pq}(S_{pq} - \delta_{pq}) \\ + \left(\sum_{ij}\sum_{ab} \tilde{t}_{ij}^{ab}\langle ij|ab\rangle + \text{c.c.}\right),\end{aligned} \tag{2.117}$$

where c.c. stands for „complex conjugate“ and denotes the corresponding complex conjugated terms. To obtain equations for the Lagrange multipliers Z_{ai} and I_{pq}, the stationarity condition with respect to the MO coefficients is required.

Stationarity Condition with respect to the MO Coefficients

For the sake of simplicity, the MO coefficients can be parametrized via

$$c'_{\mu p} = \sum_q c_{\mu q} T_{qp}, \tag{2.118}$$

using an arbitrary matrix $\mathbf{T}$, which has the same subblocks as the matrix $\mathbf{U}$ in eq. (2.95). In this way, all possible choices for the MO coefficients are covered, and stationarity with respect to $c_{\mu p}$ is equivalent to stationarity with respect to the elements of the matrix $\mathbf{T}$. Furthermore, four different equations are necessary (the derivatives with respect to T^*_{pq} give rise to the complex conjugate equations that correspond to $c^*_{\mu p}$). The derivative with respect to the occupied-occupied block is given via*

$$\begin{aligned}\left(\frac{\partial \tilde{E}}{\partial T_{ij}}\right)_{\mathbf{T}=\mathbf{1}} =& 2\delta_{ji}\varepsilon_i + D_{ij}\varepsilon_i + \sum_{pq} D_{pq}\left(\langle pj|qi\rangle - \frac{1}{2}\langle pj|iq\rangle\right) + I_{ij} \\ &+ 2\sum_m\sum_{ef} \tilde{t}_{jm}^{ef\,*}\langle ef|im\rangle = 0.\end{aligned} \tag{2.119}$$

In summary, the equations

$$\left(\frac{\partial \tilde{E}}{\partial T_{ab}}\right)_{\mathbf{T}=\mathbf{1}} = D_{ab}\varepsilon_a + I_{ab} + 2\sum_{mn}\sum_e \tilde{t}_{mn}^{be\,*}\langle ae|mn\rangle = 0, \tag{2.120}$$

$$\begin{aligned}\left(\frac{\partial \tilde{E}}{\partial T_{ai}}\right)_{\mathbf{T}=\mathbf{1}} =& D_{ai}\varepsilon_a + \sum_{pq} D_{pq}\left(\langle pi|qa\rangle - \frac{1}{2}\langle pi|aq\rangle\right) + I_{ai} \\ &+ 2\sum_m\sum_{ef} \tilde{t}_{im}^{ef\,*}\langle ef|am\rangle = 0,\end{aligned} \tag{2.121}$$

$$\left(\frac{\partial \tilde{E}}{\partial T_{ia}}\right)_{\mathbf{T}=\mathbf{1}} = D_{ia}\varepsilon_i + I_{ia} + 2\sum_{mn}\sum_e \tilde{t}_{mn}^{ae\,*}\langle mn|ie\rangle = 0 \tag{2.122}$$

are obtained for the stationarity condition with respect to the MO coefficients and now the Lagrange multiplier I_{pq} can be determined. Expressions for the occupied-occupied and virtual-

* A detailed derivation of eq. (2.119) can be found in eqs. (7.10) and (7.11)in the appendix.

virtual blocks I_{ij} and I_{ab} are derived by rearranging eqs. (2.119) and (2.120) appropriately,

$$I_{ij} = -2\delta_{ji}\varepsilon_i - D_{ij}\varepsilon_i - \sum_{pq} D_{pq}\left(\langle pj|qi\rangle - \frac{1}{2}\langle pj|iq\rangle\right) - 2\sum_{m}\sum_{ef} \tilde{t}_{jm}^{ef\,*}\langle ef|im\rangle\,, \tag{2.123}$$

$$I_{ab} = -D_{ab}\varepsilon_a - 2\sum_{mn}\sum_{e} \tilde{t}_{mn}^{be\,*}\langle mn|ae\rangle\,. \tag{2.124}$$

Since I_{pq} is symmetric with respect to an interchange of p and q, it suffices to determine the virtual-occupied block ($I_{ai} = I_{ia}$). Starting from eq. (2.121), eq. (2.122) can be added,

$$\begin{aligned} 2I_{ai} = -D_{ai}(\varepsilon_i + \varepsilon_a) - \sum_{pq} D_{pq}\left(\langle pi|qa\rangle - \frac{1}{2}\langle pi|aq\rangle\right) - 2\sum_{m}\sum_{ef} \tilde{t}_{im}^{ef\,*}\langle ef|am\rangle \\ - 2\sum_{mn}\sum_{e} \tilde{t}_{mn}^{ae\,*}\langle ie|mn\rangle\,. \end{aligned} \tag{2.125}$$

However, the equations for the Lagrange multiplier Z_{ai} and thus the virtual-occupied block of the MP2 density matrix D_{ai} are still needed (see eq. (2.116)). Corresponding equations can be derived by rewriting eq. (2.121) such that all combinations for p and q are considered, and after subtracting eq. (2.122) the Z-vector equations,[169]

$$\begin{aligned} &D_{ai}(\varepsilon_a - \varepsilon_i) + \sum_{m}\sum_{e}\left(D_{em}\left[2\langle ei|ma\rangle - \langle ei|am\rangle\right] + D_{me}\left[2\langle mi|ea\rangle - \langle mi|ae\rangle\right]\right) = -2X_{ai} \\ &\rightarrow \sum_{m}\sum_{e} D_{em}\left(4\langle ei|ma\rangle - \langle ei|am\rangle - \langle mi|ae\rangle + \delta_{ae}\delta_{im}(\varepsilon_a - \varepsilon_i)\right) = -2X_{ai}, \end{aligned} \tag{2.126}$$

are obtained. The definition of the intermediate X_{ai} is given by

$$\begin{aligned} X_{ai} =& \sum_{mn} D_{mn}\left(\langle mi|na\rangle - \frac{1}{2}\langle mi|an\rangle\right) + \sum_{ef} D_{ef}\left(\langle ei|fa\rangle - \frac{1}{2}\langle ei|af\rangle\right) \\ &+ \sum_{m}\sum_{ef} \tilde{t}_{im}^{ef\,*}\langle ef|am\rangle - \sum_{mn}\sum_{e} \tilde{t}_{mn}^{ae\,*}\langle ie|mn\rangle\,. \end{aligned} \tag{2.127}$$

In fact, the Z-vector equations can be used to simplify the equations for I_{ai} in eq. (2.125),

$$I_{ai} = -D_{ai}\varepsilon_i - \sum_{mn}\sum_{e} t_{mn}^{ae\,*}\langle ie|mn\rangle\,. \tag{2.128}$$

Hence, solving the Z-vector equations enables the determination of the virtual-occupied block of the MP2 density matrix and now, all quantities required to evaluate the MP2 energy functional in eq. (2.117) are available. Based on this, the necessary derivatives to compute the magnetic properties of interest can be computed.

Derivatives of the MP2 Energy Functional

According to the previous discussions, the NMR shielding tensor can be computed via[25,37]

$$\begin{aligned}\frac{\partial^2 \tilde{E}_{\mathrm{MP2}}}{\partial m_{Ki} \partial B_j} =& \sum_{pq} D_{pq} h_{pq}^{m_{Ki},B_j} \\ &+ \sum_{pq} \left\{ \left(\frac{\partial D_{pq}}{\partial B_j} \right) + \sum_r D_{rq} U_{pr}^{B_j *} + \sum_r D_{pr} U_{qr}^{B_j} \right\} h_{pq}^{m_{Ki}},\end{aligned} \tag{2.129}$$

where the derivatives of the HF part are not included as the HF contribution was already discussed in the last subsection. Superscripted indices mean that the MO coefficients are not differentiated. To derive eq. (2.129), the parametrization of the perturbed MO coefficients in eq. (2.94) is used. Additional terms must be taken into account[38] for the MP2 derivatives, like the mixed derivative of the one-electron integrals and the derivative of the MP2 density matrix.[37] To obtain expressions for the derivatives of the occupied-occupied and virtual-virtual blocks of the density matrix, eqs. (2.114) and (2.115) are differentiated, leading to terms that contain derivatives of the amplitudes,[37,61]

$$\frac{\partial D_{ij}}{\partial B_i} = -2 \sum_m \sum_{ef} \left(\frac{\partial t_{jm}^{ef\ *}}{\partial B_i} \tilde{t}_{im}^{ef} + \tilde{t}_{jm}^{ef\ *} \frac{\partial t_{im}^{ef}}{\partial B_i} \right) \tag{2.130}$$

and

$$\frac{\partial D_{ab}}{\partial B_i} = 2 \sum_{mn} \sum_e \left(\frac{\partial t_{mn}^{ae\ *}}{\partial B_i} \tilde{t}_{mn}^{be} + \tilde{t}_{mn}^{ae\ *} \frac{\partial t_{mn}^{be}}{\partial B_i} \right). \tag{2.131}$$

Based on eq. (2.35), the MP2 amplitude equations can be differentiated,[38]

$$\begin{aligned}\frac{\partial t_{ij}^{ab}}{\partial B_i} =& \left\{ \frac{\partial \langle ab|ij \rangle}{\partial B_i} - \sum_m \left(t_{im}^{ab} \frac{\partial f_{mj}}{\partial B_i} + t_{mj}^{ab} \frac{\partial f_{mi}}{\partial B_i} \right) \right. \\ &\left. + \sum_e \left(\frac{\partial f_{ae}}{\partial B_i} t_{ij}^{eb} + \frac{\partial f_{be}}{\partial B_i} t_{ij}^{ae} \right) \right\} \frac{1}{f_{ii} + f_{jj} - f_{aa} - f_{bb}},\end{aligned} \tag{2.132}$$

and by using the parametrization of the coefficients in eq. (2.94) again, the derivatives of the MO integrals are given by

$$\begin{aligned}\frac{\partial \langle pq|rs \rangle}{\partial B_i} =& \sum_{\mu\nu\sigma\rho} c_{\mu p}^* c_{\sigma q}^* \frac{\partial \langle \mu\sigma|\nu\rho \rangle}{\partial B_i} c_{\nu r} c_{\rho s} \\ &+ \sum_t \left(U_{tp}^{B_i *} \langle tq|rs \rangle + U_{tq}^{B_i *} \langle pt|rs \rangle + \langle pq|ts \rangle U_{tr}^{B_i} + \langle pq|rt \rangle U_{ts}^{B_i} \right).\end{aligned} \tag{2.133}$$

Since the virtual-occupied block of the MP2 density matrix is defined via the Z-vector equations, eq. (2.126) needs to be differentiated,

$$\begin{aligned}
&\sum_m \sum_e \frac{\partial D_{em}}{\partial B_i} \left(\langle mi|ae\rangle - \langle ei|am\rangle + \delta_{ae}\delta_{im}(\varepsilon_a - \varepsilon_i) \right) \\
&= -\frac{\partial X_{ai}}{\partial B_i} + \sum_m \sum_e D_{em} \left(2\frac{\partial \langle ei|ma\rangle}{\partial B_i} + 2\frac{\partial \langle mi|ea\rangle}{\partial B_i} - \frac{\partial \langle mi|ae\rangle}{\partial B_i} \right. \\
&\quad \left. - \frac{\partial \langle ei|am\rangle}{\partial B_i} + \delta_{im}\frac{\partial f_{ea}}{\partial B_i} - \delta_{ea}\frac{\partial f_{im}}{\partial B_i} \right),
\end{aligned} \tag{2.134}$$

where the derivative of the intermediate X_{ai} (eq. (2.127)) is determined via[37]

$$\begin{aligned}
\frac{\partial X_{ai}}{\partial B_i} =& \sum_{mn} \left\{ \frac{\partial D_{mn}}{\partial B_i} \left(\langle mi|na\rangle - \frac{1}{2}\langle mi|an\rangle \right) + D_{mn} \left(\frac{\partial \langle mi|na\rangle}{\partial B_i} - \frac{1}{2}\frac{\partial \langle mi|an\rangle}{\partial B_i} \right) \right\} \\
&+ \sum_{ef} \left\{ \frac{\partial D_{ef}}{\partial B_i} \left(\langle ei|fa\rangle - \frac{1}{2}\langle ei|af\rangle \right) + D_{ef} \left(\frac{\partial \langle ei|fa\rangle}{\partial B_i} - \frac{1}{2}\frac{\partial \langle ei|af\rangle}{\partial B_i} \right) \right\} \\
&+ \sum_m \sum_{ef} \left(\frac{\partial \tilde{t}_{im}^{ef\,*}}{\partial B_i} \langle ef|am\rangle + \tilde{t}_{im}^{ef\,*} \frac{\partial \langle ef|am\rangle}{\partial B_i} \right) \\
&- \sum_{mn} \sum_e \left(\frac{\partial \tilde{t}_{mn}^{ae\,*}}{\partial B_i} \langle ie|mn\rangle + \tilde{t}_{mn}^{ae\,*} \frac{\partial \langle ie|mn\rangle}{\partial B_i} \right).
\end{aligned} \tag{2.135}$$

Compared to the determination of the nuclear shielding tensor in eq. (2.129), a few more terms are required to compute the magnetizability tensor,

$$\begin{aligned}
\frac{\partial^2 \tilde{E}_{\mathrm{MP2}}}{\partial B_i \partial B_j} =& 2\sum_i \frac{\partial h_{ii}^{B_i}}{\partial B_j} + \frac{1}{2}\sum_{ij} \left(4\frac{\partial \langle ij|ij\rangle^{B_i}}{\partial B_j} - 2\frac{\partial \langle ij|ji\rangle^{B_i}}{\partial B_j} \right) \\
&+ \sum_{pq} \left\{ \left(\frac{\partial D_{pq}}{\partial B_j} \right) + \sum_r D_{rq} U_{pr}^{B_i^*} + \sum_r D_{pr} U_{qr}^{B_i} \right\} f_{pq}^{(B_i)} + \sum_{pq} D_{pq} f_{pq}^{(B_i)B_j} \\
&+ \sum_{pq} \left\{ \left(\frac{\partial I_{pq}}{\partial B_j} \right) + \sum_r I_{rq} U_{pr}^{B_i^*} + \sum_r I_{pr} U_{qr}^{B_i} \right\} S_{pq}^{B_i} + \sum_{pq} I_{pq} S_{pq}^{B_i B_j} \\
&+ \left(\sum_{ij} \sum_{ab} \tilde{t}_{ij}^{ab} \frac{\partial \langle ij|ab\rangle^{B_i}}{\partial B_j} + c.c. + \sum_{ij} \sum_{ab} \left(\frac{\partial \tilde{t}_{ij}^{ab}}{\partial B_j} \right) \langle ij|ab\rangle^{B_i} + c.c. \right).
\end{aligned} \tag{2.136}$$

The derivative of the one-electron integrals in the HF part reads

$$\frac{\partial h_{ii}^{B_i}}{\partial B_j} = \sum_p \left\{ U_{pi}^{B_j^*} h_{pi}^{B_i} + h_{ip}^{B_i} U_{pi}^{B_j} \right\} + h_{ii}^{B_i B_j}, \tag{2.137}$$

and the derivative of the two-electron integrals is given via

$$\begin{aligned}
\frac{\partial \langle pq|rs\rangle^{B_i}}{\partial B_j} = \langle pq|rs\rangle^{B_i B_j} + \sum_t \Big(& U_{tp}^{B_j^*} \langle tq|rs\rangle^{B_i} + U_{tq}^{B_j^*} \langle pt|rs\rangle^{B_i} \\
& + \langle pq|ts\rangle^{B_i} U_{tr}^{B_j} + \langle pq|rt\rangle^{B_i} U_{ts}^{B_j} \Big).
\end{aligned} \tag{2.138}$$

The derivative of the density matrix and the different blocks of the Lagrange multiplier I_{pq} can be found in eqs. (2.130), (2.131) and (7.12) to (7.14). In eqs. (2.101) and (2.132), expressions for

$f_{pq}^{(B_i)}$ and the derivative of the amplitudes can be found, whereas $f_{pq}^{(B_i)B_j}$ is defined as

$$\begin{aligned} f_{pq}^{(B_i)B_j} = &\sum_{\mu\nu} c_{\mu p}^{*} \left\{ \left(\frac{\partial^2 h_{\mu\nu}}{\partial B_i \partial B_j} \right) + \sum_{\sigma\rho} \left(\frac{D_{\sigma\rho}}{\partial B_j} \right) \left(\frac{\partial \langle \mu\sigma | \nu\rho \rangle}{\partial B_i} - \frac{1}{2} \frac{\partial \langle \mu\sigma | \rho\nu \rangle}{\partial B_i} \right) \right. \\ &\left. + \sum_{\sigma\rho} D_{\sigma\rho} \left(\frac{\partial^2 \langle \mu\sigma | \nu\rho \rangle}{\partial B_i \partial B_j} - \frac{1}{2} \frac{\partial \langle \mu\sigma | \rho\nu \rangle}{\partial B_i \partial B_j} \right) \right\} c_{\nu q}. \end{aligned} \tag{2.139}$$

With this, all terms for computing the magnetizability and the NMR chemical shielding at the MP2 level are defined.

To compute sufficiently accurate molecular properties for strongly correlated systems, the use of multi-reference methods is unavoidable, as already mentioned in section 2.2.4. The first calculations of NMR shieldings using GIAOs and a multi-configurational method were performed in 1994 by Ruud *et al.*,[39] and the corresponding theory is explained briefly in the next subsection, based on Refs. [39, 97].

2.3.9 Calculation of NMR Shifts at CASSCF Level of Theory

Analogous to HF and MP2, the NMR chemical shielding tensor σ_{ij} can be computed via the second derivative of the variational CASSCF energy E_{CASSCF},

$$\sigma_{ij} = \frac{\partial^2 E_{\mathrm{CASSCF}}}{\partial m_{K_i} \partial B_j} + \sum_{p>q} \frac{\partial^2 E_{\mathrm{CASSCF}}}{\partial m_{K_i} \partial \kappa_{pq}} \frac{\mathrm{d}\kappa_{pq}}{\mathrm{d}B_j} + \sum_{J\neq 0} \frac{\partial^2 E_{\mathrm{CASSCF}}}{\partial m_{K_i} \partial S_J} \frac{\mathrm{d}S_J}{\mathrm{d}B_j}. \tag{2.140}$$

Here, κ_{pq} and S_J relate to the parametrization for orbital and CSF coefficient variations via eq. (2.46) and eq. (2.47), respectively. As before, the indices $p, q, \ldots$ refer to generic orbitals. The first term in eq. (2.140), which is called static contribution, includes the derivative of the overlap matrix and the one-electron integrals in the MO basis, which are already given in eqs. (2.92) and (2.93). The second and third term in eq. (2.140) account for the response of the wavefunction to the perturbation through the orbital and configurational rotation operators. In the following, the vector $\boldsymbol{\lambda}$ includes the parameters $\{\kappa_{pq} : p > q\}$ and $\{S_J : J \neq 0\}$,[170]

$$\boldsymbol{\lambda} = \begin{pmatrix} \boldsymbol{\kappa} \\ \mathbf{S} \end{pmatrix}. \tag{2.141}$$

By solving the coupled-perturbed CASSCF (CP-CASSCF) equations

$$\frac{\partial^2 E_{\mathrm{CASSCF}}}{\partial \boldsymbol{\lambda} \partial \boldsymbol{\lambda}} \frac{\mathrm{d}\boldsymbol{\lambda}}{\mathrm{d}\mathbf{B}} = -\frac{\partial^2 E_{\mathrm{CASSCF}}}{\partial \mathbf{B} \partial \boldsymbol{\lambda}}, \tag{2.142}$$

which are similar to the CPHF equations, the response of the wavefunction to the perturbations can be determined. Since Cholesky decomposition, a central component of this work, is addressed in a later chapter, the following presents only those equations directly relevant to its formulation, whereas the additional terms required for the solution of the CP-CASSCF equations are available in the literature.[39,97,170] The derivative on the right-hand side of eq. (2.142) involve the derivatives of the inactive and active Fock matrix $F_{\mu\nu}^{I}$ and $F_{\mu\nu}^{A}$ (according to the partitioning of the orbitals

shown in fig. 2.2) in the AO basis,

$$\frac{\partial F^I_{\mu\nu}}{\partial B_i} = \frac{\partial h_{\mu\nu}}{\partial B_i} + \sum_{\sigma\rho} D^I_{\sigma\rho} \left\{ \frac{\partial(\mu\nu|\sigma\rho)}{\partial B_i} - \frac{1}{2}\frac{\partial(\mu\rho|\sigma\nu)}{\partial B_i} \right\}, \tag{2.143}$$

$$\frac{\partial F^A_{\mu\nu}}{\partial B_i} = \sum_{\sigma\rho} D^A_{\sigma\rho} \left\{ \frac{\partial(\mu\nu|\sigma\rho)}{\partial B_i} - \frac{1}{2}\frac{\partial(\mu\rho|\sigma\nu)}{\partial B_i} \right\}, \tag{2.144}$$

as well as the derivatives of the **Q** matrix in the MO basis, which are defined as

$$\frac{\partial Q_{xp}}{\partial B_i} = \sum_{uvy} \Gamma_{xuvy} \frac{\partial(pu|vy)}{\partial B_i}, \tag{2.145}$$

where $u, v, \ldots$ and Γ_{xuvy} denotes active MOs and the two-particle density matrix, respectively. The AO inactive density matrix $D^I_{\sigma\rho}$, that occurs in eq. (2.143), is given in eq. (2.19) and the active density matrix $D^A_{\mu\nu}$ in the AO-basis is defined via

$$D_{\mu\nu} = \sum_{uv} \gamma_{uv} c^*_{\mu u} c_{\nu v}, \tag{2.146}$$

with γ_{uv} as density matrix in the active MO-basis.
Further details of the procedure can be found in Refs. [16, 97, 171].

The calculation of NMR shieldings has now been outlined for the relevant methods in this work. Based on NMR chemical shifts and shieldings, the strength of magnetically induced ring currents of a system can be deduced, which in turn allows for an estimate of its aromaticity. This is exploited in the nucleus independent chemical shift (NICS)[172] or the aromatic ring-current shieldings (ARCS)[154] methods. The disadvantage of the NICS method is that the estimate of the ring current is done indirectly and that the strength of the current can not be determined accurately.[154] Also, with the simple ARCS model it is hard to obtain reliable results, especially for complex structures and molecules with connected rings.[96] In 2004, Jusélius *et al.* presented a method based on GIAOs, the Biot-Savart law for NMR shieldings[173] and the analytical derivative expression for the nuclear shielding tensor to provide reliable and quantitative results for the ring-current strength.[96]

2.3.10 Calculation of the Ring-Current Density based on the NMR Shielding Tensor

The term in eq. (2.73) due to the interaction between the nuclear magnetic moments and the external magnetic field cannot only be expressed in terms of the electronic energy, but also in terms of the vector potential of the magnetic moments $\mathbf{A}_K(\mathbf{r})$ in eq. (2.69) and the induced current density $\mathbf{J}(\mathbf{r})$,[96]

$$E^{\mathbf{m}_K,\mathbf{B}} = -\int \mathbf{A}_K(\mathbf{r}) \cdot \mathbf{J}(\mathbf{r}) \mathrm{d}\mathbf{r}, \tag{2.147}$$

where $\mathbf{J}(\mathbf{r})$ is defined as[96,146]

$$\mathbf{J}(\mathbf{r}) = \frac{i}{2} \int \mathrm{d}\mathbf{r}_2 ... \mathrm{d}\mathbf{r}_N \left(\Psi^* \boldsymbol{\nabla} \Psi - \Psi \boldsymbol{\nabla} \Psi^* + 2i\mathbf{A}\Psi^*\Psi \right), \tag{2.148}$$

with **A** given in eq. (2.68). Hence, the expression for the nuclear shielding tensor in eq. (2.75) can be evaluated using eq. (2.147), leading to[96]

$$\sigma_{ij} = -\varepsilon_{jkl} \int \frac{(\mathbf{r}_k - \mathbf{R}_K)_k}{|\mathbf{r} - \mathbf{R}_K|^3} \frac{\partial J_l(\mathbf{r})}{\partial B_j}, \tag{2.149}$$

where ε_{jkl} is the Levi-Civita symbol,

$$\varepsilon_{jkl} = \begin{cases} +1, & \text{if } (j,k,l) \text{ is an even permutation of (1,2,3),} \\ 0, & \text{if } (j,k,l) \text{ if any index is repeated,} \\ -1, & \text{if } (j,k,l) \text{ is an odd permutation of (1,2,3).} \end{cases} \tag{2.150}$$

After equating eq. (2.149) with eq. (2.91) and reordering the terms, the first-order induced current density tensor can be computed as[96]

$$\begin{aligned} \frac{\partial J_i(\mathbf{r})}{\partial B_j} =& \sum_{\mu\nu} D_{\mu\nu} \frac{\partial \chi_\mu^*}{\partial B_j} \frac{\partial \tilde{h}}{\partial m_{K,i}} \chi_v + \sum_{\mu\nu} D_{\mu\nu} \chi_\mu^* \frac{\partial \tilde{h}}{\partial m_{K,i}} \frac{\partial \chi_v}{\partial B_j} \\ &+ \sum_{\mu\nu} \frac{\partial D_{\mu\nu}}{\partial B_j} \chi_\mu^* \frac{\partial \tilde{h}}{\partial m_{K,i}} \chi_v - \varepsilon_{jkl} \left(\sum_{\mu\nu} D_{\mu\nu} \chi_\mu^* \frac{\partial^2 \tilde{h}}{\partial m_{K,i} \partial B_j} \chi_v \right), \end{aligned} \tag{2.151}$$

where the derivatives of the one-electron Hamiltonian can be extracted from eq. (2.92) and eq. (2.93), except that here the denominator $|\mathbf{r} - \mathbf{R}_K|^3$ does not occur, which is denoted with a tilde, $\tilde{h}$. Also, the integral signs are removed in eq. (2.151), since the integrands on both sides of the equation are identical and the derivative of $\mathbf{J}(\mathbf{r})$ is computed at discrete space points. The net current strength is obtained by integration over the current that flows through a particular bond, e.g. by using Gaussian quadrature.[174] The n-point Gaussian quadrature for a function $f(x)$ is given by the formula

$$\int_a^b f(x)\mathrm{d}x \approx \sum_{i=1}^{n} w_i f(x_i), \tag{2.152}$$

with n and w_i denoting the number of nodes x_i and the integrations weights, respectively. If the net ring-current strength is positive, negative or approximately zero, the molecule can be referred to as aromatic, anti-aromatic or non-aromatic.[152]

In summary, magnetic molecular properties like NMR shieldings, magnetizabilities and magnetically induced ring currents can be calculated as energy derivatives. For the evaluation of HF and MP2 derivatives, perturbed wavefunction parameters like the MO coefficients or the amplitudes are needed, which can be determined through the CPHF and the Z-vector equations, respectively. It is noticeable that the two-electron integrals and their corresponding first and the second derivatives appear in the working equations for the molecular properties, and thus their evaluation is inevitable. In order to evaluate two-electron integrals and their derivatives, various schemes were developed, like the recurrence relation of Obara and Saika,[175,176] the Rys-Quadrature[177] or the scheme developed by McMurchie and Davidson,[114] where the latter is chosen in this work. Based on Refs. [114] and [134], the next section introduces the basic structure of the two-electron integrals and demonstrates their calculation within the framework of the McMurchie-Davidson scheme.[114]

2.4 Integral Evaluation: The McMurchie-Davidson Scheme

2.4.1 Cartesian Gaussians as Basis Functions

The two-electron integrals in the AO basis are denoted as $\langle\mu\sigma|\nu\rho\rangle = \langle\chi_\mu\chi_\sigma|\chi_\nu\chi_\rho\rangle$, as seen in the RHF energy expression in eq. (2.18), but in the following section, the indices are redefined to $\langle\chi_A\chi_B|\chi_C\chi_D\rangle$.
As basis functions χ_A, the choice of Cartesian Gaussian functions*

$$\chi_A(\mathbf{r}) = x_A^n y_A^l z_A^m e^{-\alpha_A(\mathbf{r}-\mathbf{A})^2} = x_A^n y_A^l z_A^m e^{-\alpha_A \mathbf{r}_A^2} \tag{2.153}$$

is motivated by their favorable algebraic properties due to their computational simplicity with respect to several arithmetic operations. The function χ_A is centered at the nucleus $\mathbf{A}$ and the components of the vector $\mathbf{r}_A$ are given by x_A, y_A and z_A, while n, l and m are the Cartesian quantum numbers. The total angular momentum quantum number L is defined for a Cartesian Gaussian as the sum of the quantum numbers

$$L = n + l + m \tag{2.154}$$

and specifies the type of the function via the following mapping.

L	Function
0	S
1	P
2	D
...	...

The set of all basis functions with the same Gaussian exponent α_A and L is referred to as *shell*. The advantages of using Gaussian functions as basis functions are that integrals over Gaussian functions as well as their derivatives can be computed easily and that the product of two Gaussian functions χ_A and χ_B yields another Gaussian function at a new center $\mathbf{P}$ (Gaussian product rule[178]),

$$\Omega_{AB} = \chi_A\chi_B = \chi_P = E_{AB} x_A^{n_A} x_B^{n_B} y_A^{l_A} y_B^{l_B} z_A^{m_A} z_B^{m_B} e^{-\alpha_P \mathbf{r}_\mathbf{P}^2}, \tag{2.155}$$

where the definition of the prefactor E_{AB}, the exponent α_P and P are given by

$$E_{AB} = \exp\left(-\frac{\alpha\beta}{\alpha+\beta}(\mathbf{A}-\mathbf{B})^2\right), \tag{2.156}$$

$$\alpha_P = \alpha_A + \alpha_B, \tag{2.157}$$

and

$$P = \frac{\alpha\mathbf{A} + \beta\mathbf{B}}{\alpha+\beta}. \tag{2.158}$$

* In the discussion, primitive Gaussians are assumed, while the actual basis functions usually are chosen as contracted Gaussians.

2.4.2 McMurchie-Davidson Scheme for Unperturbed Integrals

In the McMurchie-Davidson Scheme,[114] the polynomials in eq. (2.155) are expanded in terms of the functions $\Lambda_N(x_P, \alpha_P)$

$$x_A^{n_A} x_B^{n_B} = \sum_{N=0}^{n_A+n_B} d_N^{n_A n_B} \Lambda_N(x_P, \alpha_P), \tag{2.159}$$

$$y_A^{l_A} y_B^{l_B} = \sum_{L=0}^{l_A+l_B} e_L^{l_A l_B} \Lambda_L(y_P, \alpha_P), \tag{2.160}$$

$$z_A^{m_A} z_B^{m_B} = \sum_{M=0}^{m_A+m_B} f_M^{m_A m_B} \Lambda_M(z_P, \alpha_P), \tag{2.161}$$

where the relation

$$\left(\frac{\partial}{\partial P_x}\right)^N e^{-\alpha_P x_P^2} = \Lambda_N(x_P, \alpha_P) e^{-\alpha_P x_P^2} \tag{2.162}$$

between a Hermite Gaussian and the derivative of a Gaussian is used. Since Hermite polynomials can be calculated using recursion relations, the expansion coefficients $d_N^{n_A n_B}$, $e_L^{l_A l_B}$ and $f_M^{m_A m_B}$ can be also determined via recursion relations, which is demonstrated for $d_N^{n_A n_B}$,

$$d_N^{(n_A+1)n_B} = \frac{1}{2\alpha_P} d_{N-1}^{n_A n_B} + \overline{\mathbf{PA}}_x d_N^{n_A n_B} + (N+1) d_{N+1}^{n_A n_B}, \tag{2.163}$$

$$d_N^{n_A(n_B+1)} = \frac{1}{2\alpha_P} d_{N-1}^{n_A n_B} + \overline{\mathbf{PB}}_x d_N^{n_A n_B} + (N+1) d_{N+1}^{n_A n_B}, \tag{2.164}$$

with the definition of $\overline{\mathbf{PA}}_x = P_x - A_x$ and $d_0^{00} = 1$ as starting point.

One-Electron Integrals

The easiest integral is the overlap integral which is, according to the McMurchie-Davidson scheme, given by

$$\langle \chi_B | \chi_A \rangle = E_{AB} \sum_{NLM} D_{NLM} \left[NLM | 1 \right], \tag{2.165}$$

using the following notation for the expansion coefficients

$$D_{NLM} = d_N^{n_A n_B} e_L^{l_A l_B} f_M^{m_A m_B} \tag{2.166}$$

and the basic integral $[NLM|1]$

$$[NLM|1] = \int \Lambda_N e^{-\alpha_P x_P^2} \mathrm{d}x \int \Lambda_L e^{-\alpha_P y_P^2} \mathrm{d}y \int \Lambda_M e^{-\alpha_P z_P^2} \mathrm{d}z \tag{2.167}$$

$$= \delta_{N0} \delta_{L0} \delta_{M0} \left(\frac{\pi}{\alpha_P}\right)^{\frac{3}{2}}. \tag{2.168}$$

For the sake of simplicity, the sums in eqs. (2.159) to (2.161) are combined to $\sum_{NLM}$. In general, any one-electron integral with a multiplicative operator $\hat{O}$ can be evaluated using

$$\langle \chi_B | \hat{O} | \chi_A \rangle = E_{AB} \sum_{NLM} D_{NLM} \left[NLM | O \right]. \tag{2.169}$$

A more complicated situation arises for integrals with a non-factorizable operator, like $\frac{1}{|\mathbf{r}_K - \mathbf{r}_e|}$, as it is the case for the nuclear-attraction integral

$$\left\langle \chi_B \middle| \frac{1}{r_{Ke}} \middle| \chi_A \right\rangle = E_{AB} \sum_{NLM} D_{NLM} \left[NLM \middle| \frac{1}{r_{Ke}} \right]. \tag{2.170}$$

Here, the basic integral is given by

$$\left[NLM \middle| \frac{1}{r_{Ke}} \right] = \frac{2\pi}{\alpha_P} R_{NLM}, \tag{2.171}$$

where the auxiliary function R_{NLM}

$$R_{NLM} = \left(\frac{\partial}{\partial P_x} \right)^N \left(\frac{\partial}{\partial P_y} \right)^L \left(\frac{\partial}{\partial P_z} \right)^M F_0(T) \tag{2.172}$$

is introduced. Analogous to the expansion coefficients, the auxiliary function is generated using recursion relations.[114,179] The derivatives in eq. (2.172) arise from the relation between a Hermite Gaussian and the derivative of a Gaussian function,

$$\left(\frac{\partial}{\partial P_x} \right)^N \left(\frac{\partial}{\partial P_y} \right)^L \left(\frac{\partial}{\partial P_z} \right)^M e^{-\alpha_p \mathbf{r}_P^2} = \Lambda_N(x_p, \alpha_P) \Lambda_L(y_P, \alpha_P) \Lambda_M(z_P, \alpha_P) e^{-\alpha_p \mathbf{r}_P^2}, \tag{2.173}$$

while $F_0(T)$ is the so-called Boys-function[178]

$$F_0(T) = \int_0^1 e^{\alpha_P (\mathbf{R}_K - \mathbf{P})^2 u^2} \tag{2.174}$$

$$= \int_0^1 e^{-T u^2} \mathrm{d}u. \tag{2.175}$$

Collecting all terms, the nuclear attraction integral is obtained by

$$\left\langle \chi_B \middle| \frac{1}{r_{Ke}} \middle| \chi_A \right\rangle = E_{AB} \frac{2\pi}{\alpha_P} \sum_{NLM} D_{NLM} R_{NLM}. \tag{2.176}$$

Two-Electron Integrals

The evaluation of the two-electron integrals is carried out in the same way as for the nuclear-attraction integral. Analogous to eq. (2.170), it follows

$$\left\langle \chi_B \chi_D \middle| \frac{1}{r_{12}} \middle| \chi_A \chi_C \right\rangle = E_{AB} E_{CD} \sum_{NLM} \sum_{N'L'M'} D_{NLM} D_{N'L'M'} \left[NLM \middle| \frac{1}{r_{12}} \middle| N'L'M' \right], \tag{2.177}$$

where N, L, M refer to the first electron (χ_A, χ_B) and N', L', M' to the second electron (χ_C, χ_D).

Compared to eq. (2.170), the equations for the integral

$$\left[NLM\middle|\frac{1}{r_{12}}\middle|N'L'M'\right] = (-1)^{N'+L'+M'}\lambda_0 \times R_{N+N',L+L',M+M'} \tag{2.178}$$

are more sophisticated. The definition of $F_0(t)$ is basically the same as in eq. (2.174), except that T is defined as

$$T = \frac{\alpha_P\alpha_Q}{\alpha_P+\alpha_Q}\left(\overline{\mathbf{PQ}}_x^2 + \overline{\mathbf{PQ}}_y^2 + \overline{\mathbf{PQ}}_z^2\right). \tag{2.179}$$

In eq. (2.178), the expressions for λ_0 and $R_{N+N',L+L',M+M'}$ are

$$\lambda_0 = \frac{2\pi^{\frac{5}{2}}}{\alpha_P\alpha_Q\sqrt{\alpha_P+\alpha_Q}} \tag{2.180}$$

and

$$R_{N+N',L+L',M+M'} = \left(\frac{\partial}{\partial P_x}\right)^N \left(\frac{\partial}{\partial P_y}\right)^L \left(\frac{\partial}{\partial P_z}\right)^M F_0(T), \tag{2.181}$$

respectively. Hence, the two-electron integral is computed using

$$\begin{aligned}\left\langle\chi_B\chi_D\middle|\frac{1}{r_{12}}\middle|\chi_A\chi_C\right\rangle = E_{AB}E_{CD}\sum_{NLM}\sum_{N'L'M'} & D_{NLM}D_{N'L'M'} \\ & \times (-1)^{N'+L'+M'}\lambda_0 R_{N+N',L+L',M+M'}.\end{aligned} \tag{2.182}$$

2.4.3 McMurchie-Davidson Scheme for NMR Integrals

Until now, the McMurchie-Davidson procedure was reviewed for integrals consisting of standard Cartesian Gaussian functions. However, as already mentioned in section 2.3.4, magnetic-field dependent GIAOs are usually used as basis functions in calculations that involve a magnetic field. Exploiting the definition of GIAOs in eq. (2.72), the unperturbed two-electron integrals

$$\langle\mu\sigma|\nu\rho\rangle = \int d\mathbf{r}_1 \int d\mathbf{r}_2 \cdot e^{\frac{i}{2}\mathbf{B}\times(\mathbf{R}_\mu-\mathbf{R}_\nu)\mathbf{r}_1} e^{\frac{i}{2}\mathbf{B}\times(\mathbf{R}_\sigma-\mathbf{R}_\rho)\mathbf{r}_2} \cdot \frac{\Omega_{\mu\nu}(\mathbf{r}_1)\Omega_{\sigma\rho}(\mathbf{r}_2)}{r_{12}} \tag{2.183}$$

involve phase factors, the charge distribution between two standard Cartesian Gaussians as defined in eq. (2.155) and the Coulomb operator. Noteworthy is the fact that the dependence on the gauge origin $\mathbf{R}_\mathrm{O}$ vanishes in eq. (2.183).
In the section about magnetic properties (section 2.3.4) it has been shown that for the calculation of the nuclear shielding tensor, first-order perturbed integrals,

$$\begin{aligned}\left(\frac{\partial\langle\mu\sigma|\nu\rho\rangle}{\partial B_i}\right)_{\mathbf{B}=0} &= \int \mathrm{d}\mathbf{r}_1 \int \mathrm{d}\mathbf{r}_2 \left(e^{\frac{i}{2}\mathbf{B}\{(\mathbf{R}_\mu-\mathbf{R}_\nu)\times\mathbf{r}_1+(\mathbf{R}_\sigma-\mathbf{R}_\rho)\times\mathbf{r}_2\}}\right)_{\mathbf{B}=0} \\ &\quad \cdot \frac{i}{2}\left\{(\mathbf{R}_\mu-\mathbf{R}_\nu)\times\mathbf{r}_1 + (\mathbf{R}_\sigma-\mathbf{R}_\rho)\times\mathbf{r}_2\right\}_i \frac{\Omega_{\mu\nu}(\mathbf{r}_1)\Omega_{\sigma\rho}(\mathbf{r}_2)}{r_{12}} \\ &= \frac{i}{2}\int \mathrm{d}\mathbf{r}_1 \int \mathrm{d}\mathbf{r}_2 \cdot \left\{(\mathbf{R}_\mu-\mathbf{R}_\nu)\times\mathbf{r}_1 + (\mathbf{R}_\sigma-\mathbf{R}_\rho)\times\mathbf{r}_2\right\}_i \\ &\quad \cdot \frac{\Omega_{\mu\nu}(\mathbf{r}_1)\Omega_{\sigma\rho}(\mathbf{r}_2)}{r_{12}}\end{aligned} \tag{2.184}$$

are required (as seen in eq. (2.99) for the HF and eq. (2.132) for the MP2 case). These perturbed integrals are referred to as NMR-Integrals in the following and as already mentioned, they are evaluated at the point $\mathbf{B} = 0$. To illustrate the evaluation of the NMR integrals using the McMurchie-Davidson scheme, only the derivative with respect to the x-component of the magnetic field,

$$\left(\frac{\partial \langle \mu\sigma|\nu\rho\rangle}{\partial B_x}\right)_{\mathbf{B}=0} = \int d\mathbf{r}_1 \int d\mathbf{r}_2 \frac{i}{2}\{ (\mathbf{R}_{\mu_y} - \mathbf{R}_{\nu_y})z_1 \; -(\mathbf{R}_{\mu_z} - \mathbf{R}_{\nu_z})y_1 \; +(\mathbf{R}_{\sigma_y} - \mathbf{R}_{\rho_y})z_2 \; -(\mathbf{R}_{\sigma_z} - \mathbf{R}_{\rho_z})y_2 \}_x \cdot \frac{\Omega_{\mu\nu}(\mathbf{r}_1)\Omega_{\sigma\rho}(\mathbf{r}_2)}{r_{12}}, \tag{2.185}$$

is considered; the procedure is analogous for the y and z components. To keep track of the different contributions arising due to the McMurchie-Davidson scheme, they are color-coded in this and the following equation. Based on eq. (2.177), the NMR integrals are computed via[180]

$$\begin{aligned}\left(\frac{\partial \langle \mu\sigma|\nu\rho\rangle}{\partial B_x}\right)_{\mathbf{B}=0} = {} & E_{\mu\nu}E_{\sigma\rho}\frac{i}{2}(\mathbf{R}_{\mu_y} - \mathbf{R}_{\nu_y}) \sum_{N}^{n_A+n_B} d_N^{n_A n_B} \sum_{L}^{l_A+l_B} e_L^{l_A l_B} \sum_{M}^{m_A+m_B+1} z f_M^{m_A m_B} \cdot \\ & \sum_{N'L'M'} D_{N'L'M'} \left[NLM|\tfrac{1}{r_{12}}|N'L'M'\right] \\ & -E_{\mu\nu}E_{\sigma\rho}\frac{i}{2}(\mathbf{R}_{\mu_z} - \mathbf{R}_{\nu_z}) \sum_{N}^{n_A+n_B} d_N^{n_A n_B} \sum_{L}^{l_A+l_B+1} y e_L^{l_A l_B} \sum_{M}^{m_A+m_B} f_M^{m_A m_B} \cdot \\ & \sum_{N'L'M'} D_{N'L'M'} \left[NLM|\tfrac{1}{r_{12}}|N'L'M'\right] \\ & +E_{\mu\nu}E_{\sigma\rho}\frac{i}{2}(\mathbf{R}_{\sigma_y} - \mathbf{R}_{\rho_y}) \sum_{N'}^{n_C+n_D} d_{N'}^{n_C n_D} \sum_{L'}^{l_C+l_D} e_{L'}^{l_C l_D} \sum_{M'}^{m_C+m_D+1} z f_{M'}^{m_C m_D} \cdot \\ & \sum_{NLM} D_{NLM} \left[NLM|\tfrac{1}{r_{12}}|N'L'M'\right] \\ & -E_{\mu\nu}E_{\sigma\rho}\frac{i}{2}(\mathbf{R}_{\sigma_z} - \mathbf{R}_{\rho_z}) \sum_{N'}^{n_C+n_D} d_{N'}^{n_C n_D} \sum_{L'}^{l_C+l_D+1} y e_{L'}^{l_C l_D} \sum_{M'}^{m_C+m_D} f_{M'}^{m_C m_D} \cdot \\ & \sum_{NLM} D_{NLM} \left[NLM|\tfrac{1}{r_{12}}|N'L'M'\right], \end{aligned} \tag{2.186}$$

where perturbed expansion coefficients like $z f_M^{m_A m_B}$ occur. Just as for the unperturbed coefficients in eqs. (2.163) and (2.164), they are obtained via recursion relations,[179]

$$x d_N^{n_A n_B} = -2\alpha_p d_N^{n_A (n_B+1)} + n_B d_N^{n_A (n_B-1)}, \tag{2.187}$$

which is similar for $y e_L^{l_A l_B}$ and $z f_{M'}^{m_C m_D}$. The y- and z-counterparts for eq. (2.186) can be found in eqs. (7.15) and (7.16) in the appendix.
The evaluation of the magnetizability integrals using the McMurchie-Davidson procedure is part of the theory developed in this thesis and is presented in section 3.3.

Use of the McMurchie-Davidson scheme enables an efficient calculation of the two-electron integrals and their derivatives. However, the computation of the two-electron integrals is still

demanding and a bottleneck in most quantum-chemical calculations, especially if orbitals with high angular momentum are used.[84,181] Particularly high hard disk requirements appear, if the two-electron integrals are computed and stored on disk before the SCF-procedure starts. In 1982, Almlöf and Co-workers[62] suggested a direct SCF scheme, where the required integrals are recomputed on-the-fly instead of reading them from disk or storing them on disk, respectively. In modified schemes, the integral values are estimated before the calculation (integral prescreening), which can be done using the Schwarz integral screening[67] or a density-weighted cutoff criterion,[66] for example. This can also be applied to the calculation of NMR chemical shifts or magnetizabilities on both HF and MP2 level of theory.[61,64,65] But, as a disadvantage of direct SCF methods, the many integral recalculations have to be mentioned. Moreover, linear scaling techniques[182,183] that ensure a scaling behavior of $\mathcal{O}(M)$ were developed, where often multipole expansions are used.[184–186] However, these methods only achieve good results for large systems.[84] For medium-sized systems, the resolution-of-the-identity (RI) or density fitting (DF) approaches are suitable.[69–73] In the latter methods, a product of two basis functions is expanded in a basis set of auxiliary basis functions, which is discussed in the next section.

2.5 Density Fitting and Resolution-of-the-Identity

In the DF ansatz, the integrals are approximated via

$$(\sigma\rho|\mu\nu) \approx \sum_{\mathcal{PQ}} C^{\mathcal{P}}_{\sigma\rho}(\mathcal{P}|\mathcal{Q})C^{\mathcal{Q}}_{\mu\nu}, \tag{2.188}$$

which means that the product of the basis functions is expanded in a new auxiliary basis set, consisting of real Gaussian basis functions $\mathcal{P}$ and $\mathcal{Q}$,[69,79,85]

$$(\sigma\rho| = \sum_{\mathcal{P}} C^{\mathcal{P}}_{\sigma\rho}\,(\mathcal{P}|\,. \tag{2.189}$$

Here and in the following, the Mulliken notation for the two-electron integrals,

$$(\sigma\rho|\mu\nu) = \langle\sigma\mu|\rho\nu\rangle\,,$$

is used for the sake of simplicity. Furthermore, the Coulomb metric is chosen for the integral evaluation since RI and DF work best with this choice,[69,81]

$$(\mathcal{P}|\mathcal{Q}) = \int \mathrm{dr}_1 \int \mathrm{dr}_2 \mathcal{P}(\mathrm{r}_1)\frac{1}{r_{12}}\mathcal{Q}(\mathrm{r}_2). \tag{2.190}$$

Projection on eq. (2.189) with $|\mathcal{Q})$, followed by a rearrangement of the terms, allows to determine the expansion coefficients $C^{\mathcal{P}}_{\sigma\rho}$

$$C^{\mathcal{P}}_{\sigma\rho} = \sum_{\mathcal{P}}(\sigma\rho|\mathcal{Q})(\mathcal{P}|\mathcal{Q})^{-1}, \tag{2.191}$$

which is equivalent to the linear fitting equations that are obtained by minimization of the norm of the fitting error.[85] Insertion of eq. (2.191) into eq. (2.188) finally leads to a RI-like formulation

for the approximated two-electron integrals

$$(\sigma\rho|\mu\nu) \approx \sum_{\mathcal{PQ}} (\sigma\rho|\mathcal{P})(\mathcal{P}|\mathcal{Q})^{-1}(\mathcal{Q}|\mu\nu), \tag{2.192}$$

which is also called approximate RI[187] because the relation

$$\sum_{\mathcal{PQ}} |\mathcal{P})\,(\mathcal{P}|\mathcal{Q})^{-1}\,(\mathcal{Q}| \approx 1 \tag{2.193}$$

holds. Using the DF ansatz, the evaluation of the expensive four-index two-electron integrals is avoided since they are decomposed into two- and three-center integrals. A disadvantage, however, is the necessity to choose a suitable, predefined auxiliary basis set, in view of the fact that the quality of the result depends on the choice made. Though RI basis sets have been optimized for many AO basis sets and electronic structure models, the accuracy of the auxiliary basis is biased and it is difficult to improve the accuracy.[79]

To avoid the presupposition of a pre-defined auxiliary basis, Cholesky Decomposition (CD) is a suitable method that also allows to speed up the calculations and ensures low memory requirements. The basic procedure of the CD and the advantage of its application to the unperturbed two-electron integrals and the NMR integrals are presented in the next sections.

2.6 Cholesky Decomposition of the Unperturbed Two-Electron Integrals

The concept of CD[188] can be comprehended based on the following schematic illustration.

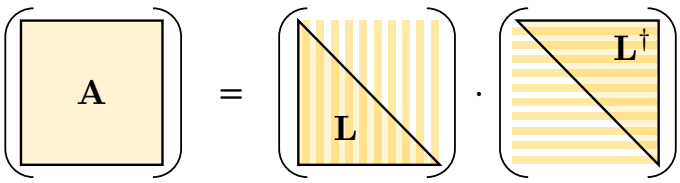

Figure 2.5: Illustration of the Cholesky Decomposition of a matrix **A**.

Figure 2.5 demonstrates the decomposition of a positive (semi-)definite matrix **A** in the product of a lower triangular matrix **L** and its adjugate $\mathbf{L}^\dagger$,

$$\mathbf{A} = \mathbf{L}\mathbf{L}^\dagger = \sum_{P}^{N} \mathbf{l}^P \mathbf{l}^{P*} \approx \sum_{P}^{N_{\mathrm{Ch}}} \mathbf{l}^P \mathbf{l}^{P*}. \tag{2.194}$$

N denotes the dimension of the matrix **A**, while **l** are the Cholesky vectors (CVs), i.e. the columns of the triangular matrix **L**. Within a rigorous treatment, it is also possible to approximate the given matrix **A** for positive definite matrices by truncating the decomposition. In this case the sum runs up to the number of CVs N_{Ch}, while for positive semidefinite matrices, N_{Ch} is always smaller than N.

Since the two-electron integrals constitute a symmetric positive semidefinite matrix,[70] CD can

be applied,[76,181]

$$(\sigma\rho|\mu\nu) \approx \sum_{P}^{N_{\mathrm{Ch}}} L_{\sigma\rho}^{P} L_{\nu\mu}^{P*}. \tag{2.195}$$

The procedure starts by determining the largest diagonal element $\max\{(\nu\mu|\mu\nu)\}$ and via a recursive procedure,[183] the CVs can be obtained,

$$L_{\sigma\rho}^{P} = (\widetilde{\nu\mu|\mu\nu})^{-\frac{1}{2}} \Big\{ (\sigma\rho|\mu\nu) - \sum_{Q=1}^{P-1} L_{\sigma\rho}^{Q} L_{\nu\mu}^{Q*} \Big\}, \tag{2.196}$$

with the index P pointing to the chosen $\mu\nu$ pair. Here, $(\widetilde{\nu\mu|\mu\nu})$ is the updated diagonal,

$$(\widetilde{\nu\mu|\mu\nu}) = (\nu\mu|\mu\nu) - \sum_{Q=1}^{P-1} L_{\nu\mu}^{Q} L_{\nu\mu}^{Q*}. \tag{2.197}$$

This procedure is repeated until all remaining diagonal elements are below the given threshold and all CVs have been determined. To perform MP2 calculations, the vectors need to be transformed into the MO basis,

$$L_{pq}^{P} = \sum_{\sigma\rho} c_{\sigma p}^{*} L_{\sigma\rho}^{P} c_{\rho q}, \tag{2.198}$$

and according to this, eq. (2.195) changes to[76,93]

$$(pq|rs) \approx \sum_{P}^{N_{\mathrm{Ch}}} L_{pq}^{P} L_{sr}^{P*}. \tag{2.199}$$

The use of the CVs leads to a scaling of $\mathcal{O}(M^3 N_{\mathrm{Ch}})$ for the AO to MO transformation instead of the $\mathcal{O}(M^5)$ scaling behavior that holds for the four-index integral transformation.[181] Actually, it can be shown that the number of CVs scales linearly with the system size, as seen in fig. 2.7, which means that the scaling behavior for the AO to MO transformation is reduced by one order of magnitude if CD is used ($\mathcal{O}(M^4)$ vs. $\mathcal{O}(M^5)$).
Because of the full eightfold permutational symmetry of the two-electron integrals,

$$\begin{aligned} &(\sigma\rho|\mu\nu) = (\mu\nu|\sigma\rho) = (\rho\sigma|\nu\mu) = (\nu\mu|\rho\sigma) \\ &= (\rho\sigma|\mu\nu) = (\sigma\rho|\nu\mu) = (\nu\mu|\sigma\rho) = (\mu\nu|\rho\sigma), \end{aligned} \tag{2.200}$$

the CVs are both symmetric with respect to an interchange of the indices,[93,189]

$$L_{\sigma\rho}^{P} = L_{\rho\sigma}^{P}, \tag{2.201}$$

and in case of real basis functions

$$L_{\sigma\rho}^{P*} = L_{\sigma\rho}^{P}. \tag{2.202}$$

To ensure numeric stability, the CD follows a partial pivoting algorithm,[76] which is described in more detail in the implementation section. Conceptually, the largest updated diagonal element is determined in each iteration step and then the CV assigned to this element is computed using eq. (2.196), as seen in fig. 2.6. As long as the largest updated diagonal element is greater than the predefined Cholesky threshold $10^{-\tau}$, the procedure continues. This procedure is also referred

to as one-step algorithm.

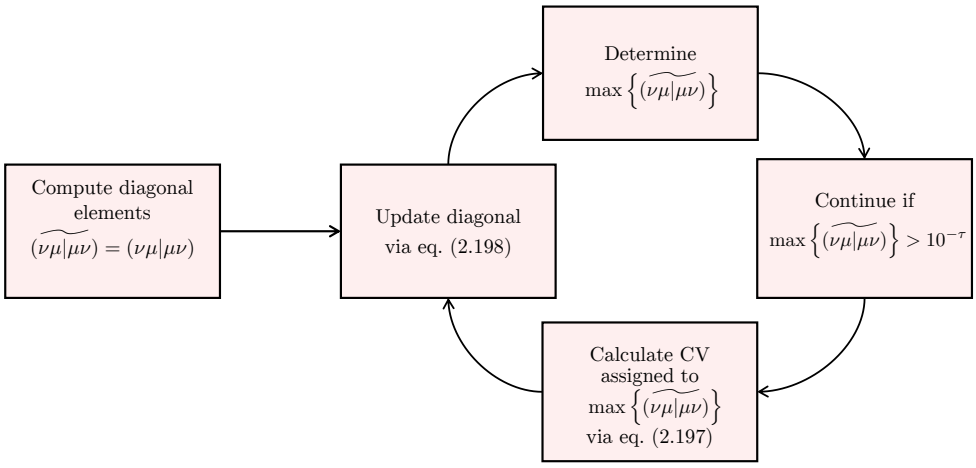

Figure 2.6: Overview of the CD partial pivoting Algorithm.

The error of the decomposition $R_{\sigma\rho\mu\nu}$ is obtained by subtracting the decomposed matrix from the original matrix,

$$R_{\sigma\rho\mu\nu} = (\sigma\rho|\mu\nu) - (\sigma\rho|\mu\nu)_{\mathrm{CD}}, \tag{2.203}$$

and since the Cauchy-Schwarz inequality

$$|R_{\sigma\rho\mu\nu}| \leq \sqrt{R_{\nu\mu\mu\nu}}\sqrt{R_{\sigma\rho\sigma\rho}} \leq 10^{-\tau} \tag{2.204}$$

holds,[70] the magnitude of the error $R_{\sigma\rho\mu\nu}$ is always smaller than the Cholesky threshold. A rigorous error control of the two-electron integrals is therefore guaranteed if CD is applied, which can be considered as an advantage over density fitting.
Instead of $\mathcal{O}(N^4)$, which indicates the performance with regard to the memory requirements for the full two-electron matrix, a more favorable scaling behavior, namely $\mathcal{O}(N_{\mathrm{Ch}}N^2)$,[76,78,190] is achieved for medium-sized molecules applying CD, and thus all CVs can be stored in core memory,[93] which would not be the case for the set of full two-electron integrals. Due to the linear relationship between the number of CVs and the system size, as shown in fig. 2.7, the memory requirement can be specified as $\mathcal{O}(N^3)$.

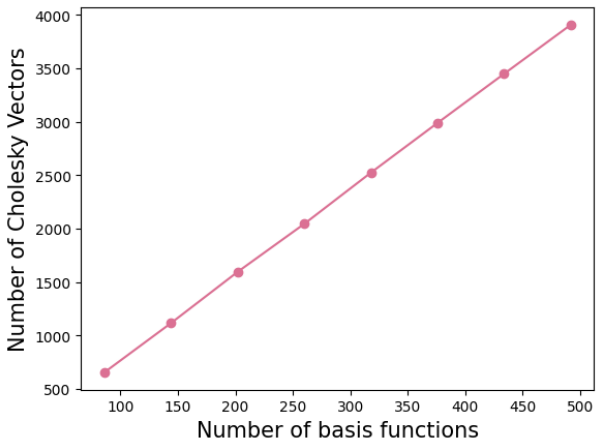

Figure 2.7: Number of CVs for the homologous series of straight-chained alkanes C_2H_{2n+2} in a cc-pVTZ[191] basis using a Cholesky threshold of 10^{-5}.

2.6.1 Connection between Density Fitting and Cholesky Decomposition

As it will be discussed later in section 3.4, the relationship between DF and CD is useful for discussing the CD for the differentiated integrals, which is why the connection between both approaches is explained, following Ref. [85].
In fact, CD is an orthonormalization of the picked order of AO product densities $|\mu\nu)$ (denoted as $|\mathcal{P})$) in the Coulomb metric, yielding orthonormal functions (denoted as $|P)$),[181]

$$|P) = \frac{1}{\sqrt{N_{\mathcal{P}}}} \left(|\mathcal{P}) - \sum_{Q}^{P-1} |Q)\,(\mathcal{P}|Q) \right), \tag{2.205}$$

with the definition of the normalization constant $N_{\mathcal{P}}$ as

$$N_{\mathcal{P}} = (\mathcal{P}|\mathcal{P}) - \sum_{Q}^{P-1} (Q|\mathcal{P})^2. \tag{2.206}$$

The set of orthonormal functions $\{|P), |Q), ...\}$, i.e. the set of $\mu\nu$-pairs that give rise to a Cholesky vector, is referred to as Cholesky basis (CB) $\mathcal{B}$,[81,94] and because the functions $|P)$ and $|Q)$ are orthonormal, the following relation holds,

$$(P|Q) = \delta_{PQ}. \tag{2.207}$$

Comparison of the Gram-Schmidt orthonormalization in eq. (2.205) with the equation for the Cholesky vector in eq. (2.196) shows the distinctive similarity between both equations. Projection with $|\sigma\rho)$ on eq. (2.205) yields

$$(\sigma\rho|P) = \frac{1}{\sqrt{N_{\mathcal{P}}}} \left((\sigma\rho|\mathcal{P}) - \sum_{Q}^{P-1} (\sigma\rho|Q)(\mathcal{P}|Q) \right), \tag{2.208}$$

where the CV can be identified as

$$(\sigma\rho|P) = L^P_{\sigma\rho}. \tag{2.209}$$

With this, the connection between DF and CD is established in the following scheme:[84]

$$\begin{aligned}
(\sigma\rho|\mu\nu) \approx & \sum_{\mathcal{P}\mathcal{Q}} (\sigma\rho|\mathcal{P})(\mathcal{P}|\mathcal{Q})^{-1}(\mathcal{Q}|\mu\nu) \quad \text{(eq. (2.192))} \\
& \Big\downarrow \text{CD} \\
& \sum_{PQ} (\sigma\rho|P)(P|Q)^{-1}(Q|\mu\nu) \\
& \Big\downarrow \text{eq. (2.207)} \\
& \sum_{P} (\sigma\rho|P)(P|\mu\nu) \\
& \Big\downarrow \\
& \sum_{P} L^P_{\sigma\rho} L^P_{\nu\mu} \quad \text{(eq. (2.196))},
\end{aligned} \tag{2.210}$$

where the interchange of the indices in the last step is allowed due to eq. (2.201). According to this, DF and CD are equivalent if the CB is chosen as auxiliary basis. However, the CB $\mathcal{B}$ differs from the standard auxiliary basis sets used in the DF approach in three points:[84]

1. $\mathcal{B}$ contains two-centered functions while DF auxiliary basis sets are solely composed of atom-centered functions.
2. $\mathcal{B}$ is always a subset of the full product set while for DF, there is no guarantee that the selected functions are in the original space of the product densities.
3. The functions in $\mathcal{B}$ are ordered with respect to their significance, enabling a rigorous error control through the Cholesky threshold.

The first point suggests that the computational benefits using CD are lower compared to DF, but on the other hand, this loss is compensated by a controllable accuracy. Modifications of the CD procedure have been developed to avoid the two-centered functions that occur in the original CD, such as the one-center CD (1C-CD) and the atomic CD (aCD).[79,80,85] In the 1C-CD approach, only nucleus-centered product functions enter the CB, while in the aCD approach separate blocks of the atomic two-electron matrix are decomposed.[84] Nevertheless, these modifications are accompanied by an indubitable loss of accuracy.[86] In fact, there is also a possibility to make CD more efficient, at least from an algorithmic point of view. In addition to the one-step algorithm presented in fig. 2.6, an efficient two-step algorithm has been developed by Folkestad *et al.*,[86] where the CB is determined in the first step and the CVs are computed in a second step.

2.6.2 Two-Step Algorithm

The two-step algorithm utilizes the insights from the last subsection, especially the concept of the Cholesky basis, and is briefly introduced based on Refs. [86, 88, 189]. Further algorithmic details can be found in the implementation section 4.1.2.
As mentioned in the last subsection, the first step is the determination of the CB. This is realized through a pivoting procedure akin to the one presented in fig. 2.6, where only the diagonal elements that give rise to a Cholesky vector are saved. After computing the CD of the metric, the CV is computed using the RI-like expression

$$(\sigma\rho|\mathcal{P}) = L^{\mathcal{P}}_{\sigma\rho} = \sum_{\mathcal{Q}} (\sigma\rho|\mathcal{Q})(\mathcal{Q}|\mathcal{P})^{-\frac{1}{2}} \tag{2.211}$$

in the second step. In comparison to the original Gram-Schmidt-like formulation, this algorithm is more efficient, since the construction of the CVs in the second step can be carried out by efficient linear algebra routines, and also has the advantage of being easily parallelizable.[84]

According to this section, it can be stated that Cholesky decomposition is a powerful tool that facilitates an efficient handling of the two-electron integrals in quantum-chemical computations. This opens up a wide range of applications, as high levels of theory like CC[78] or multi-reference methods[171,192] can be implemented in the CD framework for example, which allows the computation of larger systems with a controllable error. Furthermore, CD turns out to be useful for calculations in strong magnetic fields, which comes along with a higher computational cost since the two-electron integrals are complex.[190] Another possibility is to use CD for the computation of molecular properties, i.e. for geometry optimizations that require the derivative with respect

to the nuclear coordinates[81,90] or the computation of NMR shielding constants.[93,189] The basic theory of the latter is presented in the next section, while further improvements of this theory, as well as the CD of the magnetizability integrals, were exploited in the context of this work and can be found in sections 3.1 and 3.4.

2.7 Cholesky Decomposition of NMR Integrals

How CD can be utilized for derivative integrals, like the NMR integrals, was part of the master thesis that preceded this work[180] and is outlined in this section, following Ref. [93].
In fact, the perturbed two-electron integral matrix is not positive semidefinite like the unperturbed counterpart. However, it is still possible to apply CD by differentiating eq. (2.195), the equation for the unperturbed two-electron integrals, with respect to the magnetic field component. Hence, the matrix can be decomposed via

$$\frac{\partial(\sigma\rho|\mu\nu)}{\partial B_i} \approx \sum_{P}^{N_{\mathrm{Ch}}} \left(\frac{\partial L^{P}_{\sigma\rho}}{\partial B_i} L^{P*}_{\nu\mu} + L^{P}_{\sigma\rho} \frac{\partial L^{P*}_{\nu\mu}}{\partial B_i} \right), \tag{2.212}$$

where perturbed CVs are necessary, which can be obtained by differentiation of the corresponding expression for the unperturbed CVs in eq. (2.196),

$$\frac{\partial L^{P}_{\sigma\rho}}{\partial B_i} = \widetilde{(\nu\mu|\mu\nu)}^{-\frac{1}{2}} \left\{ \frac{\partial(\sigma\rho|\mu\nu)}{\partial B_i} - \sum_{Q=1}^{P-1} \left(\frac{\partial L^{Q}_{\sigma\rho}}{\partial B_i} L^{Q*}_{\nu\mu} + L^{Q}_{\sigma\rho} \frac{\partial L^{Q*}_{\nu\mu}}{\partial B_i} \right) \right\}. \tag{2.213}$$

Due to the fact that the NMR integrals and the differentiated CV are imaginary, the derivative of the updated diagonal element vanishes and does not need to be considered. Also, it needs to be mentioned that the perturbed two-electron integrals exhibit fourfold instead of the full eightfold permutational symmetry,

$$\frac{\partial(\sigma\rho|\mu\nu)}{\partial B_i} = \frac{\partial(\mu\nu|\sigma\rho)}{\partial B_i} = -\frac{\partial(\rho\sigma|\nu\mu)}{\partial B_i} = -\frac{\partial(\nu\mu|\rho\sigma)}{\partial B_i}. \tag{2.214}$$

By comparing the first and last term in eq. (2.214), a statement about the complex conjugation of the perturbed NMR CV can be made, where the corresponding pairs of equal vectors are color-coded,

$$\underbrace{\sum_{k=1}^{N_{\mathrm{Ch}}} \left(\frac{\partial L^{P}_{\sigma\rho}}{\partial B_i} L^{P*}_{\nu\mu} + L^{k}_{\sigma\rho} \frac{\partial L^{P*}_{\nu\mu}}{\partial B_i} \right)}_{\frac{\partial(\sigma\rho|\mu\nu)}{\partial B_i}} = \underbrace{-\sum_{k=1}^{N_{\mathrm{Ch}}} \left(\frac{\partial L^{P}_{\nu\mu}}{\partial B_i} L^{P*}_{\sigma\rho} + L^{P}_{\nu\mu} \frac{\partial L^{P*}_{\sigma\rho}}{\partial B_i} \right)}_{-\frac{\partial(\nu\mu|\rho\sigma)}{\partial B_i}}. \tag{2.215}$$

Using the fact that the unperturbed CVs are real (eq. (2.202)), it can be seen from eq. (2.215) that the NMR CVs change their sign under complex conjugation,

$$\frac{\partial L^{P*}_{\sigma\rho}}{\partial B_i} = -\frac{\partial L^{P}_{\sigma\rho}}{\partial B_i}. \tag{2.216}$$

It is, however, important to realize that this is not an independent CD of the NMR integrals since the integrals are not positive definite, as already mentioned. Instead, the integrals are represented in the Cholesky basis constituted by the unperturbed two-electron integrals, which means that the CVs in eq. (2.213) are assigned to an unperturbed $\mu\nu$-pair.

The expressions for the decomposed integrals in eqs. (2.195) and (2.212) are then used to substitute the corresponding integrals with their Cholesky-decomposed counterparts in the expressions for the computation of the NMR shielding constant given in sections 2.3.7 and 2.3.8.

2.7.1 Calculation of NMR Shielding Constants using Cholesky-Decomposed Integrals at the HF Level of Theory

The equation to compute the nuclear shielding tensor at the HF level is given in eq. (2.91) and at a first glance, it looks as if no two-electron integrals are needed. Indeed, both the unperturbed and NMR integrals appear in the CPHF equations (eq. (2.108)) that are need to be solved to determine the perturbed wavefunction parameters required to compute the derivative of the density matrix. A CD-based approach for the CPHF equations is given by

$$\begin{aligned}(\varepsilon_a - \varepsilon_i)U_{ai}^{B_i} + \sum_b \sum_j \sum_P \left\{ U_{bj}^{B_i} \left(L_{aj}^P L_{ib}^P - L_{ab}^P L_{ij}^P \right) \right\} \\ = -{}^{\mathrm{CD}} f_{ai}^{(B_i)} + \varepsilon_i S_{ai}^{B_i} + \sum_{mj} \sum_P \left\{ S_{jm}^{B_i} L_{ai}^P L_{jm}^P \right\},\end{aligned} \tag{2.217}$$

where on the left-hand side only unperturbed CVs are required. On the right-hand side, however, the CD of the Fock matrix derivative that excludes the perturbed density matrix $f_{ai}^{(B_i)}$,

$${}^{\mathrm{CD}} f_{ai}^{(B_i)} = h_{ai}^{B_i} + \sum_m \sum_P \left(\frac{\partial L_{ai}^P}{\partial B_i} L_{mm}^P - L_{ai}^P \frac{\partial L_{mm}^P}{\partial B_i} - \frac{1}{2} \left[\frac{\partial L_{am}^P}{\partial B_i} L_{im}^P - L_{am}^P \frac{\partial L_{im}^P}{\partial B_i} \right] \right) \tag{2.218}$$

appears, for which also the perturbed NMR CVs are needed.[193]

The CD expressions for the calculation of magnetizabilities on HF level of theory, as well as the calculation of MP2-based NMR shifts, were evaluated within this work and can be found in sections 3.2 and 3.5.

As it is clear from the theory outlined above, the CD-based scheme for computing molecular properties offers the possibility to compute properties for large molecules with high accuracy. This is demonstrated later in the result chapter (section 5.1), where NMR shifts are computed for systems containing more than 1000 basis functions using the CD-GIAO-MP2 scheme, as explained in section 3.2.[93] To extend the range of applications even further, a multiscale description of NMR chemical shifts[194–197] or magnetizabilities[198] is a good option, especially in order to gain insights into solvent effects. This can be realized by embedding the presented CD-based approaches in a QM/MM scheme, for example. In QM/MM approaches that were first proposed by Warshel and Levitt,[95] the system is divided in a smaller QM region that contains the molecule or the part of interest and is treated quantum-chemically, and a larger MM region, i.e. the surrounding that is described by a force field, as it is outlined in the following section, based on Refs. [199, 200].

2.8 The Quantum Mechanics/Molecular Mechanics (QM/MM) Approach

The goal of the QM/MM approach is to treat realistic chemical or biological systems up to 100 000 atoms. On the one hand, this calls for fast and computational efficient methods like force field methods, and on the other hand it is necessary to describe chemical reactions adequately in a way quantum-chemical methods do. Thus, a combination of both approaches is required which leads to the underlying idea behind the QM/MM ansatz that was first suggested by Warshel and Levitt in 1976[95] and is illustrated in fig. 2.8.

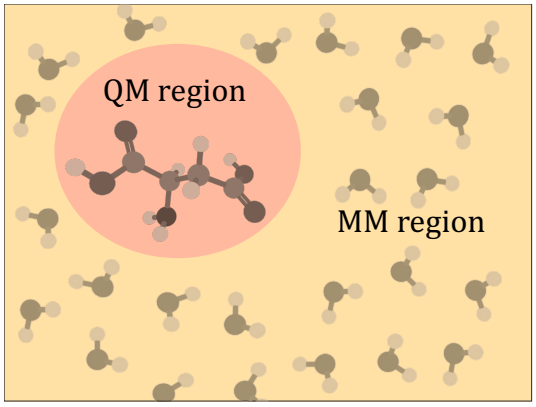

Figure 2.8: Schematic illustration of the QM/MM setup for an arbitrary system.

The whole system is divided into two parts: the region, where the change in the electronic structure takes place, which is treated by accurate QM methods (QM region), and the surrounding (MM region), for example the full molecule or the solvent. To compute the energy of the entire system, a subtractive scheme[201–204] can be used,

$$E = E_{\mathrm{QM}}(\mathrm{QM}) + E_{\mathrm{MM}}(\mathrm{QM}+\mathrm{MM}) - E_{\mathrm{MM}}(\mathrm{QM}), \tag{2.219}$$

where the index denotes the level of treatment, specifically quantum-chemically or with molecular mechanics, while the argument denotes the corresponding region. A major disadvantage of this scheme is the fact that the coupling between QM and MM region is described indirectly and only at the MM level. In this work and in the majority of current QM/MM schemes, an additive ansatz is chosen, where the QM/MM interaction $E_{\mathrm{QM/MM}}$ appears explicitly,

$$E = E_{\mathrm{MM}}(\mathrm{MM}) + E_{\mathrm{QM}}(\mathrm{QM}) + E_{\mathrm{QM/MM}}(\mathrm{QM}+\mathrm{MM}). \tag{2.220}$$

To compute the MM energy, force fields, i.e. classical potential-energy functions V_{MM}, are used, generally consisting of bonded and non-bonded terms,

$$\begin{aligned} E_{\mathrm{MM}} = V_{\mathrm{MM}} = &\sum_{\text{bonds}} k_r (r-r_0)^2 + \sum_{\text{angles}} k_\theta (\theta-\theta_0)^2 + \sum_{\text{dihedrals}} k_\phi \left[1+\cos(n\phi+\delta)\right] \\ &+ \sum_{\mathrm{AB}} \left\{ 4\varepsilon_{AB} \left[\left(\frac{\sigma_{AB}}{r_{AB}}\right)^{12} - \left(\frac{\sigma_{AB}}{r_{AB}}\right)^{6} \right] + \frac{q_A q_B}{4\pi\varepsilon_0 r_{AB}} \right\}. \end{aligned} \tag{2.221}$$

The first three terms are the bonded terms and include the bond stretching between two atoms

with the distance r, the angle deformation between three atoms with the angle θ and the torsion described by the dihedral angle ϕ, the torsional multiplicity n and the torsional phase δ. In all cases, k denotes the corresponding force constant. Non-bonded terms include the van der Waals interaction, described via a Lennard-Jones potential with the equilibrium distance σ and the parameter ε that gives information about the depth of the minimum, and the electrostatic Coulomb interaction between the partial charges q_A and q_B, where ε_0 is the vacuum permittivity.[8,129] Popular force fields are AMBER,[205] CHARMM,[206,207] GROMOS[208,209] and OPLS-AA,[210,211] for example, but it is also possible to obtain force field parameters based on machine learning.[212–215]

In principle, every quantum-chemical method, like the ones presented in section 2.2, can be used to compute the energy of the QM region $E_{\mathrm{QM}}(\mathrm{QM})$. Most commonly, Density Functional Theory (DFT)[216,217] methods are chosen as QM method, enabling QM regions consisting of a few hundreds atoms.[218] DFT methods are, in contrast to the methods presented in this work, based on the electron density and can be implemented in a way that is even faster than HF and still take electron correlation into account.[111,219] However, wavefunction-based post-HF methods guarantee a superior accuracy[8] and Cholesky decomposition can be used to extend the size of the QM system in such a way that a favorable size/accuracy ratio is achieved.

The QM/MM interaction $E_{\mathrm{QM/MM}}$ is described by the Hamiltonian $\hat{H}_{\mathrm{QM/MM}}$

$$\hat{H}_{\mathrm{QM/MM}} = \hat{H}^{\mathrm{b}}_{\mathrm{QM/MM}} + \hat{H}^{\mathrm{vdW}}_{\mathrm{QM/MM}} + \hat{H}^{\mathrm{el}}_{\mathrm{QM/MM}}, \tag{2.222}$$

consisting of the bonded contribution $\hat{H}^{\mathrm{b}}_{\mathrm{QM/MM}}$ that vanishes if the QM/MM boundary does not cross covalent bonds, the van der Waals contribution $\hat{H}^{\mathrm{vdW}}_{\mathrm{QM/MM}}$ that is described at a MM level using the Lennard-Jones potential, and the contribution to the electrostatic interactions between QM and MM region ($\hat{H}^{\mathrm{el}}_{\mathrm{QM/MM}}$). The latter contains the most involved terms and is explained in the following.

2.8.1 Electrostatic QM/MM Interaction

There are three different levels of sophistication at which the electrostatic QM/MM coupling can be handled.[220] First, mechanical embedding is to be mentioned, where the QM and the MM region are treated as rigid atomic point charges. This means that the QM/MM interaction is treated purely at an MM level. As a consequence, the QM region is not directly influenced by the MM surrounding, which is in most cases not a good approximation.

A better approximation is given by the electrostatic embedding, where the MM point charges (described by their coordinates $\mathbf{R}_A$ and partial charges q_A) are included in the electronic Hamiltonian,

$$\hat{H}^{\mathrm{el}}_{\mathrm{QM/MM}} = -\sum_{i}^{N}\sum_{A}^{M_{\mathrm{MM}}} \frac{q_A}{|\mathbf{R}_A - \mathbf{r}_i|} + \sum_{B}^{M_{\mathrm{QM}}}\sum_{A}^{M_{\mathrm{MM}}} \frac{q_A Z_B}{|\mathbf{R}_A - \mathbf{R}_B|}. \tag{2.223}$$

The terms describe the interaction between the electrons and the MM atoms and the repulsion between QM nuclei and MM atoms, respectively. Since eq. (2.223) requires a sum over all MM atoms, a high computational demand is to be expected. However, the computational effort can be reduced by partitioning the MM atoms into short-range (sr) and long-range (lr) regions, based on a cut-off radius (see fig. 2.9), as suggested by Laio and co-workers.[221] In the sr region, the

QM/MM interactions are computed explicitly and the corresponding Hamiltonian $\hat{H}^{\text{el,sr}}_{\text{QM/MM}}$ is given by[222]

$$\hat{H}^{\text{el,sr}}_{\text{QM/MM}} = -\sum_{i}^{N}\sum_{A}^{M_{\text{sr}}} \frac{q_A}{|\mathbf{R}_A - \mathbf{r}_i|} + \sum_{B}^{M_{\text{QM}}}\sum_{A}^{M_{\text{sr}}} \frac{q_A Z_B}{|\mathbf{R}_A - \mathbf{R}_I|}. \tag{2.224}$$

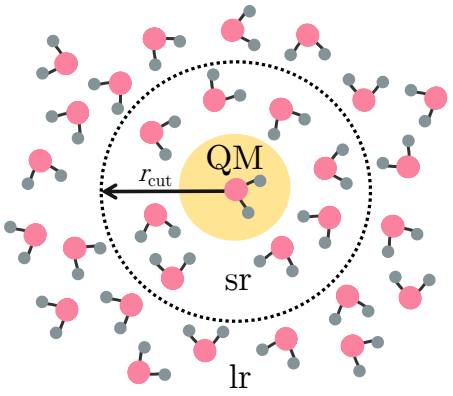

Figure 2.9: Partitioning of the MM atoms in a short-range region (sr) and a long-range region (lr) based on a cut-off radius r_{cut}.[221]

In contrast, a multipole expansion for the electric potential between MM atoms and QM electrons,[221–223]

$$\sum_{i}\sum_{A}\frac{q_A}{|\mathrm{R}_A - \mathrm{r}_i|} = \sum_{A} q_A \left[C\frac{1}{|\mathrm{R}_A|} + \sum_{\alpha}\mu^{\alpha}\frac{R^{\alpha}_A}{|\mathrm{R}_A|^3} + \frac{1}{2}\sum_{\alpha,\beta} Q^{\alpha\beta}\frac{R^{\alpha}_A R^{\beta}_A}{|\mathrm{R}_A|^5} + \ldots \right], \tag{2.225}$$

is used to avoid the explicit calculation of the QM/MM interactions in the long-range region. In eq. (2.225), C, μ^{α} and $Q^{\alpha\beta}$ denote the charge, dipole moment, and quadrupole moment, respectively. Instead of $\mathcal{O}(N_{\text{1el}-\text{int}} \cdot N_{MM})$, a significant better scaling behavior of $\mathcal{O}(N_{\text{1el}-\text{int}} + N_{MM})$ is achieved with the multipole expansion, where $N_{\text{1el}-\text{int}}$ is the number of one-electron integrals and N_{MM} the number of MM atoms.[223]

So far, the presented QM/MM scheme provides energies for a given structure, but to reproduce realistic systems, the time evolution of the system must also be taken into account. This can be realized using classical Molecular Dynamics (MD) simulations, which are elucidated briefly in the following based on Refs. [8, 129].

2.8.2 Molecular Dynamics

To describe the motion of the nuclei, it would in principle be possible to solve the nuclear Schrödinger equation, but this would be far too expensive. Instead, the classical equations of motion

$$\mathbf{F}_A = m\mathbf{a}_A, \tag{2.226}$$

with the force $\mathbf{F}_A$ that acts on the nucleus A and the associated acceleration $\mathbf{a}_A$, is a good approximation because the nuclei are heavy enough (apart from protons) to be treated as classical particles. Since the force is defined as the negative gradient of the potential, the gradient of

the Born-Oppenheimer potential in eq. (2.3) computed within a quantum-chemical framework can be used to determine the forces, which is then referred to as Born-Oppenheimer molecular dynamics (BOMD).[224–229] However, BOMD is only feasible for relatively small systems with about 500 atoms,[228] which is why it is advantageous to calculate the forces via the gradient of the force field potential in eq. (2.221) for large systems,

$$\mathbf{F}_A = -\nabla_A V_{\mathrm{MM}}. \tag{2.227}$$

In order to describe the dynamic of the system, it is necessary to determine the position of the particles after a given time step Δt, for which various algorithms[230] were developed, like the leap frog,[231] Verlet,[232] and Velocity Verlet algorithms[233,234] as well as Runge-Kutta methods,[235–237] for example. For the MD simulations in this work, the leap frog algorithm was chosen, which is based on a Taylor expansion up to the second order in the position of the particles $\mathbf{R}_A$ for positive and negative time steps $t+\Delta t/2$ and $t-\Delta t/2$, respectively. Subtracting the equation for $t - \Delta t/2$ from the equation for the positive time step leads to an expression for the subsequent position $\mathbf{R}_A(t + \Delta t)$

$$\mathbf{R}_A(t + \Delta t) = \mathbf{R}_A(t) + \mathbf{v}_A \left(t + \frac{1}{2}\Delta t \right) \Delta t \tag{2.228}$$

that depends on the previous position of the particle and the first derivative of the coordinate vector $\mathbf{R}_A$, the velocity $\mathbf{v}_A$. For the latter, an analogous Taylor series yields

$$\mathbf{v}_A \left(t + \frac{1}{2}\Delta t \right) = \mathbf{v}_A \left(t - \frac{1}{2}\Delta t \right) + \mathbf{a}_A(t)\Delta t. \tag{2.229}$$

The integration time step Δt is selected such that it does not exceed the fastest motion in a system, that is stretching vibrations. Typically, $\Delta t \approx 0.1\,\mathrm{fs}$, which means that simulations longer than 10 ns (i.e. 10^8 calculations of the energies and forces) are accompanied by a high computational effort.

Besides the dynamics, which are important to investigate realistic systems, the modeling of the system plays an important role, that is constructing a setup that represents a macroscopic system in particular with regard to surface effects and long-range electrostatic interactions. All this can be taken into account using periodic boundary conditions (PBC), where the system is assumed to be a unit cell (like a unit cell in a crystal[238]) and is surrounded by a set of nearest neighbors. If an atom or molecule exits the cell, which is also referred to as simulation box, its periodic image immediately enters on the opposite side.

In a standard MD simulation, a microcanonical (NVE) ensemble with many identical systems in equally probable microstates, is created, in which the number of particles N, the volume V and the total energy E are kept constant. Typically, MD simulations start with an equilibration period to generate a plausible configuration, which can be done in the canonical (NVT) or the NPT ensemble. In the NVT ensemble (where instead of the energy, the temperature is held constant), the system is coupled to a heat bath or thermostat, for example the Berendsen thermostat,[239] and the temperature regulation takes place via a scaling of the velocities, where a given coupling parameter controls the heat supply. To regulate the pressure P in a NPT ensemble, the volume of the system is adjusted by varying the simulation box size.[234] Both pressure and temperature can also be handled via other coupling schemes, like the Nosé-Hoover method.[240,241]

In summary, MD simulations are applied to describe the dynamics of complex systems, and the QM/MM energies and forces can be used within a MD scheme.[218,242–246] Due to the high computational demands of such a QM/MM simulation, the timescales that can be reached are in the range of a few hundreds of picoseconds.[247] However, it is also possible to run a classical MD simulation and take snapshots from the trajectory, i.e. coordinates of all atoms from the generated trajectories at a given time during the simulation, and average over these to compute properties like NMR chemical shifts in a QM/MM framework. A related topic of interest in this thesis is the calculation of NMR shifts for liquid water[248–254] (see section 5.3), especially with regard to the question of how hydrogen bonds impact these. To cover the effect of hydrogen bonding as well as possible, a large QM region is indispensable, for which the Cholesky decomposition of the perturbed two-electron integrals is relevant. This leads to the next chapter, where the theory developed in the context of this thesis is presented.

3 New Theoretical Developments

In this chapter, the focus is on the CD of the perturbed two-electron integrals. It starts with ideas of how to make the CD for the NMR two-electron integrals in section 2.7 faster through the exploitation of permutational symmetry on one side and the utilization of the two-step algorithm on the other. This is subsequently used in the CD-GIAO-MP2 scheme for computing NMR shifts using CD at the MP2 level of theory.[189] In the course of this, the calculation of NMR shifts for CASSCF using CD is briefly discussed.[171] Another major topic is the CD of the magnetizability integrals, which is less straightforward compared to the CD for the NMR integrals and therefore, additional considerations are required. The suggestion of three different schemes to compute the CD of the magnetizability integrals marks the end of the theory chapters.[94]

3.1 Improvements for the Cholesky Decomposition of the NMR Integrals

3.1.1 Exploitation of Permutational Symmetry

As already mentioned, it is possible to enhance the CD of the NMR integrals with regard to computational efficiency. This can be done by taking advantage of the permutational symmetry of the NMR integrals. In section 2.7, it is demonstrated that the NMR integrals exhibit only fourfold instead of the full eightfold permutational symmetry. For the discussion of permutational symmetry, it is convenient to use the notation introduced by Gauss *et al.* in Ref. [148], where the permutational symmetry with respect to the interchange of electron 1 and 2 is denoted by P1, the interchange of the AO indices of electron 1 by P2 and the interchange of the AO indices of electron 2 by P3. Applied to the NMR integrals it can be seen that they are not invariant with respect to P2 and P3. However, it is possible to split the integrals,[61]

$$\frac{\partial(\sigma\rho|\mu\nu)}{\partial B_i} = \left(\frac{\partial\sigma\rho}{\partial B_i}\middle|\mu\nu\right) + \left(\sigma\rho\middle|\frac{\partial\mu\nu}{\partial B_i}\right), \tag{3.1}$$

where the following permutation relations hold

$$\left(\frac{\partial\sigma\rho}{\partial B_i}\middle|\mu\nu\right) = \left(\frac{\partial\sigma\rho}{\partial B_i}\middle|\nu\mu\right) \tag{3.2a}$$

$$\left(\sigma\rho\middle|\frac{\partial\mu\nu}{\partial B_i}\right) = -\left(\sigma\rho\middle|\frac{\partial\nu\mu}{\partial B_i}\right). \tag{3.2b}$$

This means that the partial derivatives exhibit permutational symmetry with respect to P2 and P3 with an additional sign change, if the indices in the differentiated product density are swapped. Equation (3.1) is equated with the equation for the CD of the NMR integrals in eq. (2.212), indicating that the NMR CVs are antisymmetric with respect to the interchange of the indices,[93]

$$\frac{\partial L^P_{\sigma\rho}}{\partial B_i} = -\frac{\partial L^P_{\rho\sigma}}{\partial B_i}. \tag{3.3}$$

Using this result, the NMR CVs can be written as

$$\frac{\partial L^P_{\sigma\rho}}{\partial B_i} \to \frac{1}{2}\left(\frac{\partial L^P_{\sigma\rho}}{\partial B_i} - \frac{\partial L^P_{\rho\sigma}}{\partial B_i}\right), \tag{3.4}$$

and after inserting the expression for the perturbed CVs in eq. (2.213),

$$\begin{aligned}\frac{1}{2}\left(\frac{\partial L^P_{\sigma\rho}}{\partial B_i} - \frac{\partial L^P_{\rho\sigma}}{\partial B_i}\right) =& \frac{1}{2}(\widetilde{\nu\mu|\mu\nu})^{-\frac{1}{2}} \left[\left\{\frac{\partial(\sigma\rho|\mu\nu)}{\partial B_i} - \sum_{Q=1}^{P-1}\left(\frac{\partial L^Q_{\sigma\rho}}{\partial B_i}L^Q_{\nu\mu} - L^Q_{\sigma\rho}\frac{\partial L^Q_{\nu\mu}}{\partial B_i}\right)\right\}\right. \\ &\left. + \left\{\frac{\partial(\sigma\rho|\nu\mu)}{\partial B_i} - \sum_{Q=1}^{P-1}\left(\frac{\partial L^Q_{\sigma\rho}}{\partial B_i}\boxed{L^Q_{\mu\nu}} - L^Q_{\sigma\rho}\boxed{\frac{\partial L^Q_{\mu\nu}}{\partial B_i}}\right)\right\}\right],\end{aligned} \tag{3.5}$$

is obtained, where eq. (2.216) and the permutational symmetry,

$$-\frac{\partial(\rho\sigma|\mu\nu)}{\partial B_i} = \frac{\partial(\sigma\rho|\nu\mu)}{\partial B_i}, \tag{3.6}$$

are exploited. If the indices of the CVs in the blue-colored boxes in eq. (3.5) are both interchanged, this results in a change of sign only for the perturbed CV. This leads to[93]

$$\frac{\partial L^P_{\sigma\rho}}{\partial B_i} = (\widetilde{\nu\mu|\mu\nu})^{-\frac{1}{2}}\left\{\frac{1}{2}\left[\frac{\partial(\sigma\rho|\mu\nu)}{\partial B_i} + \frac{\partial(\sigma\rho|\nu\mu)}{\partial B_i}\right] - \sum_{Q=1}^{P-1}\frac{\partial L^Q_{\sigma\rho}}{\partial B_i}L^Q_{\nu\mu}\right\}, \tag{3.7}$$

the equation that was originally implemented by us in Ref. [93].

In fact, it is possible to reformulate this equation in a more advantageous way, as shown in Ref. [189]. For the integral expressions in the square brackets, the partially differentiated integrals from eq. (3.1) (including the relations in eqs. (3.2a) and (3.2b)) can be used to simplify eq. (3.7) further,

$$\frac{\partial L^P_{\sigma\rho}}{\partial B_i} = (\widetilde{\nu\mu|\mu\nu})^{-\frac{1}{2}}\left\{\left(\frac{\partial\sigma\rho}{\partial B_i}\middle|\mu\nu\right) - \sum_{Q=1}^{P-1}\frac{\partial L^Q_{\sigma\rho}}{\partial B_i}L^Q_{\nu\mu}\right\}. \tag{3.8}$$

A comparison between eqs. (3.7) and (3.8) shows that the use of the latter reduces the cost of the integral evaluation by a factor of four, since only one of the four partial derivatives is needed. A similar utilization of the CV symmetry can be used to halve the memory requirements for the CD of two-electron integrals over GIAOs in finite magnetic-field calculations, which is not part of this work, but has been also presented in Ref. [189].

In eq. (3.8), only the derivative of the left-hand side product density is required, and the product of the two GIAO basis functions (the definition of GIAOs is given in eq. (2.72)) can be written

as

$$\begin{aligned}\chi_\sigma^*(\mathbf{B})\chi_\rho(\mathbf{B}) &= \exp\left(+\frac{i}{2}\mathbf{B}\times(\mathbf{R}_\sigma-\mathbf{R_O})\cdot\mathbf{r}_1\right)\cdot\exp\left(-\frac{i}{2}\mathbf{B}\times(\mathbf{R}_\rho-\mathbf{R_O})\cdot\mathbf{r}_1\right)\\ &\quad\cdot\chi_\sigma^*(0)\chi_\rho(0)\\ &= \exp\left(+\frac{i}{2}\mathbf{B}\times(\mathbf{R}_\sigma-\mathbf{R_O}-\mathbf{R}_\rho+\mathbf{R_O})\cdot\mathbf{r}_1\right)\chi_\sigma^*(0)\chi_\rho(0)\\ &= \exp\left(\frac{i}{2}\mathbf{B}\times(\mathbf{R}_\sigma-\mathbf{R}_\rho)\cdot\mathbf{r}_1\right)\cdot\chi_\sigma^*(0)\chi_\rho(0),\end{aligned} \tag{3.9}$$

where the different signs in the phase factor arise since χ_σ is in the bra and is therefore complex conjugated. Beside the fact, that the gauge origin vanishes, it can be seen that also the phase factor vanishes if χ_σ and χ_ρ are located at the same center. In this case, there is no contribution for the corresponding derivative with respect to the magnetic field component and with a simple check, the integral calculation can be skipped, which leads to further savings of computational time.

3.1.2 Two-Step Algorithm

In section 2.6.2, it has been mentioned that the two-step algorithm for determining the CVs developed by Folkestad *et al.*[86] is more efficient than the original Gram-Schmidt based algorithm. This applies not only to the unperturbed two-electron integrals, but also to the perturbed NMR integrals, as it has been demonstrated by us in Ref. [189]. Since the NMR integrals are represented in an unperturbed CB, the first step (calculation of the CB) remains the same, while only changes in the second step are required. Analogous to the unperturbed CV in eq. (2.211), the NMR CVs are obtained via

$$\frac{\partial L_{\sigma\rho}^P}{\partial B_i} = \sum_Q \left(\frac{\partial \sigma\rho}{\partial B_i}\middle|Q\right)(Q|P)^{-\frac{1}{2}} \tag{3.10}$$

in the second step. The speed-up gained by exploiting permutational symmetry or the two-step algorithm, respectively, is shown in section 5.2.

In the previous chapter, it is explained how to incorporate the Cholesky-decomposed (NMR) integrals in NMR chemical shift calculations at the HF level of theory (section 2.7.1). Nonetheless, HF theory does not account for electron correlation effects, which must be incorporated to achieve high accuracy.[3] In some cases, the HF results are not even consistent with experimental findings,[22,38,52,255] and thus agreement between calculations and experiment can only be achieved with post-HF methods.[3] The MP2 level of theory provides a comparably favorable treatment of electron correlation that often leads to sufficiently accurate and reliable results.[22,25,37,38,255] However, MP2 calculations are accompanied by a higher computational effort, which in turn can be tackled using CD. In the next section, the CD-GIAO-MP2 scheme for computing NMR chemical shieldings is presented based on Ref. [93].

3.2 Calculation of NMR Chemical Shieldings using Cholesky Decomposition at the MP2 Level of Theory

Analogous to the CD-GIAO-HF scheme presented in section 2.7.1, the (perturbed) two-electron integrals given in section 2.3.8 need to be replaced with their corresponding Cholesky-decomposed counterparts for the MP2 based scheme. If the insertion of the CVs does not result in a more advantageous formulation of the terms, the CVs are not explicitly used. Instead, $(pq|rs)^{\mathrm{CD}}$ or $\frac{\partial (pq|rs)^{\mathrm{CD}}}{\partial B_i}$ are used, denoting the integrals reconstructed from the CVs in eqs. (2.195) and (2.212), respectively. To compute the MP2 density matrix, the MP2 amplitudes are required. In the CD-based scheme, the integral in eq. (2.35) is substituted with the Cholesky-decomposed integral,

$$ {}^{\mathrm{CD}}t_{ij}^{ab} = \frac{(ai|bj)^{\mathrm{CD}}}{\varepsilon_i + \varepsilon_j - \varepsilon_a - \varepsilon_b}, \tag{3.11} $$

which works analogously for the corresponding derivative,

$$ \begin{aligned} \frac{\partial {}^{\mathrm{CD}}t_{ij}^{ab}}{\partial B_i} = &\left\{ \frac{\partial (ai|bj)^{\mathrm{CD}}}{\partial B_i} - \sum_m \left({}^{\mathrm{CD}}t_{im}^{ab} \frac{\partial f_{mj}}{\partial B_i} + {}^{\mathrm{CD}}t_{mj}^{ab} \frac{\partial f_{mi}}{\partial B_i} \right) \right. \\ &\left. + \sum_e \left(\frac{\partial f_{ae}}{\partial B_i}\, {}^{\mathrm{CD}}t_{ij}^{eb} + \frac{\partial f_{be}}{\partial B_i}\, {}^{\mathrm{CD}}t_{ij}^{ae} \right) \right\} \frac{1}{\varepsilon_i + \varepsilon_j - \varepsilon_a - \varepsilon_b}. \end{aligned} \tag{3.12} $$

In the last two equations, the integrals are given in the MO basis and the transformation from the AO to the MO basis is carried out using eq. (2.198). Using eqs. (3.11) and (3.12), the occupied-occupied and virtual-virtual block of the MP2 density matrix in eqs. (2.114) and (2.115) and the corresponding derivatives in eqs. (2.130) and (2.131) can be computed, respectively. To obtain the virtual-occupied block, the CVs are inserted in the Z-vector equations (eq. (2.126)), leading to

$$ \begin{aligned} -2\,{}^{\mathrm{CD}}X_{ai} = &4 \sum_P L_{ia}^P \left(\sum_m \sum_e D_{em} L_{em}^P \right) - \sum_P \sum_m L_{ma}^P \left(\sum_e D_{em} L_{ie}^P \right) \\ &- \sum_P \sum_m L_{im}^P \left(\sum_e D_{em} L_{ea}^P \right) + D_{ai}(\varepsilon_a - \varepsilon_i) \end{aligned} \tag{3.13} $$

after some rearrangements. Via

$$ \begin{aligned} {}^{\mathrm{CD}}X_{ai} = &\sum_{mn} D_{mn} \left((mn|ia)^{\mathrm{CD}} - \frac{1}{2}(ma|in)^{\mathrm{CD}} \right) + \sum_P L_{ia}^P \left(\sum_{ef} D_{ef} L_{ef}^P \right) \\ &- \frac{1}{2} \sum_P \sum_e L_{ea}^P \left(\sum_f L_{if}^P D_{ef} \right) + \sum_P \sum_e L_{ea}^P \left(\sum_m \sum_f L_{fm}^P\, {}^{\mathrm{CD}}\tilde{t}_{im}^{ef\,*} \right) \\ &- \sum_{mn} \sum_e (im|en)^{\mathrm{CD}}\, {}^{\mathrm{CD}}\tilde{t}_{mn}^{ae\,*}, \end{aligned} \tag{3.14} $$

the intermediate ${}^{\mathrm{CD}}X_{ai}$ is computed.

The corresponding derivatives of eqs. (3.13) and (3.14) are obtained through

$$\begin{aligned}
-2\frac{\partial^{\mathrm{CD}} X_{ai}}{\partial B_i} =& 4\sum_P \frac{\partial L^P_{ia}}{\partial B_i}\left(\sum_m\sum_e D_{em}L^P_{em}\right)\\
&+4\sum_P L^P_{ia}\left(\sum_m\sum_e \frac{\partial D_{em}}{\partial B_i}L^P_{em}+\sum_m\sum_e D_{em}\frac{\partial L^P_{em}}{\partial B_i}\right)\\
&-\sum_P\sum_m \frac{\partial L^P_{ma}}{\partial B_i}\left(\sum_e D_{em}L^P_{ie}\right)\\
&-\sum_P\sum_m L^P_{ma}\left(\sum_e \frac{\partial D_{em}}{\partial B_i}L^P_{ie}+\sum_e D_{em}\frac{\partial L^P_{ie}}{\partial B_i}\right)\\
&-\sum_P\sum_m \frac{\partial L^P_{im}}{\partial B_i}\left(\sum_e D_{em}L^P_{ea}\right)\\
&-\sum_P\sum_m L^P_{im}\left(\sum_e \frac{\partial D_{em}}{\partial B_i}L^P_{ea}+\sum_e D_{em}\frac{\partial L^P_{ea}}{\partial B_i}\right)\\
&+\frac{\partial D_{ai}}{\partial B_i}(\varepsilon_a-\varepsilon_i)+\sum_m\sum_e D_{em}\left(\delta_{im}\frac{\partial f_{ea}}{\partial B_i}-\delta_{ea}\frac{\partial f_{im}}{\partial B_i}\right)
\end{aligned} \tag{3.15}$$

and

$$\begin{aligned}
\frac{\partial^{\mathrm{CD}} X_{ai}}{\partial B_i} =& \sum_{mn}\frac{\partial D_{mn}}{\partial B_i}\left((mn|ia)^{\mathrm{CD}}-\frac{1}{2}(ma|in)^{\mathrm{CD}}\right)\\
&+\sum_{mn}D_{mn}\left(\frac{\partial (mn|ia)^{\mathrm{CD}}}{\partial B_i}-\frac{1}{2}\frac{\partial (ma|in)^{\mathrm{CD}}}{\partial B_i}\right)+\sum_P\frac{\partial L^P_{ia}}{\partial B_i}\left(\sum_{ef}D_{ef}L^P_{ef}\right)\\
&+\sum_P L^P_{ia}\left(\sum_{ef}\frac{\partial D_{ef}}{\partial B_i}L^P_{ef}+\sum_{ef}D_{ef}\frac{\partial L^P_{ef}}{\partial B_i}\right)-\frac{1}{2}\sum_P\sum_e\frac{\partial L^P_{ea}}{\partial B_i}\left(\sum_f L^P_{if}D_{ef}\right)\\
&-\frac{1}{2}\sum_P\sum_e L^P_{ea}\left(\sum_f\frac{\partial L^P_{if}}{\partial B_i}D_{ef}+\sum_f L^P_{if}\frac{\partial D_{ef}}{\partial B_i}\right)\\
&+\sum_P\sum_e\frac{\partial L^P_{ea}}{\partial B_i}\left(\sum_m\sum_f L^P_{fm}\,{}^{\mathrm{CD}}\tilde{t}^{ef\,*}_{im}\right)\\
&+\sum_P\sum_e L^P_{ea}\left(\sum_m\sum_f\frac{\partial L^P_{fm}}{\partial B_i}{}^{\mathrm{CD}}\tilde{t}^{ef\,*}_{im}+\sum_m\sum_f L^P_{fm}\frac{\partial^{\mathrm{CD}}\tilde{t}^{ef\,*}_{im}}{\partial B_i}\right)\\
&-\sum_{mn}\sum_e\left(\frac{\partial (im|en)^{\mathrm{CD}}}{\partial B_i}{}^{\mathrm{CD}}\tilde{t}^{ae\,*}_{mn}+(im|en)^{\mathrm{CD}}\frac{\partial^{\mathrm{CD}}\tilde{t}^{ae\,*}_{mn}}{\partial B_i}\right).
\end{aligned} \tag{3.16}$$

The NMR CV in the MO representation is defined as

$$\frac{\partial L^P_{pq}}{\partial B_i}=\sum_{\sigma\rho}\left\{c^*_{\sigma p}\frac{\partial L^P_{\sigma\rho}}{\partial B_i}c_{\nu q}+\frac{\partial c^*_{\sigma p}}{\partial B_i}L^P_{\sigma\rho}c_{\nu q}+c^*_{\sigma p}L^P_{\sigma\rho}\frac{\partial c_{\rho q}}{\partial B_i}\right\}. \tag{3.17}$$

These equations are the foundation for the CD-GIAO-MP2 scheme to compute NMR chemical shieldings, which can be combined with both the one-step and the two-step CD algorithm.

In general, the CD of the NMR integrals developed in this work can be used as basis for any other quantum-chemical method with which CD-based NMR shifts can be calculated. As described previously, strongly correlated systems demand a multi-reference method like CASSCF. However, the CASSCF method involves a high computational effort, because a FCI calculation is performed in the active space, and many procedures have been developed to perform efficient CASSCF calculations for molecular properties.[97,256–260] For CASSCF calculations, the handling of the two-electron integrals and their derivatives is an even more pronounced bottleneck that cannot be ignored. The use of the CD for the calculation of NMR shieldings at CASSCF level uses the Cholesky-decomposed NMR integrals evaluated in this work, and was implemented by T. Nottoli at the Università di Pisa, as described in Ref. [97]. The procedure is briefly summarized in the next subsection.

3.2.1 Calculation of NMR Shielding Constants with Cholesky-Decomposed Integrals at CASSCF level of theory

As described in Refs. [97, 171], the CD-GIAO-CASSCF scheme works by substituting the corresponding equations from section 2.3.9 with the Cholesky-decomposed equivalents. To exemplify the procedure, the terms for the Fock matrices in eqs. (2.143) to (2.145) are evaluated using the CVs, which results in

$$\frac{\partial F^I_{\mu\nu}}{\partial B_i} = \frac{\partial h_{\mu\nu}}{\partial B_i} + \sum_P \sum_{\sigma\rho} D^I_{\sigma\rho} \left\{ \frac{\partial L^P_{\mu\nu}}{\partial B_i} L^{P*}_{\rho\sigma} + L_{\mu\nu} \frac{\partial L^{P*}_{\rho\sigma}}{\partial B_i} - \frac{1}{2} \left[\frac{\partial L^P_{\mu\rho}}{\partial B_i} L^{P*}_{\nu\sigma} + L^P_{\mu\rho} \frac{\partial L^{P*}_{\nu\sigma}}{\partial B_i} \right] \right\}, \quad (3.18)$$

$$\frac{\partial F^A_{\mu\nu}}{\partial B_i} = \sum_P \sum_{\sigma\rho} D^A_{\sigma\rho} \left\{ \frac{\partial L^P_{\mu\nu}}{\partial B_i} L^{P*}_{\rho\sigma} + L^P_{\mu\nu} \frac{\partial L^{P*}_{\rho\sigma}}{\partial B_i} - \frac{1}{4} \left[\frac{\partial L^P_{\mu\rho}}{\partial B_i} L^{P*}_{\nu\sigma} + L^P_{\mu\rho} \frac{\partial L^{P*}_{\nu\sigma}}{\partial B_i} \right] \right\}, \quad (3.19)$$

for the Fock matrices and

$$\frac{\partial Q_{xp}}{\partial B_i} = \sum_P \sum_{uvy} D_{xu} D_{vy} \left(\frac{\partial L^P_{pu}}{\partial B_i} L^{P*}_{yv} + L^P_{pu} \frac{\partial L^{P*}_{yv}}{\partial B_i} \right) \quad (3.20)$$

for the **Q** matrix.

Now that it is clear how to utilize the CD for the computation of NMR chemical shieldings at various levels of theory, the magnetizability is discussed next. Before the CD of the magnetizability integrals is elucidated, the corresponding integral evaluation following the McMurchie-Davidson scheme is briefly presented.

3.3 McMurchie-Davidson Scheme for Magnetizability Integrals

To compute the magnetizability tensor, the second derivatives of the two-electron integrals with respect to the magnetic field component are necessary as seen in eqs. (2.86) and (2.136). These magnetizability integrals can also be evaluated using the McMurchie-Davidson procedure, which works in a manner analogously to the NMR integrals. The required second derivative of the

two-electron integral,

$$\begin{aligned}\left(\frac{\partial^2 \langle\mu\sigma|\nu\rho\rangle}{\partial B_i \partial B_j}\right)_{\mathbf{B}=0} =& -\int \mathrm{d}\mathbf{r}_1 \int \mathrm{d}\mathbf{r}_2 \left(e^{\frac{i}{2}\mathbf{B}\cdot\{(\mathbf{R}_\mu-\mathbf{R}_\nu)\times\mathbf{r}_1+(\mathbf{R}_\sigma-\mathbf{R}_\rho)\times\mathbf{r}_2\}}\right)_{\mathbf{B}=0} \\ &\cdot \frac{1}{4}\left\{(\mathbf{R}_\mu-\mathbf{R}_\nu)\times\mathbf{r}_1+(\mathbf{R}_\sigma-\mathbf{R}_\rho)\times\mathbf{r}_2\right\}_i \\ &\cdot \left\{(\mathbf{R}_\mu-\mathbf{R}_\nu)\times\mathbf{r}_1+(\mathbf{R}_\sigma-\mathbf{R}_\rho)\times\mathbf{r}_2\right\}_j \cdot \frac{\Omega_{\mu\nu}(\mathbf{r}_1)\Omega_{\sigma\rho}(\mathbf{r}_2)}{r_{12}},\end{aligned} \tag{3.21}$$

is evaluated at $\mathbf{B} = 0$; therefore the exponential expression equals 1 and

$$\begin{aligned}\left(\frac{\partial^2 \langle\mu\sigma|\nu\rho\rangle}{\partial B_i \partial B_j}\right)_{\mathbf{B}=0} =& -\frac{1}{4}\int \mathrm{d}\mathbf{r}_1 \int \mathrm{d}\mathbf{r}_2 \left\{(\mathbf{R}_\mu-\mathbf{R}_\nu)\times\mathbf{r}_1+(\mathbf{R}_\sigma-\mathbf{R}_\rho)\times\mathbf{r}_2\right\}_i \\ &\cdot \left\{(\mathbf{R}_\mu-\mathbf{R}_\nu)\times\mathbf{r}_1+(\mathbf{R}_\sigma-\mathbf{R}_\rho)\times\mathbf{r}_2\right\}_j \cdot \frac{\Omega_{\mu\nu}(\mathbf{r}_1)\Omega_{\sigma\rho}(\mathbf{r}_2)}{r_{12}}\end{aligned} \tag{3.22}$$

is obtained. Accordingly, the second derivative with respect to the x-component is given by

$$\begin{aligned}\left(\frac{\partial^2 \langle\mu\sigma|\nu\rho\rangle}{\partial B_x \partial B_x}\right)_{\mathbf{B}=0} =& -\frac{1}{4}\int d\mathbf{r}_1 \int d\mathbf{r}_2 \cdot \{ (\mathbf{R}_{\mu_y}-\mathbf{R}_{\nu_y})z_1 \; -(\mathbf{R}_{\mu_z}-\mathbf{R}_{\nu_z})y_1 \\ &+(\mathbf{R}_{\sigma_y}-\mathbf{R}_{\rho_y})z_2 \; -(\mathbf{R}_{\sigma_z}-\mathbf{R}_{\rho_z})y_2 \}_x \cdot \{ (\mathbf{R}_{\mu_y}-\mathbf{R}_{\nu_y})z_1 \\ &-(\mathbf{R}_{\mu_z}-\mathbf{R}_{\nu_z})y_1 \; +(\mathbf{R}_{\sigma_y}-\mathbf{R}_{\rho_y})z_2 \; -(\mathbf{R}_{\sigma_z}-\mathbf{R}_{\rho_z})y_2 \}_x \\ &\cdot \frac{\Omega_{\mu\nu}(\mathbf{r}_1)\Omega_{\sigma\rho}(\mathbf{r}_2)}{r_{12}},\end{aligned} \tag{3.23}$$

where the various contributions are again color-coded to keep track of them in the following equation. Application of the McMurchie-Davidson scheme leads to

$$\begin{aligned}\left(\frac{\partial^2 \langle\mu\sigma|\nu\rho\rangle}{\partial B_x \partial B_x}\right)_{\mathbf{B}=0} =& -\frac{1}{4}E_{\mu\nu}E_{\sigma\rho} \\ &\cdot \Bigg\{ (\mathbf{R}_{\mu_y}-\mathbf{R}_{\nu_y})^2 \cdot \sum_N^n \sum_L^l \sum_M^{m+2} D^{zz}_{NLM} \sum_{N'L'M'}^{n'l'm'} D_{N'L'M'}[\,NLM|\tfrac{1}{r_{12}}|N'L'M'] \\ &+ (\mathbf{R}_{\mu_z}-\mathbf{R}_{\nu_z})^2 \cdot \sum_N^n \sum_L^{l+2} \sum_M^m D^{yy}_{NLM} \sum_{N'L'M'}^{n'l'm'} D_{N'L'M'}[\,NLM|\tfrac{1}{r_{12}}|N'L'M'] \\ &+ (\mathbf{R}_{\sigma_y}-\mathbf{R}_{\rho_y})^2 \cdot \sum_{N'}^{n'} \sum_{L'}^{l'} \sum_{M'}^{m'+2} D^{zz}_{N'L'M'} \sum_{NLM}^{nlm} D_{NLM}[\,NLM|\tfrac{1}{r_{12}}|N'L'M'] \\ &+ (\mathbf{R}_{\sigma_z}-\mathbf{R}_{\rho_z})^2 \cdot \sum_{N'}^{n'} \sum_{L'}^{l'+2} \sum_{M'}^{m'} D^{yy}_{N'L'M'} \sum_{NLM}^{nlm} D_{NLM}[\,NLM|\tfrac{1}{r_{12}}|N'L'M'] \\ &- 2\,(\mathbf{R}_{\mu_y}-\mathbf{R}_{\nu_y}) \sum_N^n \sum_L^{l+1} \sum_M^{m+1} D^{yz}_{NLM} \\ &\cdot (\mathbf{R}_{\mu_z}-\mathbf{R}_{\nu_z}) \sum_{N'L'M'}^{n'l'm'} D_{N'L'M'}[\,NLM|\tfrac{1}{r_{12}}|N'L'M'] \\ &+ 2\,(\mathbf{R}_{\mu_y}-\mathbf{R}_{\nu_y}) \sum_N^n \sum_L^l \sum_M^{m+1} D^{z}_{NLM}\end{aligned} \tag{3.24a}$$

$$
\begin{aligned}
&\cdot(\mathbf{R}_{\sigma_y}-\mathbf{R}_{\rho_y})\sum_{N'}^{n'}\sum_{L'}^{l'}\sum_{M'}^{m'+1} D^{z}_{N'L'M'}[\,NLM|\tfrac{1}{r_{12}}|N'L'M']\\
-2\,&(\mathbf{R}_{\mu_y}-\mathbf{R}_{\nu_y})\sum_{N}^{n}\sum_{L}^{l}\sum_{M}^{m+1} D^{z}_{NLM}\\
&\cdot(\mathbf{R}_{\sigma_z}-\mathbf{R}_{\rho_z})\sum_{N'}^{n'}\sum_{L'}^{l'+1}\sum_{M'}^{m'} D^{y}_{N'L'M'}[\,NLM|\tfrac{1}{r_{12}}|N'L'M']\\
-2\,&(\mathbf{R}_{\mu_z}-\mathbf{R}_{\nu_z})\sum_{N}^{n}\sum_{L}^{l+1}\sum_{M}^{m} D^{y}_{NLM}\\
&\cdot(\mathbf{R}_{\sigma_y}-\mathbf{R}_{\rho_y})\sum_{N'}^{n'}\sum_{L'}^{l'}\sum_{M'}^{m'+1} D^{z}_{N'L'M'}[\,NLM|\tfrac{1}{r_{12}}|N'L'M']\\
+2\,&(\mathbf{R}_{\mu_z}-\mathbf{R}_{\nu_z})\sum_{N}^{n}\sum_{L}^{l+1}\sum_{M}^{m} D^{y}_{NLM}\\
&\cdot(\mathbf{R}_{\sigma_z}-\mathbf{R}_{\rho_z})\sum_{N'}^{n'}\sum_{L'}^{l'+1}\sum_{M'}^{m'} D^{y}_{N'L'M'}[\,NLM|\tfrac{1}{r_{12}}|N'L'M']\\
-2\,&(\mathbf{R}_{\sigma_y}-\mathbf{R}_{\rho_y})\sum_{NLM}^{nlm} D_{NLM}\\
&\cdot(\mathbf{R}_{\sigma_z}-\mathbf{R}_{\rho_z})\sum_{N'}^{n'}\sum_{L'}^{l'+1}\sum_{M'}^{m'+1} D^{yz}_{N'L'M'}[\,NLM|\tfrac{1}{r_{12}}|N'L'M']
\end{aligned}
\Bigg\}
$$

where for the sums the notations

$$
\begin{aligned}
\sum_{N}^{n} &= \sum_{N}^{n_A+n_B}, \quad \sum_{N'}^{n'} = \sum_{N'}^{n_C+n_D}\\
\sum_{N}^{n+1} &= \sum_{N}^{n_A+n_B+1}, \quad \sum_{N'}^{n'+1} = \sum_{N'}^{n_C+n_D+1}\\
\sum_{N}^{n+2} &= \sum_{N}^{n_A+n_B+2}, \quad \sum_{N'}^{n'+2} = \sum_{N'}^{n_C+n_D+2},
\end{aligned}
\tag{3.25}
$$

and for the coefficients the notations

$$
\begin{aligned}
D_{NLM} &= d_N^{n_An_B}\cdot e_L^{l_Al_B}\cdot f_M^{m_Am_B}, \quad D^{x}_{NLM} = xd_N^{n_An_B}\cdot e_L^{l_Al_B}\cdot f_M^{m_Am_B},\\
D^{y}_{NLM} &= d_N^{n_An_B}\cdot ye_L^{l_Al_B}\cdot f_M^{m_Am_B}, \quad D^{z}_{NLM} = d_N^{n_An_B}\cdot e_L^{l_Al_B}\cdot zf_M^{m_Am_B},\\
D^{xx}_{NLM} &= xxd_N^{n_An_B}\cdot e_L^{l_Al_B}\cdot f_M^{m_Am_B}, \quad D^{xy}_{NLM} = xd_N^{n_An_B}\cdot ye_L^{l_Al_B}\cdot f_M^{m_Am_B},\\
D^{xz}_{NLM} &= xd_N^{n_An_B}\cdot e_L^{l_Al_B}\cdot zf_M^{m_Am_B}, \quad D^{yz}_{NLM} = d_N^{n_An_B}\cdot ye_L^{l_Al_B}\cdot zf_M^{m_Am_B},\\
D^{yy}_{NLM} &= d_N^{n_An_B}\cdot yye_L^{l_Al_B}\cdot f_M^{m_Am_B}, \quad D^{zz}_{NLM} = d_N^{n_An_B}\cdot e_L^{l_Al_B}\cdot zzf_M^{m_Am_B},
\end{aligned}
\tag{3.26}
$$

are used for the sake of clarity. The notations for N', L' and M' that refer to the second electron (χ_C, χ_D) are analogous to eq. (3.26).

For the second derivative with respect to the same magnetic field component, 10 terms are obtained, while for mixed derivatives, i.e. those with respect to two different magnetic field components, there are in total 16 terms. The remaining integral derivatives can be found in the

appendix (section 7.3.2). As seen in eq. (3.24a), perturbed coefficients like $zf_M^{m_A m_B}$, that are already defined in eq. (2.187), and $zzf_M^{m_A m_B}$ are needed for the evaluation of the magnetizability integrals, where the latter can be obtained via recursion relations,

$$xxd_N^{n_A n_B} = 4\alpha_P^2 d_N^{n_A(n_B+2)} - 2\alpha_P(2n_B+1)d_N^{n_A n_B} + n_B(n_B-1)d_N^{n_A(n_B-2)}, \tag{3.27}$$

which is analogous for the y and z component.

As already mentioned, the CD of the magnetizability integrals is not as straightforward as the CD for the NMR integrals. The difficulties that arise and how they can be resolved is explained in the next section, based on Ref. [94].

3.4 Cholesky Decomposition of Magnetizability Integrals

Like the NMR integrals, the magnetizability integrals do not form a positive semidefinite matrix, meaning that a CD expression is derived by taking the second derivative of eq. (2.195),

$$\frac{\partial^2(\sigma\rho|\mu\nu)}{\partial B_i \partial B_j} \approx \sum_P^{N_{\mathrm{Ch}}} \left(\frac{\partial^2 L_{\sigma\rho}^P}{\partial B_i \partial B_j} L_{\nu\mu}^{P*} + \frac{\partial L_{\sigma\rho}^P}{\partial B_i}\frac{\partial L_{\nu\mu}^{P*}}{\partial B_j} + \frac{\partial L_{\sigma\rho}^k}{\partial B_j}\frac{\partial L_{\nu\mu}^{P*}}{\partial B_i} + L_{\sigma\rho}^P \frac{\partial^2 L_{\nu\mu}^{P*}}{\partial B_i \partial B_j} \right). \tag{3.28}$$

Also analogous to the NMR integrals is the reduced fourfold permutational symmetry of the magnetizability integrals,

$$\frac{\partial^2(\sigma\rho|\mu\nu)}{\partial B_i \partial B_j} = \frac{\partial^2(\mu\nu|\sigma\rho)}{\partial B_i \partial B_j} = \frac{\partial^2(\rho\sigma|\nu\mu)}{\partial B_i \partial B_j} = \frac{\partial^2(\nu\mu|\rho\sigma)}{\partial B_i \partial B_j}, \tag{3.29}$$

but in this case without a sign change. The permutational symmetry with respect to P2 and P3 can be exploited if the integrals are split in the following way,

$$\frac{\partial^2(\sigma\rho|\mu\nu)}{\partial B_i \partial B_j} = \left(\frac{\partial^2 \sigma\rho}{\partial B_i \partial B_j} \middle| \mu\nu \right) + \left(\frac{\partial \sigma\rho}{\partial B_i} \middle| \frac{\partial \mu\nu}{\partial B_j} \right) + \left(\frac{\partial \sigma\rho}{\partial B_j} \middle| \frac{\partial \mu\nu}{\partial B_i} \right) + \left(\sigma\rho \middle| \frac{\partial^2 \mu\nu}{\partial B_i \partial B_j} \right). \tag{3.30}$$

Equating eqs. (3.28) and (3.30) shows that the doubly differentiated CVs (the magnetizability CVs) are symmetric with respect to an interchange of the indices,

$$\frac{\partial^2 L_{\sigma\rho}^P}{\partial B_i \partial B_j} = \frac{\partial^2 L_{\rho\sigma}^P}{\partial B_i \partial B_j}, \tag{3.31}$$

and that there is no sign change due to complex conjugation,

$$\frac{\partial^2 L_{\sigma\rho}^P}{\partial B_i \partial B_j} = \frac{\partial^2 L_{\sigma\rho}^{P*}}{\partial B_i \partial B_j}. \tag{3.32}$$

For the following discussion, it is beneficial to rewrite the CD of the magnetizability integrals in a DF-like manner, as it is described for the unperturbed integrals in section 2.6.1. At this point, it is useful to introduce the CB in relation to the complete basis, as seen in fig. 3.1.

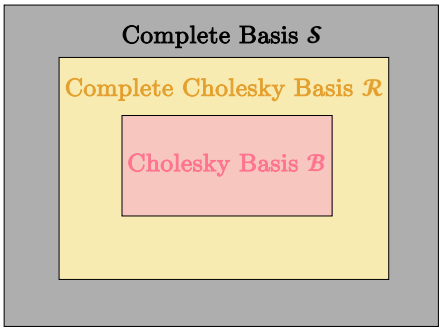

Figure 3.1: Illustration of the complete basis $\mathcal{S}$, the complete CB basis $\mathcal{R}$ and the CB $\mathcal{B}$.

The CB $\mathcal{B}$, generated in a truncated CD, is a subset of the complete CB $\mathcal{R}$ which contains all orthonormal product densities that can be obtained in a full CD. The complete CB $\mathcal{R}$ in turn is a subset of the complete basis $\mathcal{S}$, which also contains basis functions that are not part of the used AO product basis. Using this notation, the unperturbed integrals in the DF framework are given via

$$(\sigma\rho|\mu\nu) \approx \sum_{P\in\mathcal{B}} (\sigma\rho|P)(P|\mu\nu) + \sum_{P\in\mathcal{R}\setminus\mathcal{B}} (\sigma\rho|P)(P|\mu\nu) + \sum_{P\in\mathcal{S}\setminus\mathcal{R}} (\sigma\rho|P)(P|\mu\nu), \tag{3.33}$$

where the second term vanishes for a full decomposition and the third term is always zero, because it does not contribute to the CD. The NMR integrals can be represented in the unperturbed CB $\mathcal{B}$ and as seen in eq. (3.8), the perturbation-dependence of the CB functions vanishes.[189] Examining the NMR integrals from the DF perspective

$$\begin{aligned}\frac{\partial(\sigma\rho|\mu\nu)}{\partial B_i} \approx &\sum_{P\in\mathcal{B}} \left\{ \left(\frac{\partial\sigma\rho}{\partial B_i}\middle|P\right)(P|\mu\nu) + (\sigma\rho|P)\left(P\middle|\frac{\partial\mu\nu}{\partial B_i}\right)\right\} \\ &+ \sum_{P\in\mathcal{R}\setminus\mathcal{B}} \left\{ \left(\frac{\partial\sigma\rho}{\partial B_i}\middle|P\right)(P|\mu\nu) + (\sigma\rho|P)\left(P\middle|\frac{\partial\mu\nu}{\partial B_i}\right)\right\} \\ &+ \sum_{P\in\mathcal{B}\setminus\mathcal{R}} \left\{ \left(\frac{\partial\sigma\rho}{\partial B_i}\middle|P\right)(P|\mu\nu) + (\sigma\rho|P)\left(P\middle|\frac{\partial\mu\nu}{\partial B_i}\right)\right\}\end{aligned} \tag{3.34}$$

demonstrates that the third line vanishes since $(P|\mu\nu)$ is always zero, while the contributions in the second line approach zero for a Cholesky threshold of zero and is therefore assumed to be negligible. The discussion so far raises the question, whether $\mathcal{B}$ would also be sufficient to describe the CD of the magnetizability integrals accurately, as it is the case for the CD of the NMR integrals.

Analyzing the terms in

$$\begin{aligned}\frac{\partial^2(\sigma\rho|\mu\nu)}{\partial B_i\partial B_j} \approx \sum_{P\in\mathcal{B}} \Bigg\{ &\left(\frac{\partial^2\sigma\rho}{\partial B_i\partial B_j}\middle|P\right)(P|\mu\nu) + \left(\frac{\partial\sigma\rho}{\partial B_i}\middle|P\right)\left(P\middle|\frac{\partial\mu\nu}{\partial B_j}\right) \\ &+ (\sigma\rho|P)\left(P\middle|\frac{\partial^2\mu\nu}{\partial B_i\partial B_j}\right) + \left(\frac{\partial\sigma\rho}{\partial B_j}\middle|P\right)\left(P\middle|\frac{\partial\mu\nu}{\partial B_i}\right)\Bigg\} \\ + \sum_{P\in\mathcal{R}\setminus\mathcal{B}} \Bigg\{ &\left(\frac{\partial^2\sigma\rho}{\partial B_i\partial B_j}\middle|P\right)(P|\mu\nu) + \left(\frac{\partial\sigma\rho}{\partial B_i}\middle|P\right)\left(P\middle|\frac{\partial\mu\nu}{\partial B_j}\right) \\ &+ (\sigma\rho|P)\left(P\middle|\frac{\partial^2\mu\nu}{\partial B_i\partial B_j}\right) + \left(\frac{\partial\sigma\rho}{\partial B_j}\middle|P\right)\left(P\middle|\frac{\partial\mu\nu}{\partial B_i}\right)\Bigg\} \\ + \sum_{P\in\mathcal{S}\setminus\mathcal{R}} \Bigg\{ &\left(\frac{\partial^2\sigma\rho}{\partial B_i\partial B_j}\middle|P\right)(P|\mu\nu) + (\sigma\rho|P)\left(P\middle|\frac{\partial^2\mu\nu}{\partial B_i\partial B_j}\right) \\ &+ \left(\frac{\partial\sigma\rho}{\partial B_i}\middle|P\right)\left(P\middle|\frac{\partial\mu\nu}{\partial B_j}\right) + \left(\frac{\partial\sigma\rho}{\partial B_j}\middle|P\right)\left(P\middle|\frac{\partial\mu\nu}{\partial B_i}\right)\Bigg\},\end{aligned} \tag{3.35}$$

indicates that the terms in the third and fourth row vanish, if the Cholesky threshold reaches zero, analogous to the NMR integrals. Also, the terms outlined in pink disappears, since in this case $(P|\mu\nu) = 0$. However, in contrast to the NMR integrals, it cannot be shown that the terms with the orange border vanish, because the magnitude of $\left(P|\frac{\partial\mu\nu}{\partial B_j}\right)$ for $P \in \mathcal{S}\setminus\mathcal{R}$ is unknown and needs to be investigated. In order to analyze the error introduced by neglecting the term marked by the orange border, three different schemes for the CD of the magnetizability integrals are suggested, which are presented in the following.

Scheme 1

In the first scheme, the magnetizability integrals are computed via eq. (3.28), where the unperturbed and NMR CV are given by eqs. (2.196) and (3.8), respectively. The expression for the magnetizability CV is defined as

$$\frac{\partial^2 L^P_{\sigma\rho}}{\partial B_i\partial B_j} = \widetilde{(\nu\mu|\mu\nu)}^{-\frac{1}{2}} \left\{ \left(\frac{\partial^2\sigma\rho}{\partial B_i\partial B_j}\middle|\mu\nu\right) - \sum_{Q=1}^{P-1} \frac{\partial^2 L^Q_{\sigma\rho}}{\partial B_i\partial B_j} L^{Q*}_{\nu\mu} \right\}. \tag{3.36}$$

Here, the perturbation dependence of the CB functions is neglected, since the CV is only assigned to the unperturbed $\mu\nu$-pair, while the contribution of $\frac{\partial^2\mu\nu}{\partial B_i\partial B_j}$ is ignored. This can be considered equivalent to density fitting with the unperturbed Cholesky basis.[189]

Scheme 2

Scheme 2 also uses eq. (3.28) to calculate the magnetizability integrals, with the definition of the unperturbed and NMR CV given in eqs. (2.196) and (3.8). The difference is in the construction of the CV, because now the perturbation dependence is taken into account,

$$\begin{aligned}\frac{\partial^2 L^P_{\sigma\rho}}{\partial B_i \partial B_j} =& (\widetilde{\nu\mu|\mu\nu})^{-\frac{1}{2}} \left\{ \left[\left(\frac{\partial^2 \sigma\rho}{\partial B_i \partial B_j} \middle| \mu\nu \right) + \left(\sigma\rho \middle| \frac{\partial^2 \mu\nu}{\partial B_i \partial B_j} \right) \right] - \sum_{Q=1}^{P-1} \left(\frac{\partial^2 L^Q_{\sigma\rho}}{\partial B_i \partial B_j} L^{Q*}_{\nu\mu} \right. \right. \\ & \left. \left. + L^Q_{\sigma\rho} \frac{\partial^2 L^{Q*}_{\nu\mu}}{\partial B_i \partial B_j} \right) \right\} - \frac{1}{2} (\widetilde{\nu\mu|\mu\nu})^{-\frac{3}{2}} \cdot \left\{ \frac{\partial^2 (\nu\mu|\mu\nu)}{\partial B_i \partial B_j} - \sum_{Q=1}^{P-1} \left(\frac{\partial^2 L^Q_{\nu\mu}}{\partial B_i \partial B_j} L^{Q*}_{\nu\mu} \right. \right. \\ & \left. \left. + L^Q_{\nu\mu} \frac{\partial^2 L^{Q*}_{\nu\mu}}{\partial B_i \partial B_j} \right) \right\} \cdot \left\{ (\sigma\rho|\mu\nu) - \sum_{Q=1}^{P-1} L^Q_{\sigma\rho} L^{Q*}_{\nu\mu} \right\}. \end{aligned} \tag{3.37}$$

Scheme 3

The „problematic“ part in eq. (3.35) is the one containing the cross terms, that is the terms with the derivative of each product density. In fact, the $\left(\frac{\partial \sigma\rho}{\partial B_i} | \frac{\partial \mu\nu}{\partial B_i} \right)$ integrals constitute a positive semidefinite matrix and can be decomposed directly in a CD. The procedure is the same as before: in each iteration step, the largest diagonal element

$$\max \left[\left(\frac{\partial \nu\mu}{\partial B_k} \middle| \frac{\partial \mu\nu}{\partial B_k} \right) \right], \; k = x, \; y, \; z,$$

is determined. Calculation of the corresponding CVs works similar to eq. (2.196) and to avoid confusion, the magnetizability CVs are denoted as ${}^i M^P_{\sigma\rho}$,

$${}^i M^P_{\sigma\rho} = \left(\frac{\partial \nu\mu}{\partial B_k} \middle| \frac{\partial \mu\nu}{\partial B_k} \right)^{-\frac{1}{2}} \left\{ \left(\frac{\partial \sigma\rho}{\partial B_i} \middle| \frac{\partial \mu\nu}{\partial B_k} \right) - \sum_{Q=1}^{P-1} {}^i M^{Q\,k}_{\sigma\rho} M^{Q*}_{\nu\mu} \right\}. \tag{3.38}$$

As before, i denotes the magnetic field component. Via

$$\left(\frac{\partial \nu\mu}{\partial B_k} \middle| \frac{\partial \mu\nu}{\partial B_k} \right) = \left(\frac{\partial \nu\mu}{\partial B_k} \middle| \frac{\partial \mu\nu}{\partial B_k} \right) - \sum_{Q=1}^{P-1} {}^k M^{Q\,k}_{\mu\nu} M^{Q*}_{\nu\mu} \tag{3.39}$$

the diagonal elements are updated for each magnetic field component. Analogous to the unperturbed integrals, the matrix for the cross terms is reconstructed via

$$\left(\frac{\partial \sigma\rho}{\partial B_i} \middle| \frac{\partial \mu\nu}{\partial B_j} \right) + \left(\frac{\partial \sigma\rho}{\partial B_j} \middle| \frac{\partial \mu\nu}{\partial B_i} \right) \approx \sum_P \left({}^i M^{P\,j}_{\sigma\rho} M^{P*}_{\nu\mu} + {}^j M^{P\,i}_{\sigma\rho} M^{P*}_{\nu\mu} \right). \tag{3.40}$$

The CVs required for the remaining partial derivatives, that is the ones in the first and last term in eq. (3.30), can be computed both with scheme 1 or 2, and the corresponding matrices can be reconstructed using these CVs.

3.5 Calculation of Magnetizabilities using Cholesky Decomposition

3.5.1 HF Level of Theory

The procedure to compute the magnetizability tensor at the HF level of theory using CD is the same as for the calculation of NMR shieldings.[94] The only missing term to calculate eq. (2.86) is the one in the second row,

$$\xi_{ij}^{\mathrm{HF}} \leftarrow \frac{1}{2}\sum_{\mu\nu\sigma\rho} D_{\mu\nu}D_{\sigma\rho}\left(\frac{\partial^2 \langle\mu\sigma|\nu\rho\rangle}{\partial B_i \partial B_j} - \frac{1}{2}\frac{\partial^2 \langle\mu\sigma|\rho\nu\rangle}{\partial B_i \partial B_j}\right). \tag{3.41}$$

Using the CD, the term is evaluated via[94]

$$\begin{aligned}&\sum_P \left(\sum_{\sigma\rho} D_{\sigma\rho}\frac{\partial^2 L_{\sigma\rho}^P}{\partial B_i \partial B_j}\right)\left(\sum_{\mu\nu} D_{\mu\nu} L_{\mu\nu}^P\right)\\ &-\frac{1}{2}\sum_P \sum_{\mu\nu\sigma\rho} D_{\sigma\nu}D_{\mu\rho}\left(\frac{\partial^2 L_{\sigma\rho}^P}{\partial B_i \partial B_j}L_{\mu\nu}^P - \frac{\partial L_{\sigma\rho}^P}{\partial B_i}\frac{\partial L_{\mu\nu}^P}{\partial B_j}\right),\end{aligned} \tag{3.42}$$

where the magnetizability CVs are obtained from either scheme 1, 2 or 3.

3.5.2 MP2 Level of Theory

Analogous to HF, some terms that were required for the calculation NMR calculations can be reused for computing magnetizabilities at the MP2 level using CD. However, few terms are missing, like the derivative of the two-electron integrals in eq. (2.138),

$$\begin{aligned}\frac{\partial^{\mathrm{CD}}(pr|qs)^{B_i}}{\partial B_j} = {}^{\mathrm{CD}}(pr|qs)^{B_iB_j} + \sum_t \Big(&U_{tp}^{B_j^*}\ {}^{\mathrm{CD}}(tr|qs)^{B_i} + U_{tq}^{B_j^*}\ {}^{\mathrm{CD}}(pr|ts)^{B_i}\\ &+{}^{\mathrm{CD}}(pt|qs)^{B_i}U_{tr}^{B_j} + {}^{\mathrm{CD}}(pr|qt)^{B_i}U_{ts}^{B_j}\Big),\end{aligned} \tag{3.43}$$

and eq. (2.139)

$$\begin{aligned}f_{pq}^{(B_i)B_j} = \sum_{\mu\nu} c_{\mu p}^* \Bigg\{&\left(\frac{\partial^2 h_{\mu\nu}}{\partial B_i \partial B_j}\right) + \sum_{\sigma\rho}\left(\frac{D_{\sigma\rho}}{\partial B_j}\right)\left(\frac{\partial(\mu\nu|\sigma\rho)^{\mathrm{CD}}}{\partial B_i} - \frac{1}{2}\frac{\partial(\mu\rho|\sigma\nu)^{\mathrm{CD}}}{\partial B_i}\right)\\ &+\sum_{\sigma\rho} D_{\sigma\rho}\left(\frac{\partial^2(\mu\nu|\sigma\rho)^{\mathrm{CD}}}{\partial B_i \partial B_j} - \frac{1}{2}\frac{\partial(\mu\rho|\sigma\nu)^{\mathrm{CD}}}{\partial B_i \partial B_j}\right)\Bigg\} c_{\nu q},\end{aligned} \tag{3.44}$$

where CD can be applied. To compute eq. (3.43), the magnetizability CVs need to be transformed from the AO into the MO basis,

$$\frac{\partial^2 L_{pq}^P}{\partial B_i \partial B_j} = \sum_{\sigma\rho}\left\{c_{\sigma p}^* \frac{\partial^2 L_{\sigma\rho}^P}{\partial B_i \partial B_j} c_{\nu q} + \frac{\partial c_{\sigma p}^*}{\partial B_j}\frac{\partial L_{\sigma\rho}^P}{\partial B_i} c_{\nu q} + c_{\sigma p}^* \frac{\partial L_{\sigma\rho}^P}{\partial B_i}\frac{\partial c_{\rho q}}{\partial B_j}\right\}. \tag{3.45}$$

4 Implementation and Computational Details

This chapter describes how the developments presented in the last theory chapter were integrated into the CFOUR[261] program package. The new implementations enable fast and memory-efficient calculations of NMR chemical shieldings at the HF and MP2 level of theory and magnetizabilities at the HF level for medium-sized systems. Calculations for such molecules were previously associated with high memory requirements, long computing times or were often practically impossible to carry out.
The first part of this chapter deals with the improvements for the CD of the NMR integrals presented in section 3.1 that allow a faster calculation of the NMR shielding tensor compared to the original algorithm. As part of this, insights in the partial pivoting algorithm are provided, followed by algorithmic details of the efficient two-step algorithm and the workflow for calculating NMR shieldings at the MP2 level using Cholesky vectors. The second part is about magnetizability integrals, starting with the implementation of these integrals using the McMurchie-Davidson scheme. After a discussion of the three different CD schemes in section 3.4, the program handling for computing the magnetizability tensor at the HF level using CD is described. The chapter ends with the setup for computing magnetically induced ring-current strengths and simulation details for the Molecular Dynamics calculations.

4.1 Cholesky Decomposition of the NMR Integrals

The one-step algorithm for the CD of the NMR integrals was initially implemented in the master thesis that proceeded this work[180] and has been published in Ref. [93]. This implementation was improved in the course of this work as explained in section 3.1, resulting in a faster one-step algorithm on one side and on the use of a two-step procedure on the other side.[189] The CD of the NMR integrals is part of the Mainz integral package `mint`[262] developed in Mainz, Saarbrücken, and Pisa.
Table 4.1 provides an overview of the different keywords in the CFOUR input to control the CD of the NMR integrals. The calculation of molecular properties is generally controlled via the keyword `PROPS`; if NMR shieldings and the required NMR integrals are to be computed, the keyword must be specified as `PROPS=NMR`. Setting `CHOLESKY=ON` activates CD, and the keyword `CHOL_ALGORITHM` controls which algorithm is employed for the decomposition of the NMR integrals. The option `OLD` uses the implementation in Ref. [93], while `ORIGINAL` or `TWO-STEP` calls the improved one-step or the two-step algorithm presented in Ref. [189]. When `CHOL_TEST=1` is

chosen, the error associated with CD is quantified through eq. (2.203) and analogous expressions for the NMR integrals. The rigorous error control of the Cholesky decomposition is regulated by the keyword `TOL_CHOLESKY`. Since all implementations developed in the framework of this thesis do not exploit molecular point group symmetry, it is necessary to set `SYM=OFF`.

Table 4.1: Keywords in the Cfour input for computing the CD of the NMR integrals in `mint`.

Keyword	Option	Function
`PROPS`	`NMR`	Computes NMR shieldings
`CHOLESKY`	`ON` `OFF`	Turns CD on or off

`CHOL_ALGORITHM`	`OLD`
	`ORIGINAL`
	`TWO-STEP`
		Uses one-step algorithm implemented in Ref. [93]
		Uses improved one-step algorithm implemented in Ref. [189]
		Uses two-step algorithm implemented in Ref. [189]

`CHOL_TEST`	`0 (OFF)` `1 (ON)`	Tests CD by reconstructing the integrals
`TOL_CHOLESKY`	`1,2,...`	Specifies τ for Cholesky threshold $10^{-\tau}$ (stop-criterion)
`SYM`	`OFF`	No point group symmetry is used

4.1.1 One-Step Algorithm

The one-step scheme consists of macro and micro iterations, as illustrated in the flowchart in fig. 4.1. Before the macro iteration starts, all diagonal elements are computed and subjected to a prescreening that discards negligibly small elements; only those exceeding $(10^{-\tau})^2/D_{\max}$, are retained, where $D_{\max}$ is the largest diagonal element.[76] Next, the macro iteration starts, where the maximum diagonal element $D^P_{\max}$ is determined. P is assigned to the product density $\mu\nu$ that corresponds to the largest diagonal element and which is in the following denoted as $P \rightarrow |\mu\nu)$. If $D^P_{\max}$ exceeds the predefined Cholesky threshold, the procedure continues with the calculation of the corresponding unperturbed and all NMR integrals. For the CD, it would be necessary to calculate integral columns: i.e., the column associated with the pivot $\mu\nu$ in each case. However, in Cfour, the one- and two-electron integrals over the basis functions are computed in batches for given pairs or quadruples of shells $(CD|AB)$, where a shell is a collection of basis functions that share the same Gaussian exponents, total angular momentum and center. As a consequence, in a macro iteration the integrals $(\sigma\rho|\overline{\mu\nu})$ with all $\sigma\rho$, and all μ and ν from shell A and B (indicated with the bar), respectively, are computed, where shell A and B contain the current pivot. Conceptually, a set of integral columns is computed. The integrals are calculated in canonical order, using a loop structure that follows $A \geq B$, $C \geq D$ and exploits eightfold permutational symmetry. Since the NMR integrals do not exhibit the full eightfold but reduced

fourfold permutational symmetry, as demonstrated in eq. (2.214), the integrals

$$\frac{\partial(\sigma\rho|\overline{\mu\nu})}{\partial B_i} \text{ and } \frac{\partial(\sigma\rho|\overline{\nu\mu})}{\partial B_i} \tag{4.1}$$

are required in the case of the `OLD` Cholesky algorithm. If the algorithm is set to `ORIGINAL`, only the partially differentiated integrals

$$\left(\frac{\partial\sigma\rho}{\partial B_i}\middle|\overline{\mu\nu}\right) \tag{4.2}$$

are computed. To avoid the recalculation of integral batches that belong to the selected shell pair AB, the remaining integral columns in this shell quadruple are decomposed in a micro iteration. Numeric stability is ensured if only diagonal elements larger than $\delta_{\text{micro}} = D^P_{\text{max}}/1000$ are chosen, with δ_{micro} denoting the threshold for the micro iteration. The unperturbed and perturbed CVs are computed via eqs. (2.196) and (3.7), or eq. (3.8). Using the computed CVs, the diagonal is updated through eq. (2.197). The micro iteration ends if none of the remaining diagonal element exceeds $10^{-\tau_2}$ and the macro iteration is re-entered. A check is performed to determine whether the largest diagonal element is below the Cholesky threshold, in which case the CD is terminated.

A validation of the CD can be carried out by reconstructing the integrals with the CVs and comparing them to the integrals computed without CD, that is by measuring the magnitude of the error of the decomposition $R_{\mu\nu\sigma\rho}$ in eq. (2.203). The reconstruction of the unperturbed and NMR integrals follows eqs. (2.195) and (2.212), respectively. Because of the reduced permutational symmetry of the NMR integrals, two integrals are computed,

$$\frac{\partial(\sigma\rho|\mu\nu)}{\partial B_i} \approx \sum_P^{N_{\text{Ch}}} \left(\frac{\partial L^P_{\sigma\rho}}{\partial B_i} L^P_{\nu\mu} - L^P_{\sigma\rho}\frac{\partial L^P_{\nu\mu}}{\partial B_i}\right), \tag{4.3}$$

$$\frac{\partial(\sigma\rho|\nu\mu)}{\partial B_i} \approx \sum_P^{N_{\text{Ch}}} \left(\frac{\partial L^P_{\sigma\rho}}{\partial B_i} L^P_{\mu\nu} + L^P_{\sigma\rho}\frac{\partial L^P_{\nu\mu}}{\partial B_i}\right). \tag{4.4}$$

The minus sign in eq. (4.3) can be explained by the change of sign in the case of complex conjugation, as demonstrated in eq. (2.216). According to eq. (3.3),

$$\frac{\partial L^P_{\nu\mu}}{\partial B_i} = -\frac{\partial L^P_{\mu\nu}}{\partial B_i}$$

is exploited, which leads to a plus sign in eq. (4.4).

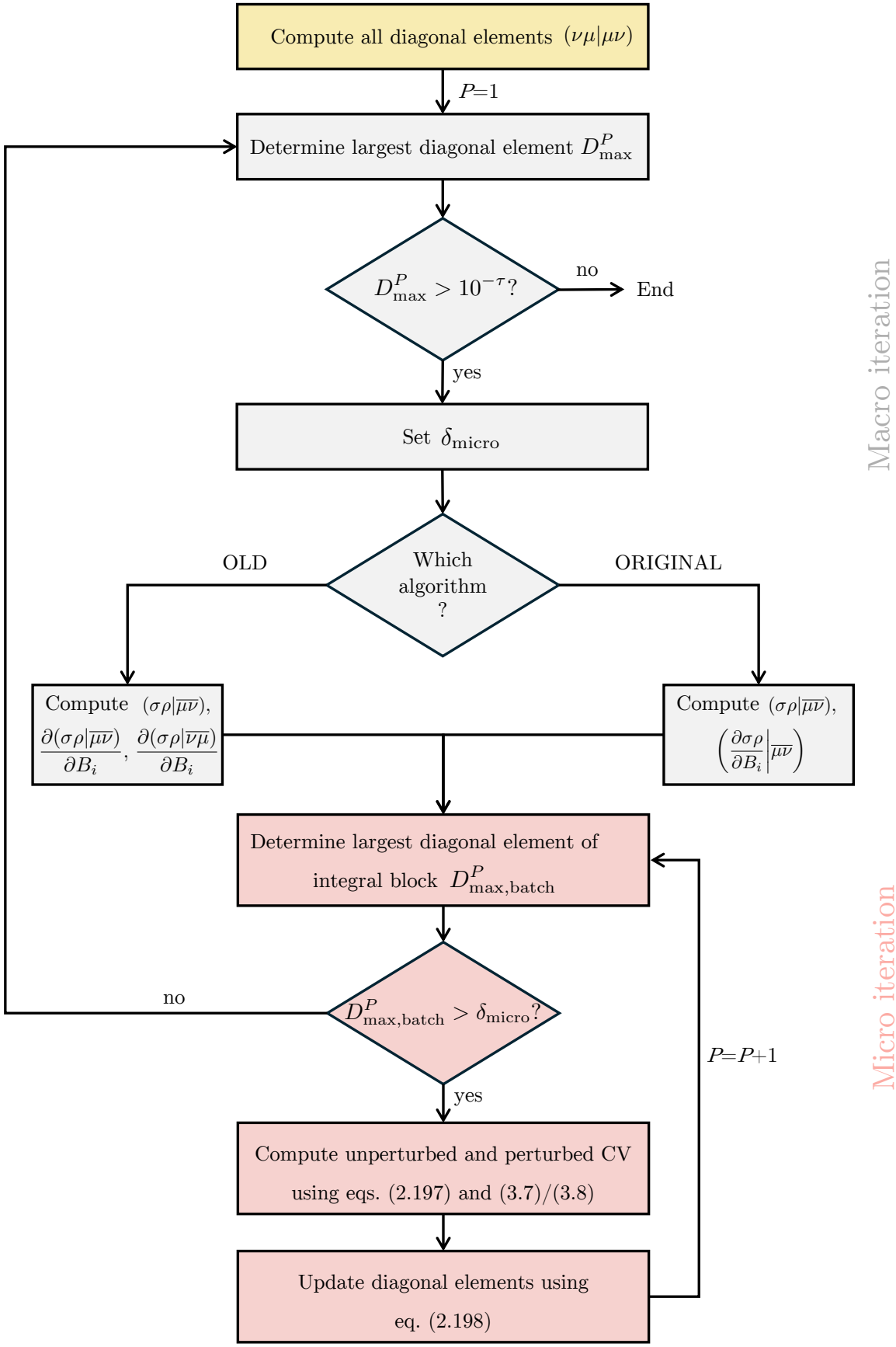

Figure 4.1: Partial pivoting algorithm for computing the CD of the NMR integrals in `mint`.

Modifications in the McMurchie-Davidson Scheme for NMR Integrals

If `CHOL_ALGORITHM=ORIGINAL` is chosen, only the partially differentiated integrals in eq. (4.2) are required. For the integral calculation this means that instead of eq. (2.185),

$$\left(\frac{\partial\sigma\rho}{\partial B_x}\middle|\mu\nu\right)_{\mathbf{B}=\mathbf{0}} = \int d\mathbf{r}_1 \int d\mathbf{r}_2 \; \frac{i}{2}\Big\{(\mathbf{R}_{\sigma_y} - \mathbf{R}_{\rho_y})z_1 - (\mathbf{R}_{\sigma_z} - \mathbf{R}_{\rho_z})y_1\Big\} \cdot \frac{\Omega_{\sigma\rho}\Omega_{\mu\nu}}{r_{12}} \tag{4.5}$$

is evaluated. Using the McMurchie-Davidson scheme, only the blue and the gray term in eq. (2.186) remain,

$$\begin{aligned}\left(\frac{\partial\sigma\rho}{\partial B_x}\middle|\mu\nu\right)_{\mathbf{B}=\mathbf{0}} = &-E_{\mu\nu}E_{\sigma\rho}\frac{i}{2}(\mathbf{R}_{\sigma_y} - \mathbf{R}_{\rho_y}) \sum_{N'}^{n_C+n_D} d_{N'}^{n_C n_D} \sum_{L'}^{l_C+l_D} e_{L'}^{l_C l_D} \sum_{M'}^{m_C+m_D+1} z f_{M'}^{m_C m_D} \cdot \\ &\sum_{NLM} D_{NLM}\left[NLM|\tfrac{1}{r_{12}}|N'L'M'\right] \\ &-E_{\mu\nu}E_{\sigma\rho}\frac{i}{2}(\mathbf{R}_{\sigma_z} - \mathbf{R}_{\rho_z}) \sum_{N'}^{n_C+n_D} d_{N'}^{n_C n_D} \sum_{L'}^{l_C+l_D+1} y e_{L'}^{l_C l_D} \sum_{M'}^{m_C+m_D} f_{M'}^{m_C m_D} \cdot \\ &\sum_{NLM} D_{NLM}\left[NLM|\tfrac{1}{r_{12}}|N'L'M'\right],\end{aligned}$$

and an appropriate check ensures that only these terms are calculated. Furthermore, if the basis functions χ_σ and χ_ρ are located at the same center, the integral evaluation is skipped since there is no contribution, as seen in eq. (3.9), which leads to further computational savings.

4.1.2 Two-Step Algorithm

The two-step algorithm originally suggested by Folkestad *et al.*[86] is computationally more efficient than the one-step procedure and the algorithmic details are outlined in this subsection based on Refs. [86] and [189]. The procedure consists of the following two steps:

1. Determination of the Cholesky basis $\mathcal{B}$
2. Construction of the CVs using the DF/RI formulation.

For the CD of the NMR integrals, only the second step needs to be adjusted since these integrals are represented in an unperturbed Cholesky basis. Thus, the first step remains the same as in the CD procedure for the unperturbed integrals. A flowchart for the first step is shown in fig. 4.2, where several sets occur which contain specific product densities. An overview of the different sets is given in table 4.2, where their contents are further described in the following.

Table 4.2: The various sets used in the two-step algorithm.

Set	Content
$\mathcal{B}$	Chosen Cholesky basis functions
$\mathcal{D}$	All diagonal elements greater than the Cholesky threshold
$\mathcal{Q}$	All qualified diagonal elements ($> \eta D^P_{\max}$, η: span factor)
$\mathcal{C}$	Indices for which the corrsponding CV was already computed in the micro iteration

Similar to the one-step algorithm, the two-step procedure starts with the calculation of all diagonal elements. Before the macro iteration starts, all sets are empty. All diagonal elements that exceed the predefined Cholesky threshold are saved in $\mathcal{D}$ and as long as this set contains elements, the Cholesky decomposition proceeds. Next, the largest of all diagonal elements in $\mathcal{D}$, $D^P_{\max}$, is determined and all diagonal elements greater than $\eta D^P_{\max}$ are added to the $\mathcal{Q}$ list, that is the list of all qualified diagonal elements. Here, η is a span factor and guarantees that the chosen qualified diagonal elements are not too small since this would cause numerical instabilities.[86] Following Ref. [86], the value of η is set to 10^{-2}. For all elements $\mu\nu$ in $\mathcal{Q}$, the corresponding integral batches, where $\sigma\rho \in \mathcal{D}$, are computed and updated with the CVs already in $\mathcal{B}$,

$$\widetilde{(\sigma\rho|\mu\nu)} = (\sigma\rho|\mu\nu) - \sum_{P\in\mathcal{B}} L^P_{\sigma\rho} L^P_{\nu\mu}. \tag{4.6}$$

Next, the micro iteration starts with the determination of the largest diagonal element in $\mathcal{Q}$ and the CV assigned to it,

$$L^P_{\sigma\rho} = \widetilde{(\nu\mu|\mu\nu)}^{-\frac{1}{2}} \left\{ \widetilde{(\sigma\rho|\mu\nu)} - \sum_{K\in\mathcal{C}} L^K_{\sigma\rho} L^K_{\nu\mu} \right\}, \tag{4.7}$$

where CVs from $\mathcal{C}$ are subtracted. The corresponding elements of the computed CV are then transferred from $\mathcal{Q}$ to $\mathcal{C}$ and the diagonal elements are updated,

$$\widetilde{(\nu\mu|\mu\nu)} = (\nu\mu|\mu\nu) - \sum_{K\in\mathcal{C}} L^K_{\nu\mu} L^K_{\mu\nu}. \tag{4.8}$$

Once there are no more qualified elements and $\mathcal{Q}$ is empty, the micro iteration ends and all elements in $\mathcal{C}$ are passed to the Cholesky basis $\mathcal{B}$. The macro iteration is re-entered and the CD is terminated, if all remaining diagonal elements in $\mathcal{D}$ are below the Cholesky threshold.
In the second step, the CVs are constructed in the unnormalized basis[189]

$$\tilde{L}^P_{\sigma\rho} = (\sigma\rho|P) \tag{4.9}$$

and then transformed to the orthonormal basis according to eq. (2.211),

$$L^P_{\sigma\rho} = \sum_Q \tilde{L}^Q_{\sigma\rho} (Q|P)^{-\frac{1}{2}}, \tag{4.10}$$

using the CD of the metric, $(P|Q)^{\frac{1}{2}}$. Via eq. (3.10), the NMR CVs are computed.
Although the formal scaling compared to the one-step algorithm is the same, the advantage of the two-step procedure is that efficient linear algebra routines can be used for the formation of the CV in eq. (2.211).[189] In case of the one-step algorithm, many steps were used to construct the CVs with the already available vectors, while in the two-step algorithm, just one step is required.

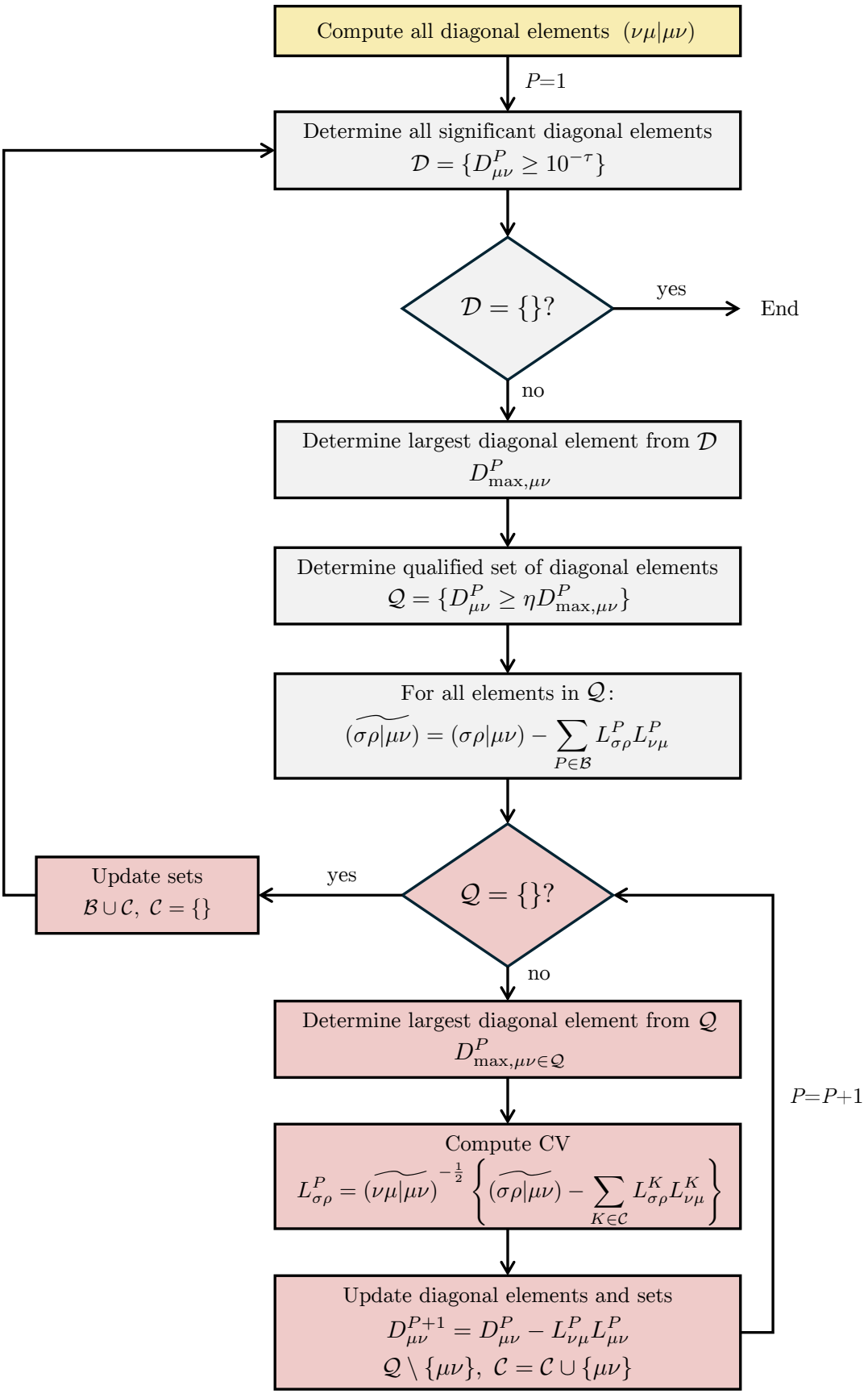

Figure 4.2: First step of the two-step algorithm for computing the CD of the NMR integrals in `mint`.

4.2 Calculation of NMR Shieldings using Cholesky Decomposition

4.2.1 Hartree-Fock Level of Theory

In order to compute the NMR shielding tensor at the HF level, the keywords in table 4.1 as well as the keyword `CALC=SCF` need to be specified. The CD-GIAO-HF scheme for computing NMR shielding constants uses the CD of the NMR integrals that was implemented in the course of this thesis.

As illustrated in fig. 4.3, the procedure starts with the CD of the unperturbed and NMR integrals. Only the unperturbed CVs are kept in memory during the whole process while the perturbed ones are stored on disk. This is followed by solving the HF-SCF equations using the unperturbed CVs. Next, the CVs are transformed from the AO to the MO basis using eq. (2.198). This step is necessary because the CVs in the MO basis are required to solve the CPHF equations in a later step. After the calculation of the perturbed one-electron integrals, the diamagnetic part of the shielding tensor is evaluated as well as the Fock matrix derivative that excludes the perturbed density matrix, $f_{ai}^{(B_i)}$. For the latter, the perturbed CVs are used to evaluate this term instead of the integrals, as shown in eq. (2.218). Next, the CPHF equations are solved for each magnetic field component. Here, the integrals that occur in the CPHF equations are substituted by their CD counterparts according to eq. (2.217). The paramagnetic terms which involve the response of the wavefunction to the magnetic field via the derivative of the density matrix, are computed in the last step.

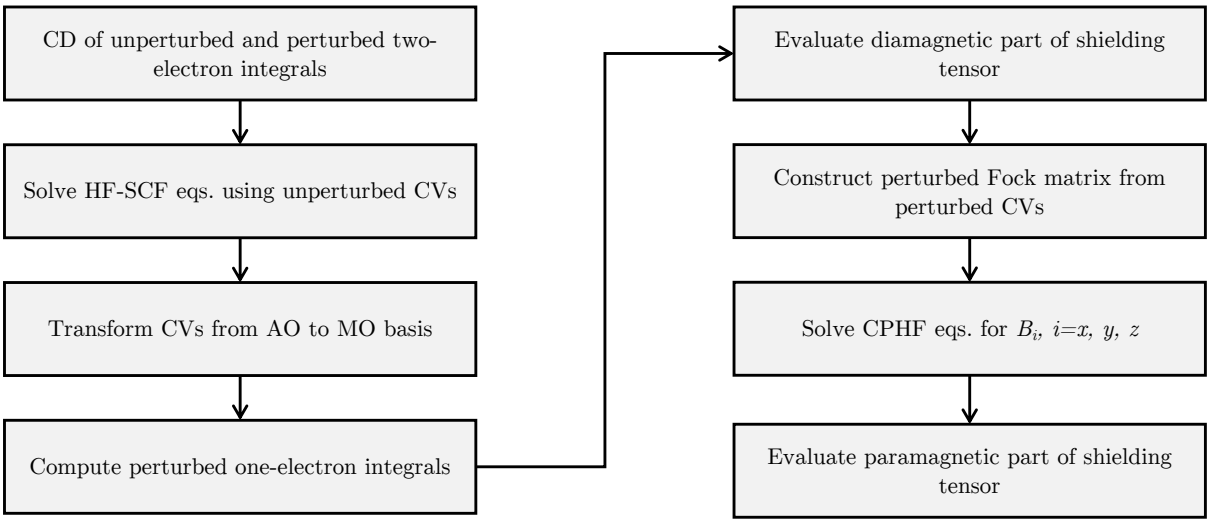

Figure 4.3: Flowchart for the calculation of NMR shielding tensors using the CD-GIAO-HF scheme.

4.2.2 MP2 Level of Theory

In order to compute the NMR shielding tensor at the MP2 level, the keywords in table 4.1 as well as the keyword `CALC=MP2` need to be specified.
The procedure for computing NMR shielding constants using the CD-GIAO-MP2 scheme has been published in Ref. [93], and is explained in the following based on this reference. The workflow is shown in fig. 4.4. The left side of the flowchart mainly deals with the unperturbed integrals. First, the unperturbed and perturbed two-electron integrals are decomposed and during the whole process, the complete set of unperturbed CVs is kept in memory. Using the latter, the HF-SCF equations are solved. In the next step, via eq. (2.198) the unperturbed CVs are transformed from the AO to the MO basis. With the transformed CVs, it is now possible to evaluate the integrals $(ij|ka)^{\mathrm{CD}}$ and $(ai|bj)^{\mathrm{CD}}$, which are explicitly formed and stored. Next, the t-amplitudes, which are also kept in memory, are constructed based on these integrals. Using the t-amplitudes, the MP2 energy is evaluated according to eq. (2.33), and the occupied-occupied and virtual-virtual blocks of the MP2 density matrix given in eqs. (2.114) and (2.115) are computed. Via eq. (3.14), the intermediate ${}^{\mathrm{CD}}X_{ai}$ is calculated using the $(ij|ka)^{\mathrm{CD}}$ and $(ai|bj)^{\mathrm{CD}}$ integrals and corresponding CVs for the $(ab|ci)$ integrals. This is followed by the computation of the virtual-occupied block of the MP2 density matrix through the solution of the Z-vector equations, which are evaluated using CVs, as shown in eq. (3.13). Next, the perturbed one-electron integrals are computed, allowing for the calculation of the diamagnetic part of the shielding tensor. Once the CPHF equations have been solved according to the CD-based expression in eq. (2.217), the procedure loops over the magnetic field components. Here, the first steps are similar to the previous ones: it starts with the transformation of one set of the perturbed CVs (either $\frac{\partial L_{\mu\nu}}{\partial B_x}$, $\frac{\partial L_{\mu\nu}}{\partial B_y}$ or $\frac{\partial L_{\mu\nu}}{\partial B_z}$) from the AO to the MO basis and the explicit formation of one set of perturbed integrals $\frac{\partial (ij|ka)^{\mathrm{CD}}}{\partial B_i}$ and $\frac{\partial (ai|bj)^{\mathrm{CD}}}{\partial B_i}$. Using these integrals, the perturbed t-amplitudes are constructed and the perturbed set of integrals are overwritten by the former. This set of perturbed amplitudes is also kept in memory. Subsequently, the occupied-occupied and virtual-virtual blocks of the perturbed MP2 density matrix are formed and via the solution of the perturbed Z-vector equations, the virtual-occupied block is computed. The procedure ends with the evaluation of the paramagnetic part of the shielding tensor.
The validation of the NMR shieldings was carried out by comparing results obtained from CD-GIAO-MP2 calculations with those from standard GIAO-MP2 calculations.

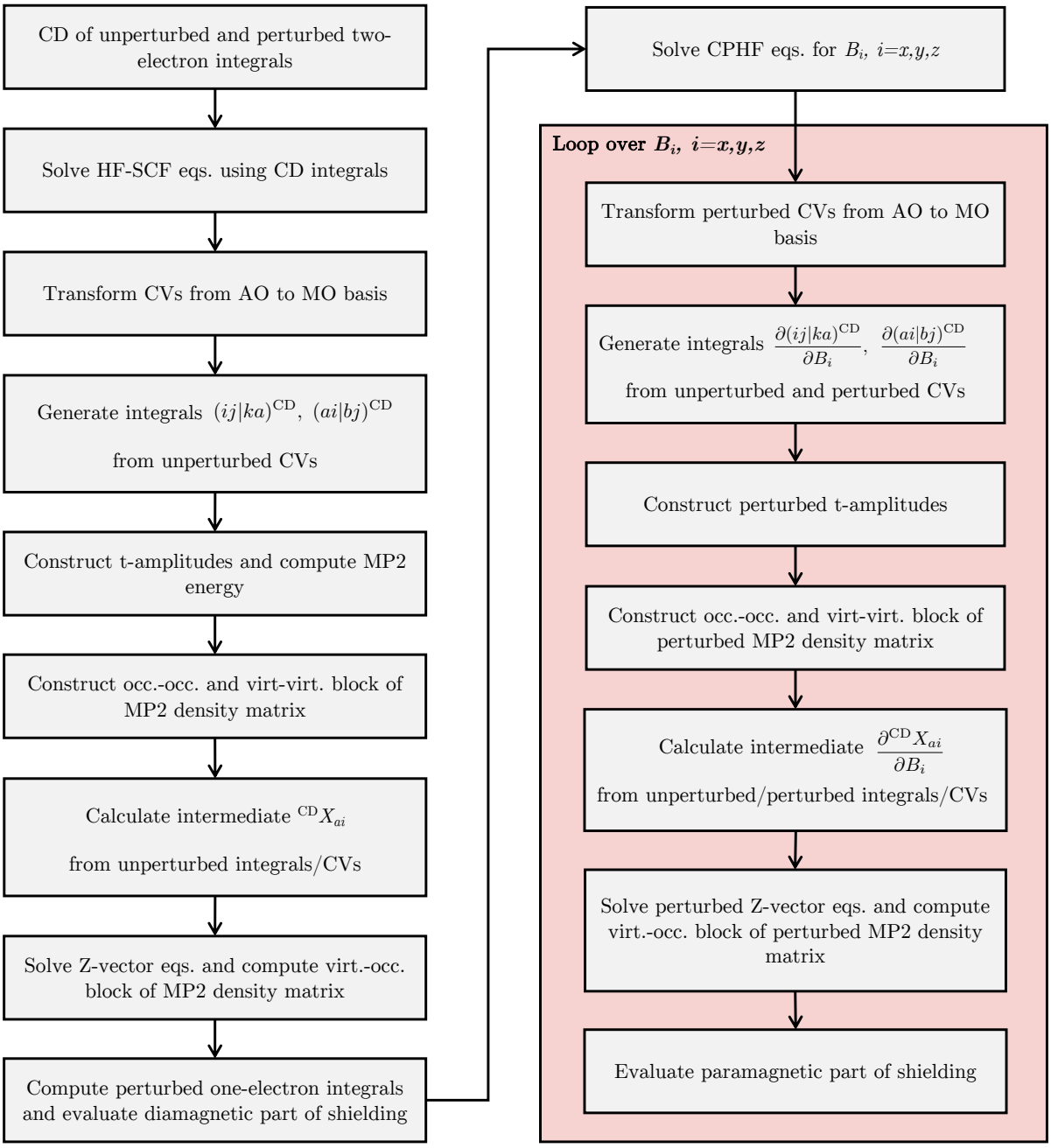

Figure 4.4: Workflow for the calculations of NMR shielding tensors using the CD-GIAO-MP2 scheme, based on the flowchart from Ref. [93].

4.3 McMurchie-Davidson Scheme for Magnetizability Integrals

The implementation of the second-derivative two-electron integrals required for the computation of the magnetizability tensor is based on already existing implementations of the unperturbed and NMR integrals in the Mainz integral package `mint` within Cfour.[262] In table 4.3, the keywords required for the computation of the magnetizability integrals are listed. Since Cfour also has another integral package (`vmol`), it needs to be specified that the `mint` package is to be used. The keyword `SYM=OFF` is necessary since the exploitation of molecular point group symmetry is not implemented yet.

Table 4.3: Keywords in the Cfour input for computing the magnetizability in `mint`.

Keyword	Function
`INTEGRALS=MINT`	Program package used for computing two-electron integrals
`SYM=OFF`	No point group symmetry is used
`PROPS=MAGNETIC`	Compute magnetizability in addition to NMR shielding tensors

Integral handling is performed by the subroutine `mint2e`, where a loop over the shells is executed, making use of the fourfold permutational symmetry to reduce the computational effort. In the subroutine `int2e_derBB`, the computation of the magnetizability integrals is divided into two steps. The first part deals with the evaluation of the intermediates $S_{N'L'M'}$, $S^i_{N'L'M'}$ and $S^{ij}_{N'L'M'}$, which are defined in the following for the x component,

$$S_{N'L'M'} = E_{AB}E_{CD} \sum_{N}^{n_A+n_b} \sum_{L}^{l_A+l_b} \sum_{M}^{m_a+m_B} D_{NLM} \cdot [NLM|\tfrac{1}{r_{12}}|N'L'M'], \tag{4.11}$$

$$S^x_{N'L'M'} = E_{AB}E_{CD} \sum_{N}^{n_A+n_b+1} \sum_{L}^{l_A+l_b} \sum_{M}^{m_a+m_B} D^x_{NLM} \cdot [NLM|\tfrac{1}{r_{12}}|N'L'M'], \tag{4.12}$$

$$S^{xx}_{N'L'M'} = E_{AB}E_{CD} \sum_{N}^{n_A+n_b+2} \sum_{L}^{l_A+l_b} \sum_{M}^{m_a+m_B} D^{xx}_{NLM} \cdot [NLM|\tfrac{1}{r_{12}}|N'L'M']. \tag{4.13}$$

These intermediates involve the basic integral $[NLM|\frac{1}{r_{12}}|N'L'M']$, the expansion coefficients and the prefactors E_{AB} defined in eqs. (2.156), (2.178) and (3.26), respectively. For the coefficients, the compact notation introduced in eq. (3.26) is used. The terms for the y and z component are computed analogously. Next, the functions of shell A and B are contracted and converted into spherical Gaussian functions. The use of spherical Gaussian functions is more efficient since fewer functions are required. This can be exemplified based on d-functions: there are six cartesian d-functions ($x^2, xy, xz, y^2, yz, z^2$), but only five spherical d-functions (xy, xz, yz, x^2-$y^2, 3z^2$-x^2-y^2). In the second part, the magnetizability integrals are computed using appropriate loop structures depending on the upper limit of the corresponding expansion coefficients, which is exemplified using the first and third term in eq. (3.24a),

- Loop over $n_D + n_D, l_C + l_D, m_C + m_D$:
  $\dfrac{\partial^2(\mu\nu|\sigma\rho)}{\partial B_x \partial B_x} \leftarrow -(\mathbf{R}_{\mu_y} - \mathbf{R}_{\nu_y})^2 \cdot S^{zz}_{N'L'M'} \cdot \sum_{N'L'M'}^{n'l'm'} D_{N'L'M'}$
- Loop over $n_D + n_D, l_C + l_D, m_C + m_D + 2$:
  $\dfrac{\partial^2(\mu\nu|\sigma\rho)}{\partial B_x \partial B_x} \leftarrow -(\mathbf{R}_{\sigma_y} - \mathbf{R}_{\rho_y})^2 \cdot S_{N'L'M'} \cdot \sum_{N'}^{n'} \sum_{L'}^{l'} \sum_{M'}^{m'+2} D^{zz}_{N'L'M'}$

According to the different summation limits, in total 10 loops are required to evaluate the magnetizability integrals. After contracting the functions of shell C and D, they are transformed to spherical Gaussian functions and the subroutine ends. Via a program for the numerical differentiation of the two-electron integrals in the presence of a finite magnetic field using GIAOs, the implementation for the magnetizability integrals was validated.

4.4 Cholesky Decomposition of the Magnetizability Integrals

For the CD of the magnetizability integrals, three different schemes were suggested as discussed in Ref. [94] and section 3.4. These three schemes were all implemented in the Mainz integral package `mint`,[262] together with the one-step algorithm. The workflow is basically the same as the one shown in fig. 4.1, with some adjustments. One modification takes place in the macro iteration where different integrals are required depending on the scheme used. An overview of the various integrals is given in table 4.4.

Table 4.4: Specification of the integrals that are calculated in the three different CD schemes for the magnetizability integrals.

Scheme	Unperturbed Integrals	NMR Integrals	Magnetizability Integrals
1	$(\sigma\rho\|\overline{\mu\nu})$	$\left(\frac{\partial\sigma\rho}{\partial B_i}\middle\|\overline{\mu\nu}\right)$	$\left(\frac{\partial^2\sigma\rho}{\partial B_i\partial B_j}\middle\|\overline{\mu\nu}\right)$
2	$(\sigma\rho\|\overline{\mu\nu})$	$\left(\frac{\partial\sigma\rho}{\partial B_i}\middle\|\overline{\mu\nu}\right)$	$\left(\frac{\partial^2\sigma\rho}{\partial B_i\partial B_j}\middle\|\overline{\mu\nu}\right) + \left(\sigma\rho\middle\|\frac{\partial^2\overline{\mu\nu}}{\partial B_i\partial B_j}\right)$
3	$(\sigma\rho\|\overline{\mu\nu})$	$\left(\frac{\partial\sigma\rho}{\partial B_i}\middle\|\overline{\mu\nu}\right)$	$\left(\frac{\partial^2\sigma\rho}{\partial B_i\partial B_j}\middle\|\overline{\mu\nu}\right)$
	-	-	$\left(\frac{\partial\sigma\rho}{\partial B_i}\middle\|\frac{\partial\overline{\mu\nu}}{\partial B_j}\right) + \left(\frac{\partial\sigma\rho}{\partial B_j}\middle\|\frac{\partial\overline{\mu\nu}}{\partial B_i}\right)$

In the first scheme, the unperturbed integrals are required as well as the partially differentiated NMR and magnetizability integrals. Since the perturbation-dependence of the Cholesky basis is neglected in scheme 1, only the bra side is differentiated twice in the case of the magnetizability integrals. These partial derivates are computed analogously to the partial derivates of the NMR integrals using the McMurchie-Davidson scheme, as explained in section 4.1.1. The unperturbed and the first-derivative CVs are obtained via eqs. (2.196) and (2.213) while the magnetizability CVs are computed via eq. (3.36). Using eq. (3.28), the magnetizability integrals can be constructed.

The second scheme is analogous to the first one in the case of the unperturbed and the first-derivative integrals. However, the perturbation-dependence is taken into account, which is why also the partial derivate in the ket is required for the magnetizability integrals. Here, the second-derivative CV is calculated through eq. (3.37). Similar to the first scheme, the magnetizability integrals are reconstructed using eq. (3.28).

In the case of the third scheme, two independent CDs are performed. The first one accounts for the unperturbed, NMR and the magnetizability integrals with the doubly differentiated product densities. The latter can be reconstructed via

$$\left(\frac{\partial^2\sigma\rho}{\partial B_i\partial B_j}\middle|\mu\nu\right) + \left(\sigma\rho\middle|\frac{\partial^2\mu\nu}{\partial B_i\partial B_j}\right) = \sum_P^{N_{\mathrm{Ch}}}\left(\frac{\partial^2 L^P_{\sigma\rho}}{\partial B_i\partial B_j}L^{P*}_{\nu\mu} + L^P_{\sigma\rho}\frac{\partial^2 L^{P*}_{\nu\mu}}{\partial B_i\partial B_j}\right), \tag{4.14}$$

where the second-derivative CVs are computed using eq. (3.36). In the second CD, the $\left(\frac{\partial\sigma\rho}{\partial B_i}\middle|\frac{\partial\mu\nu}{\partial B_i}\right)$ integrals are decomposed, where the procedure is basically the same as the one illustrated in

fig. 4.1. In the first step, all diagonal elements

$$\left(\frac{\partial\sigma\rho}{\partial B_x}\middle|\frac{\partial\mu\nu}{\partial B_x}\right),\ \left(\frac{\partial\sigma\rho}{\partial B_y}\middle|\frac{\partial\mu\nu}{\partial B_y}\right),\ \left(\frac{\partial\sigma\rho}{\partial B_z}\middle|\frac{\partial\mu\nu}{\partial B_z}\right)$$

are computed, and then the largest diagonal element is determined. After computing the CVs via eq. (3.38), all diagonal elements are updated using

$$\left(\frac{\partial\nu\widetilde{\mu}}{\partial B_i}\middle|\frac{\partial\mu\nu}{\partial B_i}\right) = \left(\frac{\partial\nu\mu}{\partial B_i}\middle|\frac{\partial\mu\nu}{\partial B_i}\right) - \sum_{Q}^{P-1} {}^{i}M_{\nu\mu}^{Q}\, {}^{i}M_{\nu\mu}^{Q*}. \tag{4.15}$$

The corresponding integrals are reconstructed based on eq. (3.40).

4.5 Calculation of the Magnetizability Tensor using Cholesky Decomposition at Hartree-Fock Level of Theory

The calculation of the magnetizability tensor using the CD-GIAO-HF scheme[94] is based on previous implementations of magnetizabilities without CD[148,263] and the NMR calculations using CD.[93,189] In fig. 4.5, the workflow is presented, where the yellow boxes indicate that these steps were implemented in the course of this work.
First, the CD of the unperturbed, NMR and magnetizability two-electron integrals is performed, where each of the three schemes can be used to decompose the magnetizability integrals. Next, the unperturbed one-electron integrals are calculated. Using the unperturbed CVs, the HF-SCF equations are solved and the unperturbed HF density matrix is obtained. This is followed by the computation of the perturbed one-electron integrals which allows the calculation of the first two terms in the equation for the magnetizability tensor defined in eq. (2.86),

$$\xi_{ij}^{\mathrm{dia}} \leftarrow \sum_{\mu\nu} D_{\mu\nu}\left(\frac{\partial^2 h_{\mu\nu}}{\partial B_i \partial B_j}\right) - \sum_{\mu\nu} W_{\mu\nu}\left(\frac{\partial^2 S_{\mu\nu}}{\partial B_i \partial B_j}\right). \tag{4.16}$$

The third term in eq. (2.86),

$$\xi_{ij}^{\mathrm{dia}} \leftarrow \frac{1}{2}\sum_{\mu\nu\sigma\rho} D_{\mu\nu} D_{\sigma\rho}\left(\frac{\partial^2(\mu\nu|\sigma\rho)}{\partial B_i \partial B_j} - \frac{1}{2}\frac{\partial^2(\mu\rho|\sigma\nu)}{\partial B_i \partial B_j}\right), \tag{4.17}$$

is evaluated using the CVs, as shown in eq. (3.42). Equation (4.17) completes the calculation of the diamagnetic part of the magnetizability tensor. To obtain the paramagnetic part, the perturbed density matrix is required. The latter is derived from the CPHF equations, which are solved for each magnetic field component. In the last step, the paramagnetic part is formed and the calculation of the magnetizability tensor is complete.

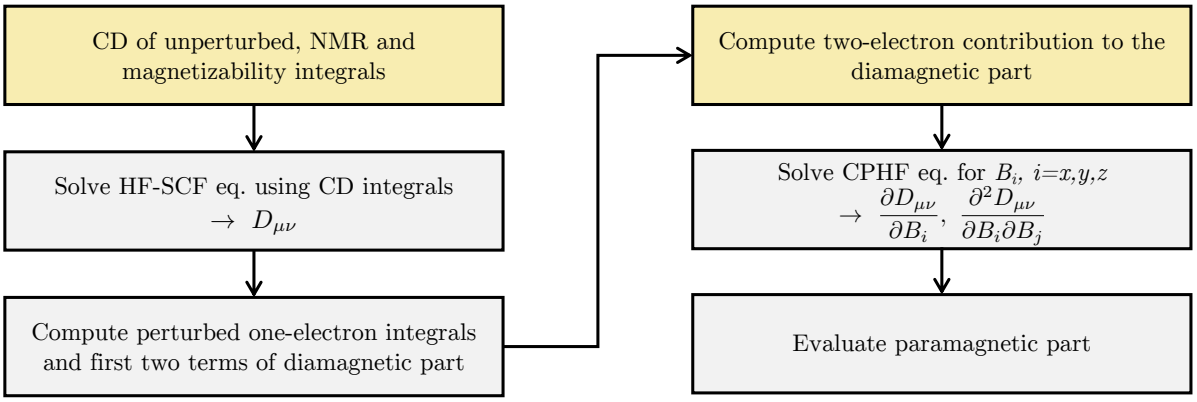

Figure 4.5: Flowchart for the calculation of the magnetizability tensor using the CD-GIAO-HF scheme presented in Ref. [94].

4.6 Calculation of the Magnetically Induced Ring Current Strengths

To calculate magnetically induced ring-current strengths, a Cfour NMR chemical shielding calculation using the CD-GIAO-MP2 scheme is performed first. This produces the files `XDENS` and `MOL`, where the former contains the perturbed and unperturbed density matrices and the latter includes information about basis set and molecular geometry. For the calculation of ring-current strengths, the program Gimic[48,96,152] (gauge-including magnetically induced currents) is used. In order to provide qualitative information about the current pathways, the current density is visualized using the program ParaView*. An interactive bash script provided by Gimic positions the integration plane across a specific bond (as exemplified for benzene in fig. 4.6) and performs a stepwise scan over the integration plane, thereby generating a current strength profile. The current strength is obtained by applying Gauss quadrature to integrate the current that passes the integration plane.

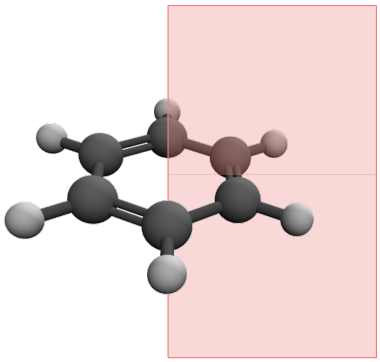

Figure 4.6: Illustration of the integration plane for benzene. The plane is placed across a specific bond and perpendicular to the molecular plane.

* ParaView is an open-source package and can be downloaded at www.paraview.org

4.7 Molecular Dynamics Simulation

In this work, QM/MM calculations are used to compute the NMR shifts of liquid water, where the program Gromacs[264] is used to perform the MD simulations. For this purpose, a $(3 \times 3 \times 3)$ nm box was created and filled with water, resulting in 909 water molecules. In this work, the TIP4P water model[265] is used. An illustration of the simulation box and the TIP4P water model can be found in fig. 4.7. The TIP4P model interacts with other molecules via non-bonding interactions, where the van der Waals interaction is only included for the oxygen. Also, the model is characterized by an additional mass on the oxygen atom, which carries the negative partial charge of the oxygen while a partial charge of zero is assigned to the oxygen atom.

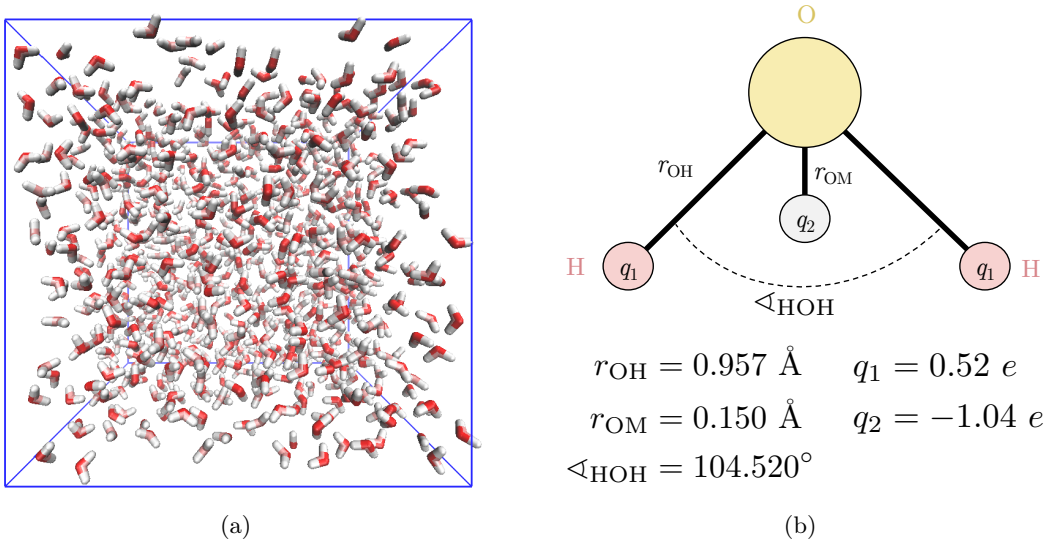

(a) (b)

Figure 4.7: (a) Simulation box for water, (b) Parameters for the TIP4P water model.[265]

Before running the actual simulation, the system needs to be equilibrated. The sequence of the steps is outlined in the following, where PBCs are used throughout:

1. Geometry optimization
2. Temperature adjustment
3. Pressure adjustment
4. MD run.

In order to obtain a reasonable starting structure, the energy of the system needs to be minimized, which is why a geometry optimization is required in the first step. In this case, steepest descent has been used for the energy minimization. This is followed by an equilibration, which is split into two phases. The first one is performed in an NVT ensemble and regulates the temperature using the Berendsen thermostat,[239] where a temperature of 275 K/300 K and a timeframe of 50 ps is chosen. The second equilibration phase is needed in order to stabilize the pressure and to preserve the correct density, for which the Parrinello-Rahman barostat[266] is used. The equilibration of the pressure is carried out in an NPT ensemble using a reference pressure of 1 bar and a timeframe of 100 ps. After this, the actual MD run starts, where the simulation runs for 500 ps with a timestep of 2 fs.

It is now possible to extract snapshots from the MD trajectory, i.e. the coordinates of all

atoms from the generated trajectories at a given time during the simulation. Using one snapshot, the NMR shieldings for different water molecules were computed. Since a single water molecule cannot represent the entire system or reflect its true properties, statistical averaging over many molecules is required to obtain reliable results. Alternatively, it is possible to average over several snapshots by computing the NMR shieldings for the same molecule in different configurations.

4.7.1 Electrostatic Embedding

In the electrostatic embedding scheme, it is necessary to include also the MM point charges and coordinates in the electronic Hamiltonian following eq. (2.223). For this purpose, a new module named `qmmm` has been added to `mint`[262] in Cfour. The module handles the QM and MM charges and coordinates such that they can be incorporated easily in the calculation of the nuclear attraction integrals in eq. (2.176). In order to use the QM/MM module in Cfour, the keywords from table 4.5 are required. The keyword `EXTERN_POT=ON` activates the calculation of the electrostatic interactions between the QM molecules and the MM molecules (the latter are saved in a file named `MMCHRGS`). Furthermore, this keyword automatically sets `SYM=OFF` and `FIXGEOM=ON`, where the latter guarantees that the QM molecules are neither rotated nor shifted independently of the MM atoms, but remain in their original position.

Table 4.5: Keywords in the Cfour input for using the QM/MM module in `mint`.

Keyword	Function
`QM/MM=1`	QM/MM module is used
`EXTERN_POT=ON`	Activates calculation of electrostatic interactions between QM and MM region; sets `SYM=OFF`, `FIXGEOM=ON`

5 Results and Applications

In this chapter, the results obtained with the methods developed in this thesis are presented in order to demonstrate their efficiency, accuracy, and applicability to chemical problems. The first part focuses on the Cholesky decomposition of the NMR integrals and examines the impact of the algorithmic improvements - achieved through the implementation of the two-step algorithm on the one hand and the exploitation of the permutational symmetry of the NMR integrals on the other. Additionally, NMR shieldings are computed using the CD-GIAO-MP2 method. The results are analyzed with respect to timings and accuracy, demonstrating that NMR calculations at the MP2 level are feasible even for large systems comprising approximately 1500 basis functions due to the use of the Cholesky decomposition. Furthermore, the CD-GIAO-HF and CD-GIAO-MP2 approaches are embedded in a QM/MM scheme, which is used to study the NMR shifts of liquid water. This framework allows to investigate the gas-to-liquid shift for water that can be compared to experimental results. Owing to the use of CD, large QM regions can be used which are shown to be essential for achieving reliable results. Concerning the CD of the magnetizability integrals, the three proposed schemes are compared to each other with respect to efficiency and accuracy. The applicability of the CD-GIAO-HF scheme for calculating magnetizabilities is demonstrated through large-scale computations involving more than 1000 basis functions. In the last section, the CD-GIAO-MP2 scheme for computing NMR chemical shieldings is used to calculate the magnetically induced ring-current densities and ring-current strengths of large systems like the polycyclic coronene molecule and several bridged annulene derivatives. Based on these results, the systems are analyzed with respect to aromaticity. In the case of the bridged annulene derivatives, the influence of the bridging atom on the ring-current strength is discussed.

5.1 NMR Shift Computations using Cholesky Decomposition

The results obtained using the Cholesky algorithm for NMR integrals, as published by us in Ref. [93], are presented in the following.

5.1.1 Accuracy of the Cholesky Decomposition for NMR Integrals

One major advantage of the CD over methods like DF and RI is the fact that a rigorous error control is guaranteed, at least for the unperturbed two-electron integrals.[181,187] It needs to be investigated whether the Cholesky threshold also provides an upper bound for the first derivatives of the integrals with respect to the magnetic field component, i.e. the NMR integrals. For

this purpose, the maximum errors in the unperturbed and NMR integrals for water (H_2O) and hydrogen peroxide (H_2O_2) in the cc-pVQZ basis[191] are computed for different Cholesky thresholds. Analogous to eq. (2.203), the error in the reconstructed integrals is determined. The geometries used for these calculations are given in fig. 5.1.

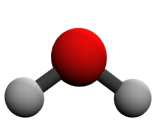

$R_{OH} = 1.0$ Å
$W_{HOH} = 100.0°$

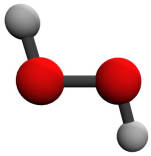

$R_{OO} = 1.5$ Å
$R_{OH} = 1.0$ Å
$W_{OOH} = 100.0°$
$\omega_{HOOH} = 120.0°$

Figure 5.1: Geometries used for the following calculations on water and hydrogen peroxide.

The results are displayed in fig. 5.2 and the figure shows that the error in the unperturbed integrals is always below the Cholesky threshold, as expected from theory. However, the Cholesky threshold is not an upper bound for the perturbed integrals and the error in these integrals is about 10-300 times larger than for the unperturbed two-electron integrals. This is explained by the fact that the Cauchy-Schwarz estimate holds only for the unperturbed, but not for the NMR integrals. The errors in the unperturbed and perturbed integrals differ more strongly for tighter Cholesky thresholds: at $\tau = 9$, the maximum error in the unperturbed two-electron integrals is 10^{-9} while the error in the NMR integrals is with 10^{-6} significantly larger. However, the errors in the NMR integrals for water and hydrogen peroxide tend toward zero and are of similar magnitude which indicates that the accuracy can still be estimated by the Cholesky threshold.

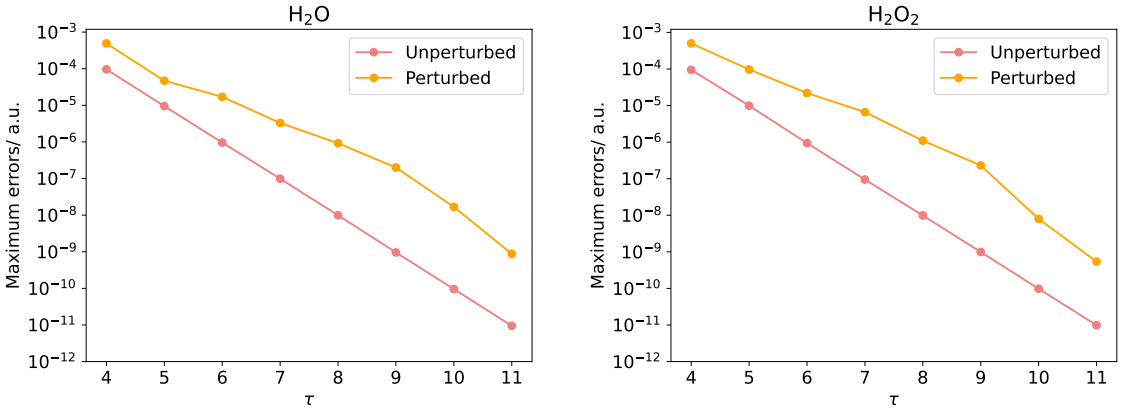

Figure 5.2: Maximum errors in a.u. in the unperturbed and perturbed (NMR) integrals for water and hydrogen peroxide, computed with different Cholesky thresholds $10^{-\tau}$, $\tau = 4, 5, 6, 7, 8, 9, 10, 11$ and the cc-pVQZ basis.[93]

5.1.2 Accuracy of NMR Shieldings

Next, the deviations that occur in the NMR shielding constants calculated with Cholesky-decomposed integrals are analyzed. As test systems, the three organic molecules acetaldehyde, vinyl alcohol, and ethylene oxide were chosen; the structure of the molecules are given in fig. 5.3. The geometries were optimized at the same level used for computing the NMR shieldings and are given in the appendix in tables 7.3 to 7.11.

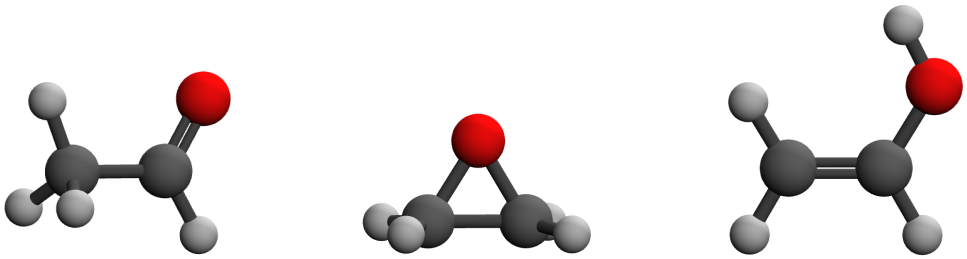

Figure 5.3: Acetaldehyde, ethylene oxide, and vinyl alcohol.

To determine the maximum absolute errors in the NMR shieldings, the shielding constants σ computed with the CD-GIAO-MP2 scheme, Cholesky thresholds of $10^{-4}/10^{-5}$ and the cc-pVXZ basis,[191] X=D, T, Q are compared to σ obtained with the standard GIAO-MP2 scheme. The results are visualized in fig. 5.4.

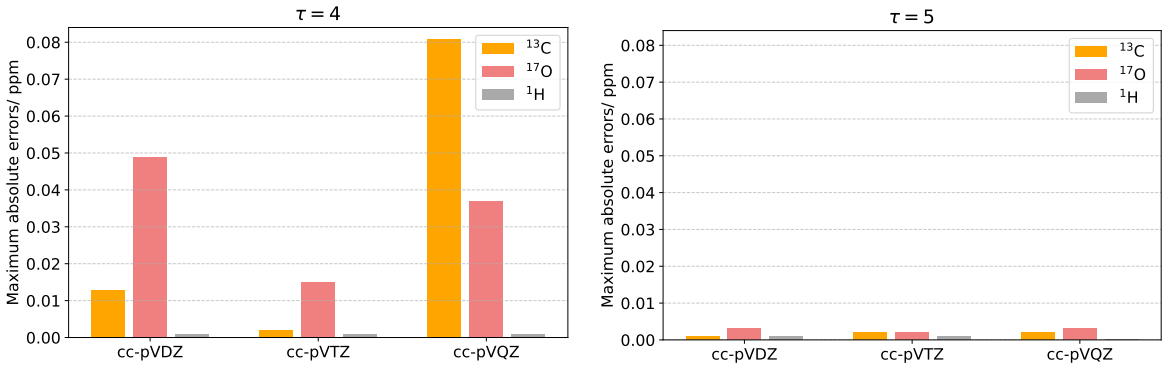

Figure 5.4: Maximum errors (with respect to a standard GIAO-MP2 calculation) in ppm in the shielding constants of acetaldehyde, vinyl alcohol, and ethylene oxide computed with CD-GIAO-MP2/cc-pVXZ, X=D, T, Q for different Cholesky thresholds $10^{-\tau}$, $\tau = 4,\ 5$.[93]

First, it is noted that there are no significant deviations, and the errors are in all cases lower than 0.09 ppm. The error for the ^{13}C and ^{17}O nuclei is in most cases greater than the one for ^{1}H which is due to the fact that the range of the shifts for hydrogen is smaller (about 0-10 ppm) compared to the range of carbon and oxygen shifts (about 0-220 ppm[267] for ^{13}C and 0-250 ppm[268] for ^{17}O). If a threshold of 10^{-5} instead of 10^{-4} is chosen, the errors decrease and become negligible, which is in line with theory. Based on the results in fig. 5.4, it can be concluded that a Cholesky threshold of 10^{-5} suffices to obtain accurate shieldings.
Nevertheless, it needs to be investigated if this also holds for larger systems like coronene, a polycyclic system shown in fig. 5.5. For this purpose, the shielding constants of coronene have

been computed both at the GIAO-MP2 and the CD-GIAO-MP2 level using the Karlsruhe dzp basis.[269] The difference between both results can be found in table 5.1. It can be seen that for larger systems the error is still of no relevance, and that a Cholesky threshold of $\tau = 5$ produces accurate chemical shieldings. As demonstrated in Ref. [46], the absolute errors for RI-MP2 calculations are about 0.035 ppm for carbon, 0.055 ppm for oxygen and 0.002 ppm for hydrogen shieldings. Compared to our results, this in the same range as the errors obtained with a Cholesky threshold of 10^{-5}. In contrast to the CD, it is not possible to improve the results for the shielding constants systematically when using density fitting.

Table 5.1: Maximum errors (with respect to a standard GIAO-MP2 calculation) in ppm in the shielding constants of coronene computed with CD-GIAO-MP2/dzp and Cholesky thresholds of $10^{-\tau}$, $\tau = 4,\ 5$.[93]

Nucleus	$\tau = 4$	$\tau = 5$
^{13}C	0.080	0.030
^{1}H	0.003	0.002

5.1.3 Representative Calculations

To demonstrate the applicability of the CD-GIAO-MP2 scheme for computing NMR chemical shieldings, calculations on various large molecules involving up to 100 atoms and more than 1000 basis functions are presented. Without the application of CD, calculations on large systems like this were infeasible due to excessive memory demands and prohibitively long computational timings. As mentioned in the introduction, at the time the GIAO-MP2 scheme was developed, calculations were restricted to systems involving at most 200 basis functions. This limitation can be overcome through CD, which enables the efficient handling of unperturbed and perturbed two-electron integrals, as will be demonstrated below. The set of molecules includes buckminsterfullerene C_{60}, coronene $C_{24}H_{12}$, hexabenzocoronene (HBC) $C_{42}H_{18}$, tetrameric cyclopentadienyl aluminum(I) $Al_4C_{20}H_{20}$, tetrakis(t-butyl)tetraborane $B_4C_{16}H_{36}$ and a tweezer host-guest complex $C_{54}N_2H_{36}$. In fig. 5.5, the structures of these molecules are shown, while the Cartesian coordinates for all molecules are given in the appendix in tables 7.12 to 7.17.

First, it is briefly discussed why NMR shift calculations for these molecules are of relevance. Aromatic polycyclic systems like HBC and coronene are of particular interest since these molecules are known to form a columnar mesophase[270,271] which can be roughly conceived as stacked coins. Because of this property, they can be used as vectorial charge transport layers,[271] that is a layer which transports charge in a specific direction. As demonstrated in Ref. [270], the interplay between quantum-chemical calculations of NMR shifts and corresponding experiments enables structural elucidations in solid-state ensembles of these molecules. The tetrakis(t-butyl)tetraborane, a clear glassy solid whose structure was determined by Mennekes *et al.*,[272] was synthesized and analyzed 1981, as described in Ref. [273]; T. Davan and J. A. Morrison observed extremely deshielded boron atoms (δ=135 ppm).[272,273] Quantum-chemical calculations revealed that inclusion of electron correlation is necessary to obtain sufficiently accurate results that agree well with experimental data.[22,274] Tetrameric cyclopentadienyl aluminum(I) has a molecular structure similar to B_4tBu_4. As described by Gauss *et al.* in Ref. [20], quantum-

chemical calculations predicted not only the tetramer, but also a monomer in solution which were in good agreement with corresponding NMR spectra. This example again demonstrates that computed NMR shifts can provide insights into molecular structures and help to explain experimental NMR data. Furthermore, the structure of the tweezer host-guest complex, which is relevant for supramolecular chemistry, has been investigated using experimental NMR data and corresponding quantum-chemical calculations.[275]

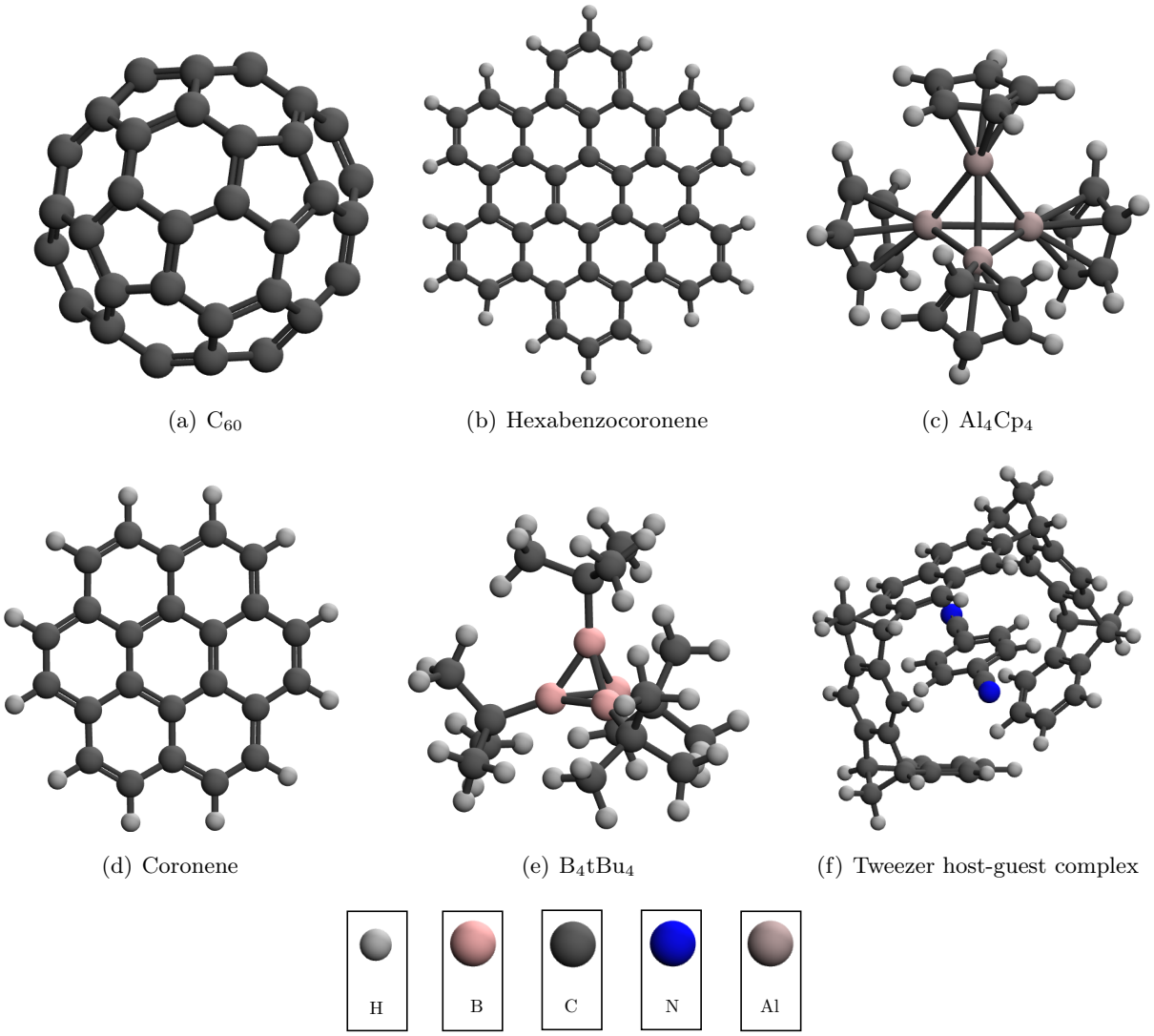

(a) C_{60} (b) Hexabenzocoronene (c) Al_4Cp_4

(d) Coronene (e) B_4tBu_4 (f) Tweezer host-guest complex

Figure 5.5: Structures of buckminsterfullerene, hexabenzocoronene (HBC), tetrameric cyclopentadienyl aluminum(I), coronene, tetrakis(t-butyl)tetraborane, and a tweezer host-guest complex.

Versions of the Karlsruhe basis sets dzp* and tz2p† have been used to calculate the shielding tensors of all molecules except the tweezer host-guest complex for which the smaller tzp‡ basis was used instead of tz2p. In table 5.2, the number of basis functions N_{BF}, the number of electrons N_{e} and the number of CPUs N_{CPU} used for the CD-based NMR shielding calculations are shown. All computations were carried out with two different Cholesky thresholds: $10^{-\tau}$, $\tau = 4,\ 5$. The

* 4s1p/2s1p for H, 8s4p1d/4s2p1d for B, C, N, O, 11s7p1d/6s4p1d for Al
† 5s2p/3s2p for H, 9s5p2d/5s3p2d for B, C, N, O, 12s9p2d/7s5p2d for Al
‡ 5s1p/3s1p for H, 9s5p1d/5s3p1d for C, N

number of generated CVs N_{CV}, the required virtual memory in GB, the wall-clock time t_{wall} as well as the compression rate ζ are showed in fig. 5.6. The latter is defined as the ratio between the theoretically maximum number of CVs N_{full} and the actual number of CVs,

$$\zeta = \frac{N_{\mathrm{full}}}{N_{\mathrm{CV}}}. \tag{5.1}$$

Higher compression rates mean that fewer CVs are generated, and that the calculation is more efficient.

Table 5.2: The number of basis functions N_{bf}, number of electrons N_{el}, number of CPUs N_{CPU} used in the CD-GIAO-MP2 calculations for the molecules depicted in fig. 5.5. All calculations have been performed on an Intel Xeon(R) E5-2443 node @ 3.4 GHz - except the calculations for C_{60}/tz2p and the calculations for the Tweezer host-guest complex, which were carried out on a Intel Xeon(R) Gold 5215M node @ 2.5 GHz.

Molecule	N_{el}	Basis	N_{bf}	N_{CPU}
(a) C_{60}	360	dzp	900	8
		tz2p	1440	20
(b) Hexabenzocoronene	270	dzp	720	8
		tz2p	1170	8
(c) Al_4Cp_4	192	dzp	492	8
		tz2p	788	8
(d) Coronene	156	dzp	420	8
		tz2p	684	8
(e) B_4tBu_4	152	dzp	480	8
		tz2p	804	8
(f) Tweezer host-guest complex	374	dzp	1020	20
		tzp	1280	20

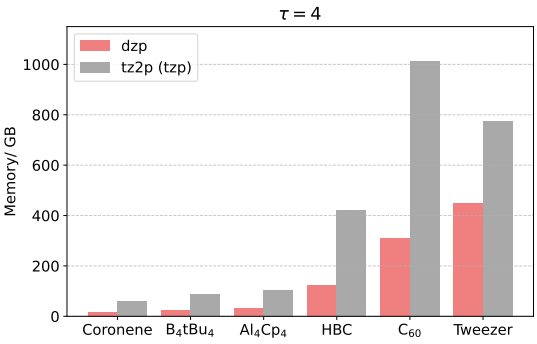

(a) Memory in GB for τ=4

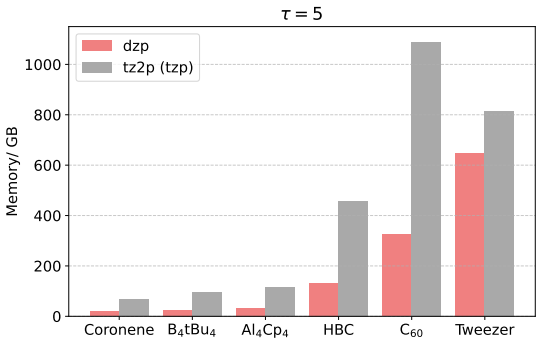

(b) Memory in GB for τ=5

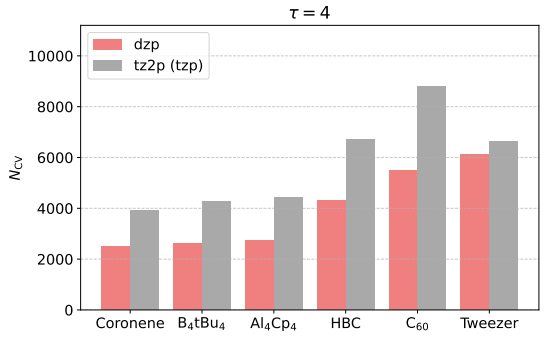

(c) Number of CVs for τ=4

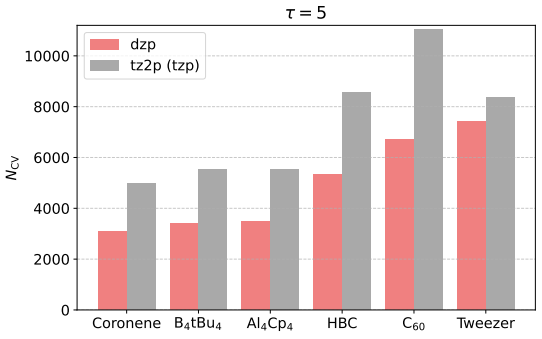

(d) Number of CVs for τ=5

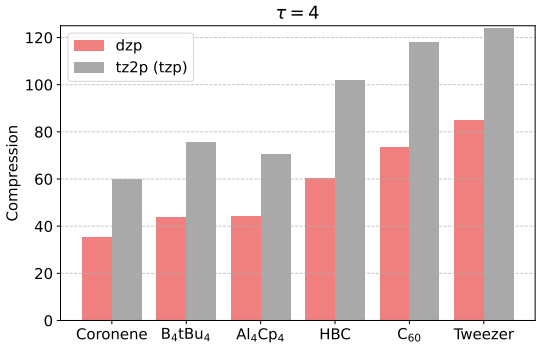

(e) Compression rate for τ=4

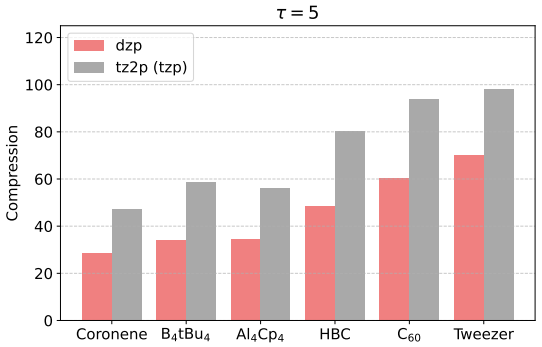

(f) Compression rate for τ=5

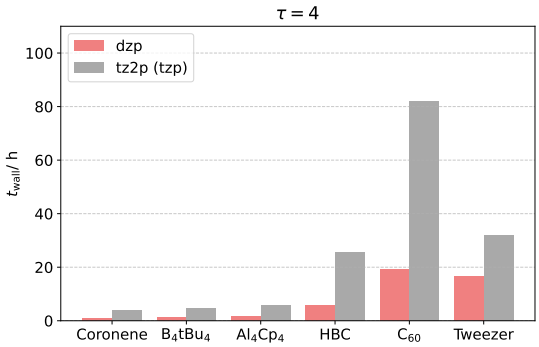

(g) Wall-clock time in hours for τ=4

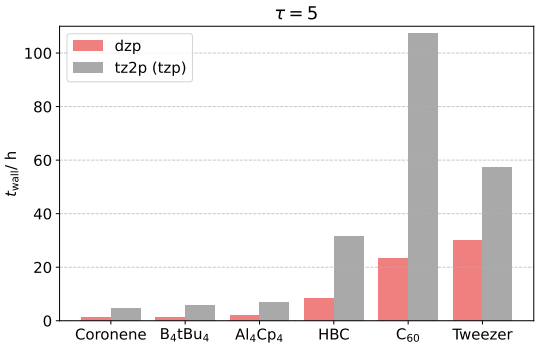

(h) Wall-clock time in hours for τ=5

Figure 5.6: Computational requirements for the NMR shielding calculations using the CD-GIAO-MP2 scheme and Cholesky thresholds $10^{-\tau}$, τ=4, 5.

In general, the results in fig. 5.6 show that the calculations for coronene, B_4tBu_4, Al_4Cp_4, HBC, C_{60}, and the tweezer host-guest complex are feasible in all cases, though the calculations for molecules with significantly more than 1000 basis functions are quite demanding. Only in the case of C_{60} and the tweezer host-guest complex, the memory requirements are in the terabyte range, which is affordable nowadays. The NMR shieldings for most molecules can be computed within less than one day, except for the largest systems for which calculations require more than one day. Considering the fact that the calculations for C_{60}, HBC, and the tweezer host-guest complex comprise more than 1000 basis functions, the total runtimes and the memory demands are reasonable, especially with regard to the fact that the GIAO-MP2 computations without CD would be infeasible. NMR shielding calculations on Al_4Cp_4 were already performed in 1993, as described in Ref. [20], but this involved an extremely high computational effort and was

only possible using a rather small basis set (dzp). The disk bottleneck in standard GIAO-MP2 calculations was removed three years later by means of an integral-direct scheme,[61] and due to the additional exploitation of molecular point group symmetry and a coarse-grain parallelization, NMR shieldings for the highly symmetric Al_4Cp_4 (D_{2d} symmetry) and B_4tBu_4 (T_d symmetry) molecules could be carried out, as described in Ref. [68]. Kollwitz *et al.*[68] report a runtime of about 18 days for the calculation of B_4tBu_4 comprising 616 basis functions. Furthermore, they estimated that the standard GIAO-MP2 calculation would require about 16 months which is infeasible. The CD-GIAO-MP2 scheme presented in this section required only about five hours for the NMR shielding calculation of B_4tBu_4 without the exploitation of molecular point group symmetry, which is still 86 times faster* as the calculations from Ref. [68]. The CD-based scheme guarantees efficient calculations for all systems with up to 1500 basis functions and is not restricted to highly symmetric molecules, but it has to be noted that the utilization of molecular point group symmetry would significantly decrease the computational cost. However, there are also further ways to improve the computational performance, as presented in the next section.
The difference in timings and memory demands between the CD-GIAO-MP2 and the standard scheme is again exemplified based on coronene (dzp basis) where the standard scheme needed nine hours, 42 minutes and around 750 GB while the CD-based scheme requires only two hours, five minutes and only 18 GB memory, i.e. the latter is about a factor of 4.6 faster and reduces the memory requirement by about 97.6%†. At this point, it should be noted that parallelization is an essential tool to accelerate computations, and has been employed in form of threaded matrix-matrix multiplication routines from a BLAS library in the calculations presented here. In order to investigate the effect of parallelization, the calculation for the tweezer host-guest complex (dzp basis) has been performed using a single and multiple CPUs. A speed-up of about 4.1 is achieved when using 20 CPUs instead of only one CPU (one day and five hours vs. five days)‡. In fig. 5.6 (e) and (f), it can also be seen that the compression rates are high for all cases, which indicates a significant reduction of the memory requirements for the two-electron integrals, as expected from theory.
Furthermore, the required resources depend on the chosen Cholesky threshold; a tighter threshold increases the computational demands as seen in fig. 5.6. The results for C_{60} using the tz2p basis set show that the memory requirement is reduced by around 6% if τ=4 (1023 GB) is used instead of $\tau = 5$ (1089 GB). The same holds for the number of CVs (8776 vs. 11022) and the timings (three days, nine hours and 49 minutes vs. four days, eleven hours and 31 minutes). As expected, the compression rates are higher for loose Cholesky thresholds (118 vs. 94), which corresponds to a difference of approximately 20%.

In this context, it is also interesting to investigate how different Cholesky thresholds impact the computed NMR shieldings. For this purpose, the difference between the results obtained with a threshold of τ=4 and τ=5 is presented in fig. 5.7 for the ^{13}C and ^{1}H shieldings of coronene using the tz2p basis set.

* It should be noted that modern computers are generally faster than those used around 1998.
† The calculations were performed on an Intel Xeon(R) Gold 5125M node running at 2.5 GHz.
‡ The calculations were performed on an Intel Xeon(R) Gold 5125M node running at 2.5 GHz.

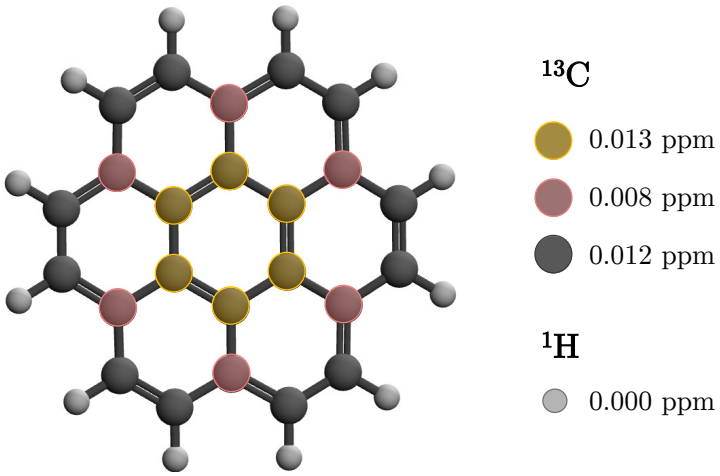

Figure 5.7: Maximum errors (in ppm) in the ^{13}C and ^{1}H NMR shieldings obtained with a Cholesky threshold of 10^{-4} with respect to a calculation performed with a Cholesky threshold of 10^{-5} for coronene using the tz2p basis set.

For coronene, the ^{13}C NMR shieldings differ by at most 0.013 ppm while in the ^{1}H isotropic shieldings, there is no difference within the reported digits. The results for the other systems in fig. 5.6 differ by at most 0.02 ppm, which is a negligible difference for most chemical applications. In order to be sure that converged results are obtained, τ=5 is recommended because this choice is a good compromise between accuracy and efficiency.

Based on the findings in this section, it can be concluded that computations involving 100 basis functions are already beyond the break-even point while calculations with around 400 electrons and 1500 basis functions mark the current limit of the application of the CD. To perform NMR calculations with significantly more than 1500 basis functions, schemes like the DLPNO-MP2[75] approach can be used. However, it has been shown that the CD-GIAO-MP2 scheme enables calculations on large systems that were previously infeasible with the standard scheme. Regarding the timings, the improved Cholesky decomposition algorithms are even more efficient, as demonstrated in the next section.

5.2 NMR Shift Computations using the Improved Cholesky Decomposition Algorithms

In this section, the results obtained with the improved CD algorithms are presented. The improvements were achieved through the use of permutational symmetry on the one hand and by using a two-step procedure one the other hand, as discussed in sections 2.6 and 2.6.2, respectively. They have been published by us in Ref. [189].

The efficiency of the improved one-step and the two-step procedure is demonstrated based on the molecules shown in fig. 5.6. All calculations were performed using only one CPU* in order to eliminate the effects of different parallelization in the three schemes. In fig. 5.8, the timings for the integral evaluation, the construction of the CVs and the total timings for the CD of the

* The calculations were performed on an Intel Xeon(R) Gold 6342M node running at 2.8 GHz.

unperturbed and the NMR integrals using the tz2p basis and a Cholesky threshold of 10^{-5} are shown for all three algorithms.

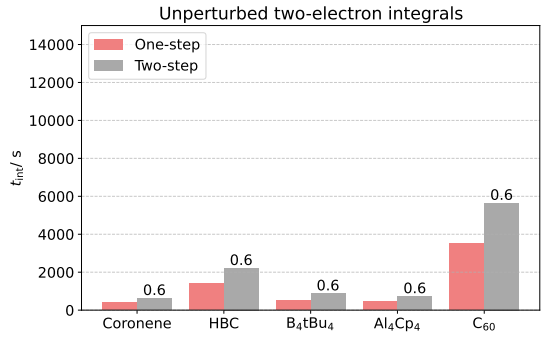

(a) Unperturbed integral evaluation.

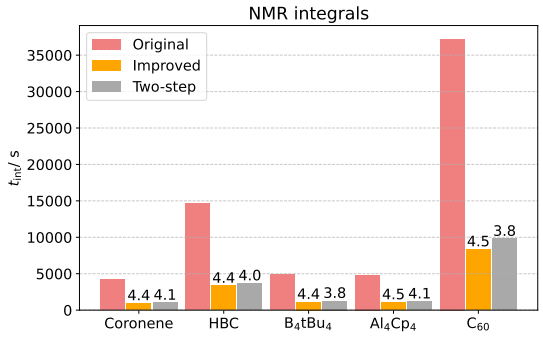

(b) NMR integral evaluation.

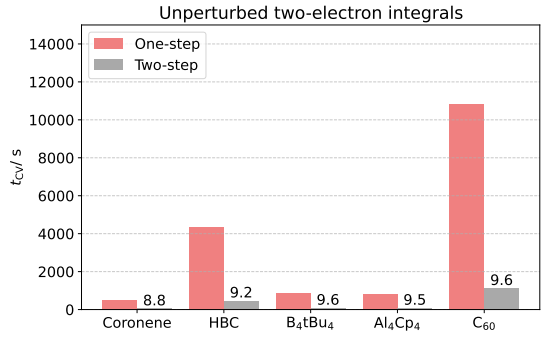

(c) Constructing unperturbed CVs.

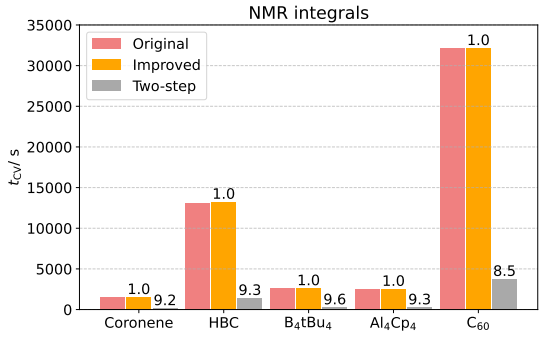

(d) Constructing NMR CVs.

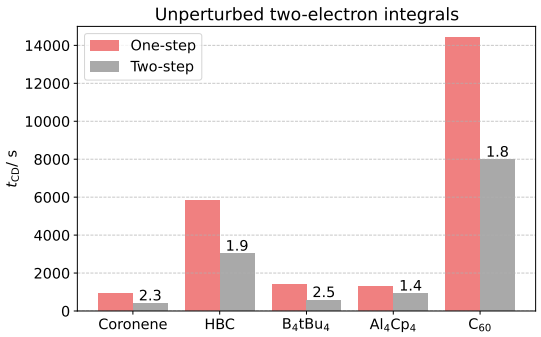

(e) Total CD of unperturbed integrals.

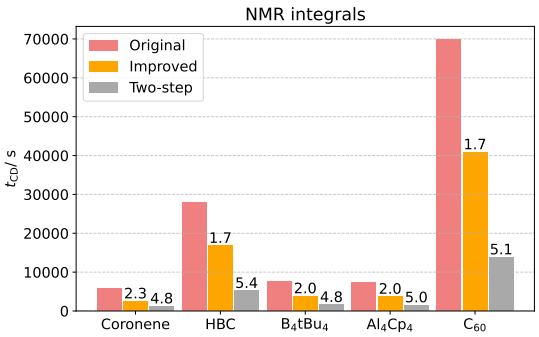

(f) Total CD of NMR integrals.

Figure 5.8: Timings (in seconds) for the CD of the unperturbed and NMR integrals, using the old, original, and two-step algorithm (tz2p basis, $\tau = 5$). The corresponding speed-up compared to the old procedure is given as number above the bar. All calculations were performed on an Intel Xeon(R) Gold 6342M node running at 2.8 GHz.

Regarding the evaluation of NMR integrals, a speed-up of about four was expected when using the partial derivatives instead of the full derivatives. The actual speed-up is even larger (4.4 and 4.5); for example, the NMR integral calculation for C_{60} required about ten hours in the case of the original algorithm while the improved one-step algorithm needed only about two hours. However, the timings for the unperturbed integrals are increased when using the two-step procedure. This is due to the fact that some integrals need to be calculated both in the first and the second step, in order to construct the Cholesky basis and to compute the CVs. Since the same Cholesky basis as for the unperturbed two-electron integrals are used for the CD of the

NMR integrals, the NMR integrals are not evaluated in the first step. The partial derivatives are also used in the two-step procedure, which is why a significant speed-up about a factor of four is observed. As seen in fig. 5.8 (c) and (d), the construction of the CVs (actually their orthonormalization according to eq. (2.211)) is the bottleneck of the one-step algorithm, which can be overcome by using the two-step scheme because the orthonormalization of the CVs can be carried out by efficient linear algebra routines. In the case of B_4tBu_4, the calculation of the CVs required 2623 seconds using the old algorithm and only 272 seconds using the two-step scheme, that is a factor of 9.6 faster. In general, substantial savings in the timings for constructing the CVs are realized for all molecules. Concerning the total CD procedure, savings in the range of 1.4 to 1.9 can be observed for the unperturbed integrals when using the two-step algorithm. Important to note is that the calculations have been carried out using only one core, as already mentioned. It is also possible to use, for example, threaded matrix-matrix multiplication routines from a BLAS library to make the calculations even faster.[93]

5.2.1 Comparison with Experimental NMR Spectra

Based on the shieldings obtained with the CD-GIAO-MP2 scheme, the NMR shifts can be computed via eq. (2.54) in order to compare them with experimental data. As an example, the NMR shifts of coronene have been computed according to eq. (2.54). As reference compound, tetramethylsilane (TMS) has been used, where first a geometry optimization at the RI-MP2[276–278]/cc-pVTZ level of theory (the geometry is given in the appendix in table 7.18) and then a NMR shielding calculation using CD-GIAO-MP2/$\tau = 10^{-5}$/tz2p has been carried out. The RI-MP2 geometry optimizations were performed using Turbomole.[279] For coronene, the geometry was optimized at the same level as for TMS (the geometry is given in table 7.19) and the NMR shielding tensor has been computed using the CD-GIAO-MP2 scheme with a Cholesky threshold of $\tau = 10^{-5}$ and the tz2p basis set. The calculated and experimental results[280] are reported in table 5.3.

Table 5.3: Computed NMR shielding constants σ(C) and shifts $\delta(^{13}C)$ for TMS, and coronene obtained at the CD-GIAO-MP2/$\tau = 10^{-5}$/tz2p level of theory. Experimental NMR shifts δ_{exp}(C) were taken from Refs. [280]. The shifts for coronene can be assigned using the colors/indices in fig. 5.9.

Molecule	Indices	σ(C)	δ(C)	δ_{exp}(C)
Coronene	1-6	74.28	124.95	121.00
	7-12	66.59	132.65	124.00
	13-24	70.47	128.76	123.00
TMS		199.23	0.00	

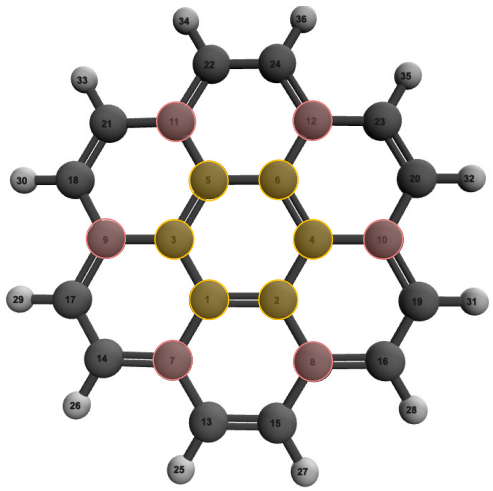

Figure 5.9: Color-coded/indexed C-atoms in coronene which can be assigned to the NMR data in table 5.3.

The shifts for the outer carbon atoms with hydrogen and the inner carbon atoms are in reasonable agreement with the experimental data, with a maximum difference of 5.8 ppm. A larger deviation of 8.7 ppm is observed for the carbon atoms at the rim. The differences could be explained by the lack of vibrational corrections, higher-order correlation effects as well as basis-set errors and by not using the exact geometry.[38] Using the same optimized geometry for coronene (RI-MP2/cc-pVTZ), the tz2p basis set and a Cholesky threshold of 10^{-5} for computing NMR shieldings, the shifts at the HF level of theory have been determined as 133.0 ppm, 139.7 ppm and 136.8 ppm. It can be seen that the MP2 values are appreciably closer to the experiment, which demonstrates the importance of including electron correlation. However, in Ref. [280], Orendt *et al.* also calculated the NMR shifts for coronene at the HF level and their results are actually closer to the experiment than the presented MP2 results, with a maximum deviation of 1 ppm (δ(C)=121 ppm, 123 ppm, 122 ppm). This may seem surprising at first glance, but can be explained as follows. First, Orendt *et al.*[280] optimized the geometry of coronene at the HF level of theory which leads to pronounced differences in the NMR shifts (using a HF-optimized geometry and performing a CD-GIAO-HF/$\tau = 10^{-5}$/tz2p calculation leads to δ(C)=122.1 ppm, 126.5 ppm, 122.0 ppm). As mentioned in Ref. [270], the bond alternation is larger at the HF than at the MP2 level, indicating shortcomings in the HF approach. However, MP2 overestimates electron correlation, does not yield highly accurate geometries,[38] and tends to overshoot in the case of absolute NMR shieldings.[42] According to Ref. [42], CC methods are necessary to obtain reliable results if MP2 and HF results differ significantly. Furthermore, Gauss[38] found that the inclusion of electron correlation is more important for absolute shielding constants than for the calculation of relative shifts since the latter often benefits from the cancellation of correlation effects, which might explain the good HF results in Ref. [280]. The ^{1}H shifts obtained using the RI-MP2/cc-pVTZ geometry and CD-GIAO-MP2/$\tau = 10^{-5}$/tz2p can be compared to experimental data from Ref. [270]. In this case, the value for the NMR shift deviates from the experimental value by 0.93 ppm. However, given the range of hydrogen shifts (about 0-10 ppm), this is a rather large discrepancy which might be attributed to the neglect of solvent and vibrational effects.

Table 5.4: Computed NMR shielding constants σ(H) and shifts $\delta(^1\mathrm{H})$ for TMS and coronene obtained at the CD-GIAO-MP2/$\tau = 10^{-5}$/tz2p level of theory. Experimental NMR shifts δ_{exp}(H) were taken from Ref. [270].

Molecule	σ(H)	δ(H)	δ_{exp}(H)
Coronene	21.81	9.78	8.85
TMS	31.96	0.00	

The calculations on coronene presented in this section were performed without considering the solvent. Nonetheless, the influence of the surrounding medium is also of relevance and can be accounted for, for example, within a QM/MM framework. The QM/MM approach is used in the next section, where NMR shifts of liquid water are computed using the CD-GIAO-MP2 scheme. In the case of water, this means that the surrounding water molecules are included, which comprises the molecular environment of interest in the liquid phase.

5.3 NMR Shift Calculations for Liquid Water using Cholesky Decomposition and QM/MM

The previous sections demonstrated the computational efficiency of the CD of the NMR integrals and that it is possible to carry out NMR shielding calculations for rather large systems using the CD-GIAO-MP2 scheme. To extend the range of applications even further, the CD-GIAO-MP2 procedure was embedded within a QM/MM framework, enabling the incorporation of the molecular environment in NMR shielding computations, for example to describe molecules in solution or in the liquid phase. To obtain accurate results, it is crucial to encompass as many molecules as possible in the QM region. Here, CD plays a central role, as its computational efficiency makes it possible to treat a large part of the system quantum-chemically.

In this section, the CD-GIAO-MP2 scheme has been used in QM/MM calculations to compute the NMR shifts of liquid water. In NMR experiments, water is a common solvent, and thus accurate computations of its NMR shifts are desirable. It is well established that hydration and hydrogen-bond formation impacts the chemical shifts;[248–250,252,281] a fact that can also be easily demonstrated theoretically by taking a snapshot of an MD simulation (in this case $T = 275\,\mathrm{K}^*$) and placing an arbitrarily chosen water molecule in the QM region. The NMR shieldings were then calculated at the MP2/cc-pVDZ level, where the other water molecules in the MM region were taken into account in the first calculation while in the second calculation, the MM surrounding was ignored. The values of the isotropic shielding constants are given in tables 5.5 and 5.6.

* For details see section 4.7

Table 5.5: NMR shielding constants of one water molecule taken from a snapshot of an MD simulation at $T = 275\,\mathrm{K}$, without the surrounding MM water molecules.

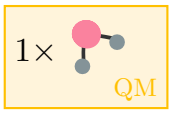

Atom	σ/ppm
O	363.854
H	31.478
H	31.872

Table 5.6: NMR shielding constants of one water molecule taken from a snapshot of an MD simulation at $T = 275\,\mathrm{K}$, including the surrounding MM water molecules.

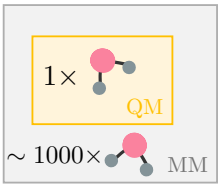

Atom	σ/ppm
O	345.680
H	31.555
H	31.321

The results clearly indicate that the MM atoms affect the shielding constants; for oxygen, σ differs by about 18 ppm. It can be seen that the value for the shielding constant is reduced when the surrounding water molecules are included. This finding can be explained by the fact that a hydrogen bond „pulls“ electron density away from the oxygen atom, thereby reducing its shielding constant, which in turn corresponds to an increase in the chemical shift according to eq. (2.54). The results support the statement that the solvent has a pronounced effect on the chemical shieldings. Hence, it is essential to account for the surrounding environment when computing NMR shieldings of liquid water. There is also the possibility of using implicit solvent models like the conductor-like screening model (COSMO)[282–285] or the polarizable continuum model (PCM),[285–288] but an explicit solvent method is better suited to describe hydrogen-bond formation.[289]

In order to judge the reliability of NMR shift calculations on liquid water, the gas-to-liquid shifts for the oxygen and hydrogen nuclei, $\Delta\sigma$,

$$\Delta\sigma = \sigma_{\mathrm{liquid}} - \sigma_{\mathrm{gas}}, \tag{5.2}$$

can be computed and compared to experimental results.[249] To investigate the effect of hydration, it is crucial to describe the hydrogen bonds as accurate as possible. However, it is infeasible to include all water molecules from the simulation box in a quantum-chemical calculation. In this work, a QM/MM approach has been combined with the CD-GIAO-MP2 scheme as an engine for the treatment of the QM part to compute the gas-to-liquid shifts for water. This approach is advantageous for two reasons: first, the molecular environment is treated explicitly, and secondly, the CD enables the inclusion of large water clusters in the QM region. The latter is important to obtain reliable results which will be demonstrated in the following.

5.3.1 NMR Shielding Convergence

In order to examine how the nuclear shielding constants change with increasing water cluster size in the QM region, the NMR shieldings for one water molecule with $n = 2, 4, 8, 12, 16, 20, 22$ neighboring water molecules have been computed. This has been done both for the QM part only, as shown in fig. 5.10, and for the case where also the additional MM molecules are included in the calculation, which is shown in fig. 5.11.

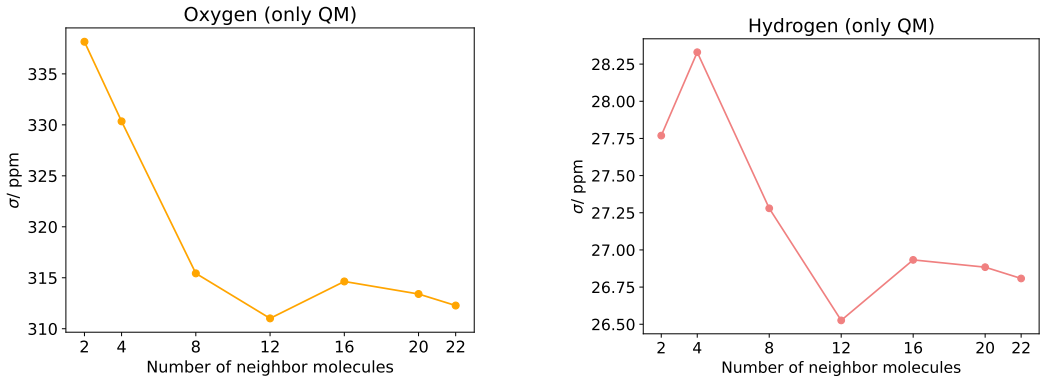

Figure 5.10: Convergence for the NMR constants of the central water molecule surrounded by 2, 4, 8, 12, 16, 20, 22 neighboring molecules, neglecting the MM molecules. (NMR shieldings computed with CD-GIAO-MP2/$\tau = 5$/cc-pVTZ).

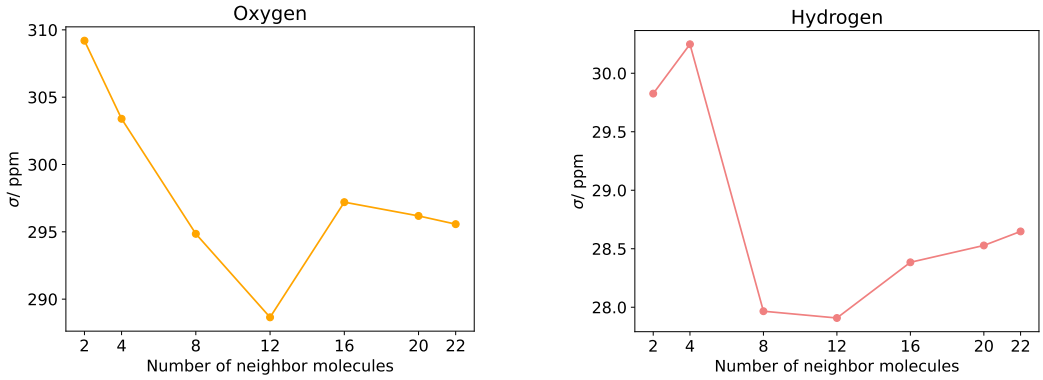

Figure 5.11: Convergence for the NMR constants of the central water molecule surrounded by 2, 4, 8, 12, 16, 20, 22 neighboring molecules, including all MM molecules. (NMR shieldings computed with CD-GIAO-MP2/$\tau = 5$/cc-pVTZ).

In fig. 5.10, it can be seen that the values for the shielding constant significantly decrease both for ^{17}O and ^{1}H when the cluster size is increased from two to twelve. This makes sense because the immediate environment has the greatest influence on the NMR shieldings due to hydrogen-bond formation. The differences are less pronounced for a cluster size of 16, which means that at least 16 neighboring water molecules should be included in the QM region. This is a rather large QM part: using the cc-pVTZ basis set, for example, there are 968 basis functions, which would be infeasible to compute with the standard GIAO-MP2 scheme. Figure 5.11 shows that the inclusion of the MM molecule changes the results, even for QM regions containing 22 neighboring molecules. This again emphasizes the relevance of a QM/MM approach since the

inclusion of the MM molecules affects the result. In this case, too, at least 16 neighboring water molecules are needed to cover hydration effects adequately. Furthermore, it can be observed that the NMR shielding constants seem to converge less well when the MM molecules are taken into account. It should be noted that the results presented in fig. 5.11 were only obtained for one central water molecule and an average value over many such calculations would produce more conclusive results.
Nonetheless, these findings demonstrate the need of the CD of the unperturbed and perturbed two-electron integrals for sufficiently large QM regions, which are required to obtain reliable results. Nevertheless, the calculation of $H_2O(H_2O)_{22}$ clusters using the cc-pVTZ basis set are close to the limit of the CD: There are 1334 basis functions and the computation required around 500 GB memory and about one day, which is feasible for one calculation but becomes quite demanding for a hundred or more calculations of this type.

The findings in this section suggest that inclusion of the first solvation shell (around four neighboring water molecules, as outlined in the next subsection) should not suffice to provide accurate gas-to-liquid shifts for water. This statement will be discussed in the next subsection.

5.3.2 Inclusion of the First Solvation Shell

To determine how many neighbors a water molecule has in the first solvation shell, the radial distribution function defined by[129]

$$\frac{1}{V} g_{AB}(\mathbf{r}) = \frac{1}{N_A N_B} \left\langle \sum_{i=1}^{N_A} \sum_{j=1}^{N_B} \delta \left[r - r_{A_i B_j} \right] \right\rangle \tag{5.3}$$

has been determined for all oxygen atoms. In this equation, V is the volume, δ is the Dirac delta function while N_A and N_B are the total number of atoms A and B, respectively (in this case A, B=O). A plot of the radial distribution function can be found in fig. 5.12.

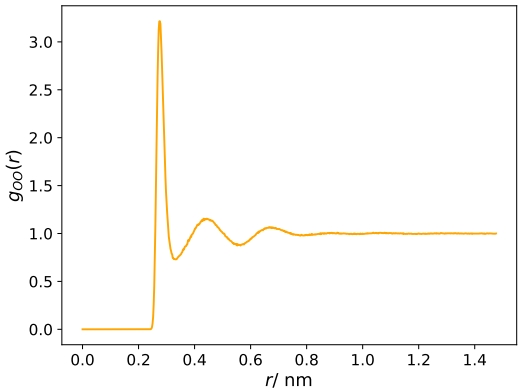

Figure 5.12: Radial distribution function for oxygen (MD simulation at $T = 275\,\mathrm{K}$).

As expected,[8,290–293] the radial distribution function for liquid water shows a structured local environment. Based on this function, it is possible to compute the mean distance between an oxygen atom and its nearest neighbors by computing the maximum value of $g_{OO}(\mathbf{r})$. This distance generally describes the first coordination shell, that is the typical distance at which the first layer

of neighboring molecules is located around a central atom. Here, the mean distance is 0.276 nm. By integrating the area of the first peak, the coordination number of the first solvation shell can be determined, which is in this case four (tetrahedral) and is illustrated in fig. 5.13.

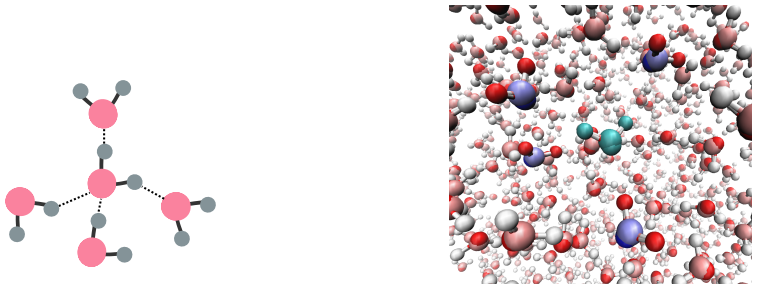

(a) (b)

Figure 5.13: (a) Conceptual illustration of the first coordination sphere and (b) tetrahedral water cluster in the simulation box, where the central water molecule is colored light blue.

From the MD simulation, a single snapshot was extracted for the following calculations. A hundred water molecules from this snapshot were selected as central water molecule to provide statistical significance, as a single water molecule would not sufficiently capture the characteristics of the molecular ensemble. All water molecules within an oxygen-oxygen distance of 0.276 nm at most were included in the QM region, such that each central water molecule has 2-8 nearest neighbors. The NMR shielding constants have been computed with the CD-GIAO-MP2 scheme using a Cholesky threshold of 10^{-5} and the cc-pVTZ basis set. The values of the isotropic shieldings for all central water molecules have been averaged, which is denoted with $\bar{\sigma}$ in the following. The standard error of the sample mean (SEM),

$$\mathrm{SEM}(\bar{\sigma}) = \frac{1}{\sqrt{n}} \cdot s(\sigma), \tag{5.4}$$

with n as the number of values (in this case 100) and $s(\sigma)$ as the sample variance

$$s(\sigma) = \sqrt{\frac{1}{n-1}\sum_{i=1}^{n}(\sigma_i - \bar{\sigma})^2} \tag{5.5}$$

has also been determined for the averaged NMR shielding constants. The statistical uncertainty occurs due to the finite number of water molecules/snapshots.[248] The results are given in table 5.7 and the distribution of all computed shielding constants is shown in fig. 5.14. As expected from the central limit theorem, which states that the distribution of a sample follows approximately a normal distribution, the plots for the distribution of the shielding constants for oxygen and hydrogen in fig. 5.14 show a Gaussian shape. The width of the distributions is around 70 ppm and 15 ppm for the ^{17}O and the ^{1}H shielding, respectively, which is in accordance with the findings in Refs. [253, 294]. Concerning the SEM, the relative error is about 0.51% for oxygen and about 1.02% for hydrogen, which is why the calculated mean value can be assumed to be comparatively precise.

Table 5.7: Averaged shielding constants $\bar{\sigma}$ and SEM (in ppm) for oxygen and hydrogen of 100 water molecules with 2-8 neighbors each (one snapshot of an MD simulation at $T = 275\,\mathrm{K}$, NMR shieldings computed with CD-GIAO-MP2/$\tau = 5$/cc-pVTZ).

Atom	$\bar{\sigma}$/ppm
O	317.80 ± 1.62
H	28.086 ± 0.287
H	27.611 ± 0.281

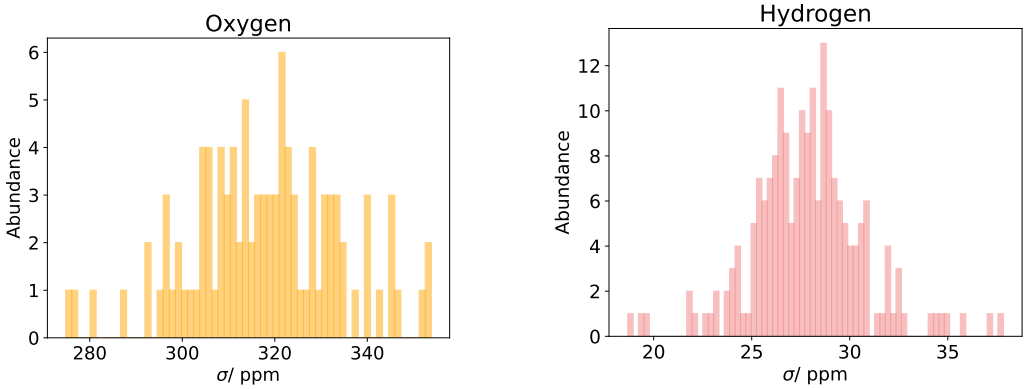

Figure 5.14: Distribution of the shielding constants for the oxygen and hydrogen nuclei of the central water molecule in H_2O-$(H_2O)_n$, n=2-6 clusters (taken from one snapshot of an MD simulation at $T = 275\,\mathrm{K}$), NMR shieldings computed with CD-GIAO-MP2/$\tau = 5$/cc-pVTZ.

To calculate the gas-to-liquid shift $\Delta\sigma$ via eq. (5.2), an MD simulation for a single water molecule has been performed at $T = 275\,\mathrm{K}$ in order to obtain values for σ_{gas}. For this purpose, 100 snapshots were taken from the MD simulation and for all snapshots, the shielding constant has been calculated for the single water molecule, using the same method as for the 100 water molecules. The averaged NMR shielding constants as well as the corresponding distributions can be found in table 5.8 and fig. 5.15. Since only one water molecule is involved, the relative error based on the SEM in eq. (5.4) is in this case around 0.03% and 0.05% for oxygen and hydrogen, respectively.

Table 5.8: Mean value $\bar{\sigma}$ and SEM (in ppm) for one water molecule (100 snapshots from an MD simulation at $T = 275\,\mathrm{K}$, NMR shieldings computed with CD-GIAO-MP2/$\tau = 5$/cc-pVTZ).

Atom	$\bar{\sigma}$/ppm
O	352.68 ± 0.11
H	30.987 ± 0.015
H	30.989 ± 0.013

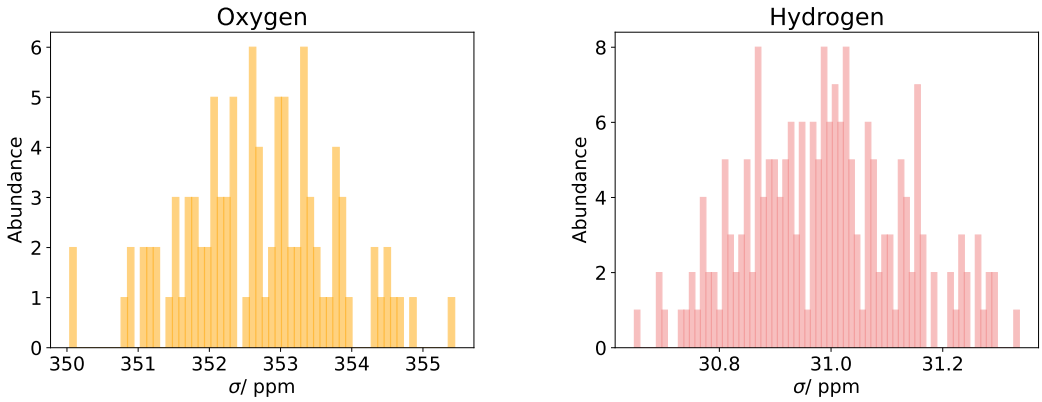

Figure 5.15: Distribution of the shielding constants for 100 snapshots of one water molecule; MD simulation at $T = 275\,\mathrm{K}$, NMR shieldings computed with CD-GIAO-MP2/τ = 5/cc-pVTZ.

Based on the results in tables 5.7 and 5.8, the gas-to-liquid shift $\Delta\sigma_{\mathrm{comput}}$ for oxygen and hydrogen has been determined and is presented together with the experimental values[248,295–297] $\Delta\sigma_{\mathrm{exp}}$ in table 5.9. The gas-to-liquid shift for hydrogen has been determined by averaging over the NMR shielding constants for both hydrogen atoms.

Table 5.9: Computed ($\Delta\sigma_{\mathrm{comput}}$) and experimental[248,295–297] ($\Delta\sigma_{\mathrm{exp}}$) values for the gas-to-liquid shifts. $\Delta\sigma_{\mathrm{comput}}$ has been computed at the CD-GIAO-MP2/τ = 5/cc-pVTZ level.

Atom	$\Delta\sigma_{\mathrm{comput}}$/ppm	$\Delta\sigma_{\mathrm{exp}}$/ppm
O	-34.9 ± 1.6	-36.1
H	-3.1 ± 0.3	-4.3

The results in table 5.9 show that the computed gas-to-liquid shift for oxygen agrees well with the experimental result with a deviation of about 1.2 ppm, and the experimental value lies within the error range. However, the differences are rather high (about 1.2 ppm) for the gas-to-liquid shift of hydrogen. Based on the findings in section 5.3.1, the deviations can be explained by the fact that 2-8 neighboring water molecules are not enough to cover the effect of hydrogen-bond formation. This means that the differences should be minimized by including more water molecules into the QM region, which is feasible due to the CD-based scheme. In the next subsection, the gas-to-liquid shift is computed taking into account the second coordination sphere. For this purpose, the tzp basis set was chosen because it is large enough, but computationally not too demanding compared to the cc-pVTZ basis set, as outlined in section 5.3.1. The computational cost when using the tzp basis set can be exemplified based on a calculation including in total 23 QM water molecules: although 682 basis functions are involved, the calculation required only around four hours and about 90 GB of memory, while the same calculation with the cc-pVTZ set (1334 basis functions) requires one day and about 500 GB. However, a smaller basis set implies less accuracy which is reflected in the results from table 5.10; the computed gas-to-liquid shifts agree less well with the experimental data*. In this case, the differences in the shifts for oxygen and hydrogen

* The mean value $\bar{\sigma}$, SEM and the distributions of the NMR shieldings for the calculation on one water molecule using the tzp basis set is given in table 7.1 and fig. 7.1 in the appendix.

are around 2.7 ppm and 1.4 ppm, respectively.

Table 5.10: Averaged shielding constants $\bar{\sigma}$ and SEM for oxygen and hydrogen of 100 water molecules with 2-8 neighbors each (one snapshot from an MD simulation at $T = 275\,\mathrm{K}$, NMR shieldings computed with CD-GIAO-MP2/$\tau = 5$/tzp), computed ($\Delta\sigma_{\mathrm{comput}}$) and experimental[248,295–297] ($\Delta\sigma_{\mathrm{exp}}$) values for the gas-to-liquid shifts.

Atom	$\bar{\sigma}$/ppm	$\Delta\sigma_{\mathrm{comput}}$/ppm	$\Delta\sigma_{\mathrm{exp}}$/ppm
O	321.94 ± 1.34	-33.4 ± 1.3	-36.1
H	28.861 ± 0.242	-2.9 ± 0.2	-4.3
H	28.551 ± 0.233		

5.3.3 Inclusion of the Second Solvation Shell

Based on the radial distribution function in fig. 5.12, the second maximum is given at 0.432 nm and the coordination number is 20. Again, a single snapshot was extracted from the MD simulation at $T = 275\,\mathrm{K}$. From this snapshot, a hundred water molecules were chosen as central water molecules and all water molecules within a maximum oxygen-oxygen distance of 0.432 nm were included in the QM region. This leads to $H_2O(H_2O)_n$ clusters with n=17-24. The corresponding NMR shielding calculation were performed using CD-GIAO-MP2/$\tau = 5$/tzp level of theory. In terms of timing and memory requirement, 100 such calculations are affordable due to the CD, whereas calculations with the standard GIAO-MP2 scheme would not be practically possible. The averaged shielding constants as well as the corresponding SEM for the central water molecules and the resulting gas-to-liquid shifts are given in table 5.11, while the corresponding distributions can be found in fig. 7.2 in the appendix.
In comparison to the values for the first coordination sphere obtained with the cc-pVTZ and tzp basis in tables 5.9 and 5.10, no improvements are observed in the computed gas-to-liquid shift for ^{17}O when including the second coordination sphere. The deviation is even larger with a difference of about 4.9 ppm. This can be explained by an advantageous error cancellation from which the results in tables 5.9 and 5.10 may profit. However, the differences in the hydrogen shifts are better in comparison both to the shifts computed with the cc-pVTZ and the tzp basis set with a difference of about 0.8 ppm, indicating that a larger QM region is required to provide better results.

Table 5.11: Averaged shielding constants $\bar{\sigma}$ and SEM for oxygen and hydrogen of 100 water molecules with 17-24 neighbors each (one snapshot from an MD simulation at $T = 275\,\mathrm{K}$, NMR shieldings computed with CD-GIAO-MP2/$\tau = 5$/tzp), computed ($\Delta\sigma_{\mathrm{comput}}$) and experimental[248,295–297] ($\Delta\sigma_{\mathrm{exp}}$) values for the gas-to-liquid shifts.

Atom	$\bar{\sigma}$/ppm	$\Delta\sigma_{\mathrm{comput}}$/ppm	$\Delta\sigma_{\mathrm{exp}}$/ppm
O	314.37 ± 1.16	-41.0 ± 1.2	-36.1
H	28.166 ± 0.233	-3.5 ± 0.2	-4.3
H	27.939 ± 0.223		

One possible explanation for the differences between computed and measured gas-to-liquid shift

might be that the geometries taken from the MD snapshots are not accurate enough.[248] Even small variations in geometry have a significant impact on the chemical shielding;[298] for example, an elongated O-H bond results in weaker shielding at the hydrogen nucleus. Malkin *et al.*[250] analyzed the effect of different force fields on the gas-to-liquid shift and showed that the results differ by up to 25 ppm for oxygen and 1 ppm for hydrogen. As seen in tables 5.9 and 5.11, the statistical uncertainty is relatively high. This could be reduced by increasing the number of random samples, i.e. more than one hundred water clusters and more than one snapshot. Furthermore, neglecting the zero-point energy and vibrational effects introduces additional error sources to the computational results.[248,250] It should also be noted that the MP2 method neglects higher order correlation effects[38] and overestimates the correlation contribution, which may introduce errors in the computed shielding constants.[25,38,40]

5.3.4 Comparison to DFT Results

The results presented so far were obtained from an MD simulation at 275 K. Changing the temperature in the MD simulations can lead to changes in the NMR shielding constants since the density of water changes for different temperatures, as shown in fig. 5.16 for the TIP4P water model. The DFT-values for the gas-to-liquid shifts in Ref. [249] are based on an MD simulation at 300 K, and in order to compare them with the CD-GIAO-MP2 results from this work, the calculations for the second solvation sphere were repeated using a snapshot from an MD simulation at 300 K. According to the corresponding radial distribution function, a distance of 0.448 nm has been determined for the second solvation sphere (18-28 neighboring atoms). The NMR shielding calculations were performed using the CD-GIAO-MP2/$\tau = 5$/tzp level of theory and the results are reported in table 5.12 (the corresponding distributions are given in fig. 7.4). The σ_{gas} values and distributions obtained via calculations on one water molecule at 300 K (100 snapshots) can be found in table 7.2 and fig. 7.4 in the appendix.

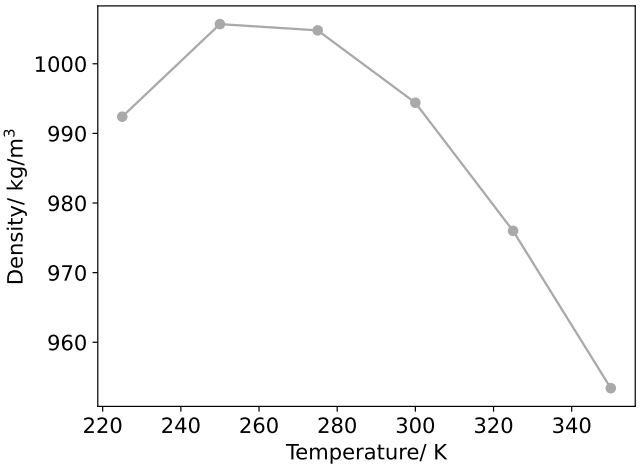

T/ K	Density/ kg/m^3
225	992.4
250	1005.7
275	1004.8
300	994.4
325	976.0
350	953.4

Figure 5.16: Density (in kg/m^3) of the TIP4P water molecule for different temperatures.

Table 5.12: Averaged shielding constants $\bar{\sigma}$ and SEM for oxygen and hydrogen of 100 water molecules with 18-28 neighbors each (one snapshot from an MD simulation at $T = 300\,\mathrm{K}$, NMR shieldings computed with CD-GIAO-MP2/$\tau = 5$/cc-pVTZ), computed ($\Delta\sigma_{\mathrm{comput}}$) and experimental[248,295–297] ($\Delta\sigma_{\mathrm{exp}}$) values for the gas-to-liquid shifts.

Atom	$\bar{\sigma}$/ ppm	$\Delta\sigma_{\mathrm{comput}}$/ ppm	$\Delta\sigma_{\mathrm{exp}}$/ ppm
O	317.41 ± 1.17	-37.7 ± 1.2	-36.1
H	28.590 ± 0.201	-3.1 ± 0.2	-4.3
H	28.333 ± 0.244		

The computed gas-to-liquid shifts for oxygen and hydrogen in table 5.12 differ from the experimental data by about 1.6 ppm and 1.2 ppm, respectively. These results can be compared to gas-to-liquid shifts obtained via DFT calculations, as presented in Ref. [249]. Cuny *et al.* carried out ab initio MD simulations using both PBE[299] and optB88-vdW[300–303] functionals, and performed NMR shielding computations using B3LYP and different Pople basis sets[304–306*] for 1000 water molecules taken from 50 different frames (MD simulation at 300 K), where the central water molecule is surrounded by 20 (± 3) other water molecules. The largest deviation for the oxygen nucleus is at around 16 ppm for the 6-311++G(d,p) basis set while the smallest deviation is around 4 ppm for the 6-31G(2d,2p) basis set. Concerning the hydrogen nuclei, the differences range from 1.5 ppm to 2.8 ppm. Both for ^{17}O and ^{1}H, the CD-GIAO-MP2 scheme outperforms the DFT calculations presented in Ref. [249] in terms of accuracy. In all cases, the differences are smaller when the CD-GIAO-MP2 scheme is used, even though no ab initio MD simulation has been performed. This demonstrates that our scheme can produce results that are at least as good as, or even better than those achieved with a DFT approach. However, the results in Ref. [249] benefit from a broader statistical sampling. While electron correlation is explicitly incorporated in methods like MP2, DFT methods only provide an implicit treatment. As explained in more detail in Ref. [25], there are also some issues concerning DFT calculations of magnetic properties since the Hohenberg-Kohn theorems do not hold in the presence of a magnetic field.

The results presented in this section demonstrate that QM/MM calculations involving large QM regions can be performed using the CD-GIAO-MP2 scheme. In this case, the use of CD enabled to include up to 29 water molecules in the QM region which was previously only possible for DFT calculations and rather small basis sets[248,249,253,294,307] due to memory and time limitations. However, none of the calculations presented here provided an accurate value for the experimental gas-to-liquid shifts which indicates that further improvements are required. For example, the simulation box and the simulation run time could be increased. Furthermore, the error originating from finite-size effects could be decreased by including more water molecules in the QM region which would be possible by utilizing the partitioning of the MM atoms in a short-range and a long-range region,[221] as discussed in section 2.8.1. It is also possible that the remaining errors are due to the use of electrostatic embedding and maybe a polarized embedding scheme[199,200,308–310] would provide better results. Nonetheless, the combination of the CD-GIAO-MP2 scheme with the QM/MM approach lays the foundation for the suggested extensions and enables the study of chemical processes in explicit solvent with sufficient accuracy. In principle, this methodology

* 6-31G(d,p), 6-31G(2d,2p), 6-311G(d,p), 6-31+G(d,p), 6-31++G(d,p), 6-311+G(d,p), 6-311++G(d,p), 6-311++G8(2d,2p)

can also be applied to solid-state and biomolecular systems, thereby allowing a wide range of chemical processes to be studied theoretically, which are not accessible with the standard GIAO-MP2 scheme.

5.4 Computation of Magnetizabilities using Cholesky Decomposition

First, the performance of the three different schemes for the CD of the magnetizability integrals presented in section 3.4 is compared and analyzed with respect to accuracy and computational efficiency. Representative calculations involving systems with about 1000 basis functions are presented to demonstrate the applicability of the CD-GIAO-HF scheme for computing magnetizabilities. All results presented in this section, except the calculations for HBC and C_{60}, have been published by us in Ref. [94].

5.4.1 Performance of the Three Proposed Schemes

To obtain information about the accuracy of the different schemes, the magnetizability integrals are split according to eq. (3.30), where the following notation is used:

$$\left(\frac{\partial^2 \sigma\rho}{\partial B_i \partial B_j}\middle|\mu\nu\right) + \left(\sigma\rho\middle|\frac{\partial^2 \mu\nu}{\partial B_i \partial B_j}\right) \rightarrow \text{type A}$$

$$\left(\frac{\partial \sigma\rho}{\partial B_i}\middle|\frac{\partial \mu\nu}{\partial B_j}\right) + \left(\frac{\partial \sigma\rho}{\partial B_j}\middle|\frac{\partial \mu\nu}{\partial B_i}\right) \rightarrow \text{type B}.$$

The test set comprises HeH^+, BH, CH_4, H_2O, and vinyl alcohol. Unless otherwise stated, the calculations were carried out using Dunning's cc-pVTZ basis set and a Cholesky threshold of 10^{-5}. The geometries for all systems except vinyl alcohol and the number of basis functions are given in fig. 5.17. For vinyl alcohol, the same geometry as in section 5.1.2 has been used.

Figure 5.17: Geometries and basis functions for the test systems HeH^+, BH, CH_4, H_2O. For vinyl alcohol (VA), the same geometry as in section 5.1.2 (cc-pVTZ) was used.

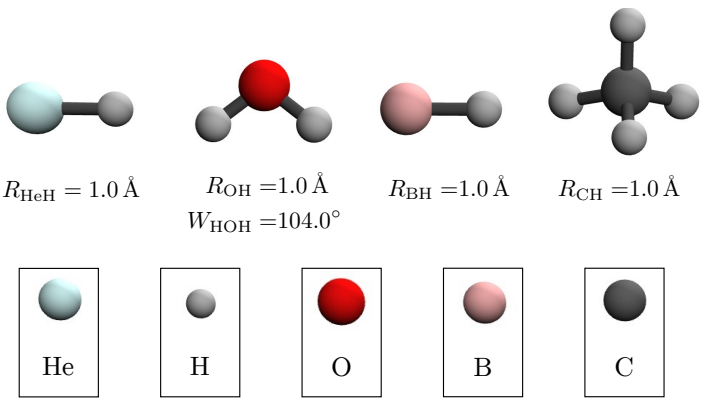

Molecule	N_{BF}
HeH^+	28
BH	44
CH_4	86
H_2O	58
VA	146

The number of generated CVs, the theoretical maximum number of CV N_{CV}^{total}, and the corresponding compression rates are given in fig. 5.18 and table 5.13, respectively; for scheme 3, the

number of CVs in the second CD is shown while for the first CD, the number of CVs is identical to scheme 1 (or scheme 2). It can be seen that only fractions of the total number of CVs are generated. While for the small systems HeH^+ and BH, the number of CVs for scheme 3 is only slightly larger than for schemes 1 and 2, about 1.9-2.5 times as many CVs are generated in case of the larger systems. Compared to fig. 5.6, the compression rates are rather low. This is because the CD has a significant effect only on larger molecules that involve more basis functions, but it can still be concluded that the CD reduces the memory requirements for the magnetizability integrals even for systems with less than 100 basis functions.

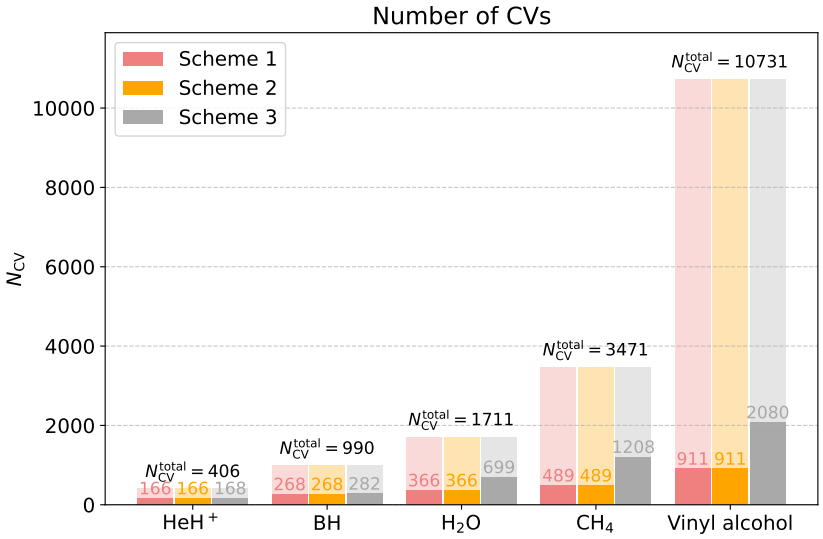

Figure 5.18: Number of actual CV (N_{CV}) for the test systems HeH^+, BH, CH_4, H_2O, and vinyl alcohol using the cc-pVTZ basis set. The theoretical maximum number of CV N_{CV}^{total} is plotted in the corresponding transparent color and is additionally given as number above the bar.

Table 5.13: Compression rates according to fig. 5.18.

Molecules	Scheme 1/2	Scheme 3
HeH^+	2.45	2.45
BH	3.69	3.51
H_2O	4.67	2.45
CH_4	7.10	2.87
Vinyl alcohol	11.78	5.16

However, the calculations presented here were not carried out to demonstrate the efficiency of the procedure, but rather to investigate the error of the CD for the three proposed schemes. The errors in the reconstructed type A and B integrals are given in table 5.14, where the following notation is used:

$$\frac{\partial^2(\sigma\rho|\mu\nu)}{\partial B_x \partial B_x} \rightarrow xx, \quad \frac{\partial^2(\sigma\rho|\mu\nu)}{\partial B_y \partial B_y} \rightarrow yy, \quad \frac{\partial^2(\sigma\rho|\mu\nu)}{\partial B_z \partial B_z} \rightarrow zz.$$

Table 5.14: Maximum absolute errors in the reconstructed magnetizability integrals (type A and B) using the three CD schemes (cc-pVTZ basis, $\tau = 5$) for HeH^+, BH, CH_4, H_2O, and vinyl alcohol (VA).[94]

	Type A			Type B		
Molecule	xx	yy	zz	xx	yy	zz
			Scheme 1			
HeH^+	$3.7 \cdot 10^{-5}$	$3.7 \cdot 10^{-5}$	0.0	$1.9 \cdot 10^{-3}$	$1.9 \cdot 10^{-3}$	0.0
BH	$1.1 \cdot 10^{-4}$	$1.1 \cdot 10^{-4}$	0.0	$6.3 \cdot 10^{-4}$	$6.3 \cdot 10^{-4}$	0.0
CH_4	$5.3 \cdot 10^{-4}$	$5.2 \cdot 10^{-4}$	$2.6 \cdot 10^{-4}$	$6.2 \cdot 10^{-4}$	$6.1 \cdot 10^{-4}$	$3.0 \cdot 10^{-4}$
H_2O	$2.5 \cdot 10^{-4}$	$9.5 \cdot 10^{-5}$	$1.6 \cdot 10^{-4}$	$7.4 \cdot 10^{-4}$	$1.7 \cdot 10^{-4}$	$2.1 \cdot 10^{-3}$
VA	$2.7 \cdot 10^{-4}$	$4.7 \cdot 10^{-4}$	$3.7 \cdot 10^{-3}$	$4.5 \cdot 10^{-4}$	$8.5 \cdot 10^{-4}$	$3.9 \cdot 10^{-3}$
			Scheme 2			
HeH^+	$3.2 \cdot 10^{-5}$	$3.2 \cdot 10^{-5}$	0.0			
BH	$1.1 \cdot 10^{-4}$	$1.1 \cdot 10^{-4}$	0.0			
CH_4	$5.3 \cdot 10^{-4}$	$5.2 \cdot 10^{-4}$	$2.6 \cdot 10^{-4}$	as for scheme 1		
H_2O	$2.7 \cdot 10^{-4}$	$9.7 \cdot 10^{-5}$	$1.6 \cdot 10^{-4}$			
VA	$2.7 \cdot 10^{-4}$	$4.7 \cdot 10^{-4}$	$3.7 \cdot 10^{-3}$			
			Scheme 3			
HeH^+				$8.5 \cdot 10^{-6}$	$8.0 \cdot 10^{-7}$	0.0
BH				$9.0 \cdot 10^{-6}$	$8.9 \cdot 10^{-6}$	0.0
CH_4	as for scheme 1			$9.7 \cdot 10^{-6}$	$9.7 \cdot 10^{-6}$	$9.6 \cdot 10^{-6}$
H_2O				$9.9 \cdot 10^{-6}$	$8.3 \cdot 10^{-6}$	$9.5 \cdot 10^{-6}$
VA				$9.5 \cdot 10^{-6}$	$9.6 \cdot 10^{-6}$	$9.9 \cdot 10^{-6}$

As already seen in fig. 5.2 for the NMR integrals, the Cholesky threshold does no longer provide an upper bound for the magnetizability integrals computed with scheme 1 and 2, for the same reason as mentioned in section 5.1.1. As shown in table 5.14, the errors for the type A integrals do not consistently decrease when the magnetic-field dependence of the Cholesky basis in included, as done in scheme 2. In fact, the errors are slightly smaller for scheme 2, but this can only be seen when the standard deviation $s(\text{int})$

$$s(\text{int}) = \sqrt{\sum_{\text{all integrals}} (I - I_{\text{CD}})^2}, \tag{5.6}$$

is considered. Here, I represents the magnetizability integrals and I_{CD} the reconstructed magnetizability integrals. As an example, the standard deviation of the reconstructed type A integrals from the standard magnetizability integrals is shown in fig. 5.19 for vinyl alcohol.

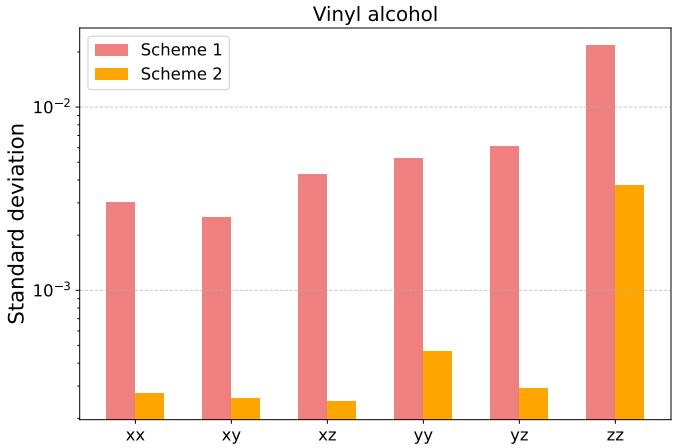

Figure 5.19: Standard deviation of the reconstructed magnetizability integrals (type A) relative to the standard integrals for vinyl alcohol.

As expected, the standard deviation is always smaller for scheme 2, but the differences are rather marginal. An explanation for this is that many of the Cholesky basis functions are independent of the magnetic field since the phase factor vanishes if the basis functions χ_μ and χ_ν are located at the same center, as seen in eq. (3.9). In case of the type B integrals, remarkable improvements in the accuracy are observed when comparing schemes 1 (or scheme 2) with scheme 3. Actually, the errors are all below the Cholesky threshold (10^{-5}) since the Cholesky threshold again is an upper bound for the error. This is because the Cauchy-Schwarz estimation is performed based on the perturbed diagonal elements $\left(\frac{\partial\nu\mu}{\partial B_k}\middle|\frac{\partial\mu\nu}{\partial B_k}\right)$. For the sake of completeness, the values for all components of the magnetizability tensor ξ_{ij} and the isotropic magnetizability ξ_{iso}

$$\xi_{\text{iso}} = \frac{1}{3}\text{Tr}(\boldsymbol{\xi}) \tag{5.7}$$

can be found in table 5.15, where the tensor is structured as

$$\begin{pmatrix} xx & xy & xz \\ yx & yy & yz \\ zx & zy & zz \end{pmatrix}. \tag{5.8}$$

The values are all the same for the three schemes within the reported digits (and also the same results were obtained by computing the magnetizability tensor without using CD). Negative values for the magnetizability mean that the system is diamagnetic while paramagnetic molecules exhibit a positive magnetizability, which is the case for the BH molecule only. So far, the error of the reconstructed magnetizability integrals has only been analyzed using one Cholesky threshold, but it is also interesting to investigate how the error changes with the threshold. Calculations for $\tau = 4, 5, 6, 7, 8, 9$ have been carried out for vinyl alcohol using Dunning's cc-pVDZ basis set. The maximum errors in the reconstructed type A and B integrals are plotted as a function of the threshold in fig. 5.20 for the three schemes.

Table 5.15: Magnetizability tensor ξ_{ij}, $i,j = x,y,z$ and isotropic magnetizability ξ_{iso} (in a.u.) computed with all three schemes (cc-pVTZ basis, CD threshold 10^{-5}) for HeH^+, BH, CH_4, H_2O, and vinyl alcohol.

Molecule	ξ_{ij}	ξ_{iso}
HeH^+	$\begin{pmatrix} -0.412 & 0.000 & 0.000 \\ 0.000 & -0.412 & 0.000 \\ 0.000 & 0.000 & -0.354 \end{pmatrix}$	-0.939
BH	$\begin{pmatrix} 7.912 & 0.000 & 0.000 \\ 0.000 & 7.912 & 0.000 \\ 0.000 & 0.000 & -2.402 \end{pmatrix}$	4.474
CH_4	$\begin{pmatrix} -3.816 & 0.000 & 0.000 \\ 0.000 & -3.816 & 0.000 \\ 0.000 & 0.000 & -3.816 \end{pmatrix}$	-3.816
H_2O	$\begin{pmatrix} -2.937 & 0.000 & 0.000 \\ 0.000 & -2.843 & 0.000 \\ 0.000 & 0.000 & -2.905 \end{pmatrix}$	-2.895
Vinyl alcohol	$\begin{pmatrix} -6.248 & -0.057 & 0.000 \\ -0.057 & -5.148 & 0.000 \\ 0.000 & 0.000 & -6.676 \end{pmatrix}$	-6.024

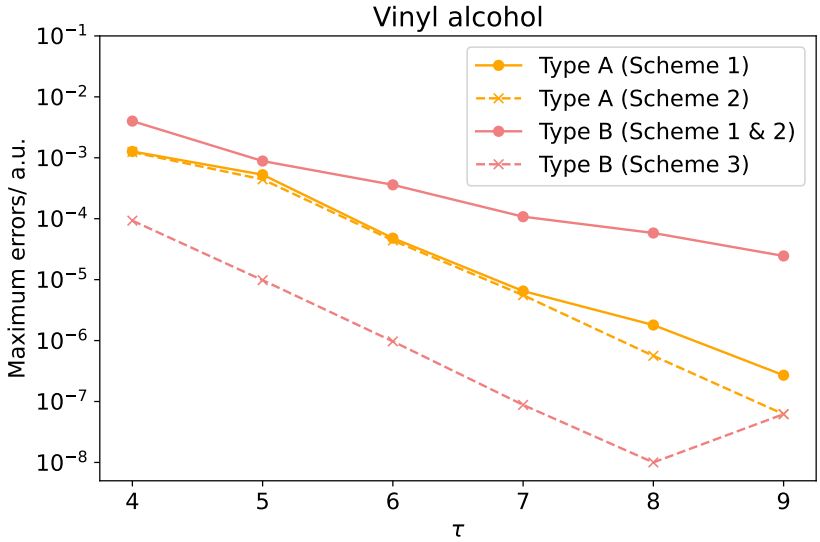

Figure 5.20: Maximum absolute errors of the reconstructed type A and B integrals computed with different Cholesky thresholds $10^{-\tau}$ using the cc-pVDZ basis set.

Concerning the reconstructed type A integrals, the errors obtained with scheme 1 are basically the same as for scheme 2 when using loose thresholds, while scheme 2 only performs better for tight thresholds. As mentioned previously, some Cholesky basis functions are independent of the magnetic field if the AO pairs are located at the same center. In fact, the number of these AO pairs is higher for loose Cholesky thresholds than for tight thresholds, as visualized in fig. 5.21. This means that the effect of including the magnetic field dependence of the Cholesky basis functions is relevant for tight thresholds like 10^{-8} and 10^{-9}, where only about one third of all CVs arise from AO pairs located at the same center, while for thresholds like 10^{-4}, about two thirds of all vectors are independent of the magnetic field.

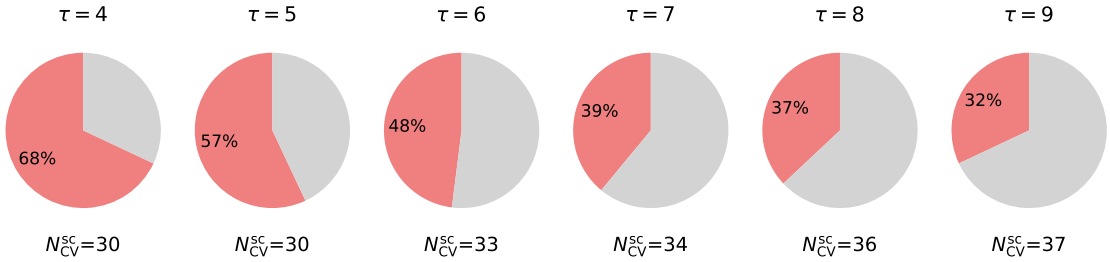

Figure 5.21: Percentage and number of CVs $N_{\mathrm{CV}}^{\mathrm{sc}}$ that are assigned to a $|\mu\nu)$-pair located at the same center for different Cholesky thresholds (vinyl alcohol, cc-pVDZ).

Nevertheless, the error of the type A integrals becomes increasingly smaller when the Cholesky threshold approaches zero which is in line with the theory discussed in section 3.4 (see eq. (3.35)). However, this is not the case for the error of the type B integrals computed with scheme 1 and 2 since here, the error never seems to drop below 10^{-4}. This confirms the assumption from section 3.4 that the use of finite basis sets leads to an error in the integrals. Using scheme 3, it is possible to tackle this problem, and it can be seen that the errors for the type B integrals are below the Cholesky threshold (except for the error at $\tau = 9$ which is most likely due to numerical instabilities in the partial pivoting procedure).

Now the question is whether the error in the type B integrals for scheme 1 and 2 have any noticeable effect on the magnetizability tensor at all. As already indicated in table 5.15, the remaining error in the integrals has almost no impact on the computed magnetizability tensor and in terms of computing time and memory requirements, scheme 1 is the preferred scheme, since no additional CD for the cross terms is required (as in scheme 3) and compared to scheme 2, it is also not necessary to compute the right-hand side partial derivatives. Thus, it can be concluded that scheme 1 is the most efficient procedure for routinely computing magnetizabilities. The errors in the magnetizability integrals using scheme 1 can now be considered in relation to the unperturbed and the NMR integrals, as visualized in fig. 5.22. It can be seen that the Cholesky threshold only provides an upper bound to the unperturbed two-electron integrals. However, since the errors of the perturbed reconstructed integrals become smaller with a tighter threshold, it is still possible to correlate the accuracy of the reconstructed NMR and magnetizability integrals with the Cholesky threshold.

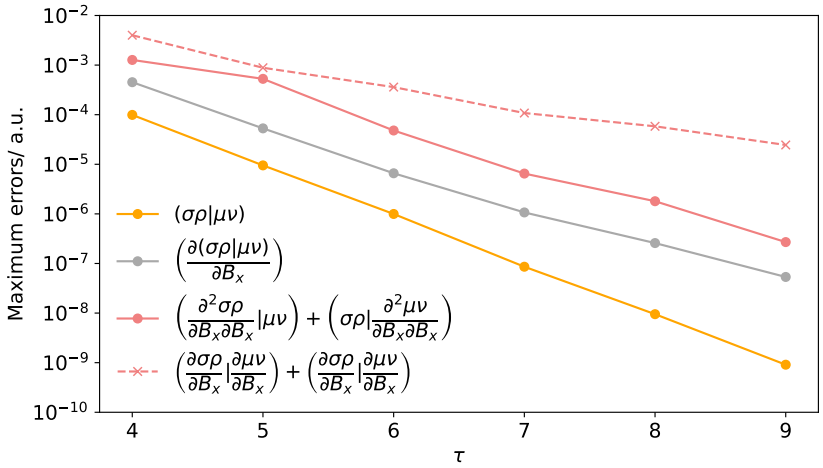

Figure 5.22: Maximum absolute errors in the reconstructed unperturbed, NMR and magnetizability integrals (for the latter, type A and B are considered separately) computed for vinyl alcohol with different Cholesky thresholds $10^{-\tau}$ and the cc-pVDZ basis set.

5.4.2 Representative Calculations

Using the HF-CD-GIAO scheme, it is possible to compute magnetizabilities for large systems like coronene, hexabenzocoronene, and C_{60} (the structures of the molecule have been shown in fig. 5.6). For all calculations, a Cholesky threshold of 10^{-6} or 10^{-5} and the tz2p or tzp basis have been used, involving up to 1170 basis functions (see table 5.2). To check the performance of the three schemes for larger systems, the calculation for coronene has been performed utilizing all schemes. These results are analyzed with respect to computational efficiency; the number of Cholesky vectors, the timings for the CD and the whole calculation are shown in fig. 5.23.* In table 5.16, the non-vanishing components of the magnetizability tensor as well as the isotropic magnetizability are reported.

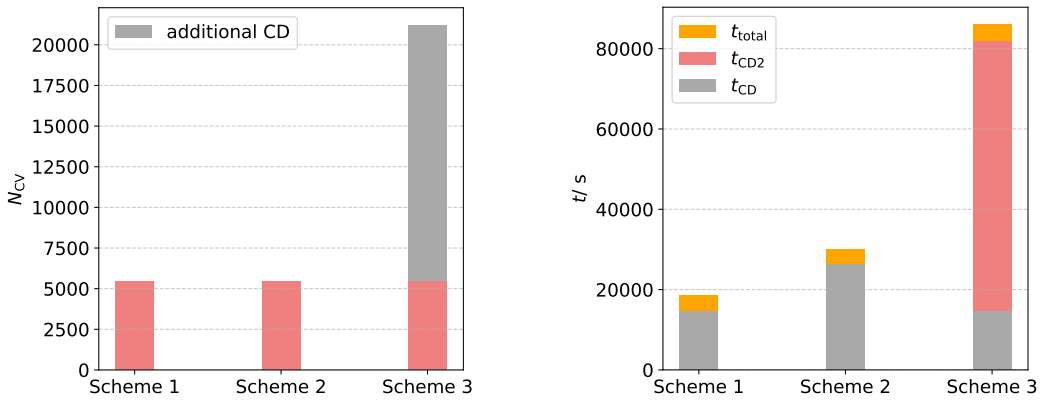

Figure 5.23: Number of CVs N_{CV}, total timings t_{total} and timings needed to carry out the CD t_{CD} for coronene using CD-GIAO-HF/10^{-6}/tz2p. In the case of scheme 3, the number of CVs and the timings for the CD of the type B integrals (t_{CD2}) are given separately.

* All calculations for coronene have been performed using 8 CPUs and a Intel(R) Xeon(R) CPU E5-2643 v3 @ 3.40 GHz.

Table 5.16: Values for the non-vanishing components of the magnetizability tensor ξ_{ij} and isotropic magnetizability ξ_{iso} (in a.u.) for coronene computed using CD-GIAO-HF/10^{-6}/tz2p and all three schemes.

Scheme	ξ_{xx}	ξ_{yy}	ξ_{zz}	ξ_{iso}
1	-25.083	-25.088	-130.301	-60.157
2	-25.083	-25.088	-130.301	-60.157
3	-25.082	-25.087	-130.300	-60.157

Scheme 3 becomes rather inefficient for larger systems due to the additional CD for the cross terms, and the effects on the magnetizability tensor are negligible. Also, scheme 2 requires more times compared to scheme 1, although there is no difference in the values for the magnetizability. These results again suggest that scheme 1 is the favored scheme for computing the magnetizability since it provides the lowest computational effort with no significance difference in the accuracy in comparison with the other two schemes. This is why the calculations on HBC and C_{60} have been performed using only scheme 1. The values for the non-vanishing magnetizability tensor and the isotropic magnetizability are shown in table 5.17.*

Table 5.17: Values for the non-vanishing components of the magnetizability tensor ξ_{ij} and isotropic magnetizability ξ_{iso} (in a.u.) for HBC and C_{60} computed using CD-GIAO-HF/10^{-6}/tz2p in the case of HBC and CD-GIAO-HF/10^{-5}/tzp in the case of C_{60}.

Molecule	ξ_{xx}	ξ_{yy}	ξ_{zz}	ξ_{iso}
HBC	-41.662	-41.662	-182.434	-88.586
C_{60}	-66.423	-66.422	-66.423	-66.423

Concerning the computational effort, the calculation for HBC required one day 19 hours and 29 minutes and 517 GB memory. Prior to this work, calculating magnetizabilities of HBC and C_{60} at HF level of theory were infeasible due to memory and time constraints. These limitations were overcome by applying CD to the unperturbed, NMR, and magnetizability integrals, making theoretical magnetizabilities accessible even for large systems. Although those are only HF results, the computation of the magnetizability tensor for systems with more than 1000 basis functions becomes quite demanding. Computing magnetizabilities is more elaborate than computing NMR shieldings since more terms need to be computed as discussed in sections 2.3.7 and 2.3.8 and concerning the CD of the integrals, three types of CVs (unperturbed, NMR and magnetizability CVs) are necessary.

What is striking about the results in tables 5.16 and 5.17 is the anisotropy of the magnetizability for coronene and HBC, i.e. that one of the three values for the magnetizability tensor (in both cases the values for ξ_{zz}) is completely different in comparison with the others. In fact, this is the value for the direction perpendicular to the molecular plane (as seen below in fig. 5.25). In section 2.3.2 it has been mentioned that aromatic molecules exhibit a negative net magnetic susceptibility (and according to eq. (2.60) this also holds for the isotropic magnetizability). To

* The calculations for HBC have been performed using 8 CPUs and an Intel(R) Xeon(R) CPU E5-2643 v3 @ 3.40 GHz.

confirm the aromaticity of coronene and to quantify its aromaticity, both the CD-GIAO-MP2 and the CD-GIAO-HF scheme for computing NMR shieldings and magnetizabilities are used.

5.5 Calculations of Ring-Current Densities and Ring-Current Strengths using Cholesky Decomposition

5.5.1 Coronene

Coronene is an interesting system to be analyzed with respect to the magnetically induced ring-current density and the ring-current strength since it has a relatively complicated structure with connected rings and the current pathways are not obvious. It has been proposed that coronene is an aromatic system which has a weakly paratropic ring current around the inner benzene ring and a significant diatropic ring-current flow along the perimeter.[311,312] These finding have been confirmed by Fliegl *et al.* in Ref. [152]; they performed DFT calculations using the BP86 functional.[313–315] Using our CD-based scheme, it is now possible to perform MP2 calculations for this molecule, where in this case, a Cholesky threshold of 10^{-5} and the dzp basis has been used for the computations. In fig. 5.24, the ring-current density is plotted for the planes above and below the molecule in which the current is nonzero, viewed from a top-down perspective.

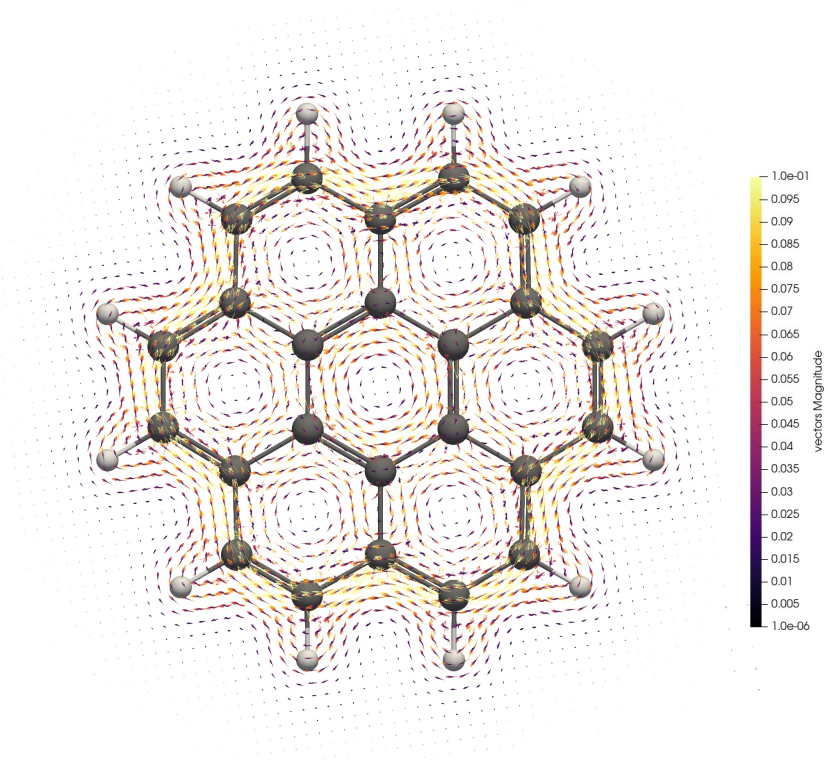

Figure 5.24: Induced current density for coronene at the CD-GIAO-MP2/dzp level for a magnetic field applied perpendicular to the molecular plane.

Based on fig. 5.24, information about the main current pathways can be obtained. There is a significant current in the inner ring and another one along the perimeter. This is in accordance with Hückel's $(4n+2)\pi$ rule since the inner benzene ring has six π-electrons while the outer path involves 18 π-electrons. However, those are just qualitative plots and no rigorous statement

about aromaticity can be made so far. To quantify aromaticity, the ring-current strength has also been calculated for both current pathways, where two different integration planes were chosen, as shown in fig. 5.25. Integration plane A covers the current along the outer edges of the molecule and is placed through the carbon atoms with the indices 14 and 17 while integration plane B crosses the bond between the carbon atoms 1 and 3 in the inner ring.

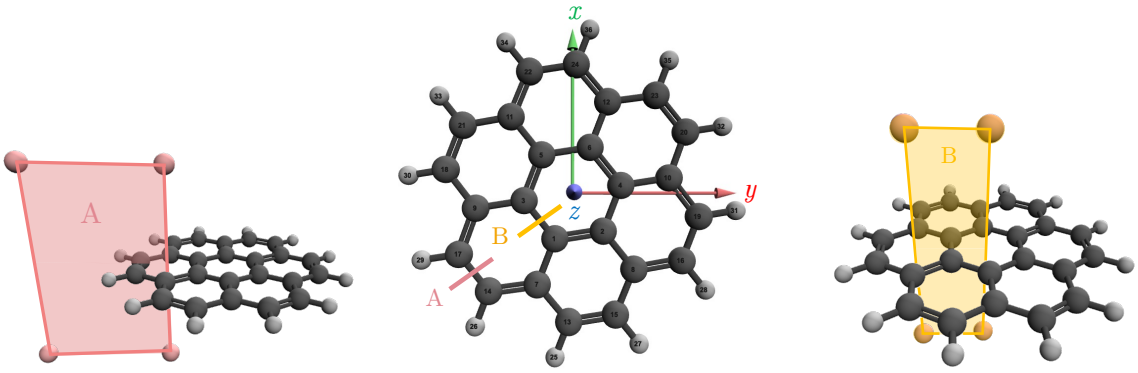

(a) (b) (c)

Figure 5.25: (a), (c) Illustration of the integration planes across a specific bond perpendicular to the molecular plane for coronene and (b) x, y, and z axis and chosen bonds for the integration plane A and B.

Table 5.18: Paratropic $J^{\mathbf{B}}_{\text{para}}$, diatropic $J^{\mathbf{B}}_{\text{dia}}$, and total ring-current strength $J^{\mathbf{B}}_{\text{total}}$ (in nA/T) for the two integration planes A and B (see fig. 5.25) in coronene. The magnetic field has been applied perpendicular to the molecular plane (z-direction).

Integration plane	$J^{\mathbf{B}}_{\text{para}}$	$J^{\mathbf{B}}_{\text{dia}}$	$J^{\mathbf{B}}_{\text{total}}$
A	-4.16	21.31	17.15
B	-11.47	5.81	-5.66

The total ring-current strength $J^{\mathbf{B}}_{\text{total}}$ is given by the sum of the para- and diatropic contributions

$$J^{\mathbf{B}}_{\text{total}} = J^{\mathbf{B}}_{\text{para}} + J^{\mathbf{B}}_{\text{dia}}, \tag{5.9}$$

and is reported in table 5.18 for both integration planes. The inner ring sustains a net current strength of $-5.66\,\text{nA/T}$: the paratropic contribution is $-11.47\,\text{nA/T}$ but the paratropic ring current of $-5.66\,\text{nA/T}$ in the outer benzene rings cancels about half of it, as indicated in fig. 5.26. This result is in good agreement with the DFT results from Ref. [152]; they determined a paratropic ring strength of $-10\,\text{nA/T}$ and a net current strength of $-5\,\text{nA/T}$. The strengths of the diatropic current along the outer edge is $21.31\,\text{nA/T}$, which differs from the result in Ref. [152] by about $3\,\text{nA/T}$ (they obtained a diatropic ring current of $18\,\text{nA/T}$). In Ref. [96], Jusélius *et al.* carried out DFT-BP86 and MP2 calculations on benzene, and it can be seen that also in this case, the ring-current strength computed with DFT is lower than the value yielded with MP2. For the CD-GIAO-MP2 calculation presented here, the rather small dzp basis set has been used and using a larger basis set like tz2p would probably provide improved results.[38]

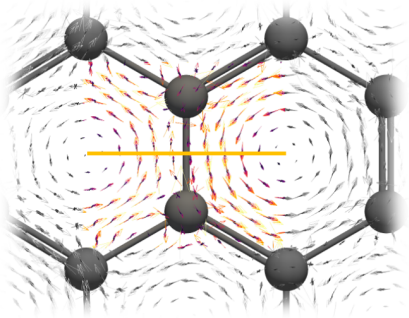

Figure 5.26: Close-up view of the central ring, containing integration plane B.

5.5.2 Annulene Derivatives

Further systems that are interesting to analyze with respect to their aromaticity are bridged annulenes like 1,6-methano-[10]annulene, 1,6-imino-[10]annulene, and 1,6-oxido-[10]annulene. Pictures of their molecule structures can be found in fig. 5.27.

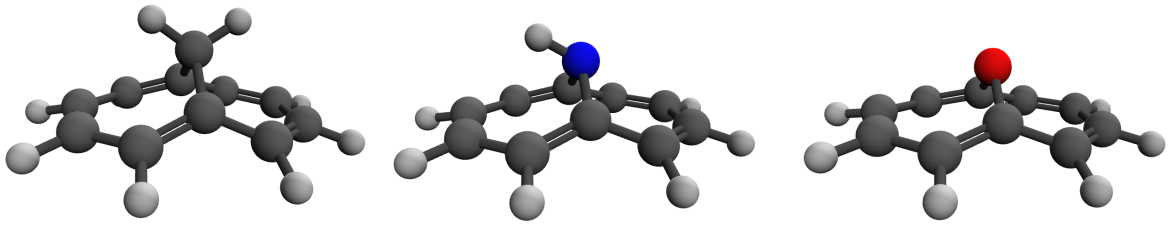

Figure 5.27: Molecular structures of 1,6-methano-[10]annulene, 1,6-imino-[10]annulene, and 1,6-oxido-[10]annulene.

As E. Vogel wrote in Ref. [316], 1,6-methano-[10]annulene is a suitable compound for examining Hückel's rule for the case of a neutral 10 π-electron system since there is no unusual deformation of the bond angles. He was investigating whether there are two tautomers with five localized bonds or whether mesomerism is present. Based on experimental results like NMR spectra, he attributed an aromatic character to this annulene.[316] The delocalized structure was also proposed later by L. Farnell and L. Radom in Ref. [317], who used HF calculations to investigate the structure of the molecule. In this context, it is also insightful to examine the impact of the bridging atom on the aromaticity, specifically how the bridging atom affects the ring current.
The results presented in the following were obtained in collaboration with M. Schneider as part of his bachelor thesis.[318] The geometry optimizations for these molecules (performed with Turbomole[279] using RI-MP2[276–278] and the cc-pVTZ basis set) as well as the NMR calculations (performed with Cfour using the tz2p* basis set and the CD-GIAO-MP2 scheme with a Cholesky threshold of 10^{-5} to generate the perturbed and unperturbed density matrices) carried out by M. Schneider were used to calculate the magnetically induced ring-current densities and ring-current strength of these systems. The optimized geometries can be found in the appendix in tables 7.20 to 7.22.
First, the computed NMR shifts for 1,6-methano-[10]annulene have been compared to the experimental results obtained by E. Vogel in Ref. [316]. To do this, the NMR shielding constants

* 5s2p/3s2p for H, 9s5p2d/5s3p2d for C, N, O

of tetramethylsilane (TMS) have been calculated, performing first a geometry optimization at the same level of theory as for 1,6-methano-[10]annulene (the geometry is given in the appendix in table 7.18) and a NMR shielding calculation using CD-GIAO-MP2/$\tau = 10^{-5}$/tz2p. The NMR shielding constants of 1,6-methano-[10]annulene have also been computed at CD-GIAO-MP2/$\tau = 10^{-5}$/tz2p level and via eq. (2.54), the NMR shifts in table 5.19 have been obtained. In table 5.20, the shieldings and shifts for the carbon atoms can be found.

Table 5.19: Computed NMR shielding constants σ(H) and shifts δ(H) for TMS and 1,6-methano-[10]annulene obtained at the CD-GIAO-MP2/$\tau = 10^{-5}$/tz2p level of theory. Experimental NMR shifts δ_{exp}(H) were taken from Ref. [316]. The shifts for the molecule can be assigned using the colors/indices in fig. 5.28.

Molecule	Indices	σ(H)	δ(H)	δ_{exp}(H)
1,6-methano-[10]annulene	12,13,15,16	24.21	7.75	6.80
	14,17,18,21	23.95	8.01	7.50
	19, 20	33.00	-1.04	-0.50
TMS		31.96	0.00	

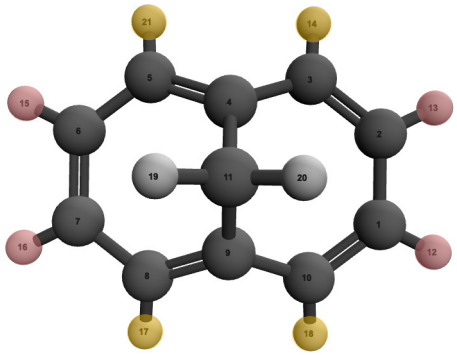

Figure 5.28: Color-coded/indexed atoms in 1,6-methano-[10]annulene; they can be assigned to the NMR data shown in tables 5.19 and 5.20.

Table 5.20: Computed NMR shielding constants σ(C) and shifts δ(C) for TMS and 1,6-methano-[10]annulene obtained at the CD-GIAO-MP2/$\tau = 10^{-5}$/tz2p level of theory. The shifts for the molecule can be assigned using the indices in fig. 5.28. Experimental NMR shifts δ_{exp}(C) were taken from *nmrshiftdb2*.[319]

Molecule	Indices	σ(C)	δ(C)	δ_{exp}(C)
1,6-methano-[10]annulene	1,2,7,6	69.61	129.62	126.10
	3,10,5,8	67.11	132.12	128.70
	4,9	79.46	119.77	114.60
	11	159.72	39.51	34.80
TMS		199.23	0.00	

The calculated NMR shifts are consistent with the expectations for an aromatic system: the outer protons appear downfield ($7.50 - 8.01$ ppm) since they are deshielded, which is in line with the theory explained in section 2.3.2. According to the theory, the protons inside and above

the ring system should be shielded by the induced magnetic field and that is exactly what is observed in the theoretical results, where the shifts of the protons at the bridging atom are upfield. The same can be observed for the carbon shifts. A comparison between theoretical and experimental results reveals that the shifts are in good agreement with experiment, with differences in the range of 0.51-0.95 ppm for the hydrogen atoms and 3.42-5.17 ppm for the carbon atoms. The deviations might be explained by the fact that MP2 overestimates the correlation contribution[25,38,40] which can lead to an overestimation of the ring-current strengths. This in turn causes a more pronounced than expected upfield shift for the inner protons, and a more pronounced downfield shift for the hydrogen/carbon atoms along the perimeter. The shieldings and shifts for 1,6-imino-[10]annulene and 1,6-oxido-[10]annulene have also been determined and can be found in table 7.23 in the appendix. However, for both molecules, the literature[320] reports only the center of a broad signal for the outer protons, which is why comparison with experimental data is challenging. It can be noted that the calculated shifts lie in a range comparable to the measured ones.

Next, the magnetically induced ring-current densities have been computed for all three molecules, and the corresponding vector plots are visualized in fig. 5.29.

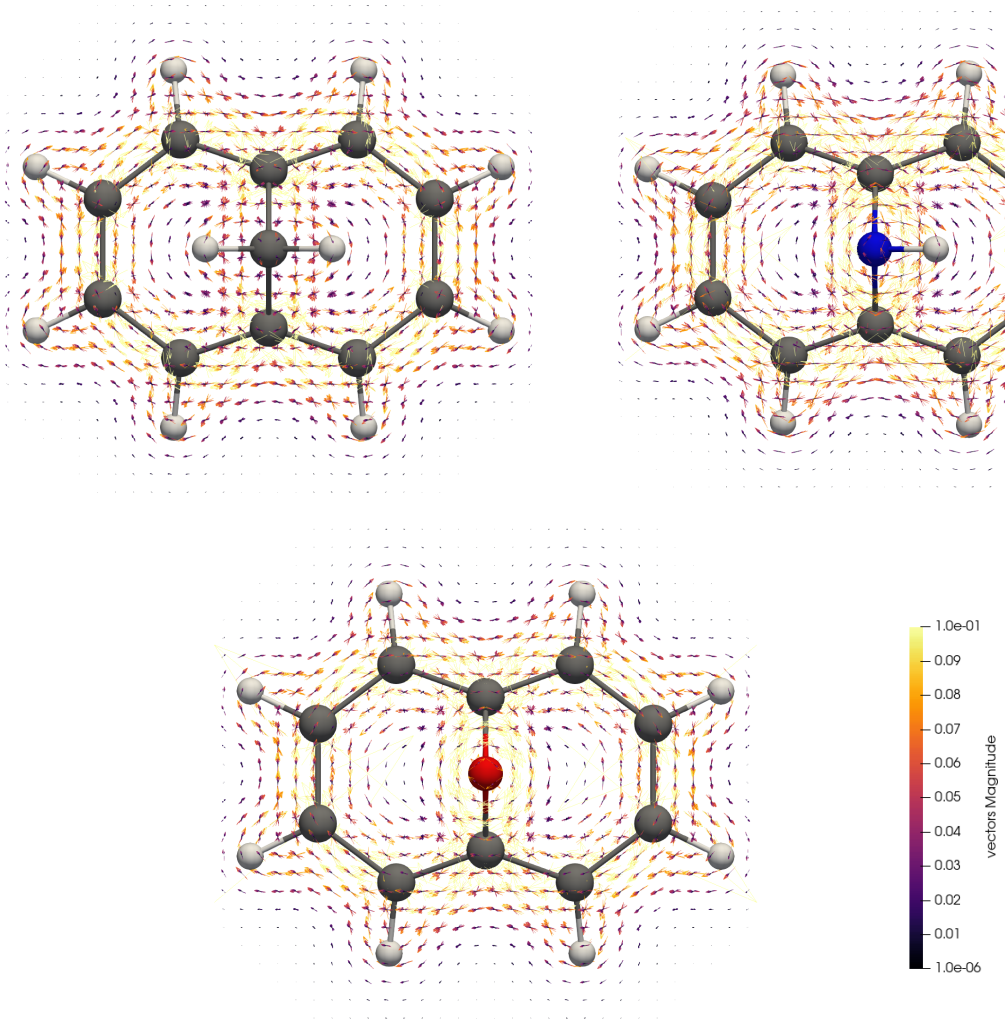

Figure 5.29: Ring current density plots for 1,6-methano-[10]annulene, 1,6-imino-[10]annulene, and 1,6-oxido-[10]annulene (**B** points out of the plane in the reader's direction). The ring-current density is plotted for the planes above and below the molecule in which the current is nonzero.

For this purpose, an external magnetic field is applied perpendicular to the „approximate molecular plane“, i.e. the plane obtained by conceptually flattening the bent structure into a single plane. In accordance with the theory in section 2.3.2, a paratropic ring current that flows anticlockwise with respect to the external magnetic field is observed inside the ring, while the diatropic ring current flows clockwise with respect to $\mathbf{B}_{\text{ext}}$ outside the ring system. At and between the atoms, the ring current is strongest since the delocalization of the electrons mainly occurs in the π-electron cloud. It can also be seen that a current circulates around the bridging atoms which appears stronger in 1,6-imino-[10]annulene and 1,6-oxido-[10]annulene compared to 1,6-methano-[10]annulene.

To extract information about the aromaticity via the ring-current strength, the integration plane was positioned in such a way as to minimize the bias introduced by the current flow around the bridge. As an example, the chosen integration plane is shown for 1,6-methano[10]annulene in fig. 5.30 (a). The calculated ring current is multiplied by a factor of two because the integration plane covers only half of the density, as the integration plane is halved. The results can be found in table 5.21 for the three bridged annulenes. Through a current profile analysis, the results in table 5.21 can also be visualized as shown in fig. 5.31. Such a current profile analysis is performed by a stepwise scan over the whole integration plane, where in this case steps of $\Delta x = 0.02\,\text{bohr}$ were chosen. The current profile analysis is visualized in fig. 5.30 (b).

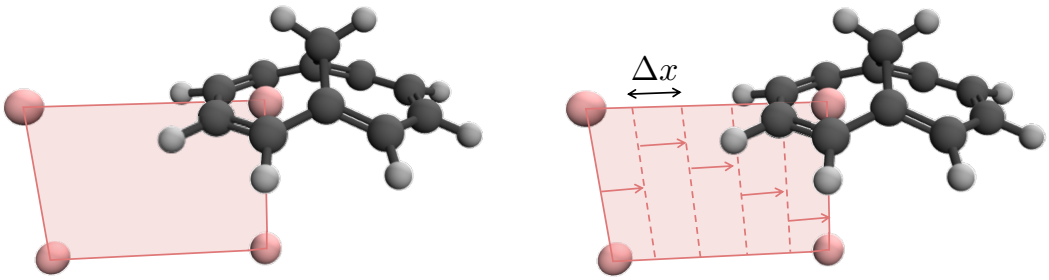

(a) (b)

Figure 5.30: (a) Schematic illustration of the integration plane across two bonds in 1,6-methano-[10]annulene and (b) illustration of the stepwise scan over the integration plane.

Table 5.21: Paratropic $J^{\mathbf{B}}_{\text{para}}$, diatropic $J^{\mathbf{B}}_{\text{dia}}$, and total ring-current strength $J^{\mathbf{B}}_{\text{total}}$ (in nA/T) of 1,6-methano-[10]annulene, 1,6-imino-[10]annulene, and 1,6-oxido-[10]annulene. The magnetic field is applied perpendicular to the approximate molecular plane.

Molecule	$J^{\mathbf{B}}_{\text{para}}$	$J^{\mathbf{B}}_{\text{dia}}$	$J^{\mathbf{B}}_{\text{total}}$
1,6-methano-[10]annulene	-2.31	21.42	19.11
1,6-imino-[10]annulene	-2.99	21.65	18.66
1,6-oxido-[10]annulene	-2.73	23.00	20.26

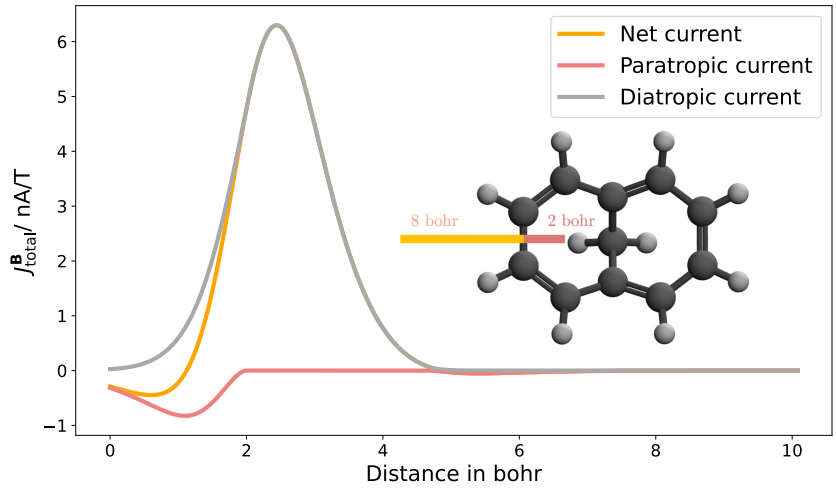

Figure 5.31: Current profile analysis for 1,6-methano-[10]annulene using the integration plane illustrated in fig. 5.30.

The results from table 5.21 and fig. 5.31 show that the paratropic contributions for all molecules are small in magnitude compared to the diatropic current, and a positive diatropic net current is observed. Based on fig. 5.31, it can also be seen that the paratropic ring current occurs only inside the ring and vanishes outside the ring. The diatropic ring current, however, is already present inside the ring and reaches its maximum approximately between the two carbon atoms. This makes sense since the ring current is induced in the π-electron cloud, as already mentioned.[96] The computed values for the ring-current strength confirm E. Vogels statement that 1,6-methano-[10]annulene is aromatic[316] and also that 1,6-imino-[10]annulene and 1,6-oxido-[10]annulene are aromatic systems. These findings are further supported by the calculated magnetizabilities at the CD-GIAO-HF/tz2p level of theory, as reported in table 5.22. All molecules show an anisotropic magnetizability, i.e. a large diamagnetic susceptibility only in the direction of the applied magnetic field. Furthermore, the values for the isotropic magnetizability are negative, which confirms the aromaticity of these systems. Based on the presented ring-current strengths in table 5.21, which are different for all three annulene derivatives, it is obvious that the bridging atoms have an impact on the aromaticity. According to the presented results, 1,6-oxido-[10]annulene exhibits the strongest net ring current (20.26 nA/T) when compared to 1,6-methano-[10]annulene (19.11 nA/T) and 1,6-imino-[10]annulene (18.66 nA/T). It can be argued that the two lone-pairs on the oxygen atom might interact with the π-system in a way that enhances delocalization. As mentioned in section 2.3.2, aromaticity is favored by planarity and among the molecules studied, 1,6-oxido-[10]annulene is the most planar, as depicted in fig. 5.32. The difference in the ring-current strength between 1,6-imino-[10]annulene and 1,6-methano-[10]annulene is only about 0.45 nA/T and can be regarded as negligible.

Concerning the magnetic susceptibility in table 5.22, a different order is obtained with respect to aromaticity, if it is assumed that a more negative value for the magnetizability indicates the strongest ring current. In this case, only the component perpendicular to the approximate molecular plane is relevant. 1,6-imino-[10]annulene and 1,6-oxido-[10]annulene approximately have the same values while the value for 1,6-methano-[10]annulene is slightly reduced. However, those are just HF results and more accurate post-HF methods like MP2 or CCSD(T) would provide better values and maybe a different order. Also, it is not clear if the magnetizability is a reliable tool

to measure aromaticity; it rather indicates whether molecules are aromatic or not. M. Schneider investigated also the heavier homologues of the molecules studied here, with silicon, phosphor, and sulfur as bridging atoms, and found out that the same trend is observed as in the preceding period.[318]

Table 5.22: Magnetizability tensor ξ_{ij}, $i, j = x, y, z$ and isotropic magnetizability ξ_{iso} (in a.u.) computed at the CD-GIAO-HF/$\tau = 10^{-5}$/tz2p level for 1,6-methano-[10]annulene, 1,6-imino-[10]annulene, and 1,6-oxido-[10]annulene, applying a magnetic field perpendicular to the approximate molecular plane (z-direction).

Molecule	ξ_{ij}	ξ_{iso}
1,6-methano-[10]annulene	$\begin{pmatrix} -17.827 & 0.000 & 0.000 \\ 0.000 & -16.621 & 0.000 \\ 0.000 & 0.000 & -45.721 \end{pmatrix}$	-26.723
1,6-imino-[10]annulene	$\begin{pmatrix} -15.850 & 0.000 & 0.000 \\ 0.000 & -16.798 & -0.177 \\ 0.000 & -0.177 & -46.256 \end{pmatrix}$	-26.302
1,6-oxido-[10]annulene	$\begin{pmatrix} -16.090 & 0.000 & 0.000 \\ 0.000 & -14.918 & 0.000 \\ 0.000 & 0.000 & -46.229 \end{pmatrix}$	-25.746

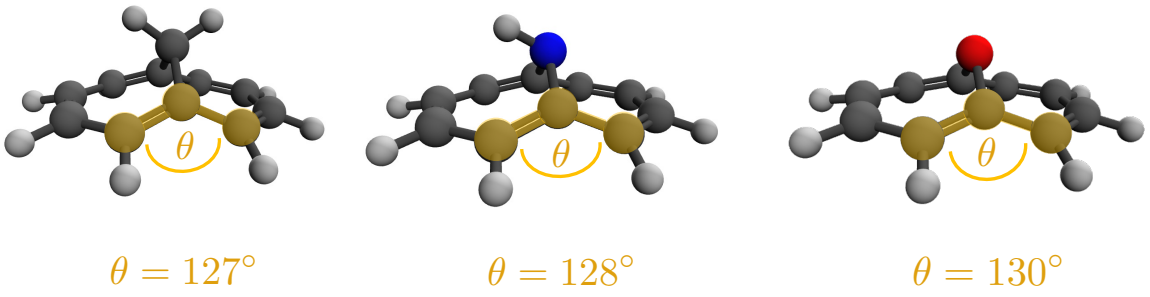

Figure 5.32: Angle specifications to estimate the planarity of 1,6-methano-[10]annulene, 1,6-imino-[10]annulene, and 1,6-oxido-[10]annulene.

The results presented in this section demonstrated that aromaticity or large molecules can be quantified by using the CD-GIAO-MP2 scheme for computing the perturbed and unperturbed density matrices required to evaluate the magnetically induced current density and the ring-current strength. The obtained NMR shifts agree reasonably well with the experimental data, indicating sufficiently accurate NMR shielding constants and, consequently, accurate ring-current densities and ring-current strengths. The aromaticity of 1,6-methano-[10]annulene could be confirmed and the effect of the bridging atoms on the aromaticity has been investigated. For calculations like the ones reported here, it is important to incorporate electron correlation. Jusélius *et al.*[96] found that the influence of electron correlation changes the ring-current strengths by about 10% in the case of benzene. The CD-GIAO-MP2 scheme is therefore well suited for such

applications. The results presented in this section are consistent, but since MP2 has some disadvantages like overestimation of electron correlation,[25,38] a CD-GIAO-CC scheme is necessary to obtain more accurate results that are in better agreement with experiments.

6 Conclusion and Outlook

The interplay between experiment and theory is of major relevance for advancing the understanding of fundamental chemical phenomena. In particular, molecular properties form a bridge between theory and experiment, as they can be obtained both from quantum-chemical calculations and from measurements. One of the goals of theoretical chemistry is to provide results that are as accurate and reliable as possible. Achieving high accuracy in theoretical predictions, however, requires higher computational demands, and for larger molecules, which are usually of interest to experimentalists, the use of highly accurate quantum-chemical methods is often infeasible. One major bottleneck in quantum-chemical calculations is the storage and evaluation of the two-electron integrals, especially when molecular properties are computed, as this task mostly necessitates the additional calculation of perturbed, i.e. differentiated, two-electron integrals. The latter significantly increase the computational effort, since the number of perturbed integrals scales with the number of perturbations, and in many cases the full permutational symmetry can no longer be exploited. In calculations involving an external magnetic field as perturbation, the perturbed two-electron integrals arise due to the fact that GIAOs have been employed to ensure gauge-origin invariance of the results. The developments in this work mitigate the limitations associated with the two-electron integrals through the application of Cholesky decomposition to the unperturbed and perturbed two-electron integrals, where the latter are required to compute magnetic molecular properties. The CD of the two-electron integrals has two major advantages. First, the generated Cholesky vectors provide a compact representation of the two-electron integrals, which significantly reduces the memory requirements.[76,84,181] Second, the accuracy of the decomposition can be controlled via the Cholesky threshold, allowing for an estimate of the error. For these reasons, CD was chosen as a tool to improve computational efficiency in the calculation of NMR shieldings and magnetizabilities. Prior to this work, CD had neither been employed for magnetic properties nor for second derivative integrals in general.

This work introduced the CD-GIAO-MP2 scheme for computing NMR shieldings at the MP2 level of theory,[93,189] and the CD-GIAO-HF scheme for computing magnetizabilities at the HF level of theory.[94] For the former, magnetic two-electron integral derivatives (the so-called NMR integrals) are required, and, as already suggested in the context of nuclear gradients,[89,90] the equations for their CD can be obtained by differentiating the corresponding equations for the CD of the unperturbed two-electron integrals. This approach turns out to be equivalent to density fitting with the unperturbed Cholesky basis.[189] A comparison between the CD-GIAO-MP2 and the standard GIAO-MP2 scheme[38] revealed a remarkable speed-up in terms of computational timings without a significant loss of accuracy: For coronene with a dzp basis (420 basis functions), calculations carried out with both the standard scheme and the CD-based approach

showed that the latter is about a factor of 4.6 faster while reducing the memory requirements by about 97.6%. In this context, a Cholesky threshold of 10^{-5} proved to be a good compromise between accuracy and efficiency, as the errors are negligible for chemical applications (e.g., about 0.013 ppm for ^{13}C shieldings) and the computational timings remain reasonable. The applicability of this scheme has been demonstrated through large-scale computations of NMR shieldings on systems like hexabenzocoronene and buckminsterfullerene C_{60}, comprising up to about 1500 basis functions. Using a Cholesky threshold of 10^{-5}, only the largest computations required more than one day and about one terabyte of memory, while calculations on systems with around 800 basis functions needed less than seven hours and only around 100 GB memory. Such computations would not be feasible with the standard GIAO-MP2 scheme alone, highlighting the computational efficiency of the CD-GIAO-MP2 approach.

In addition, an improved CD procedure was implemented which exploits the permutational symmetry of the perturbed two-electron integrals. In comparison with the original CD scheme, this leads to a speed-up of about a factor of four in the NMR integral evaluation. However, in both the original and the improved scheme, the most time-consuming step is not the integral evaluation but the construction of the Cholesky vectors, and in particular their orthogonalization via a Gram-Schmidt like scheme. This bottleneck was overcome by the use of a two-step algorithm,[86] where in the first step the Cholesky basis is constructed and in the second step the CVs are evaluated. Due to the use of the two-step algorithm, the construction of the CVs is about a factor of nine to ten faster than in the original and the improved scheme. In the two-step scheme, the integrals need to be computed both for the selection of the Cholesky basis in the first step and the calculation of the CVs in the second step, which is why an overall speedup factor of 5 (rather than 9) in comparison to the original scheme is found. Since the unperturbed Cholesky basis is used for the CD of the NMR integrals, it is not necessary to calculate these integrals in the first step.

Furthermore, the CD-GIAO-MP2 scheme was embedded in a QM/MM framework, expanding the scope of the CD-based approach even further. In a QM/MM calculation, the molecular environment can be considered explicitly, thereby enabling the description of molecules in solution or in the liquid phase. The combination of the CD-GIAO-MP2 scheme with the QM/MM approach was applied to compute the NMR shifts of liquid water, where the accuracy was estimated by comparing the calculated gas-to-liquid shifts to experimental results. For this purpose, an MD simulation was performed, and a snapshot was extracted, representing the atomic coordinates at a given point along the trajectory. The NMR shieldings of the central water molecule were computed for one hundred water clusters from the snapshot and averaged to obtain statistically reliable results. Due to the use of the CD for the unperturbed and perturbed integrals, it is possible to increase the size of the QM region, which is of major importance to provide accurate results. It has been shown that at least 17 water molecules (first and second solvation shell) need to be incorporated in the QM region to obtain reliable nuclear shieldings, demonstrating that the use of CD is crucial for MP2 calculations on such large systems. In previous studies,[248–250,253,298,307] calculations of the gas-to-liquid shifts were limited to HF or DFT methods, as the inclusion of large QM regions is computationally demanding and could not be addressed with more accurate methods. A comparison between CD-GIAO-MP2 and DFT results[249] demonstrated that the results obtained with the former scheme are closer to experiment (in case of oxygen, the deviation is smaller by about 2.4 ppm), emphasizing the accuracy and the wide applicability of the

CD-GIAO-MP2 approach.
Concerning the CD-GIAO-HF scheme for computing magnetizabilities,[94] second derivatives of the two-electron integrals are required. In this case, it had not been obvious whether the CD expressions can also be derived via differentiation of the equations for the unperturbed integrals, in analogy to the procedure that had been employed for the NMR integrals. Three schemes were suggested where the first one exploits density fitting with the unperturbed Cholesky basis, the second takes the perturbed Cholesky basis functions into account, and the third one uses an additional CD for the cross terms of the second-derivative integrals. The reason for the latter is the fact that the error in the cross terms does not go to zero for tight Cholesky thresholds when using the first two schemes. Since the cross term integrals constitute a positive semidefinite matrix, they can be decomposed separately, which allows to represent them with arbitrary accuracy. Based on test calculations, however, the error in the cross terms was found to be negligible for the calculation of the magnetizability tensor. Considering that the first scheme involves the lowest computational effort, it is recommended for the routine computation of magnetizabilities. Using this scheme, magnetizabilities have been computed for large systems like C_{60} involving more than 1000 basis functions, which was previously infeasible due to time and memory constraints. Both the CD-GIAO-MP2 and CD-GIAO-HF schemes for computing NMR shieldings and magnetizabilities, respectively, were applied to investigate the aromaticity of coronene and several bridged annulene derivatives with different bridging atoms. For this purpose, the magnetically induced ring-current densities and ring-current strengths were computed to provide insight into current pathways and the total net current. A positive (diatropic) value of the latter indicates aromaticity. The expressions for the ring-current density and the ring-current strength are based on perturbed and unperturbed density matrices, which were obtained via CD-GIAO-MP2 NMR shielding calculations. The magnetizability tensor can also be used to estimate the aromaticity of molecules, which is why the CD-GIAO-HF scheme for computing magnetizabilities was employed here as well. The results confirmed the aromaticity of all systems and allowed the influence of the bridging atoms to be analyzed. Overall, these calculations further demonstrated the broad range of applications of the CD-GIAO schemes.

While this work has substantially advanced the accessibility of molecular property calculations for large systems, additional developments are possible to extend the applicability of the implemented schemes. Regarding the QM/MM CD-GIAO-MP2 procedure, the computational demands can be further decreased by an advantageous partitioning of the MM atoms into a short-range and a long-range region, as has been proposed by Laio *et al.*[221] In this ansatz, the QM/MM interactions are treated explicitly in the short-range region while a multipole expansion for the electric potential between MM atoms and QM electrons is used in the long-range region. Using this approach would hence significantly reduce the computational effort.[221,222]
The CD-GIAO-MP2 scheme is feasible for systems with about 1500 basis functions, but for calculations involving significantly more basis functions, additional strategies are required. In this case, local correlation schemes[47,75,321] are well suited, where the idea is to use spatially localized orbitals and to restrict the excitations from each orbital pair to local domains.[321] Gauss and Werner[321] showed that the error due to the local approximation is small, amounting to less than 1 ppm in the case of ^{13}C shieldings. The performance of the local MP2 scheme was illustrated by Loibl and Schütz,[47] who computed NMR shielding for systems with up to 2636 basis functions and 296 correlated electrons. The recently developed DLPNO-MP2 scheme[75] enables calcula-

tions involving even 4700 basis functions. Therefore, a combination of local treatments with the CD-based schemes would extend their scope even further. Exploitation of molecular point group symmetry would lead to additional reductions in computational costs.[68,322] Concerning the accuracy of NMR shieldings, MP2 is known to overshoot[42] and, in some cases, fails to provide accurate NMR shifts.[24,323] In this work, the examination of the NMR shifts of coronene revealed significant differences between the MP2 and the HF results. These findings indicate that extensions to more sophisticated approaches, such as coupled-cluster methods,[41,42,49] are inevitable to achieve highly accurate results.[25] There is already extensive literature on the CD approach within CC treatments,[77,78,90,322,324–326] but so far this has not been used in NMR shielding calculations. With regard to the CD-GIAO-HF scheme for computing magnetizabilities, post-HF methods are desirable. Accordingly, future work will focus on extending this scheme toward MP2 and CASSCF, drawing on the evaluated theory presented in this thesis and on existing implementations for the NMR shielding constants.[93,97] Moreover, further second derivatives, like the Hessian required for the calculation of vibrational frequencies, can be derived based on the CD-based approach for magnetizabilities.

The developments in this work enable efficient computations of molecular magnetic properties for large molecules, thereby reinforcing the interplay between theory and experiment. Referring back to the quotation from the introduction, in which Gauss and Stanton[49] remarked that „it would be desirable if the currently available methods were extended to treat larger molecules. On the other hand, there is a demand for more accurate treatment of correlation in the calculations of magnetic properties“, it can be concluded that the developments presented in this thesis mark an important milestone in achieving this vision. This work does not only demonstrate what is currently realizable, but also lays the foundation for even broader future applications.

List of Abbreviations

AO Atomic Orbital

ARCS Aromatic Ring-Current Shieldings

CASSCF Complete Active Space SCF

CB Cholesky Basis

CC Coupled-Cluster

CD Cholesky Decomposition

CP-CASSCF Coupled-Perturbed CASSCF

CPHF Coupled-Perturbed HF

CSF Configuration State Function

CV Cholesky Vector

DF Density Fitting

DFT Density Functional Theory

FCI Full Configuration Interaction

GIAO Gauge-Including Atomic Orbitals

HF Hartree-Fock

IGLO Individual Gauge for Localized Orbitals

LCAO Linear Combination of Atomic Orbitals

LORG Localized Orbital/Localized Origin

lr Long-range

MBPT2 Second-Order Many-Body Perturbation Theory

MCSCF Multi-Configurational SCF

MD Molecular Dynamics

MO Molecular Orbital

MP2 Second-Order Møller-Plesset

NICS Nucleus Independent Chemical Shift

NMR Nuclear Magnetic Resonance

occ Occupied

PBC Periodic Boundary Conditions

QM/MM Quantum Mechanics/Molecular Mechanics

RHF Restricted HF

RI Resolution-of-the-Identity

SCF Self-Consistent Field

SEM Standard Error of the Sample Mean

sr Short-range

virt Virtual

Bibliography

(1) Peltzer, R. M.; Gauss, J.; Eisenstein, O.; Cascella, M. *J. Am. Chem. Soc.* **2020**, *142*, 2984–2994.

(2) J. Gauss In *Modern Methods and Algorithms of Quantum Chemistry*, J. Grotendorst, Ed., 2nd ed.; NIC Series, Vol. 3; John von Neumann Institute for Computing: Jülich, 2000, pp 541–592.

(3) Gauss, J. *Bunsenges. Phys. Chem.* **1995**, *99*, 1001–1008.

(4) Kutzelnigg, W. *Angew. Chem. Int. Ed. Engl.* **1966**, *5*, 823–835.

(5) Hückel, E. *Z. Physik* **1931**, *70*, 204–286.

(6) Head-Gordon, M. *J. Phys. Chem.* **1996**, *100*, 13213–13225.

(7) Zerner, M. C. In *Reviews in Computational Chemistry*, Lipkowitz, K. B., Boyd, D. B., Eds., 1st ed.; Wiley: 1991; Vol. 2, pp 313–365.

(8) Jensen, F., *Introduction to Computational Chemistry*, 2nd ed.; J. Wiley & Sons: Chichester, England Hoboken, NJ, 2007.

(9) Löwdin, P.-O. *Int. J. Quantum Chem.* **1995**, *55*, 77–102.

(10) Møller, C.; Plesset, M. S. *Phys. Rev.* **1934**, *46*, 618–622.

(11) Coester, F.; Kümmel, H. *Nucl. Phys.* **1960**, *17*, 477–485.

(12) Čížek, J. *J. Chem. Phys.* **1966**, *45*, 4256–4266.

(13) Roos, B. O. In *Methods in Computational Molecular Physics*, Diercksen, G. H. F., Wilson, S., Eds.; Springer Netherlands: Dordrecht, 1983, pp 161–187.

(14) Dalgaard, E.; Jørgensen, P. *J. Chem. Phys.* **1978**, *69*, 3833–3844.

(15) Werner, H.-J.; Meyer, W. *J. Chem. Phys.* **1981**, *74*, 5794–5801.

(16) Jensen, H. J. Aa.; Ågren, H. *Chem. Phys.* **1986**, *104*, 229–250.

(17) Werner, H.-J.; Meyer, W. *J. Chem. Phys.* **1980**, *73*, 2342–2356.

(18) Yeager, D. L.; Jørgensen, P. *Chem. Phys. Lett.* **1979**, *65*, 77–80.

(19) Atkins, P. W.; de Paula, J., *Physikalische Chemie*, Fünfte Auflage; Wiley-VCH: Weinheim, 2013.

(20) Gauss, J.; Schneider, U.; Ahlrichs, R.; Dohmeier, C.; Schnöckel, H. *J. Am. Chem. Soc.* **1993**, *115*, 2402–2408.

(21) Siehl, H.-U.; Müller, T.; Gauss, J.; Buzek, P.; Schleyer, P. v. R. *J. Am. Chem. Soc.* **1994**, *116*, 6384–6387.

(22) Bühl, M.; Gauss, J.; Hofmann, M.; Schleyer, P. v. R. *J. Am. Chem. Soc.* **1993**, *115*, 12385–12390.

(23) Klemp, C.; Bruns, M.; Gauss, J.; Häussermann, U.; Stösser, G.; van Wüllen, L.; Jansen, M.; Schnöckel, H. *J. Am. Chem. Soc.* **2001**, *123*, 9099–9106.

(24) Harding, M. E.; Gauss, J.; Schleyer, P. v. R. *J. Phys. Chem. A* **2011**, *115*, 2340–2344.
(25) Gauss, J.; Stanton, J. F. In *Advances in Chemical Physics*, Prigogine, I., Rice, S. A., Eds., 1st ed.; Wiley: 2002; Vol. 123, pp 355–422.
(26) Wolinski, K.; Hinton, J. F.; Pulay, P. *J. Am. Chem. Soc.* **1990**, *112*, 8251–8260.
(27) Ramsey, N. F. *Phys. Rev.* **1950**, *78*, 699–703.
(28) Ramsey, N. F. *Phys. Rev.* **1953**, *91*, 303–307.
(29) Ditchfield, R. *Chem. Phys. Lett.* **1976**, *40*, 53–56.
(30) London, F. *J. Phys. Radium* **1937**, *8*, 397–409.
(31) Hameka, H. *Mol. Phys.* **1958**, *1*, 203–215.
(32) Ditchfield, R. *Mol. Phys.* **1974**, *27*, 789–807.
(33) Kutzelnigg, W. *J. Mol. Struct. THEOCHEM* **1989**, *202*, 11–61.
(34) Kutzelnigg, W. *Isr. J. Chem.* **1980**, *19*, 193–200.
(35) Schindler, M.; Kutzelnigg, W. *J. Chem. Phys.* **1982**, *76*, 1919–1933.
(36) Pulay, P.; Hinton, J. F.; Wolinski, K. In *Nuclear Magnetic Shielding and Molecular Structure*, Tossell, J. A., Ed.; Kluwer Academic Publishers: 1993, p 243.
(37) Gauss, J. *Chem. Phys. Lett.* **1992**, *191*, 614–620.
(38) Gauss, J. *J. Chem. Phys.* **1993**, *99*, 3629–3643.
(39) Ruud, K.; Helgaker, T.; Kobayashi, R.; Jørgensen, P.; Bak, K. L.; Jensen, H. J. Aa. *J. Chem. Phys.* **1994**, *100*, 8178–8185.
(40) Gauss, J. *Chem. Phys. Lett.* **1994**, *229*, 198–203.
(41) Gauss, J.; Stanton, J. F. *J. Chem. Phys.* **1995**, *102*, 251–253.
(42) Gauss, J.; Stanton, J. F. *J. Chem. Phys.* **1996**, *104*, 2574–2583.
(43) Schreckenbach, G.; Ziegler, T. *J. Phys. Chem.* **1995**, *99*, 606–611.
(44) Skachkov, D.; Krykunov, M.; Kadantsev, E.; Ziegler, T. *J. Chem. Theory Comput.* **2010**, *6*, 1650–1659.
(45) Kussmann, J.; Ochsenfeld, C. *J. Chem. Phys.* **2007**, *127*, 054103.
(46) Stoychev, G. L.; Auer, A. A.; Izsák, R.; Neese, F. *J. Chem. Theory Comput.* **2018**, *14*, 619–637.
(47) Loibl, S.; Schütz, M. *J. Chem. Phys.* **2012**, *137*, 084107.
(48) Taubert, S.; Sundholm, D.; Jusélius, J. *J. Chem. Phys.* **2011**, *134*, 054123.
(49) Gauss, J.; Stanton, J. F. *J. Chem. Phys.* **1995**, *103*, 3561–3577.
(50) Sieber, S.; Schleyer, P. v. R.; Otto, A. H.; Gauss, J.; Reichel, F.; Cremer, D. *J. Phys. Org. Chem.* **1993**, *6*, 445–464.
(51) de Dios, A. C. *Prog. Nucl. Magn. Reson. Spectrosc.* **1996**, *29*, 229–278.
(52) Schleyer, P. v. R.; Gauss, J.; Bühl, M.; Greatrex, R.; Fox, M. A. *J. Chem. Soc., Chem. Commun.* **1993**, 1766–1768.
(53) Wolinski, K.; Hsu, C.-L.; Hinton, J. F.; Pulay, P. *J. Chem. Phys.* **1993**, *99*, 7819–7824.
(54) Xu, T.; Barich, D. H.; Torres, P. D.; Nicholas, J. B.; Haw, J. F. *J. Am. Chem. Soc.* **1997**, *119*, 396–405.
(55) Buzek, P.; Schleyer, P. v. R.; Vančik, H.; Mihalic, Z.; Gauss, J. *Angew. Chem.* **1994**, *106*, 470–473.
(56) Sulzbach, H. M.; Schleyer, P. v. R.; Schaefer, H. F. *J. Am. Chem. Soc.* **1994**, *116*, 3967–3972.
(57) Magyarfalvi, G.; Pulay, P. *Chem. Phys. Lett.* **1994**, *225*, 280–284.

(58) Steiner, D.; Balzereit, C.; Winkler, H.-J.; Stamatis, N.; Hofmann, M.; Schleyer, P. v. R.; Massa, W.; Berndt, A. *Angew. Chem.* **1994**, *106*, 2391–2394.
(59) Bühl, M.; Thiel, W.; Fleischer, U.; Kutzelnigg, W. *J. Phys. Chem.* **1995**, *99*, 4000–4007.
(60) Olah, G. A.; Burrichter, A.; Rasul, G.; Prakash, G. K. S.; Hachoumy, M. *J. Am. Chem. Soc.* **1997**, *119*, 12929–12933.
(61) Kollwitz, M.; Gauss, J. *Chem. Phys. Lett.* **1996**, *260*, 639–646.
(62) Almlöf, J.; Fægri, K.; Korsell, K. *J. Comput. Chem.* **1982**, *3*, 385–399.
(63) Haase, F.; Ahlrichs, R. *J. Comput. Chem.* **1993**, *14*, 907–912.
(64) Meier, U.; van Wüllen, C.; Schindler, M. *J. Comput. Chem.* **1992**, *13*, 551–559.
(65) Häser, M.; Ahlrichs, R.; Baron, H. P.; Weis, P.; Horn, H. *Theor. Chim. Acta* **1992**, *83*, 455–470.
(66) Cremer, D.; Gauss, J. *J. Comput. Chem.* **1986**, *7*, 274–282.
(67) Häser, M.; Ahlrichs, R. *J. Comput. Chem.* **1989**, *10*, 104–111.
(68) Kollwitz, M.; Häser, M.; Gauss, J. *J. Chem. Phys.* **1998**, *108*, 8295–8301.
(69) Vahtras, O.; Almlöf, J.; Feyereisen, M. *Chem. Phys. Lett.* **1993**, *213*, 514–518.
(70) Whitten, J. L. *J. Chem. Phys.* **1973**, *58*, 4496–4501.
(71) Feyereisen, M.; Fitzgerald, G.; Komornicki, A. *Chem. Phys. Lett.* **1993**, *208*, 359–363.
(72) Dunlap, B. I.; Connolly, J. W. D.; Sabin, J. R. *J. Chem. Phys.* **1979**, *71*, 3396–3402.
(73) Eichkorn, K.; Treutler, O.; Öhm, H.; Häser, M.; Ahlrichs, R. *Chem. Phys. Lett.* **1995**, *240*, 283–290.
(74) Maurer, M.; Ochsenfeld, C. *J. Chem. Phys.* **2013**, *138*, 174104.
(75) Stoychev, G. L.; Auer, A. A.; Gauss, J.; Neese, F. *J. Chem. Phys.* **2021**, *154*, 164110.
(76) Koch, H.; Sánchez de Merás, A.; Pedersen, T. B. *J. Chem. Phys.* **2003**, *118*, 9481–9484.
(77) Pedersen, T. B.; Lehtola, S.; Fdez. Galván, I.; Lindh, R. *WIREs Comput. Mol. Sci.* **2024**, *14*, e1692.
(78) Epifanovsky, E.; Zuev, D.; Feng, X.; Khistyaev, K.; Shao, Y.; Krylov, A. I. *J. Chem. Phys.* **2013**, *139*, 134105.
(79) Aquilante, F.; Lindh, R.; Pedersen, T. B. *J. Chem. Phys.* **2007**, *127*, 114107.
(80) Aquilante, F.; Gagliardi, L.; Pedersen, T. B.; Lindh, R. *J. Chem. Phys.* **2009**, *130*, 154107.
(81) Aquilante, F.; Lindh, R.; Pedersen, T. B. *J. Chem. Phys.* **2008**, *129*, 034106.
(82) Aquilante, F.; Pedersen, T. B. *Chem. Phys. Lett.* **2007**, *449*, 354–357.
(83) Røeggen, I.; Johansen, T. *J. Chem. Phys.* **2008**, *128*, 194107.
(84) Aquilante, F.; Boman, L.; Boström, J.; Koch, H.; Lindh, R.; Sánchez de Merás, A.; Pedersen, T. B. In *Linear-Scaling Techniques in Computational Chemistry and Physics*, Zalesny, R., Papadopoulos, M. G., Mezey, P. G., Leszczynski, J., Eds.; Springer Netherlands: Dordrecht, 2011; Vol. 13, pp 301–343.
(85) Pedersen, T. B.; Aquilante, F.; Lindh, R. *Theor. Chem. Acc.* **2009**, *124*, 1–10.
(86) Folkestad, S. D.; Kjønstad, E. F.; Koch, H. *J. Chem. Phys.* **2019**, *150*, 194112.
(87) Boman, L.; Koch, H.; Sánchez de Merás, A. *J. Chem. Phys.* **2008**, *129*, 134107.
(88) Zhang, T.; Liu, X.; Valeev, E. F.; Li, X. *J. Phys. Chem. A* **2021**, *125*, 4258–4265.
(89) Boström, J.; Veryazov, V.; Aquilante, F.; Pedersen, T. B.; Lindh, R. *Int. J. Quantum Chem.* **2014**, *114*, 321–327.
(90) Feng, X.; Epifanovsky, E.; Gauss, J.; Krylov, A. I. *J. Chem. Phys.* **2019**, *151*, 014110.

(91) Schnack-Petersen, A. K.; Koch, H.; Coriani, S.; Kjønstad, E. F. *J. Chem. Phys.* **2022**, *156*, 244111.
(92) Delcey, M. G.; Freitag, L.; Pedersen, T. B.; Aquilante, F.; Lindh, R.; González, L. *J. Chem. Phys.* **2014**, *140*, 174103.
(93) Burger, S.; Lipparini, F.; Gauss, J.; Stopkowicz, S. *J. Chem. Phys.* **2021**, *155*, 074105.
(94) Burger, S.; Stopkowicz, S.; Gauss, J. *J. Phys. Chem. A* **2025**, *129*, 623–632.
(95) Warshel, A.; Levitt, M. *J. Mol. Biol.* **1976**, *103*, 227–249.
(96) Jusélius, J.; Sundholm, D.; Gauss, J. *J. Chem. Phys.* **2004**, *121*, 3952–3963.
(97) Nottoli, T.; Burger, S.; Stopkowicz, S.; Gauss, J.; Lipparini, F. *J. Chem. Phys.* **2022**, *157*, 084122.
(98) Nanda, K. D.; Krylov, A. I.; Gauss, J. *J. Chem. Phys.* **2018**, *149*, 141101.
(99) Jagau, T.-C.; Gauss, J. *J. Chem. Phys.* **2012**, *137*, 044115.
(100) Salek, P.; Helgaker, T.; Vahtras, O.; Ågren, H.; Jonsson, D.; Gauss, J. *Mol. Phys.* **2005**, *103*, 439–450.
(101) Coriani, S.; Halkier, A.; Jørgensen, P.; Gauss, J.; Christiansen, O.; Rizzo, A. *J. Chem. Phys.* **2000**, *113*, 1688–1697.
(102) Larsen, H.; Olsen, J.; Hättig, C.; Jørgensen, P.; Christiansen, O.; Gauss, J. *J. Chem. Phys.* **1999**, *111*, 1917–1925.
(103) Christiansen, O.; Gauss, J.; Stanton, J. F. *Chem. Phys. Lett.* **1999**, *305*, 147–155.
(104) Christiansen, O.; Gauss, J.; Stanton, J. F. *Chem. Phys. Lett.* **1998**, *292*, 437–446.
(105) Christiansen, O.; Hättig, C.; Gauss, J. *J. Chem. Phys.* **1998**, *109*, 4745–4757.
(106) Tew, D. P.; Klopper, W.; Heckert, M.; Gauss, J. *J. Phys. Chem. A* **2007**, *111*, 11242–11248.
(107) Larsen, H.; Olsen, J.; Jørgensen, P.; Gauss, J. *Chem. Phys. Lett.* **2001**, *342*, 200–206.
(108) Ruden, T. A.; Helgaker, T.; Jørgensen, P.; Olsen, J. *J. Chem. Phys.* **2004**, *121*, 5874–5884.
(109) Kállay, M.; Gauss, J.; Szalay, P. G. *J. Chem. Phys.* **2003**, *119*, 2991–3004.
(110) Musiał, M.; Kucharski, S. A.; Bartlett, R. J. *J. Mol. Struct. THEOCHEM* **2001**, *547*, 269–278.
(111) Stratmann, R. E.; Scuseria, G. E.; Frisch, M. J. *Chem. Phys. Lett.* **1996**, *257*, 213–223.
(112) Scott, A. P.; Radom, L. *J. Phys. Chem.* **1996**, *100*, 16502–16513.
(113) Kucharski, S. A.; Watts, J. D.; Bartlett, R. J. *Chem. Phys. Lett.* **1999**, *302*, 295–301.
(114) McMurchie, L. E.; Davidson, E. R. *J. Comput. Phys.* **1978**, *26*, 218–231.
(115) Szabo, A.; Ostlund, N. S., *Modern Quantum Chemistry: Introduction to Advanced Electronic Structure Theory*; Dover Publications, Inc: Mineola, New York, 2012.
(116) Hartree, D. R. *Math. Proc. Camb. Phil. Soc.* **1928**, *24*, 89–110.
(117) Fock, V. *Z. Phys.* **1930**, *61*, 126–148.
(118) Paldus, J. *J. Chem. Phys.* **1977**, *67*, 303–318.
(119) Gauss, J. In *Encyclopedia of Computational Chemistry*, Schleyer, P. v. R., Allinger, N. L., Clark, T., Gasteiger, J., Kollman, P., Schaefer, H. F., Schreiner, P. R., Eds., 1st ed.; Wiley: 1998, pp 615–636.
(120) Ekeland, I. *J. Math. Anal. App.* **1974**, *47*, 324–353.
(121) Roothaan, C. C. J. *Rev. Mod. Phys.* **1951**, *23*, 69–89.
(122) Hall, G. G. *Proc. R. Soc. Lond. A* **1951**, *205*, 541–552.

(123) Olsen, J.; Christiansen, O.; Koch, H.; Jørgensen, P. *J. Chem. Phys.* **1996**, *105*, 5082–5090.

(124) Crawford, T. D.; Schaefer, H. F. In *Reviews in Computational Chemistry*, Lipkowitz, K. B., Boyd, D. B., Eds., 1st ed.; Wiley: 2000; Vol. 14, pp 33–136.

(125) Purvis, G. D.; Bartlett, R. J. *J. Chem. Phys.* **1982**, *76*, 1910–1918.

(126) Raghavachari, K.; Trucks, G. W.; Pople, J. A.; Head-Gordon, M. *Chem. Phys. Lett.* **1989**, *157*, 479–483.

(127) Guo, Y.; Riplinger, C.; Becker, U.; Liakos, D. G.; Minenkov, Y.; Cavallo, L.; Neese, F. *J. Chem. Phys.* **2018**, *148*, 011101.

(128) Roos, B. O.; Taylor, P. R.; Siegbahn, P. E. *Chem. Phys.* **1980**, *48*, 157–173.

(129) Cramer, C. J., *Essentials of Computational Chemistry: Theories and Models*, 2nd ed; J. Wiley & Sons: Chichester, 2004.

(130) Werner, H.-J. *Adv. Chem. Phys.* **1987**, *69*, 1–62.

(131) Shepard, R. *Adv. Chem. Phys.* **1987**, *69*, 63–200.

(132) Roos, B. O. *Adv. Chem. Phys.* **1987**, *69*, 399–445.

(133) Helgaker, T.; Jørgensen, P. *J. Chem. Phys.* **1991**, *95*, 2595–2601.

(134) Helgaker, T.; Jørgensen, P.; Olsen, J., *Molecular Electronic-Structure Theory*; John Wiley & Sons Ltd.: Chichester, 2014.

(135) Szalay, P. G.; Müller, T.; Gidofalvi, G.; Lischka, H.; Shepard, R. *Chem. Rev.* **2012**, *112*, 108–181.

(136) Gauss, J.; Cremer, D. *Chem. Phys. Lett.* **1987**, *133*, 420–424.

(137) Neugebauer, J.; Reiher, M.; Kind, C.; Hess, B. A. *J. Comput. Chem.* **2002**, *23*, 895–910.

(138) Stanton, J. F.; Lopreore, C. L.; Gauss, J. *J. Chem. Phys.* **1998**, *108*, 7190–7196.

(139) Puzzarini, C.; Stanton, J. F.; Gauss, J. *Int. Rev. Phys. Chem.* **2010**, *29*, 273–367.

(140) Melosso, M.; Jiang, N.; Gauss, J.; Puzzarini, C. *J. Chem. Phys.* **2023**, *158*, 174310.

(141) Winnewisser, G.; Lewen, F.; Thorwirth, S.; Behnke, M.; Hahn, J.; Gauss, J.; Herbst, E. *Chem. Eur. J.* **2003**, *9*, 5501–5510.

(142) Puzzarini, C.; Cazzoli, G.; Gauss, J. *J. Chem. Phys.* **2012**, *137*, 154311.

(143) Puzzarini, C. *Int. J. Quantum Chem.* **2017**, *117*, 129–138.

(144) Ditchfield, R. *J. Chem. Phys.* **1972**, *56*, 5688–5691.

(145) Facelli, J. C. *Concepts Magn. Reson. A* **2004**, *20A*, 42–69.

(146) Helgaker, T.; Jaszuński, M.; Ruud, K. *Chem. Rev.* **1999**, *99*, 293–352.

(147) Sundholm, D.; Gauss, J.; Schäfer, A. *J. Chem. Phys.* **1996**, *105*, 11051–11059.

(148) Gauss, J.; Ruud, K.; Kállay, M. *J. Chem. Phys.* **2007**, *127*, 074101.

(149) Chesnut, D. In *Annu. Rep. NMR Spectrosc.* Elsevier: 1994; Vol. 29, pp 71–122.

(150) Lutnæs, O. B.; Teale, A. M.; Helgaker, T.; Tozer, D. J.; Ruud, K.; Gauss, J. *J. Chem. Phys.* **2009**, *131*, 144104.

(151) Lehtola, S.; Dimitrova, M.; Fliegl, H.; Sundholm, D. *J. Chem. Theory Comput.* **2021**, *17*, 1457–1468.

(152) Fliegl, H.; Taubert, S.; Lehtonen, O.; Sundholm, D. *Phys. Chem. Chem. Phys.* **2011**, *13*, 20500.

(153) Jusélius, J.; Sundholm, D. *Phys. Chem. Chem. Phys.* **2001**, *3*, 2433–2437.

(154) Jusélius, J.; Sundholm, D. *Phys. Chem. Chem. Phys.* **1999**, *1*, 3429–3435.

(155) Sundholm, D.; Dimitrova, M.; Berger, R. J. F. *Chem. Commun.* **2021**, *57*, 12362–12378.

(156) Jusélius, J.; Sundholm, D. *Phys. Chem. Chem. Phys.* **2000**, *2*, 2145–2151.
(157) Jusélius, J.; Sundholm, D. *J. Org. Chem.* **2000**, *65*, 5233–5237.
(158) Sundholm, D.; Fliegl, H.; Berger, R. J. F. *WIREs Comput. Mol. Sci.* **2016**, *6*, 639–678.
(159) Schleyer, P. v. R.; Jiao, H. *Pure Appl. Chem.* **1996**, *68*, 209–218.
(160) *The IUPAC Compendium of Chemical Terminology: The Gold Book*, 4th ed.; Gold, V., Ed.; International Union of Pure and Applied Chemistry (IUPAC): Research Triangle Park, NC, 2019.
(161) Halliday, D.; Resnick, R.; Walker, J.; Halliday, D., *Physik*, Bachelor-Ed; Koch, S. W., Ed.; Wiley-VCH: Weinheim, 2007.
(162) Ruud, K.; Skaane, H.; Helgaker, T.; Bak, K. L.; Jørgensen, P. *J. Am. Chem. Soc.* **1994**, *116*, 10135–10140.
(163) Hansen, A. E.; Bouman, T. D. *J. Chem. Phys.* **1985**, *82*, 5035–5047.
(164) Pople, J. A.; Krishnan, R.; Schlegel, H. B.; Binkley, J. S. *Int. J. Quantum Chem.* **2009**, *16*, 225–241.
(165) Ángyán, J. G. *J. Math. Chem.* **2009**, *46*, 1–14.
(166) Kvasnička, V.; Laurinc, V.; Biskupič, S. *Mol. Phys.* **1980**, *39*, 143–161.
(167) Koopmans, T. *Physica* **1934**, *1*, 104–113.
(168) Gerratt, J.; Mills, I. M. *J. Chem. Phys.* **1968**, *49*, 1719–1729.
(169) Handy, N. C.; Schaefer, H. F. *J. Chem. Phys.* **1984**, *81*, 5031–5033.
(170) Helgaker, T.; Almlöf, J. *Int. J. Quantum Chem.* **1984**, *26*, 275–291.
(171) Nottoli, T.; Gauss, J.; Lipparini, F. *J. Chem. Theory Comput.* **2021**, *17*, 6819–6831.
(172) Schleyer, P. v. R.; Maerker, C.; Dransfeld, A.; Jiao, H.; van Eikema Hommes, N. J. R. *J. Am. Chem. Soc.* **1996**, *118*, 6317–6318.
(173) Lazzeretti, P.; Malagoli, M.; Zanasi, R. *Chem. Phys. Lett.* **1994**, *220*, 299–304.
(174) *Handbook of Mathematical Functions: With Formulas, Graphs, and Mathematical Tables*, 9. Dover print; Abramowitz, M., Stegun, I. A., Eds.; Dover Books on Mathematics; Dover Publ: New York, NY, 2013.
(175) Obara, S.; Saika, A. *J. Chem. Phys.* **1986**, *84*, 3963–3974.
(176) Head-Gordon, M.; Pople, J. A. *J. Chem. Phys.* **1988**, *89*, 5777–5786.
(177) Dupuis, M.; Rys, J.; King, H. F. *J. Chem. Phys.* **1976**, *65*, 111–116.
(178) Boys, S. F. *Proc. R. Soc. Lond. A* **1950**, *200*, 542–554.
(179) Stopkowicz, S. Higher-Order Perturbative Relativistic Corrections to Energies and Properties., Ph.D. Thesis, Johannes Gutenberg-Universität Mainz, 2012.
(180) Burger, S. Cholesky-Zerlegung der für die Quantenchemische Berechnung von NMR-Verschiebungen Notwendigen gestörten Zweielektronen-Integrale., MA thesis, Johannes Gutenberg-Universität Mainz, 2020.
(181) Beebe, N. H. F.; Linderberg, J. *Int. J. Quantum Chem.* **1977**, *12*, 683–705.
(182) Ochsenfeld, C.; Kussmann, J.; Lambrecht, D. S. In *Reviews in Computational Chemistry*, Lipkowitz, K. B., Cundari, T. R., Eds., 1st ed.; Wiley: 2007; Vol. 23, pp 1–82.
(183) Zalesny, R.; Papadopoulos, M. G.; Mezey, P. G.; Leszczynski, J., *Linear-Scaling Techniques in Computational Chemistry and Physics: Methods and Applications*; Challenges and Advances in Computational Chemistry and Physics 13; Springer Science+Business Media B.V: Dordrecht, 2011.
(184) White, C. A.; Head-Gordon, M. *J. Chem. Phys.* **1994**, *101*, 6593–6605.

(185) White, C. A.; Head-Gordon, M. *J. Chem. Phys.* **1996**, *105*, 5061–5067.
(186) White, C. A.; Johnson, B. G.; Gill, P. M. W.; Head-Gordon, M. *Chem. Phys. Lett.* **1994**, *230*, 8–16.
(187) Weigend, F.; Kattannek, M.; Ahlrichs, R. *J. Chem. Phys.* **2009**, *130*, 164106.
(188) Benoît, C. *Bulletin Géodésique* **1924**, *2*, 67–77.
(189) Gauss, J.; Blaschke, S.; Burger, S.; Nottoli, T.; Lipparini, F.; Stopkowicz, S. *Mol. Phys.* **2023**, *121*, e2101562.
(190) Blaschke, S.; Stopkowicz, S. *J. Chem. Phys.* **2022**, *156*, 044115.
(191) Dunning, T. H. *J. Chem. Phys.* **1989**, *90*, 1007–1023.
(192) Aquilante, F.; Pedersen, T. B.; Lindh, R.; Roos, B. O.; Sánchez de Merás, A.; Koch, H. *J. Chem. Phys.* **2008**, *129*, 024113.
(193) Gauss, J. *Unpublished* **2020**.
(194) Sebastiani, D.; Rothlisberger, U. *J. Phys. Chem. B* **2004**, *108*, 2807–2815.
(195) Hashem, S.; Cupellini, L.; Lipparini, F.; Mennucci, B. *Mol. Phys.* **2020**, *118*, e1771449.
(196) Gascón, J. A.; Sproviero, E. M.; Batista, V. S. *J. Chem. Theory Comput.* **2005**, *1*, 674–685.
(197) Kongsted, J.; Nielsen, C. B.; Mikkelsen, K. V.; Christiansen, O.; Ruud, K. *J. Chem. Phys.* **2007**, *126*, 034510.
(198) Aidas, K.; Kongsted, J.; Nielsen, C. B.; Mikkelsen, K. V.; Christiansen, O.; Ruud, K. *Chem. Phys. Lett.* **2007**, *442*, 322–328.
(199) Senn, H. M.; Thiel, W. *Angew. Chem. Int. Ed.* **2009**, *48*, 1198–1229.
(200) Senn, H. M.; Thiel, W. In *Atomistic Approaches in Modern Biology*, Reiher, M., Ed.; Springer Berlin Heidelberg: 2007; Vol. 268, pp 173–290.
(201) Maseras, F.; Morokuma, K. *J. Comput. Chem.* **1995**, *16*, 1170–1179.
(202) Svensson, M.; Humbel, S.; Froese, R. D. J.; Matsubara, T.; Sieber, S.; Morokuma, K. *J. Phys. Chem.* **1996**, *100*, 19357–19363.
(203) Vreven, T.; Morokuma, K. *Theor. Chem. Acc.* **2003**, *109*, 125–132.
(204) Ryde, U. *J. Comput. Aided Mol. Des.* **1996**, *10*, 153–164.
(205) Pearlman, D. A.; Case, D. A.; Caldwell, J. W.; Ross, W. S.; Cheatham, T. E.; DeBolt, S.; Ferguson, D.; Seibel, G.; Kollman, P. *Comput. Phys. Commun.* **1995**, *91*, 1–41.
(206) Brooks, B. R.; Bruccoleri, R. E.; Olafson, B. D.; States, D. J.; Swaminathan, S.; Karplus, M. *J. Comput. Chem.* **1983**, *4*, 187–217.
(207) Vanommeslaeghe, K.; Hatcher, E.; Acharya, C.; Kundu, S.; Zhong, S.; Shim, J.; Darian, E.; Guvench, O.; Lopes, P.; Vorobyov, I.; Mackerell, A. D. *J. Comput. Chem.* **2010**, *31*, 671–690.
(208) Oostenbrink, C.; Villa, A.; Mark, A. E.; Van Gunsteren, W. F. *J. Comput. Chem.* **2004**, *25*, 1656–1676.
(209) Scott, W. R. P.; Hünenberger, P. H.; Tironi, I. G.; Mark, A. E.; Billeter, S. R.; Fennen, J.; Torda, A. E.; Huber, T.; Krüger, P.; Van Gunsteren, W. F. *J. Phys. Chem. A* **1999**, *103*, 3596–3607.
(210) Jorgensen, W. L.; Tirado-Rives, J. *J. Am. Chem. Soc.* **1988**, *110*, 1657–1666.
(211) Jorgensen, W. L.; Maxwell, D. S.; Tirado-Rives, J. *J. Am. Chem. Soc.* **1996**, *118*, 11225–11236.

(212) Carrer, M.; Cezar, H. M.; Bore, S. L.; Ledum, M.; Cascella, M. *J. Chem. Inf. Model.* **2024**, *64*, 5510–5520.

(213) Smith, J. S.; Nebgen, B.; Lubbers, N.; Isayev, O.; Roitberg, A. E. *J. Chem. Phys.* **2018**, *148*, 241733.

(214) Wang, H.; Zhang, L.; Han, J.; E, W. *Comput. Phys. Commun.* **2018**, *228*, 178–184.

(215) Zeng, J.; Zhang, D.; Lu, D.; Mo, P.; Li, Z.; Chen, Y.; Rynik, M.; Huang, L.; Li, Z.; Shi, S.; Wang, Y.; Ye, H.; Tuo, P.; Yang, J.; Ding, Y.; Li, Y.; Tisi, D.; Zeng, Q.; Bao, H.; Xia, Y.; Huang, J.; Muraoka, K.; Wang, Y.; Chang, J.; Yuan, F.; Bore, S. L.; Cai, C.; Lin, Y.; Wang, B.; Xu, J.; Zhu, J.; Luo, C.; Zhang, Y.; Goodall, R. E. A.; Liang, W.; Singh, A. K.; Yao, S.; Zhang, J.; Wentzcovitch, R.; Han, J.; Liu, J.; Jia, W.; York, D. M.; E, W.; Car, R.; Zhang, L.; Wang, H. *J. Chem. Phys.* **2023**, *159*, 054801.

(216) Hohenberg, P.; Kohn, W. *Phys. Rev.* **1964**, *136*, B864–B871.

(217) Kohn, W.; Sham, L. J. *Phys. Rev.* **1965**, *140*, A1133–A1138.

(218) Brunk, E.; Rothlisberger, U. *Chem. Rev.* **2015**, *115*, 6217–6263.

(219) Fonseca Guerra, C.; Snijders, J. G.; Te Velde, G.; Baerends, E. J. *Theor. Chem. Acc.* **1998**, *99*, 391–403.

(220) Bakowies, D.; Thiel, W. *J. Phys. Chem.* **1996**, *100*, 10580–10594.

(221) Laio, A.; VandeVondele, J.; Rothlisberger, U. *J. Chem. Phys.* **2002**, *116*, 6941–6947.

(222) Kirsch, T.; Olsen, J. M. H.; Bolnykh, V.; Meloni, S.; Ippoliti, E.; Rothlisberger, U.; Cascella, M.; Gauss, J. *J. Chem. Theory Comput.* **2022**, *18*, 13–24.

(223) Kirsch, T. S. N. AIMD- und QM/MM-MD Implementierung für wellenfunktionsbasierte quantenchemische Methoden., Ph.D. Thesis, Johannes Gutenberg-Universität Mainz, 2023.

(224) Car, R.; Parrinello, M. *Phys. Rev. Lett.* **1985**, *55*, 2471–2474.

(225) Warshel, A.; Karplus, M. *Chem. Phys. Lett.* **1975**, *32*, 11–17.

(226) Payne, M. C.; Teter, M. P.; Allan, D. C.; Arias, T. A.; Joannopoulos, J. D. *Rev. Mod. Phys.* **1992**, *64*, 1045–1097.

(227) Helgaker, T.; Uggerud, E.; Jensen, H. J. Aa. *Chem. Phys. Lett.* **1990**, *173*, 145–150.

(228) Peters, L. D. M.; Kussmann, J.; Ochsenfeld, C. *J. Chem. Theory Comput.* **2017**, *13*, 5479–5485.

(229) Niklasson, A. M. N. *Phys. Rev. Lett.* **2008**, *100*, 123004.

(230) Leimkuhler, B. J.; Reich, S.; Skeel, R. D. In *Mathematical Approaches to Biomolecular Structure and Dynamics*; Springer: New York, 1996, pp 161–185.

(231) Hockney, R.; Goel, S.; Eastwood, J. *Chem. Phys. Lett.* **1973**, *21*, 589–591.

(232) Verlet, L. *Phys. Rev.* **1967**, *159*, 98–103.

(233) Swope, W. C.; Andersen, H. C.; Berens, P. H.; Wilson, K. R. *J. Chem. Phys.* **1982**, *76*, 637–649.

(234) Andersen, H. C. *J. Chem. Phys.* **1980**, *72*, 2384–2393.

(235) Runge, C. *Math. Ann.* **1895**, *46*, 167–178.

(236) Kutta, W. *Z. Math. Phys.* **1901**, *46*, 435–453.

(237) Janezic, D.; Orel, B. *J. Chem. Inf. Comput.* **1993**, *33*, 252–257.

(238) Makov, G.; Payne, M. C. *Phys. Rev. B* **1995**, *51*, 4014–4022.

(239) Berendsen, H. J. C.; Postma, J. P. M.; Van Gunsteren, W. F.; DiNola, A.; Haak, J. R. *J. Chem. Phys.* **1984**, *81*, 3684–3690.

(240) Nosé, S. *Mol. Phys.* **1984**, *52*, 255–268.

(241) Hoover, W. G. *Phys. Rev. A* **1985**, *31*, 1695–1697.
(242) Zhou, Y.; Wang, S.; Li, Y.; Zhang, Y. In *Methods in Enzymology*; Elsevier: 2016; Vol. 577, pp 105–118.
(243) Wu, R.; Gong, W.; Liu, T.; Zhang, Y.; Cao, Z. *J. Phys. Chem. B* **2012**, *116*, 1984–1991.
(244) Chudyk, E. I.; Limb, A. L.; Jones, C.; Spencer, J.; Van Der Kamp, M. W.; Mulholland, A. J. *Chem. Commun.* **2014**, *50*, 14736–14739.
(245) Van Keulen, S. C.; Gianti, E.; Carnevale, V.; Klein, M. L.; Rothlisberger, U.; Delemotte, L. *J. Phys. Chem. B* **2017**, *121*, 3340–3351.
(246) Hu, P.; Wang, S.; Zhang, Y. *J. Am. Chem. Soc.* **2008**, *130*, 16721–16728.
(247) Groenhof, G. In *Biomolecular Simulations*, Monticelli, L., Salonen, E., Eds.; Humana Press: Totowa, NJ, 2013; Vol. 924, pp 43–66.
(248) Pfrommer, B. G.; Mauri, F.; Louie, S. G. *J. Am. Chem. Soc.* **2000**, *122*, 123–129.
(249) Cuny, J.; Jolibois, F.; Gerber, I. C. *J. Chem. Theory Comput.* **2018**, *14*, 4041–4051.
(250) Malkin, V. G.; Malkina, O. L.; Steinebrunner, G.; Huber, H. *Chem. Eur. J.* **1996**, *2*, 452–457.
(251) Cybulski, H.; Sadlej, J. *Chem. Phys.* **2006**, *323*, 218–230.
(252) Klein, R. A.; Mennucci, B.; Tomasi, J. *J. Phys. Chem. A* **2004**, *108*, 5851–5863.
(253) Pennanen, T. S.; Lantto, P.; Sillanpää, A. J.; Vaara, J. *J. Phys. Chem. A* **2007**, *111*, 182–192.
(254) Fileti, E. E.; Georg, H. C.; Coutinho, K.; Canuto, S. *J. Braz. Chem. Soc.* **2007**, *18*, 74–84.
(255) Sieber, S.; Schleyer, P. v. R.; Gauss, J. *J. Am. Chem. Soc.* **1993**, *115*, 6987–6988.
(256) Dudley, T. J.; Olson, R. M.; Schmidt, M. W.; Gordon, M. S. *J. Comput. Chem.* **2006**, *27*, 352–362.
(257) Snyder, J. W.; Hohenstein, E. G.; Luehr, N.; Martínez, T. J. *J. Chem. Phys.* **2015**, *143*, 154107.
(258) Hohenstein, E. G.; Bouduban, M. E. F.; Song, C.; Luehr, N.; Ufimtsev, I. S.; Martínez, T. J. *J. Chem. Phys.* **2015**, *143*, 014111.
(259) Snyder, J. W.; Fales, B. S.; Hohenstein, E. G.; Levine, B. G.; Martínez, T. J. *J. Chem. Phys.* **2017**, *146*, 174113.
(260) Helmich-Paris, B. *J. Chem. Phys.* **2019**, *150*, 174121.
(261) Matthews, D. A.; Cheng, L.; Harding, M. E.; Lipparini, F.; Stopkowicz, S.; Jagau, T.-C.; Szalay, P. G.; Gauss, J.; Stanton, J. F. *J. Chem. Phys.* **2020**, *152*, 214108.
(262) Gauss, J.; Lipparini, F.; Burger, S.; Blaschke, S.; Kitsaras, M.-P.; Nottoli, T.; Oswald, J.; Stopkowicz, S.; Uhlířová, T. *Johannes Gutenberg-Universität Mainz, unpublished* **2025**.
(263) Ruud, K.; Helgaker, T.; Bak, K. L.; Jørgensen, P.; Jensen, H. J. Aa. *J. Chem. Phys.* **1993**, *99*, 3847–3859.
(264) Berendsen, H.; Van Der Spoel, D.; Van Drunen, R. *Comput. Phys. Commun.* **1995**, *91*, 43–56.
(265) Jorgensen, W. L.; Chandrasekhar, J.; Madura, J. D.; Impey, R. W.; Klein, M. L. *J. Chem. Phys.* **1983**, *79*, 926–935.
(266) Parrinello, M.; Rahman, A. *Phys. Rev. Lett.* **1980**, *45*, 1196–1199.
(267) Mazur, A. S.; Vovk, M. A.; Tolstoy, P. M. *Fuller. Nanotub. Car. N.* **2020**, *28*, 202–213.
(268) Gerothanassis, I. P. *Prog. Nucl. Magn. Reson. Spectrosc.* **2010**, *56*, 95–197.
(269) Schäfer, A.; Horn, H.; Ahlrichs, R. *J. Chem. Phys.* **1992**, *97*, 2571–2577.

(270) Ochsenfeld, C.; Brown, S. P.; Schnell, I.; Gauss, J.; Spiess, H. W. *J. Am. Chem. Soc.* **2001**, *123*, 2597–2606.

(271) Brown, S. P.; Schnell, I.; Brand, J. D.; Müllen, K.; Spiess, H. W. *J. Am. Chem. Soc.* **1999**, *121*, 6712–6718.

(272) Mennekes, T.; Paetzold, P.; Boese, R.; Bläser, D. *Angew. Chem. Int. Ed. Engl.* **1991**, *30*, 173–175.

(273) Davan, T.; Morrison, J. A. *J. Chem. Soc., Chem. Commun.* **1981**, 250.

(274) Bühl, M.; Schleyer, P. v. R. *J. Am. Chem. Soc.* **1992**, *114*, 477–491.

(275) Brown, S. P.; Schaller, T.; Seelbach, U. P.; Koziol, F.; Ochsenfeld, C.; Klärner, F.-G.; Spiess, H. W. *Angew. Chem. Int. Ed.* **2001**, *40*, 717–720.

(276) Weigend, F.; Häser, M. *Theor. Chim. Acta* **1997**, *97*, 331–340.

(277) Weigend, F.; Häser, M.; Patzelt, H.; Ahlrichs, R. *Chem. Phys. Lett.* **1998**, *294*, 143–152.

(278) Weigend, F.; Köhn, A.; Hättig, C. *J. Chem. Phys.* **2002**, *116*, 3175–3183.

(279) Balasubramani, S. G.; Chen, G. P.; Coriani, S.; Diedenhofen, M.; Frank, M. S.; Franzke, Y. J.; Furche, F.; Grotjahn, R.; Harding, M. E.; Hättig, C.; Hellweg, A.; Helmich-Paris, B.; Holzer, C.; Huniar, U.; Kaupp, M.; Marefat Khah, A.; Karbalaei Khani, S.; Müller, T.; Mack, F.; Nguyen, B. D.; Parker, S. M.; Perlt, E.; Rappoport, D.; Reiter, K.; Roy, S.; Rückert, M.; Schmitz, G.; Sierka, M.; Tapavicza, E.; Tew, D. P.; van Wüllen, C.; Voora, V. K.; Weigend, F.; Wodyński, A.; Yu, J. M. *J. Chem. Phys.* **2020**, *152*, 184107.

(280) Orendt, A. M.; Facelli, J. C.; Bai, S.; Rai, A.; Gossett, M.; Scott, L. T.; Boerio-Goates, J.; Pugmire, R. J.; Grant, D. M. *J. Phys. Chem. A* **2000**, *104*, 149–155.

(281) Ceriotti, M.; Cuny, J.; Parrinello, M.; Manolopoulos, D. E. *Proc. Natl. Acad. Sci. U.S.A.* **2013**, *110*, 15591–15596.

(282) Klamt, A. *J. Phys. Chem.* **1995**, *99*, 2224–2235.

(283) Klamt, A. *WIREs Comput. Mol. Sci.* **2011**, *1*, 699–709.

(284) Klamt, A.; Jonas, V.; Bürger, T.; Lohrenz, J. C. W. *J. Phys. Chem. A* **1998**, *102*, 5074–5085.

(285) Tomasi, J.; Mennucci, B.; Cammi, R. *Chem. Rev.* **2005**, *105*, 2999–3094.

(286) Miertuš, S.; Scrocco, E.; Tomasi, J. *Chem. Phys.* **1981**, *55*, 117–129.

(287) Amovilli, C.; Barone, V.; Cammi, R.; Cancès, E.; Cossi, M.; Mennucci, B.; Pomelli, C. S.; Tomasi, J. In *Advances in Quantum Chemistry*, Löwdin, P.-O., Ed.; Elsevier: 1998; Vol. 32, pp 227–261.

(288) Cossi, M.; Barone, V. *J. Chem. Phys.* **1998**, *109*, 6246–6254.

(289) Zhang, J.; Zhang, H.; Wu, T.; Wang, Q.; Van Der Spoel, D. *J. Chem. Theory Comput.* **2017**, *13*, 1034–1043.

(290) Ortega, J.; Lewis, J. P.; Sankey, O. F. *J. Chem. Phys.* **1997**, *106*, 3696–3702.

(291) Soper, A. *Chem. Phys.* **2000**, *258*, 121–137.

(292) Camisasca, G.; Pathak, H.; Wikfeldt, K. T.; Pettersson, L. G. M. *J. Chem. Phys.* **2019**, *151*, 044502.

(293) Soper, A. K. *Phys. Chem.* **2013**, *2013*, 1–67.

(294) Sebastiani, D.; Parrinello, M. *Chem. Phys. Chem.* **2002**, *3*, 675.

(295) Florin, A. E.; Alei, M. *J. Chem. Phys.* **1967**, *47*, 4268–4269.

(296) Hindman, J. C. *J. Chem. Phys.* **1966**, *44*, 4582–4592.

(297) Balevicius, V.; Aidas, K. *Appl. Magn. Reson.* **2007**, *32*, 363–376.

(298) Chesnut, D. B.; Rusiloski, B. E. *J. Mol. Struct. THEOCHEM* **1994**, *314*, 19–30.
(299) Perdew, J. P.; Burke, K.; Ernzerhof, M. *Phys. Rev. Lett.* **1996**, *77*, 3865–3868.
(300) Dion, M.; Rydberg, H.; Schröder, E.; Langreth, D. C.; Lundqvist, B. I. *Phys. Rev. Lett.* **2004**, *92*, 246401.
(301) Román-Pérez, G.; Soler, J. M. *Phys. Rev. Lett.* **2009**, *103*, 096102.
(302) Klimeš, J.; Bowler, D. R.; Michaelides, A. *J. Phys.: Condens. Matter* **2010**, *22*, 022201.
(303) Klimeš, J.; Bowler, D. R.; Michaelides, A. *Phys. Rev. B* **2011**, *83*, 195131.
(304) Hehre, W. J.; Ditchfield, R.; Pople, J. A. *J. Chem. Phys.* **1972**, *56*, 2257–2261.
(305) Hariharan, P. C.; Pople, J. A. *Theor. Chim. Acta* **1973**, *28*, 213–222.
(306) Frisch, M. J.; Pople, J. A.; Binkley, J. S. *J. Chem. Phys.* **1984**, *80*, 3265–3269.
(307) Pennanen, T. S.; Vaara, J.; Lantto, P.; Sillanpää, A. J.; Laasonen, K.; Jokisaari, J. *J. Am. Chem. Soc.* **2004**, *126*, 11093–11102.
(308) Yu, H.; Van Gunsteren, W. F. *Comput. Phys. Commun.* **2005**, *172*, 69–85.
(309) Ponder, J. W.; Case, D. A. In *Advances in Protein Chemistry*; Elsevier: 2003; Vol. 66, pp 27–85.
(310) Rick, S. W.; Stuart, S. J. In *Reviews in Computational Chemistry*, Lipkowitz, K. B., Boyd, D. B., Eds.; John Wiley & Sons, Inc.: Hoboken, New Jersey, 2002; Vol. 18, pp 89–146.
(311) Fias, S.; Fowler, P. W.; Delgado, J. L.; Hahn, U.; Bultinck, P. *Chem. Eur. J.* **2008**, *14*, 3093–3099.
(312) Balaban, T.; Bean, D. E.; Fowler, P. W. *Acta Chim. Slov.* **2010**, *57*, 507–512.
(313) Becke, A. D. *Phys. Rev. A* **1988**, *38*, 3098–3100.
(314) Perdew, J. P. *Phys. Rev. B* **1986**, *33*, 8822–8824.
(315) Vosko, S. H.; Wilk, L.; Nusair, M. *Can. J. Phys.* **1980**, *58*, 1200–1211.
(316) Vogel, E. *Pure Appl. Chem.* **1969**, *20*, 237–262.
(317) Farnell, L.; Radom, : *J. Am. Chem. Soc.* **1982**, *104*, 7650–7654.
(318) Schneider, M. Berechnung von Ringströmen in Aromatischen Systemen., Bachelors Thesis, Johannes Gutenberg-Universität Mainz, 2025.
(319) Nmrshiftdb2., https://nmrshiftdb.nmr.uni-koeln.de.
(320) Vogel, E. *CHIMIA* **1968**, *22*, 21.
(321) Gauss, J.; Werner, H.-J. *Phys. Chem. Chem. Phys.* **2000**, *2*, 2083–2090.
(322) Nottoli, T.; Gauss, J.; Lipparini, F. *J. Chem. Phys.* **2023**, *159*, 231101.
(323) Stanton, J. F.; Gauss, J.; Siehl, H.-U. *Chem. Phys. Lett.* **1996**, *262*, 183–186.
(324) Pedersen, T. B.; Sánchez de Merás, A. M. J.; Koch, H. *J. Chem. Phys.* **2004**, *120*, 8887–8897.
(325) Zhang, C.; Lipparini, F.; Stopkowicz, S.; Gauss, J.; Cheng, L. *J. Chem. Theory Comput.* **2024**, *20*, 787–798.
(326) Uhlířová, T.; Cianchino, D.; Nottoli, T.; Lipparini, F.; Gauss, J. *J. Phys. Chem. A* **2024**, *128*, 8292–8303.

7 Appendix

7.1 Additional Equations: Coupled-Perturbed Hartree-Fock Theory

The terms that exclude the derivative of the MO coefficients are denoted as $f_{\mu\nu}^{(B_i)}$ in the following,

$$\begin{aligned} 0 = \sum_{\mu\nu} \Bigg\{ & \sum_p c_{\mu p}^* U_{pa}^{B_i *} f_{\mu\nu} c_{\nu i} + c_{\mu a}^* f_{\mu\nu} \sum_p c_{\nu p} U_{pi}^{B_i} + c_{\mu a}^* f_{\mu\nu}^{(B_i)} c_{\nu i} \\ & + c_{\mu a}^* \sum_j \sum_p 2(c_{\sigma p}^* U_{pj}^{B_i *} c_{\rho j} + c_{\sigma j}^* c_{\rho p} U_{pj}^{B_i}) \left(\langle \mu\sigma | \nu\rho \rangle - \frac{1}{2} \langle \mu\sigma | \rho\nu \rangle \right) c_{\nu i} \Bigg\}. \end{aligned} \tag{7.1}$$

Insertion of the LCAO ansatz (eq. (2.16)) makes it possible to rewrite eq. (7.1) to

$$\begin{aligned} 0 = & \sum_p f_{pi} U_{pa}^{B_i *} + \sum_p f_{ap} U_{pi}^{B_i} + f_{ai}^{(B_i)} \\ & + \sum_j \sum_p \left(U_{pj}^{B_i *} (2 \langle ap | ij \rangle - \langle ap | ji \rangle) + U_{pj}^{B_i} (2 \langle aj | ip \rangle - \langle aj | pi \rangle) \right). \end{aligned} \tag{7.2}$$

Using the fact that the Fock operator acting on the spin orbitals yields the orbital energy,

$$\begin{aligned} \langle \phi_p | \hat{F} | \phi_i \rangle &= \varepsilon_i \langle \phi_p | \phi_i \rangle = \varepsilon_i \delta_{pi} = \varepsilon_i \\ \langle \phi_a | \hat{F} | \phi_p \rangle &= \varepsilon_a \langle \phi_a | \phi_p \rangle = \varepsilon_a \delta_{ap} = \varepsilon_a, \end{aligned} \tag{7.3}$$

eq. (7.2) can be written as eq. (2.100).
The derivative of the orthogonality constraint is given as

$$\begin{aligned} \frac{\mathrm{d}}{\mathrm{d}B_i} \langle \phi_p | \phi_q \rangle = 0 &= \sum_{\mu\nu} \left\{ \left(\frac{\partial c_{\mu p}^*}{\partial B_i} \right) S_{\mu\nu} c_{\nu q} + c_{\mu p}^* \left(\frac{\partial S_{\mu\nu}}{\partial B_i} \right) c_{\nu q} + c_{\mu p}^* S_{\mu\nu} \left(\frac{\partial c_{\nu q}}{\partial B_i} \right) \right\} \\ &= \sum_{\mu\nu} \left\{ \sum_r c_{\mu r}^* U_{rp}^{B_i *} S_{\mu\nu} c_{\nu q} + c_{\mu p}^* \left(\frac{\partial S_{\mu\nu}}{\partial B_i} \right) c_{\nu q} + \sum_r c_{\mu p}^* S_{\mu\nu} c_{\nu r} U_{rq}^{B_i} \right\} \\ &= \sum_r U_{rp}^{B_i *} \delta_{rq} + S_{pq}^{B_i} + \sum_r \delta_{pr} U_{rq}^{B_i} \\ &= U_{qp}^{B_i *} + S_{pq}^{B_i} + U_{pq}^{B_i}. \end{aligned} \tag{7.4}$$

The sum in eq. (2.107) contains a sum over generic orbitals that can be split into two sums. The first sum runs over virtual orbitals,

$$\begin{aligned}\sum_b \sum_j \left\{ U_{bj}^{B_i *} (2\langle ab|ij\rangle - \langle ab|ji\rangle) + U_{bj}^{B_i} (2\langle aj|ib\rangle - \langle aj|bi\rangle) \right\} \\ = \sum_b \sum_j \left\{ U_{bj}^{B_i} (2\langle aj|ib\rangle - \langle aj|bi\rangle - 2\langle ab|ij\rangle + \langle ab|ji\rangle) \right\},\end{aligned} \tag{7.5}$$

where eqs. (2.104) and (2.105) are used to simplify the equation. The second sum runs over occupied orbitals,

$$\sum_m \sum_j \left\{ U_{mj}^{B_i *} (2\langle am|ij\rangle - \langle am|ji\rangle) + U_{mj}^{B_i} (2\langle aj|im\rangle - \langle aj|mi\rangle) \right\}, \tag{7.6}$$

and can be merged, since m and j are both indices for occupied orbitals,

$$\begin{aligned}&\frac{1}{2} \sum_{mj} \left\{ U_{mj}^{B_i *} (2\langle am|ij\rangle - \langle am|ji\rangle) + U_{mj}^{B_i} (2\langle aj|im\rangle - \langle aj|mi\rangle) \right\} \\ &+ \frac{1}{2} \sum_{mj} \left\{ U_{jm}^{B_i *} (2\langle aj|im\rangle - \langle aj|mi\rangle) + U_{jm}^{B_i} (2\langle am|ij\rangle - \langle am|ji\rangle) \right\} \\ &= \sum_{mj} S_{jm}^{B_i} \langle am|ji\rangle\end{aligned} \tag{7.7}$$

where eq. (2.104) and the symmetry of the perturbed overlap matrix ($S_{mj}^{B_i} = S_{jm}^{B_i *} = -S_{jm}^{B_i}$) are exploited.

7.2 Additional Equations: Z-Vector Equations

The energy functional in eq. (2.111) can be simplified using the expressions for the MP2 density matrix in eqs. (2.114) to (2.116). This is demonstrated for the fourth term in eq. (2.111)

$$\begin{aligned}&\sum_{ij} \sum_{ab} \lambda_{ab}^{ij} \sum_e f_{ae} t_{ij}^{eb} \quad | \text{ Insert eq. (2.113)} \\ &\rightarrow \sum_{ij} \sum_{ab} \sum_e \tilde{t}_{ij}^{ab*} f_{ae} t_{ij}^{eb} \quad | \text{ Use eq. (2.115)} \\ &\rightarrow \frac{1}{2} \sum_{ae} D_{ae} f_{ae}.\end{aligned} \tag{7.8}$$

Additionally,

$$2 \sum_a \sum_i Z_{ai} f_{ai} = \sum_a \sum_i (Z_{ai} f_{ai} + Z_{ia}^* f_{ia}) = \sum_a \sum_i D_{ai} f_{ai}, \tag{7.9}$$

is exploited.

The derivative with respect to the occupied-occupied block in eq. (2.119) is derived, where the first term is from the HF part,

$$\sum_i 2h_{ii} + \frac{1}{2} \sum_{ij} (4\langle ij|ij\rangle - 2\langle ij|ji\rangle) = 2 \sum_i \sum_\nu \langle i|\hat{h}|\nu\rangle c_{\nu i} + \frac{1}{2} \sum_{ij} \sum_\nu 4\langle ij|\nu j\rangle c_{\nu i}$$

$$
\begin{aligned}
&- \frac{1}{2}\sum_{ij}\sum_{\nu} 2\,\langle ij|j\nu\rangle\, c_{\nu i} \qquad (7.10)\\
&+ \frac{1}{2}\sum_{ij}\sum_{\nu} 4\,\langle ij|i\nu\rangle\, c_{\nu j}\\
&- \frac{1}{2}\sum_{ij}\sum_{\nu} 2\,\langle ij|\rho j\rangle\, c_{\nu j}.
\end{aligned}
$$

In the previous equation, only the coefficients containing T_{pq} are considered, since the other coefficients contains T^*_{pq}. Subsequent differentiation provides

$$
\begin{aligned}
\frac{\partial \tilde{E}}{\partial T_{ij}} \to \frac{\partial \tilde{E}}{\partial T_{kl}} &= 2h_{lk} + \frac{1}{2}\left(4\,\langle lj|kj\rangle + 4\,\langle il|ik\rangle - 2\,\langle il|ki\rangle - 2\,\langle lj|ik\rangle\right)\\
&= 2\sum_{kl}\left\{h_{lk} + \left(2\,\langle lj|kj\rangle - \langle lj|jk\rangle\right)\right\} = 2f_{kl} = \delta_{kl}\varepsilon_k \;\; | \; k \to j,\; l \to i \qquad (7.11)\\
&= 2\delta_{ji}\varepsilon_i,
\end{aligned}
$$

and the procedure continues in the same way for all other terms, leading to eq. (2.119). Equations for the occupied-occupied block of the Lagrange multiplier I_{pq},

$$
\begin{aligned}
\frac{\partial I_{ij}}{\partial B_j} = &- \left(\frac{\partial D_{ij}}{\partial B_j}\right)\varepsilon_i - \sum_{pq}\left(\frac{\partial D_{pq}}{\partial B_j}\right)\left(\langle pj|qi\rangle - \frac{1}{2}\langle pj|iq\rangle\right) - \sum_{pq} D_{pq}\left(\frac{\partial\,\langle pj|qi\rangle}{\partial B_j} - \frac{1}{2}\frac{\partial\,\langle pj|iq\rangle}{\partial B_j}\right)\\
&- 2\sum_{m}\sum_{ef}\left(\frac{\partial t^{ef\,*}_{jm}}{\partial B_j}\langle ef|im\rangle\right) - 2\sum_{m}\sum_{ef} t^{ef\,*}_{jm}\left(\frac{\partial\,\langle ef|im\rangle}{\partial B_j}\right),
\end{aligned}
\qquad (7.12)
$$

the virtual-virtual block,

$$
\frac{\partial I_{ab}}{\partial B_j} = - \left(\frac{\partial D_{ab}}{\partial B_j}\right)\varepsilon_a - 2\sum_{mn}\sum_{e}\left(\frac{\partial t^{be\,*}_{mn}}{\partial B_j}\langle mn|ae\rangle\right) - 2\sum_{mn}\sum_{e} t^{be\,*}_{mn}\left(\frac{\partial\,\langle mn|ae\rangle}{\partial B_j}\right), \qquad (7.13)
$$

and the virtual-occupied block

$$
\frac{\partial I_{ai}}{\partial B_j} = - \left(\frac{\partial D_{ai}}{\partial B_j}\right)\varepsilon_i - \sum_{mn}\sum_{e}\left(\frac{\partial t^{ae\,*}_{mn}}{\partial B_j}\langle ie|mn\rangle\right) - \sum_{mn}\sum_{e} t^{ae\,*}_{mn}\left(\frac{\partial\,\langle ie|mn\rangle}{\partial B_j}\right), \qquad (7.14)
$$

are presented.

7.3 Additional Equations: McMurchie-Davidson Scheme

7.3.1 NMR Integrals

$$\begin{aligned}\left(\frac{\partial \langle\mu\sigma|\nu\rho\rangle}{\partial B_y}\right)_{\mathbf{B}=0} =& E_{\mu\nu}E_{\sigma\rho}\frac{i}{2}(\mathbf{R}_{\mu_z}-\mathbf{R}_{\nu_z})\sum_N x d_N^{n_An_B}\sum_L e_L^{l_Al_B}\sum_M f_M^{m_Am_B}\cdot\\ &\sum_{N'L'M'} D_{N'L'M'}\left[NLM|\tfrac{1}{r_{12}}|N'L'M'\right]\\ &- E_{\mu\nu}E_{\sigma\rho}\frac{i}{2}(\mathbf{R}_{\mu_x}-\mathbf{R}_{\nu_x})\sum_N d_N^{n_An_B}\sum_L e_L^{l_Al_B}\sum_M z f_M^{m_Am_B}\cdot\\ &\sum_{N'L'M'} D_{N'L'M'}\left[NLM|\tfrac{1}{r_{12}}|N'L'M'\right]\\ &+ E_{\mu\nu}E_{\sigma\rho}\frac{i}{2}(\mathbf{R}_{\sigma_z}-\mathbf{R}_{\rho_z})\sum_{N'} x d_{N'}^{n_Cn_D}\sum_{L'} e_{L'}^{l_Cl_D}\sum_{M'} f_{M'}^{m_Cm_D}\cdot\\ &\sum_{NLM} D_{NLM}\left[NLM|\tfrac{1}{r_{12}}|N'L'M'\right]\\ &- E_{\mu\nu}E_{\sigma\rho}\frac{i}{2}(\mathbf{R}_{\sigma_x}-\mathbf{R}_{\rho_x})\sum_{N'} d_{N'}^{n_Cn_D}\sum_{L'} e_{L'}^{l_Cl_D}\sum_{M'} z f_{M'}^{m_Cm_D}\cdot\\ &\sum_{NLM} D_{NLM}\left[NLM|\tfrac{1}{r_{12}}|N'L'M'\right]\end{aligned} \tag{7.15}$$

$$\begin{aligned}\left(\frac{\partial \langle\mu\sigma|\nu\rho\rangle}{\partial B_z}\right)_{\mathbf{B}=0} =& E_{\mu\nu}E_{\sigma\rho}\frac{i}{2}(\mathbf{R}_{\mu_x}-\mathbf{R}_{\nu_x})\sum_N d_N^{n_An_B}\sum_L y e_L^{l_Al_B}\sum_M f_M^{m_Am_B}\cdot\\ &\sum_{N'L'M'} D_{N'L'M'}\left[NLM|\tfrac{1}{r_{12}}|N'L'M'\right]\\ &- E_{\mu\nu}E_{\sigma\rho}\frac{i}{2}(\mathbf{R}_{\mu_y}-\mathbf{R}_{\nu_y})\sum_N x d_N^{n_An_B}\sum_L e_L^{l_Al_B}\sum_M f_M^{m_Am_B}\cdot\\ &\sum_{N'L'M'} D_{N'L'M'}\left[NLM|\tfrac{1}{r_{12}}|N'L'M'\right]\\ &+ E_{\mu\nu}E_{\sigma\rho}\frac{i}{2}(\mathbf{R}_{\sigma_x}-\mathbf{R}_{\rho_x})\sum_{N'} d_{N'}^{n_Cn_D}\sum_{L'} y e_{L'}^{l_Cl_D}\sum_{M'} f_{M'}^{m_Cm_D}\cdot\\ &\sum_{NLM} D_{NLM}\left[NLM|\tfrac{1}{r_{12}}|N'L'M'\right]\\ &- E_{\mu\nu}E_{\sigma\rho}\frac{i}{2}(\mathbf{R}_{\sigma_y}-\mathbf{R}_{\rho_y})\sum_{N'} x d_{N'}^{n_Cn_D}\sum_{L'} e_{L'}^{l_Cl_D}\sum_{M'} f_{M'}^{m_Cm_D}\cdot\\ &\sum_{NLM} D_{NLM}\left[NLM|\tfrac{1}{r_{12}}|N'L'M'\right]\end{aligned} \tag{7.16}$$

7.3.2 Magnetizability Integrals

In this subsection, the additional magnetizability integrals are given, using the shorthand notations in eq. (3.26) and eq. (3.25).

$$\left(\frac{\partial(\mu\nu|\sigma\rho)}{\partial B_y\partial B_y}\right)_{\mathrm{B}=0} = -\frac{1}{4}E_{\mu\nu}E_{\sigma\rho}$$

$$
\begin{aligned}
&\cdot\Bigg\{(\mathbf{R}_{\mu_z}-\mathbf{R}_{\nu_z})^2\sum_{NLM}^{n+2,l,m}D^{xx}_{NLM}\sum_{N'L'M'}^{n'l'm'}D_{N'L'M'}[\,NLM|\tfrac{1}{\mathrm{r}_{12}}|N'L'M']\\
&+(\mathbf{R}_{\mu_x}-\mathbf{R}_{\nu_x})^2\sum_{NLM}^{n,l,m+2}D^{zz}_{NLM}\sum_{N'L'M'}^{n'l'm'}D_{N'L'M'}[\,NLM|\tfrac{1}{\mathrm{r}_{12}}|N'L'M']\\
&+(\mathbf{R}_{\sigma_z}-\mathbf{R}_{\rho_z})^2\sum_{N'L'M'}^{n'+2,l',m'}D^{xx}_{N'L'M'}\sum_{NLM}^{nlm}D_{NLM}[\,NLM|\tfrac{1}{\mathrm{r}_{12}}|N'L'M']\\
&+(\mathbf{R}_{\sigma_x}-\mathbf{R}_{\rho_x})^2\sum_{N'L'M'}^{n',l',m'+2}D^{zz}_{N'L'M'}\sum_{NLM}^{nlm}D_{NLM}[\,NLM|\tfrac{1}{\mathrm{r}_{12}}|N'L'M']\\
&-2(\mathbf{R}_{\mu_z}-\mathbf{R}_{\nu_z})(\mathbf{R}_{\mu_x}-\mathbf{R}_{\nu_x})\sum_{NLM}^{n+1,l,m+1}D^{xz}_{NLM}\sum_{N'L'M'}^{n'l'm'}D_{N'L'M'}\\
&\quad\cdot[\,NLM|\tfrac{1}{\mathrm{r}_{12}}|N'L'M']\\
&+2(\mathbf{R}_{\mu_z}-\mathbf{R}_{\nu_z})(\mathbf{R}_{\sigma_z}-\mathbf{R}_{\rho_z})\sum_{NLM}^{n+1,l,m}D^{x}_{NLM}\sum_{N'L'M'}^{n'+1,l',m'}D^{x}_{N'L'M'}\\
&\quad\cdot[\,NLM|\tfrac{1}{\mathrm{r}_{12}}|N'L'M']\\
&-2(\mathbf{R}_{\mu_z}-\mathbf{R}_{\nu_z})(\mathbf{R}_{\sigma_x}-\mathbf{R}_{\rho_x})\sum_{NLM}^{n+1,l,m}D^{x}_{NLM}\sum_{N'L'M'}^{n',l',m'+1}D^{z}_{N'L'M'}\\
&\quad\cdot[\,NLM|\tfrac{1}{\mathrm{r}_{12}}|N'L'M']\\
&-2(\mathbf{R}_{\mu_x}-\mathbf{R}_{\nu_x})(\mathbf{R}_{\sigma_z}-\mathbf{R}_{\rho_z})\sum_{NLM}^{n,l,m+1}D^{z}_{NLM}\sum_{N'L'M'}^{n'+1,l',m'}D^{x}_{N'L'M'}\\
&\quad\cdot[\,NLM|\tfrac{1}{\mathrm{r}_{12}}|N'L'M']\\
&+2(\mathbf{R}_{\mu_x}-\mathbf{R}_{\nu_x})(\mathbf{R}_{\sigma_x}-\mathbf{R}_{\rho_x})\sum_{NLM}^{n,l,m+1}D^{z}_{NLM}\sum_{N'L'M'}^{n',l',m'+1}D^{z}_{N'L'M'}\\
&\quad\cdot[\,NLM|\tfrac{1}{\mathrm{r}_{12}}|N'L'M']\\
&-2(\mathbf{R}_{\sigma_z}-\mathbf{R}_{\rho_z})(\mathbf{R}_{\sigma_x}-\mathbf{R}_{\rho_x})\sum_{NLM}^{nlm}D_{NLM}\sum_{N'L'M'}^{n'+1,l',m'+1}D^{xz}_{N'L'M'}\\
&\quad\cdot[\,NLM|\tfrac{1}{\mathrm{r}_{12}}|N'L'M']\Bigg\}
\end{aligned}
\tag{7.17a}
$$

$$
\begin{aligned}
\left(\frac{\partial(\mu\nu|\sigma\rho)}{\partial B_z\partial B_z}\right)_{\mathrm{B}=0} =& -\frac{1}{4}E_{\mu\nu}E_{\sigma\rho}\\
&\cdot\Bigg\{(\mathbf{R}_{\mu_x}-\mathbf{R}_{\nu_x})^2\sum_{NLM}^{n,l+2,m}D^{yy}_{NLM}\sum_{N'L'M'}^{n'l'm'}D_{N'L'M'}[\,NLM|\tfrac{1}{\mathrm{r}_{12}}|N'L'M']\\
&+(\mathbf{R}_{\mu_y}-\mathbf{R}_{\nu_y})^2\sum_{NLM}^{n+2,l,m}D^{xx}_{NLM}\sum_{N'L'M'}^{n'l'm'}D_{N'L'M'}[\,NLM|\tfrac{1}{\mathrm{r}_{12}}|N'L'M']\\
&+(\mathbf{R}_{\sigma_x}-\mathbf{R}_{\rho_x})^2\sum_{N'L'M'}^{n',l'+2,m'}D^{yy}_{N'L'M'}\sum_{NLM}^{nlm}D_{NLM}[\,NLM|\tfrac{1}{\mathrm{r}_{12}}|N'L'M']
\end{aligned}
$$

$$
\begin{aligned}
&+ (\mathbf{R}_{\sigma_y} - \mathbf{R}_{\rho_y})^2 \sum_{N'L'M'}^{n'+2,l',m'} D^{xx}_{N'L'M'} \sum_{NLM}^{nlm} D_{NLM}[\,NLM|\tfrac{1}{\mathrm{r}_{12}}|N'L'M'] \qquad (7.18a)\\
&- 2(\mathbf{R}_{\mu_x} - \mathbf{R}_{\nu_x})(\mathbf{R}_{\mu_y} - \mathbf{R}_{\nu_y}) \sum_{NLM}^{n+1,l+1,m} D^{xy}_{NLM} \sum_{N'L'M'}^{n'l'm'} D_{N'L'M'}\\
&\quad \cdot [\,NLM|\tfrac{1}{\mathrm{r}_{12}}|N'L'M']\\
&+ 2(\mathbf{R}_{\mu_x} - \mathbf{R}_{\nu_x})(\mathbf{R}_{\sigma_x} - \mathbf{R}_{\rho_x}) \sum_{NLM}^{n,l+1,m} D^{y}_{NLM} \sum_{N'L'M'}^{n',l'+1,m'} D^{y}_{N'L'M'}\\
&\quad \cdot [\,NLM|\tfrac{1}{\mathrm{r}_{12}}|N'L'M']\\
&- 2(\mathbf{R}_{\mu_x} - \mathbf{R}_{\nu_x})(\mathbf{R}_{\sigma_y} - \mathbf{R}_{\rho_y}) \sum_{NLM}^{n,l+1,m} D^{y}_{NLM} \sum_{N'L'M'}^{n'+1,l',m'} D^{x}_{N'L'M'}\\
&\quad \cdot [\,NLM|\tfrac{1}{\mathrm{r}_{12}}|N'L'M']\\
&- 2(\mathbf{R}_{\mu_y} - \mathbf{R}_{\nu_y})(\mathbf{R}_{\sigma_x} - \mathbf{R}_{\rho_x}) \sum_{NLM}^{n+1,l,m} D^{x}_{NLM} \sum_{N'L'M'}^{n',l'+1,m'} D_{N'L'M'}{}^{y}\\
&\quad \cdot [\,NLM|\tfrac{1}{\mathrm{r}_{12}}|N'L'M']\\
&+ 2(\mathbf{R}_{\mu_y} - \mathbf{R}_{\nu_y})(\mathbf{R}_{\sigma_y} - \mathbf{R}_{\rho_y}) \sum_{NLM}^{n+1,l,m} D^{x}_{NLM} \sum_{N'L'M'}^{n'+1,l',m'} D^{x}_{N'L'M'}\\
&\quad \cdot [\,NLM|\tfrac{1}{\mathrm{r}_{12}}|N'L'M']\\
&- 2(\mathbf{R}_{\sigma_x} - \mathbf{R}_{\rho_x})(\mathbf{R}_{\sigma_y} - \mathbf{R}_{\rho_y}) \sum_{NLM}^{nlm} D_{NLM} \sum_{N'L'M'}^{n'+1,l'+1,m'} D^{xy}_{N'L'M'}\\
&\quad \cdot [\,NLM|\tfrac{1}{\mathrm{r}_{12}}|N'L'M'] \Big\}
\end{aligned}
$$

$$
\begin{aligned}
\left(\frac{\partial(\mu\nu|\sigma\rho)}{\partial B_x \partial B_y}\right)_{\mathrm{B}=0} = &-\frac{1}{4} E_{\mu\nu} E_{\sigma\rho}\\
&\cdot \Big\{ (\mathbf{R}_{\mu_y} - \mathbf{R}_{\nu_y})(\mathbf{R}_{\mu_z} - \mathbf{R}_{\nu_z}) \sum_{NLM}^{n+1,l,m+1} D^{xz}_{NLM} \sum_{N'L'M'}^{n'l'm'} D_{N'L'M'}\\
&\quad \cdot [\,NLM|\tfrac{1}{\mathrm{r}_{12}}|N'L'M']\\
&\quad - (\mathbf{R}_{\mu_y} - \mathbf{R}_{\nu_y})(\mathbf{R}_{\mu_x} - \mathbf{R}_{\nu_x}) \sum_{NLM}^{n,l,m+2} D^{zz}_{NLM} \sum_{N'L'M'}^{n'l'm'} D_{N'L'M'}\\
&\quad \cdot [\,NLM|\tfrac{1}{\mathrm{r}_{12}}|N'L'M']\\
&\quad - (\mathbf{R}_{\mu_z} - \mathbf{R}_{\nu_z})(\mathbf{R}_{\mu_z} - \mathbf{R}_{\nu_z}) \sum_{NLM}^{n+1,l+1,m} D^{xy}_{NLM} \sum_{N'L'M'}^{n'l'm'} D_{N'L'M'}\\
&\quad \cdot [\,NLM|\tfrac{1}{\mathrm{r}_{12}}|N'L'M']\\
&\quad + (\mathbf{R}_{\mu_z} - \mathbf{R}_{\nu_z})(\mathbf{R}_{\mu_x} - \mathbf{R}_{\nu_x}) \sum_{NLM}^{n,l+1,m+1} D^{yz}_{NLM} \sum_{N'L'M'}^{n'l'm'} D_{N'L'M'}\\
&\quad \cdot [\,NLM|\tfrac{1}{\mathrm{r}_{12}}|N'L'M']
\end{aligned}
$$

$$
\begin{aligned}
&+ (\mathbf{R}_{\mu_y} - \mathbf{R}_{\nu_y})(\mathbf{R}_{\sigma_z} - \mathbf{R}_{\rho_z}) \sum_{NLM}^{n,l,m+1} D^z_{NLM} \sum_{N'L'M'}^{n'+1,l',m'} D^x_{N'L'M'} \\
&\quad \cdot [\, NLM|\tfrac{1}{\mathrm{r}_{12}}|N'L'M'] \qquad (7.19a) \\
&- (\mathbf{R}_{\mu_z} - \mathbf{R}_{\nu_z})(\mathbf{R}_{\sigma_z} - \mathbf{R}_{\rho_z}) \sum_{NLM}^{n,l+1,m} D^y_{NLM} \sum_{N'L'M'}^{n'+1,l',m'} D^x_{N'L'M'} \\
&\quad \cdot [\, NLM|\tfrac{1}{\mathrm{r}_{12}}|N'L'M'] \\
&- (\mathbf{R}_{\mu_y} - \mathbf{R}_{\nu_y})(\mathbf{R}_{\sigma_x} - \mathbf{R}_{\rho_x}) \sum_{NLM}^{n,l,m+1} D^z_{NLM} \sum_{N'L'M'}^{n',l',m'+1} D^z_{N'L'M'} \\
&\quad \cdot [\, NLM|\tfrac{1}{\mathrm{r}_{12}}|N'L'M'] \\
&+ (\mathbf{R}_{\mu_z} - \mathbf{R}_{\nu_z})(\mathbf{R}_{\sigma_x} - \mathbf{R}_{\rho_x}) \sum_{NLM}^{n,l+1,m} D^y_{NLM} \sum_{N'L'M'}^{n',l',m'+1} D^z_{N'L'M'} \\
&\quad \cdot [\, NLM|\tfrac{1}{\mathrm{r}_{12}}|N'L'M'] \\
&+ (\mathbf{R}_{\mu_z} - \mathbf{R}_{\nu_z})(\mathbf{R}_{\sigma_y} - \mathbf{R}_{\rho_y}) \sum_{NLM}^{n+1,l,m} D^x_{NLM} \sum_{N'L'M'}^{n',l',m'+1} D^z_{N'L'M'} \\
&\quad \cdot [\, NLM|\tfrac{1}{\mathrm{r}_{12}}|N'L'M'] \\
&- (\mathbf{R}_{\mu_x} - \mathbf{R}_{\nu_x})(\mathbf{R}_{\sigma_y} - \mathbf{R}_{\rho_y}) \sum_{NLM}^{n,l,m+1} D^z_{NLM} \sum_{N'L'M'}^{n',l',m'+1} D^z_{N'L'M'} \\
&\quad \cdot [\, NLM|\tfrac{1}{\mathrm{r}_{12}}|N'L'M'] \\
&- (\mathbf{R}_{\mu_z} - \mathbf{R}_{\nu_z})(\mathbf{R}_{\sigma_z} - \mathbf{R}_{\rho_z}) \sum_{NLM}^{n+1,l,m} D^x_{NLM} \sum_{N'L'M'}^{n',l'+1,m'} D^y_{N'L'M'} \\
&\quad \cdot [\, NLM|\tfrac{1}{\mathrm{r}_{12}}|N'L'M'] \\
&+ (\mathbf{R}_{\mu_x} - \mathbf{R}_{\nu_x})(\mathbf{R}_{\sigma_z} - \mathbf{R}_{\rho_z}) \sum_{NLM}^{n,l,m+1} D^z_{NLM} \sum_{N'L'M'}^{n',l'+1,m'} D^y_{N'L'M'} \\
&\quad \cdot [\, NLM|\tfrac{1}{\mathrm{r}_{12}}|N'L'M'] \\
&+ (\mathbf{R}_{\sigma_y} - \mathbf{R}_{\rho_y})(\mathbf{R}_{\sigma_z} - \mathbf{R}_{\rho_z}) \sum_{NLM}^{n,l,m} D_{NLM} \sum_{N'L'M'}^{n'+1,l',m'+1} D^{xz}_{N'L'M'} \\
&\quad \cdot [\, NLM|\tfrac{1}{\mathrm{r}_{12}}|N'L'M'] \\
&- (\mathbf{R}_{\sigma_y} - \mathbf{R}_{\rho_y})(\mathbf{R}_{\sigma_x} - \mathbf{R}_{\rho_x}) \sum_{NLM}^{n,l,m} D_{NLM} \sum_{N'L'M'}^{n',l',m'+2} D^{zz}_{N'L'M'} \\
&\quad \cdot [\, NLM|\tfrac{1}{\mathrm{r}_{12}}|N'L'M'] \\
&+ (\mathbf{R}_{\sigma_z} - \mathbf{R}_{\rho_z})(\mathbf{R}_{\sigma_x} - \mathbf{R}_{\rho_x}) \sum_{NLM}^{n,l,m} D_{NLM} \sum_{N'L'M'}^{n',l'+1,m'+1} D^{yz}_{N'L'M'} \\
&\quad \cdot [\, NLM|\tfrac{1}{\mathrm{r}_{12}}|N'L'M'] \\
&- (\mathbf{R}_{\sigma_z} - \mathbf{R}_{\rho_z})(\mathbf{R}_{\sigma_z} - \mathbf{R}_{\rho_z}) \sum_{NLM}^{n,l,m} D_{NLM} \sum_{N'L'M'}^{n'+1,l'+1,m'} D^{xy}_{N'L'M'} \\
&\quad \cdot [\, NLM|\tfrac{1}{\mathrm{r}_{12}}|N'L'M'] \Big\}
\end{aligned}
$$

$$
\begin{aligned}
\left(\frac{\partial(\mu\nu|\sigma\rho)}{\partial B_x \partial B_z}\right)_{\mathrm{B=0}} = &-\frac{1}{4}E_{\mu\nu}E_{\sigma\rho} \\
&\cdot\Bigg\{(\mathbf{R}_{\mu_y}-\mathbf{R}_{\nu_y})(\mathbf{R}_{\mu_x}-\mathbf{R}_{\nu_x})\sum_{NLM}^{n,l+1,m+1} D^{yz}_{NLM}\sum_{N'L'M'}^{n'l'm'} D_{N'L'M'} \\
&\quad\cdot[\,NLM|\tfrac{1}{\mathrm{r}_{12}}|N'L'M'] \\
&-(\mathbf{R}_{\mu_y}-\mathbf{R}_{\nu_y})(\mathbf{R}_{\mu_y}-\mathbf{R}_{\nu_y})\sum_{NLM}^{n+1,l,m+1} D^{xz}_{NLM}\sum_{N'L'M'}^{n'l'm'} D_{N'L'M'} \\
&\quad\cdot[\,NLM|\tfrac{1}{\mathrm{r}_{12}}|N'L'M'] \\
&-(\mathbf{R}_{\mu_z}-\mathbf{R}_{\nu_z})(\mathbf{R}_{\mu_x}-\mathbf{R}_{\nu_x})\sum_{NLM}^{n,l+2,m} D^{yy}_{NLM}\sum_{N'L'M'}^{n'l'm'} D_{N'L'M'} \\
&\quad\cdot[\,NLM|\tfrac{1}{\mathrm{r}_{12}}|N'L'M'] \\
&+(\mathbf{R}_{\mu_z}-\mathbf{R}_{\nu_z})(\mathbf{R}_{\mu_y}-\mathbf{R}_{\nu_y})\sum_{NLM}^{n+1,l+1,m} D^{xy}_{NLM}\sum_{N'L'M'}^{n'l'm'} D_{N'L'M'} \\
&\quad\cdot[\,NLM|\tfrac{1}{\mathrm{r}_{12}}|N'L'M'] \\
&+(\mathbf{R}_{\mu_y}-\mathbf{R}_{\nu_y})(\mathbf{R}_{\sigma_x}-\mathbf{R}_{\rho_x})\sum_{NLM}^{n,l,m+1} D^{z}_{NLM}\sum_{N'L'M'}^{n',l'+1,m'} D^{y}_{N'L'M'} \\
&\quad\cdot[\,NLM|\tfrac{1}{\mathrm{r}_{12}}|N'L'M'] \qquad (7.20a)\\
&-(\mathbf{R}_{\mu_z}-\mathbf{R}_{\nu_z})(\mathbf{R}_{\sigma_x}-\mathbf{R}_{\rho_x})\sum_{NLM}^{n,l+1,m} D^{y}_{NLM}\sum_{N'L'M'}^{n',l'+1,m'} D^{y}_{N'L'M'} \\
&\quad\cdot[\,NLM|\tfrac{1}{\mathrm{r}_{12}}|N'L'M'] \\
&-(\mathbf{R}_{\mu_x}-\mathbf{R}_{\nu_x})(\mathbf{R}_{\sigma_z}-\mathbf{R}_{\rho_z})\sum_{NLM}^{n,l+1,m} D^{y}_{NLM}\sum_{N'L'M'}^{n',l'+1,m'} D^{y}_{N'L'M'} \\
&\quad\cdot[\,NLM|\tfrac{1}{\mathrm{r}_{12}}|N'L'M'] \\
&+(\mathbf{R}_{\mu_y}-\mathbf{R}_{\nu_y})(\mathbf{R}_{\sigma_z}-\mathbf{R}_{\rho_z})\sum_{NLM}^{n+1,l,m} D^{x}_{NLM}\sum_{N'L'M'}^{n',l'+1,m'} D^{y}_{N'L'M'} \\
&\quad\cdot[\,NLM|\tfrac{1}{\mathrm{r}_{12}}|N'L'M'] \\
&+(\mathbf{R}_{\mu_x}-\mathbf{R}_{\nu_x})(\mathbf{R}_{\sigma_y}-\mathbf{R}_{\rho_y})\sum_{NLM}^{n,l+1,m} D^{y}_{NLM}\sum_{N'L'M'}^{n',l',m'+1} D^{z}_{N'L'M'} \\
&\quad\cdot[\,NLM|\tfrac{1}{\mathrm{r}_{12}}|N'L'M'] \\
&-(\mathbf{R}_{\mu_y}-\mathbf{R}_{\nu_y})(\mathbf{R}_{\sigma_y}-\mathbf{R}_{\rho_y})\sum_{NLM}^{n+1,l,m} D^{x}_{NLM}\sum_{N'L'M'}^{n',l',m'+1} D^{z}_{N'L'M'} \\
&\quad\cdot[\,NLM|\tfrac{1}{\mathrm{r}_{12}}|N'L'M'] \\
&-(\mathbf{R}_{\sigma_z}-\mathbf{R}_{\rho_z})(\mathbf{R}_{\sigma_x}-\mathbf{R}_{\rho_x})\sum_{NLM}^{n,l,m} D_{NLM}\sum_{N'L'M'}^{n',l',m'+2} D^{yy}_{N'L'M'} \\
&\quad\cdot[\,NLM|\tfrac{1}{\mathrm{r}_{12}}|N'L'M'] \\
\end{aligned}
$$

$$
\begin{aligned}
&- (\mathbf{R}_{\mu_y} - \mathbf{R}_{\nu_y})(\mathbf{R}_{\sigma_y} - \mathbf{R}_{\rho_y}) \sum_{NLM}^{n,l,m+1} D^z_{NLM} \sum_{N'L'M'}^{n'+1,l',m'} D^x_{N'L'M'} \\
&\quad \cdot [\, NLM|\tfrac{1}{\mathrm{r}_{12}}|N'L'M'] \\
&+ (\mathbf{R}_{\mu_z} - \mathbf{R}_{\nu_z})(\mathbf{R}_{\sigma_y} - \mathbf{R}_{\rho_y}) \sum_{NLM}^{n,l+1,m} D^y_{NLM} \sum_{N'L'M'}^{n'+1,l',m'} D^x_{N'L'M'} \\
&\quad \cdot [\, NLM|\tfrac{1}{\mathrm{r}_{12}}|N'L'M'] \\
&+ (\mathbf{R}_{\sigma_y} - \mathbf{R}_{\rho_y})(\mathbf{R}_{\sigma_x} - \mathbf{R}_{\rho_x}) \sum_{NLM}^{n,l,m} D_{NLM} \sum_{N'L'M'}^{n',l'+1,m'+1} D^{yz}_{N'L'M'} \\
&\quad \cdot [\, NLM|\tfrac{1}{\mathrm{r}_{12}}|N'L'M'] \\
&+ (\mathbf{R}_{\sigma_z} - \mathbf{R}_{\rho_z})(\mathbf{R}_{\sigma_y} - \mathbf{R}_{\rho_y}) \sum_{NLM}^{n,l,m} D_{NLM} \sum_{N'L'M'}^{n'+1,l'+1,m'} D^{xy}_{N'L'M'} \\
&\quad \cdot [\, NLM|\tfrac{1}{\mathrm{r}_{12}}|N'L'M'] \\
&- (\mathbf{R}_{\sigma_y} - \mathbf{R}_{\rho_y})(\mathbf{R}_{\sigma_y} - \mathbf{R}_{\rho_y}) \sum_{NLM}^{n,l,m} D_{NLM} \sum_{N'L'M'}^{n'+1,l',m'+1} D^{xz}_{N'L'M'} \\
&\quad \cdot [\, NLM|\tfrac{1}{\mathrm{r}_{12}}|N'L'M'] \Big\}
\end{aligned}
$$

$$
\begin{aligned}
\left(\frac{\partial(\mu\nu|\sigma\rho)}{\partial B_y \partial B_z}\right)_{\mathrm{B}=0} = &- \frac{1}{4} E_{\mu\nu} E_{\sigma\rho} \\
&\cdot \Big\{ (\mathbf{R}_{\mu_z} - \mathbf{R}_{\nu_z})(\mathbf{R}_{\mu_x} - \mathbf{R}_{\nu_x}) \sum_{NLM}^{n+1,l+1,m} D^{xy}_{NLM} \sum_{N'L'M'}^{n'l'm'} D_{N'L'M'} \\
&\quad \cdot [\, NLM|\tfrac{1}{\mathrm{r}_{12}}|N'L'M'] \\
&- (\mathbf{R}_{\mu_z} - \mathbf{R}_{\nu_z})(\mathbf{R}_{\mu_y} - \mathbf{R}_{\nu_y}) \sum_{NLM}^{n+2,l,m} D^{xx}_{NLM} \sum_{N'L'M'}^{n'l'm'} D_{N'L'M'} \\
&\quad \cdot [\, NLM|\tfrac{1}{\mathrm{r}_{12}}|N'L'M'] \\
&- (\mathbf{R}_{\mu_x} - \mathbf{R}_{\nu_x})(\mathbf{R}_{\mu_x} - \mathbf{R}_{\nu_x}) \sum_{NLM}^{n,l+1,m+1} D^{yz}_{NLM} \sum_{N'L'M'}^{n'l'm'} D_{N'L'M'} \\
&\quad \cdot [\, NLM|\tfrac{1}{\mathrm{r}_{12}}|N'L'M'] \\
&+ (\mathbf{R}_{\mu_x} - \mathbf{R}_{\nu_x})(\mathbf{R}_{\mu_y} - \mathbf{R}_{\nu_y}) \sum_{NLM}^{n+1,l,m+1} D^{xz}_{NLM} \sum_{N'L'M'}^{n'l'm'} D_{N'L'M'} \\
&\quad \cdot [\, NLM|\tfrac{1}{\mathrm{r}_{12}}|N'L'M'] \\
&+ (\mathbf{R}_{\mu_z} - \mathbf{R}_{\nu_z})(\mathbf{R}_{\sigma_x} - \mathbf{R}_{\rho_x}) \sum_{NLM}^{n+1,l,m} D^x_{NLM} \sum_{N'L'M'}^{n',l'+1,m'} D^y_{N'L'M'} \\
&\quad \cdot [\, NLM|\tfrac{1}{\mathrm{r}_{12}}|N'L'M'] \\
&- (\mathbf{R}_{\mu_x} - \mathbf{R}_{\nu_x})(\mathbf{R}_{\sigma_x} - \mathbf{R}_{\rho_x}) \sum_{NLM}^{n,l,m+1} D^z_{NLM} \sum_{N'L'M'}^{n',l'+1,m'} D^y_{N'L'M'} \\
&\quad \cdot [\, NLM|\tfrac{1}{\mathrm{r}_{12}}|N'L'M'] \qquad (7.21a)
\end{aligned}
$$

$$
\begin{aligned}
&- (\mathbf{R}_{\sigma_z} - \mathbf{R}_{\rho_z})(\mathbf{R}_{\sigma_y} - \mathbf{R}_{\rho_y}) \sum_{NLM}^{n,l,m} D_{NLM} \sum_{N'L'M'}^{n'+2,l',m'} D^{xx}_{N'L'M'} \\
&\quad \cdot [\, NLM|\tfrac{1}{\mathrm{r}_{12}}|N'L'M'] \\
&- (\mathbf{R}_{\mu_z} - \mathbf{R}_{\nu_z})(\mathbf{R}_{\sigma_y} - \mathbf{R}_{\rho_y}) \sum_{NLM}^{n+1,l,m} D^{x}_{NLM} \sum_{N'L'M'}^{n'+1,l',m'} D^{x}_{N'L'M'} \\
&\quad \cdot [\, NLM|\tfrac{1}{\mathrm{r}_{12}}|N'L'M'] \\
&+ (\mathbf{R}_{\mu_x} - \mathbf{R}_{\nu_x})(\mathbf{R}_{\sigma_y} - \mathbf{R}_{\rho_y}) \sum_{NLM}^{n,l,m+1} D^{z}_{NLM} \sum_{N'L'M'}^{n'+1,l',m'} D^{x}_{N'L'M'} \\
&\quad \cdot [\, NLM|\tfrac{1}{\mathrm{r}_{12}}|N'L'M'] \\
&+ (\mathbf{R}_{\mu_x} - \mathbf{R}_{\nu_x})(\mathbf{R}_{\sigma_z} - \mathbf{R}_{\rho_z}) \sum_{NLM}^{n,l+1,m} D^{y}_{NLM} \sum_{N'L'M'}^{n'+1,l',m'} D^{x}_{N'L'M'} \\
&\quad \cdot [\, NLM|\tfrac{1}{\mathrm{r}_{12}}|N'L'M'] \\
&- (\mathbf{R}_{\mu_y} - \mathbf{R}_{\nu_y})(\mathbf{R}_{\sigma_z} - \mathbf{R}_{\rho_z}) \sum_{NLM}^{n+1,l,m} D^{x}_{NLM} \sum_{N'L'M'}^{n'+1,l',m'} D^{x}_{N'L'M'} \\
&\quad \cdot [\, NLM|\tfrac{1}{\mathrm{r}_{12}}|N'L'M'] \\
&- (\mathbf{R}_{\mu_x} - \mathbf{R}_{\nu_x})(\mathbf{R}_{\sigma_x} - \mathbf{R}_{\rho_x}) \sum_{NLM}^{n,l+1,m} D^{y}_{NLM} \sum_{N'L'M'}^{n',l',m'+1} D^{z}_{N'L'M'} \\
&\quad \cdot [\, NLM|\tfrac{1}{\mathrm{r}_{12}}|N'L'M'] \\
&+ (\mathbf{R}_{\mu_z} - \mathbf{R}_{\nu_z})(\mathbf{R}_{\sigma_x} - \mathbf{R}_{\rho_x}) \sum_{NLM}^{n+1,l,m} D^{x}_{NLM} \sum_{N'L'M'}^{n',l'+1,m'} D^{y}_{N'L'M'} \\
&\quad \cdot [\, NLM|\tfrac{1}{\mathrm{r}_{12}}|N'L'M'] \\
&+ (\mathbf{R}_{\sigma_z} - \mathbf{R}_{\rho_z})(\mathbf{R}_{\sigma_x} - \mathbf{R}_{\rho_x}) \sum_{NLM}^{n,l,m} D_{NLM} \sum_{N'L'M'}^{n'+1,l'+1,m'} D^{xy}_{N'L'M'} \\
&\quad \cdot [\, NLM|\tfrac{1}{\mathrm{r}_{12}}|N'L'M'] \\
&- (\mathbf{R}_{\sigma_x} - \mathbf{R}_{\rho_x})(\mathbf{R}_{\sigma_x} - \mathbf{R}_{\rho_x}) \sum_{NLM}^{n,l,m} D_{NLM} \sum_{N'L'M'}^{n',l'+1,m'+1} D^{yz}_{N'L'M'} \\
&\quad \cdot [\, NLM|\tfrac{1}{\mathrm{r}_{12}}|N'L'M'] \\
&+ (\mathbf{R}_{\sigma_x} - \mathbf{R}_{\rho_x})(\mathbf{R}_{\sigma_y} - \mathbf{R}_{\rho_y}) \sum_{NLM}^{n,l,m} D_{NLM} \sum_{N'L'M'}^{n'+1,l',m'+1} D^{xz}_{N'L'M'} \\
&\quad \cdot [\, NLM|\tfrac{1}{\mathrm{r}_{12}}|N'L'M'] \Big\}
\end{aligned}
$$

7.4 Additional Material: NMR Shifts of Liquid Water

Table 7.1: Mean value $\bar{\sigma}$ and SEM (in ppm) for one water molecule (100 snapshots from an MD simulation at $T = 275\,\mathrm{K}$, NMR shieldings computed with CD-GIAO-MP2/$\tau = 5$/tzp).

Atom	$\bar{\sigma}$/ppm
O	355.36 ± 0.11
H	31.575 ± 0.015
H	31.577 ± 0.013

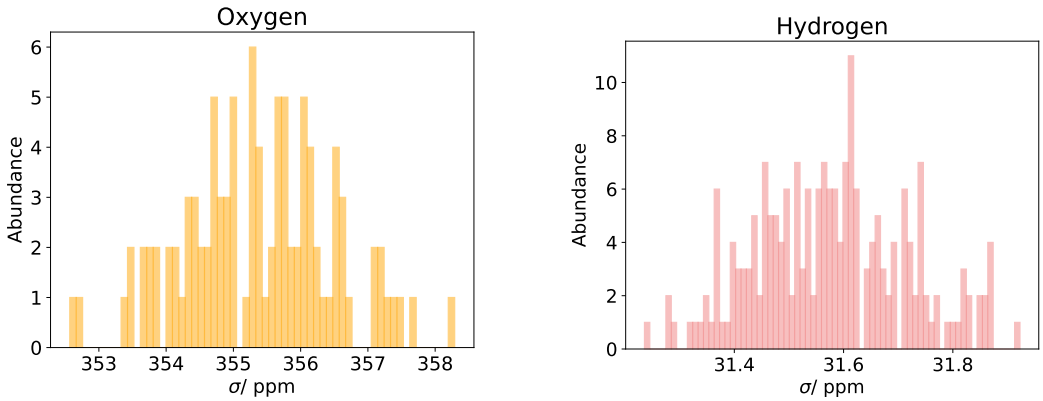

Figure 7.1: Distribution of the shielding constants for one water molecule (taken from 100 snapshots of an MD simulation at $T = 275\,\mathrm{K}$), NMR shieldings computed with CD-GIAO-MP2/$\tau = 5$/tzp.

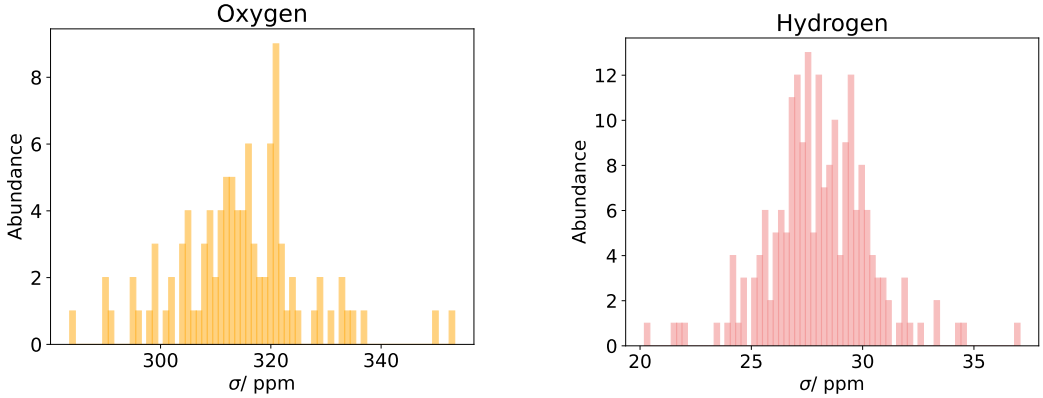

Figure 7.2: Distribution of the shielding constants for the oxygen and hydrogen nuclei of the central water molecule in H_2O-$(H_2O)_n$, n=17-24 clusters (taken from one snapshot of an MD simulation at $T = 275\,\mathrm{K}$), 100 water clusters, NMR shieldings computed with CD-GIAO-MP2/$\tau = 5$/tzp.

Table 7.2: Mean value $\bar{\sigma}$ and SEM (in ppm) for one water molecule (100 snapshots from an MD simulation at $T = 300\,\mathrm{K}$, NMR shieldings computed with CD-GIAO-MP2/$\tau = 5$/tzp).

Atom	$\bar{\sigma}$/ppm
O	355.16 ± 0.12
H	31.571 ± 0.014
H	31.548 ± 0.014

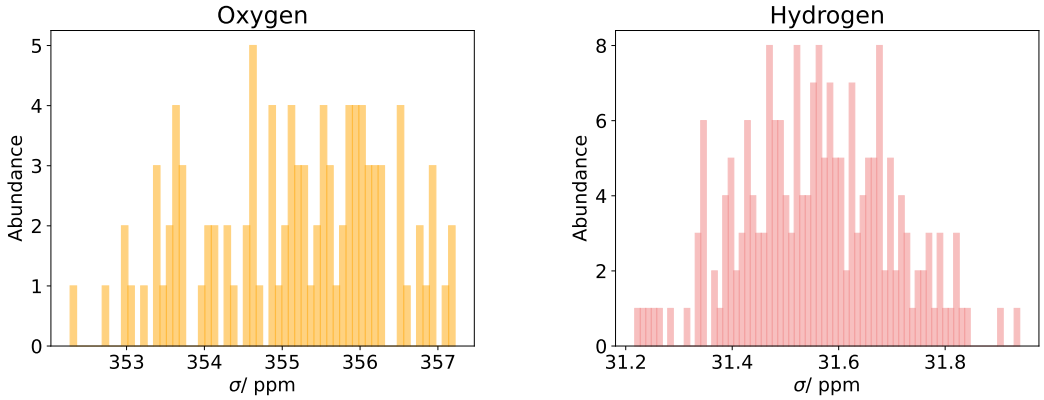

Figure 7.3: Distribution of the shielding constants for one water molecule (taken from 100 snapshots of an MD simulation at $T = 300\,\mathrm{K}$), NMR shieldings computed with CD-GIAO-MP2/$\tau = 5$/tzp.

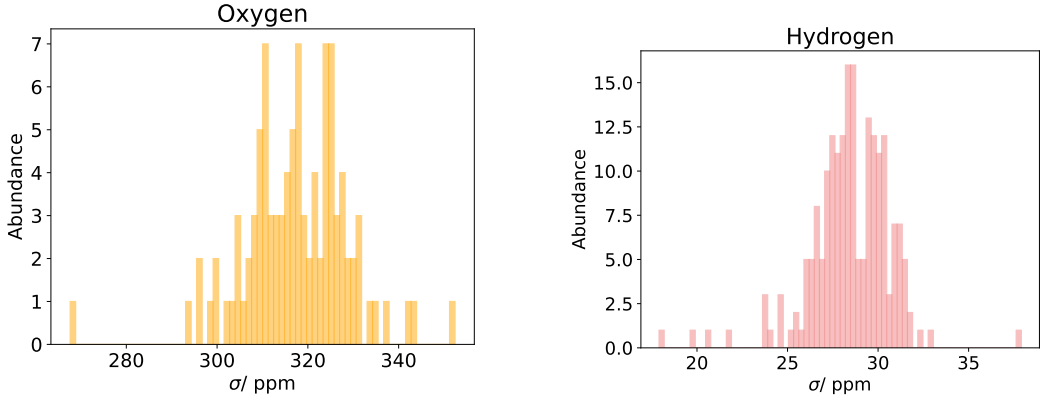

Figure 7.4: Distribution of the shielding constants for the oxygen and hydrogen nuclei of the central water molecule in H_2O-$(H_2O)_n$, n=18-28 clusters (taken from one snapshot of an MD simulation at $T = 300\,\mathrm{K}$), 100 water clusters, NMR shieldings computed with CD-GIAO-MP2/$\tau = 5$/tzp.

7.5 Additional Material: NMR Shift Computations using Cholesky Decomposition

Table 7.3: Geometry (MP2/cc-pVDZ) for acetaldehyde (in Bohr).

O	-2.176345	0.437762	0.000000
C	-0.233835	-0.796044	0.000000
C	2.390462	0.315797	0.000000
H	-0.295756	-2.912532	0.000000
H	2.292683	2.389344	0.000000
H	3.432333	-0.353093	1.675865
H	3.432333	-0.353093	-1.675865

Table 7.4: Geometry (MP2/cc-pVTZ) for acetaldehyde (in Bohr).

O	-2.157138	0.433831	0.000000
C	-0.226917	-0.790827	0.000000
C	2.367010	0.314211	0.000000
H	-0.304339	-2.868243	0.000000
H	2.273238	2.356737	0.000000
H	3.392359	-0.349361	1.651161
H	3.392359	-0.349361	-1.651161

Table 7.5: Geometry (MP2/cc-pVQZ) for acetaldehyde (in Bohr).

O	-2.154064	0.434689	0.000000
C	-0.227412	-0.791047	0.000000
C	2.364522	0.314014	0.000000
H	-0.313976	-2.871364	0.000000
H	2.275560	2.356394	0.000000
H	3.389391	-0.351954	1.649950
H	3.389391	-0.351954	-1.649950

Table 7.6: Geometry (MP2/cc-pVDZ) for ethylene oxide (in Bohr).

O	0.000000	0.000000	1.518392
C	0.000000	-1.391598	-0.804999
C	0.000000	1.391598	-0.804999
H	-1.753811	-2.405014	-1.232003
H	1.753811	-2.405014	-1.232003
H	1.753811	2.405014	-1.232003
H	-1.753811	2.405014	-1.232003

Table 7.7: Geometry (MP2/cc-pVTZ) for ethylene oxide (in Bohr).

O	0.000000	0.000000	1.513368
C	0.000000	-1.377163	-0.804016
C	0.000000	1.377163	-0.804016
H	-1.729801	-2.369231	-1.217918
H	1.729801	-2.369231	-1.217918
H	1.729801	2.369231	-1.217918
H	-1.729801	2.369231	-1.217918

Table 7.8: Geometry (MP2/cc-pVQZ) for ethylene oxide (in Bohr).

O	0.000000	0.000000	1.512662
C	0.000000	-1.374824	-0.804542
C	0.000000	1.374824	-0.804542
H	-1.730505	-2.369892	-1.211989
H	1.730505	-2.369892	-1.211989
H	1.730505	2.369892	-1.211989
H	-1.730505	2.369892	-1.211989

Table 7.9: Geometry (MP2/cc-pVDZ) for vinyl alcohol (in Bohr).

O	-2.195129	0.256379	0.000000
C	0.145030	-0.813296	0.000000
C	2.386197	0.391993	0.000000
H	-1.954247	2.071961	0.000000
H	0.007505	-2.875585	0.000000
H	4.129754	-0.704610	0.000000
H	2.516403	2.455690	0.000000

Table 7.10: Geometry (MP2/cc-pVTZ) for vinyl alcohol (in Bohr).

O	-2.176019	0.251176	0.000000
C	0.155473	-0.811182	0.000000
C	2.358031	0.394718	0.000000
H	-1.971516	2.058132	0.000000
H	0.030762	-2.839102	0.000000
H	4.081182	-0.672971	0.000000
H	2.466711	2.426366	0.000000

Table 7.11: Geometry (MP2/cc-pVQZ) for vinyl alcohol (in Bohr).

O	-2.172420	0.251449	0.000000
C	0.156075	-0.812299	0.000000
C	2.354254	0.395731	0.000000
H	-1.982705	2.056406	0.000000
H	0.027488	-2.842957	0.000000
H	4.078310	-0.673308	0.000000
H	2.464738	2.429187	0.000000

Table 7.12: Geometry for Al_4Cp_4 (in Bohr).

AL	-1.784891	1.784891	-1.801681
AL	-1.784891	-1.784891	1.801681
AL	1.784891	-1.784891	-1.801681
C	2.132792	5.206823	4.601171
C	3.781041	5.679799	2.532231
C	5.679799	3.781041	2.532231
C	5.206823	2.132792	4.601171
C	3.017080	3.017080	5.880905
H	0.457173	6.302569	5.090921
H	3.590764	7.201741	1.155413
H	7.201741	3.590764	1.155413
H	6.302569	0.457173	5.090921
H	2.134157	2.134157	7.521003
AL	1.784891	1.784891	1.801681
C	-5.206823	2.132792	-4.601171
C	-2.132792	-5.206823	4.601171
C	5.206823	-2.132792	-4.601171
C	2.132792	-5.206823	-4.601171
C	-5.206823	-2.132792	4.601171
C	-2.132792	5.206823	-4.601171
C	-5.679799	3.781041	-2.532231
C	-3.781041	-5.679799	2.532231
C	5.679799	-3.781041	-2.532231
C	3.781041	-5.679799	-2.532231
C	-5.679799	-3.781041	2.532231
C	-3.781041	5.679799	-2.532231
C	-3.017080	3.017080	-5.880905
C	-3.017080	-3.017080	5.880905
C	3.017080	-3.017080	-5.880905
H	-6.302569	0.457173	-5.090921
H	-0.457173	-6.302569	5.090921
H	6.302569	-0.457173	-5.090921
H	0.457173	-6.302569	-5.090921

H	-6.302569	-0.457173	5.090921
H	-0.457173	6.302569	-5.090921
H	-7.201741	3.590764	-1.155413
H	-3.590764	-7.201741	1.155413
H	7.201741	-3.590764	-1.155413
H	3.590764	-7.201741	-1.155413
H	-7.201741	-3.590764	1.155413
H	-3.590764	7.201741	-1.155413
H	-2.134157	2.134157	-7.521003
H	-2.134157	-2.134157	7.521003
H	2.134157	-2.134157	-7.521003

Table 7.13: Geometry for B_4tBu_4 (in Bohr).

B	1.169049	1.169049	1.169049
B	-1.169049	1.169049	-1.169049
B	-1.169049	-1.169049	1.169049
B	1.169049	-1.169049	-1.169049
C	2.956474	2.956474	2.956474
C	2.454018	5.821514	2.454018
C	2.454018	2.454018	5.821514
C	5.821514	2.454018	2.454018
H	1.030876	6.155695	1.030876
H	1.812217	6.790370	4.160741
H	4.160741	6.790370	1.812217
H	1.030876	1.030876	6.155695
H	4.160741	1.812217	6.790370
H	1.812217	4.160741	6.790370
H	6.155695	1.030876	1.030876
H	6.790370	4.160741	1.812217
H	6.790370	1.812217	4.160741
C	-2.956474	2.956474	-2.956474
C	-2.956474	-2.956474	2.956474
C	2.956474	-2.956474	-2.956474
C	-5.821514	2.454018	-2.454018
C	-2.454018	-5.821514	2.454018
C	5.821514	-2.454018	-2.454018
C	2.454018	-2.454018	-5.821514
C	-2.454018	5.821514	-2.454018
C	-2.454018	2.454018	-5.821514
C	-5.821514	-2.454018	2.454018
C	-2.454018	-2.454018	5.821514
C	2.454018	-5.821514	-2.454018
H	-6.155695	1.030876	-1.030876

H	-1.030876	-6.155695	1.030876
H	6.155695	-1.030876	-1.030876
H	1.030876	-1.030876	-6.155695
H	-1.030876	6.155695	-1.030876
H	-1.030876	1.030876	-6.155695
H	-6.155695	-1.030876	1.030876
H	-1.030876	-1.030876	6.155695
H	1.030876	-6.155695	-1.030876
H	-6.790370	1.812217	-4.160741
H	-1.812217	-6.790370	4.160741
H	6.790370	-1.812217	-4.160741
H	-4.160741	-6.790370	1.812217
H	4.160741	-1.812217	-6.790370
H	-4.160741	6.790370	-1.812217
H	-1.812217	4.160741	-6.790370
H	6.790370	-4.160741	-1.812217
H	-6.790370	-4.160741	1.812217
H	-4.160741	-1.812217	6.790370
H	-4.160741	1.812217	-6.790370
H	4.160741	-6.790370	-1.812217
H	1.812217	-4.160741	-6.790370
H	-6.790370	4.160741	-1.812217
H	-1.812217	-4.160741	6.790370
H	-6.790370	-1.812217	4.160741
H	-1.812217	6.790370	-4.160741
H	1.812217	-6.790370	-4.160741

Table 7.14: Geometry for C_{60} (in Bohr).

C	0.000000	-2.332479	6.311729
C	2.218320	-0.720776	6.311729
C	1.370997	1.887015	6.311729
C	-1.370997	1.887015	6.311729
C	-2.218320	-0.720776	6.311729
C	4.923464	4.444087	1.134893
C	2.705144	6.055790	1.134893
C	1.334147	5.610327	3.467373
C	2.705144	3.723311	4.908924
C	4.923464	3.002536	3.467373
C	-2.705144	6.055790	1.134893
C	-4.923464	4.444087	1.134893
C	-4.923464	3.002536	3.467373
C	-2.705144	3.723311	4.908924
C	-1.334147	5.610327	3.467373

C	-6.595334	-0.701403	1.134893
C	-5.748012	-3.309194	1.134893
C	-4.377015	-3.754658	3.467373
C	-4.377015	-1.422178	4.908924
C	-5.748012	0.464837	3.467373
C	-1.370997	-6.489281	1.134893
C	1.370997	-6.489281	1.134893
C	2.218320	-5.323042	3.467373
C	0.000000	-4.602266	4.908924
C	-2.218320	-5.323042	3.467373
C	5.748012	-3.309194	1.134893
C	6.595334	-0.701403	1.134893
C	5.748012	0.464837	3.467373
C	4.377015	-1.422178	4.908924
C	4.377015	-3.754658	3.467373
C	5.748012	-0.464837	-3.467373
C	4.377015	1.422178	-4.908924
C	4.377015	3.754658	-3.467373
C	5.748012	3.309194	-1.134893
C	6.595334	0.701403	-1.134893
C	2.218320	5.323042	-3.467373
C	0.000000	4.602266	-4.908924
C	-2.218320	5.323042	-3.467373
C	-1.370997	6.489281	-1.134893
C	1.370997	6.489281	-1.134893
C	-4.377015	3.754658	-3.467373
C	-4.377015	1.422178	-4.908924
C	-5.748012	-0.464837	-3.467373
C	-6.595334	0.701403	-1.134893
C	-5.748012	3.309194	-1.134893
C	-4.923464	-3.002536	-3.467373
C	-2.705144	-3.723311	-4.908924
C	-1.334147	-5.610327	-3.467373
C	-2.705144	-6.055790	-1.134893
C	-4.923464	-4.444087	-1.134893
C	1.334147	-5.610327	-3.467373
C	2.705144	-3.723311	-4.908924
C	4.923464	-3.002536	-3.467373
C	4.923464	-4.444087	-1.134893
C	2.705144	-6.055790	-1.134893
C	1.370997	-1.887015	-6.311729
C	-1.370997	-1.887015	-6.311729
C	-2.218320	0.720776	-6.311729
C	0.000000	2.332479	-6.311729

C	2.218320	0.720776	-6.311729

Table 7.15: Geometry for coronene (in Å).

C	-0.515149	-1.337548	0.000025
C	0.900713	-1.114666	0.000032
C	-1.415886	-0.222738	0.000019
C	1.415903	0.222760	0.000031
C	-0.900696	1.114688	0.000018
C	0.515165	1.337570	0.000025
C	-1.030023	-2.674617	0.000026
C	1.801114	-2.229165	0.000038
C	-2.831321	-0.445493	0.000013
C	2.831338	0.445515	0.000038
C	-1.801097	2.229187	0.000012
C	1.030040	2.674639	0.000024
C	-0.107792	-3.767248	0.000032
C	-2.446919	-2.866601	0.000020
C	1.259004	-3.552179	0.000038
C	3.208445	-1.976781	0.000044
C	-3.316572	-1.790447	0.000013
C	-3.705806	0.685730	0.000006
C	3.705822	-0.685708	0.000044
C	3.316588	1.790469	0.000037
C	-3.208428	1.976803	0.000006
C	-1.258987	3.552201	0.000011
C	2.446935	2.866624	0.000030
C	0.107809	3.767270	0.000017
H	-0.507491	-4.793413	0.000033
H	-2.838757	-3.895787	0.000020
H	1.954169	-4.406366	0.000043
H	3.897339	-2.835959	0.000049
H	-4.405014	-1.957667	0.000009
H	-4.793104	0.511169	0.000002
H	4.793120	-0.511146	0.000049
H	4.405030	1.957689	0.000042
H	-3.897322	2.835981	0.000000
H	-1.954152	4.406388	0.000006
H	2.838774	3.895810	0.000030
H	0.507508	4.793435	0.000017

Table 7.16: Geometry for hexabenzocoronene (in Bohr).

C	2.345539	-1.354198	0.000000
C	2.345539	1.354198	0.000000
C	0.000000	2.708396	0.000000
C	-2.345539	1.354198	0.000000
C	-2.345539	-1.354198	0.000000
C	0.000000	-2.708396	0.000000
C	4.720085	-2.725142	0.000000
C	4.720085	2.725142	0.000000
C	0.000000	5.450284	0.000000
C	-4.720085	2.725142	0.000000
C	-4.720085	-2.725142	0.000000
C	0.000000	-5.450284	0.000000
C	7.076929	-1.384290	0.000000
C	4.737295	5.436655	0.000000
C	-2.339634	6.820945	0.000000
C	-7.076929	1.384290	0.000000
C	-4.737295	-5.436655	0.000000
C	2.339634	-6.820945	0.000000
C	4.737295	-5.436655	0.000000
C	-2.339634	-6.820945	0.000000
C	-7.076929	-1.384290	0.000000
C	-4.737295	5.436655	0.000000
C	2.339634	6.820945	0.000000
C	7.076929	1.384290	0.000000
C	9.359592	-2.766526	0.000000
C	7.075678	6.722381	0.000000
C	-2.283914	9.488908	0.000000
C	-9.359592	2.766526	0.000000
C	-7.075678	-6.722381	0.000000
C	2.283914	-9.488908	0.000000
C	7.075678	-6.722381	0.000000
C	-2.283914	-9.488908	0.000000
C	-9.359592	-2.766526	0.000000
C	-7.075678	6.722381	0.000000
C	2.283914	9.488908	0.000000
C	9.359592	2.766526	0.000000
C	9.361832	-5.405056	0.000000
C	9.361832	5.405056	0.000000
C	0.000000	10.810112	0.000000
C	-9.361832	5.405056	0.000000
C	-9.361832	-5.405056	0.000000
C	0.000000	-10.810112	0.000000
H	11.180924	1.774362	0.000000

H	4.053819	10.570145	0.000000
H	-7.127104	8.795783	0.000000
H	-11.180924	-1.774362	0.000000
H	-4.053819	-10.570145	0.000000
H	7.127104	-8.795783	0.000000
H	4.053819	-10.570145	0.000000
H	-7.127104	-8.795783	0.000000
H	-11.180924	1.774362	0.000000
H	-4.053819	10.570145	0.000000
H	7.127104	8.795783	0.000000
H	11.180924	-1.774362	0.000000
H	11.162923	-6.444917	0.000000
H	11.162923	6.444917	0.000000
H	0.000000	12.889833	0.000000
H	-11.162923	6.444917	0.000000
H	-11.162923	-6.444917	0.000000
H	0.000000	-12.889833	0.000000

Table 7.17: Geometry for the tweezer host guest complex (in Å).

N	5.323376	8.894292	15.683438
H	6.008335	5.939395	14.844914
H	6.728273	6.998069	12.237493
H	6.392142	9.727046	13.165319
C	6.262998	8.852781	16.387144
H	6.051308	5.626441	20.711084
H	5.997106	6.772760	23.401417
H	5.617173	9.514511	22.461966
H	6.237570	8.810903	19.088449
H	6.792653	12.530158	13.779448
H	6.146629	12.155297	16.583965
H	5.919504	12.377819	21.940614
H	5.887650	12.104602	19.050723
C	9.377810	6.257590	14.164567
C	9.926215	5.682276	15.310076
H	11.016157	5.625785	15.456396
C	9.043718	5.168591	16.287568
H	9.453991	4.700972	17.193732
C	7.653156	5.254527	16.118705
H	6.982243	4.857714	16.895181
C	7.098333	5.850326	14.964286
C	7.971701	6.334060	13.992072
C	7.734770	7.093126	12.681579
C	10.002059	6.977921	12.959177

H	11.070414	6.772643	12.766310
C	8.962299	6.579807	11.862203
H	9.107111	7.132495	10.912229
H	8.930308	5.487680	11.674779
C	9.615596	8.451991	13.149839
C	10.361156	9.570561	13.551983
H	11.450394	9.514603	13.705777
C	9.647310	10.759931	13.767308
C	8.238262	10.815569	13.615030
C	7.489468	9.695039	13.230985
C	8.207833	8.518363	12.984638
C	9.822090	8.807060	17.515059
H	10.830319	8.810852	17.079487
C	8.704796	8.801295	16.680516
H	8.825175	8.794557	15.590961
C	7.409615	8.815193	17.246689
N	11.744423	8.894566	20.484590
C	7.689681	6.257865	22.003064
C	7.141251	5.682810	20.857440
C	8.023735	5.169353	19.879815
H	7.613453	4.702048	18.973497
C	9.414299	5.255172	20.048710
H	10.085188	4.858583	19.272100
C	9.969149	5.850705	21.203255
H	11.059154	5.939670	21.322668
C	9.095797	6.334290	22.175558
C	9.332758	7.093158	23.486168
H	10.339256	6.998017	23.930233
C	7.065467	6.978023	23.208564
C	7.451967	8.452089	23.018039
C	6.706388	9.570635	22.615891
C	7.420209	10.760032	22.400636
C	8.829257	10.815687	22.552950
C	9.578069	9.695153	22.936969
H	10.675398	9.727174	23.002606
C	8.859721	8.518453	23.183282
C	7.245799	8.807116	18.652873
C	8.363097	8.801538	19.487410
H	8.242844	8.795009	20.576979
C	9.658272	8.815336	18.921232
C	10.804862	8.853097	19.780803
C	8.105225	6.579754	24.305478
H	7.960428	7.132316	25.255527
H	8.137203	5.487602	24.492756

C	7.801513	12.203787	14.087750
C	10.077315	12.123644	14.325068
H	11.148005	12.377749	14.227276
C	9.032288	13.039536	13.608919
H	9.029798	14.077357	13.998843
H	9.146406	13.040106	12.506286
C	9.500504	12.159341	15.745115
C	10.085405	12.124874	16.993644
H	11.179915	12.104696	17.117201
C	7.813286	12.136269	18.007769
C	7.242342	12.157645	16.694460
C	8.075197	12.193467	15.595946
C	9.265995	12.203911	22.080216
H	10.274844	12.530296	22.388538
C	6.990201	12.123729	21.842854
C	8.035195	13.039648	22.559005
H	8.037675	14.077461	22.169059
H	7.921053	13.040238	23.661635
C	7.567042	12.159396	20.422822
C	6.982154	12.124844	19.174292
C	9.254279	12.136280	18.160177
C	9.825212	12.157730	19.473495
H	10.920926	12.155458	19.583996
C	8.992346	12.193556	20.572007

Table 7.18: Geometry (RI-MP2/cc-pVTZ) for tetramethylsilane (TMS) (in Å).

Si	0.000000	0.000000	0.000000
C	-1.082203	1.082203	1.082203
C	1.082203	-1.082203	1.082203
H	-1.721065	1.721065	0.478646
H	-0.478646	1.721065	1.721065
H	-1.721065	0.478646	1.721065
H	1.721065	-1.721065	0.478646
H	0.478646	-1.721065	1.721065
H	1.721065	-0.478646	1.721065
C	1.082203	1.082203	-1.082203
C	-1.082203	-1.082203	-1.082203
H	1.721065	1.721065	-0.478646
H	0.478646	1.721065	-1.721065
H	1.721065	0.478646	-1.721065
H	-1.721065	-1.721065	-0.478646
H	-0.478646	-1.721065	-1.721065
H	-1.721065	-0.478646	-1.721065

Table 7.19: Geometry (RI-MP2/cc-pVTZ) for coronene (in Å).

C	1.221872	-0.705448	0.000000
C	1.221872	0.705448	0.000000
C	0.000000	-1.410902	0.000000
C	0.000000	1.410902	0.000000
C	-1.221872	-0.705448	0.000000
C	-1.221872	0.705448	0.000000
C	2.446038	-1.412222	0.000000
C	2.446038	1.412222	0.000000
C	0.000000	-2.824445	0.000000
C	0.000000	2.824445	0.000000
C	-2.446038	-1.412222	0.000000
C	-2.446038	1.412222	0.000000
C	3.653002	-0.684306	0.000000
C	2.419129	-2.821440	0.000000
C	3.653002	0.684306	0.000000
C	2.419129	2.821440	0.000000
C	1.233873	-3.505749	0.000000
C	-1.233873	-3.505749	0.000000
C	1.233873	3.505749	0.000000
C	-1.233873	3.505749	0.000000
C	-2.419129	-2.821440	0.000000
C	-3.653002	-0.684306	0.000000
C	-2.419129	2.821440	0.000000
C	-3.653002	0.684306	0.000000
H	4.586359	-1.226066	0.000000
H	3.354986	-3.358869	0.000000
H	4.586359	1.226066	0.000000
H	3.354986	3.358869	0.000000
H	1.231373	-4.584939	0.000000
H	-1.231373	-4.584939	0.000000
H	1.231373	4.584939	0.000000
H	-1.231373	4.584939	0.000000
H	-3.354986	-3.358869	0.000000
H	-4.586359	-1.226066	0.000000
H	-3.354986	3.358869	0.000000
H	-4.586359	1.226066	0.000000

7.6 Additional Material: Magnetically Induced Ring-Current Strengths and Densities

Table 7.20: Geometry (RI-MP2/cc-pVTZ) for 1,6-imino-[10]annulene (in Å).

C	0.083245	-2.318323	-0.706293
C	0.083245	-2.318323	0.706293
C	0.066756	-1.211289	-1.544473
C	-0.346978	0.045521	-1.094782
C	0.065381	1.300406	-1.537845
C	0.057270	2.407054	-0.705121
C	0.057270	2.407054	0.705121
C	0.065381	1.300406	1.537845
C	-0.346978	0.045521	1.094782
C	0.066756	-1.211289	1.544473
N	-1.253534	0.060273	0.000000
H	0.311626	-3.267785	-1.165064
H	0.311626	-3.267785	1.165064
H	0.449738	-1.313831	-2.548354
H	0.510994	1.388710	-2.516756
H	0.298584	3.354987	-1.161428
H	0.298584	3.354987	1.161428
H	0.510994	1.388710	2.516756
H	0.449738	-1.313831	2.548354
H	-1.739698	-0.831173	0.000000

Table 7.21: Geometry (RI-MP2/cc-pVTZ) for 1,6-methano-[10]annulene (in Å).

C	2.353517	-0.707834	0.187099
C	2.353517	0.707834	0.187099
C	1.252449	1.547959	0.155667
C	0.000000	1.117454	-0.295002
C	-1.252449	1.547959	0.155667
C	-2.353517	0.707834	0.187099
C	-2.353517	-0.707834	0.187099
C	-1.252449	-1.547959	0.155667
C	0.000000	-1.117454	-0.295002
C	1.252449	-1.547959	0.155667
C	0.000000	0.000000	-1.260321
H	3.295448	-1.160224	0.457861
H	3.295448	1.160224	0.457861
H	1.347848	2.529951	0.595697
H	-1.347848	2.529951	0.595697
H	-3.295448	1.160224	0.457861
H	-3.295448	-1.160224	0.457861
H	-1.347848	-2.529951	0.595697
H	1.347848	-2.529951	0.595697
H	-0.898995	0.000000	-1.867487
H	0.898995	0.000000	-1.867487

Table 7.22: Geometry (RI-MP2/cc-pVTZ) for 1,6-oxido-[10]annulene (in Å).

C	-2.372706	-0.703610	-0.037295
C	-2.372706	0.703610	-0.037295
C	-1.263759	1.535159	-0.007475
C	0.000000	1.080117	-0.367397
C	1.263759	1.535159	-0.007475
C	2.372706	0.703610	-0.037295
C	2.372706	-0.703610	-0.037295
C	1.263759	-1.535159	-0.007475
C	0.000000	-1.080117	-0.367397
C	-1.263759	-1.535159	-0.007475
H	-3.328750	-1.165315	0.154253
H	-3.328750	1.165315	0.154253
H	-1.364909	2.535581	0.382250
H	1.364909	2.535581	0.382250
H	3.328750	1.165315	0.154253
H	3.328750	-1.165315	0.154253
H	1.364909	-2.535581	0.382250
H	-1.364909	-2.535581	0.382250
O	0.000000	0.000000	-1.232141

Table 7.23 reports the computed and experimental[320] NMR chemical shifts for 1,6-imino-[10]annulene and 1,6-oxido-[10]annulene. The experimental values were obtained from Ref. [320], where the shifts for the outer protons of 1,6-imino-[10]annulene and 1,6-oxido-[10]annulene are reported as a broad signal centered at $\delta = 7.20\,\text{ppm}$ and $\delta = 7.35\,\text{ppm}$, respectively. The molecules with corresponding atom indices are shown in figs. 7.5 and 7.6.

Table 7.23: Computed NMR shielding constants σ(C), σ(H) and shifts δ(C), δ(H) for TMS, 1,6-imino-[10]annulene (imino-annulene), and 1,6-oxido-[10]annulene (oxido-annulene) obtained at the CD-GIAO-MP2/$\tau = 10^{-5}$/tz2p level of theory. The shifts for the molecules can be assigned using the indices in figs. 7.5 and 7.6. Experimental NMR shifts δ_{exp}(H) were taken from Ref. [320].

Molecule	Indices(C)	σ(C)	δ(C)	Indices(H)	σ(H)	δ(H)	δ_{exp}(H)
Imino-annulene	1,2	71.20	128.03	12,13	24.110	7.846	7.20
	6,7	66.89	132.34	16,17	23.974	7.982	
	3,10	67.39	131.84	14,19	23.588	8.368	
	5,8	70.64	128.59	15,18	24.085	7.871	
	4,9	72.86	126.37	20	34.582	-2.626	-1.10
Oxido-annulene	1,2,6,7	68.33	130.91	11,12,15,16	23.923	8.033	7.35
	3,5,8,10	72.21	127.03	13,14,17,18	23.829	8.127	
	4,9	62.70	136.53				
TMS		199.23			31.956		

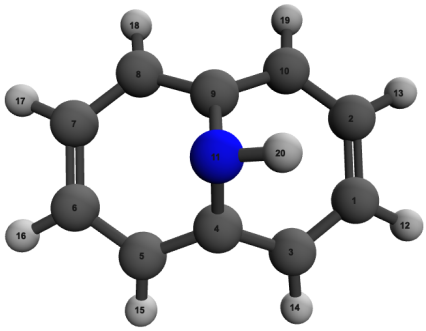

Figure 7.5: Indexed atoms in 1,6-imino-[10]annulene; they can be assigned to the NMR data shown in table 7.23.

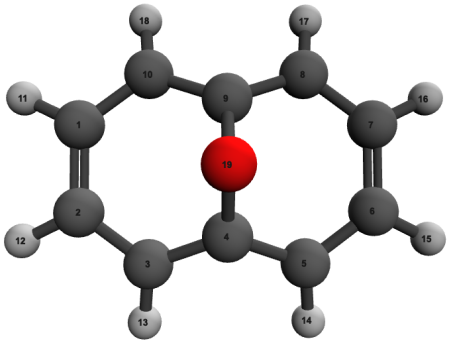

Figure 7.6: Indexed atoms in 1,6-oxido-[10]annulene; they can be assigned to the NMR data shown in table 7.23.

8 List of Publications

- Burger, S.; Lipparini, F.; Gauss, J.; Stopkowicz, S. *J. Chem. Phys.* **2021**, *155*, 074105
- Nottoli, T.; Burger, S.; Stopkowicz, S.; Gauss, J.; Lipparini, F. *J. Chem. Phys.* **2022**, *157*, 084122
- Gauss, J.; Blaschke, S.; Burger, S.; Nottoli, T.; Lipparini, F.; Stopkowicz, S. *Mol. Phys.* **2023**, *121*, e2101562
- Burger, S.; Stopkowicz, S.; Gauss, J. *J. Phys. Chem. A* **2025**, *129*, 623–632